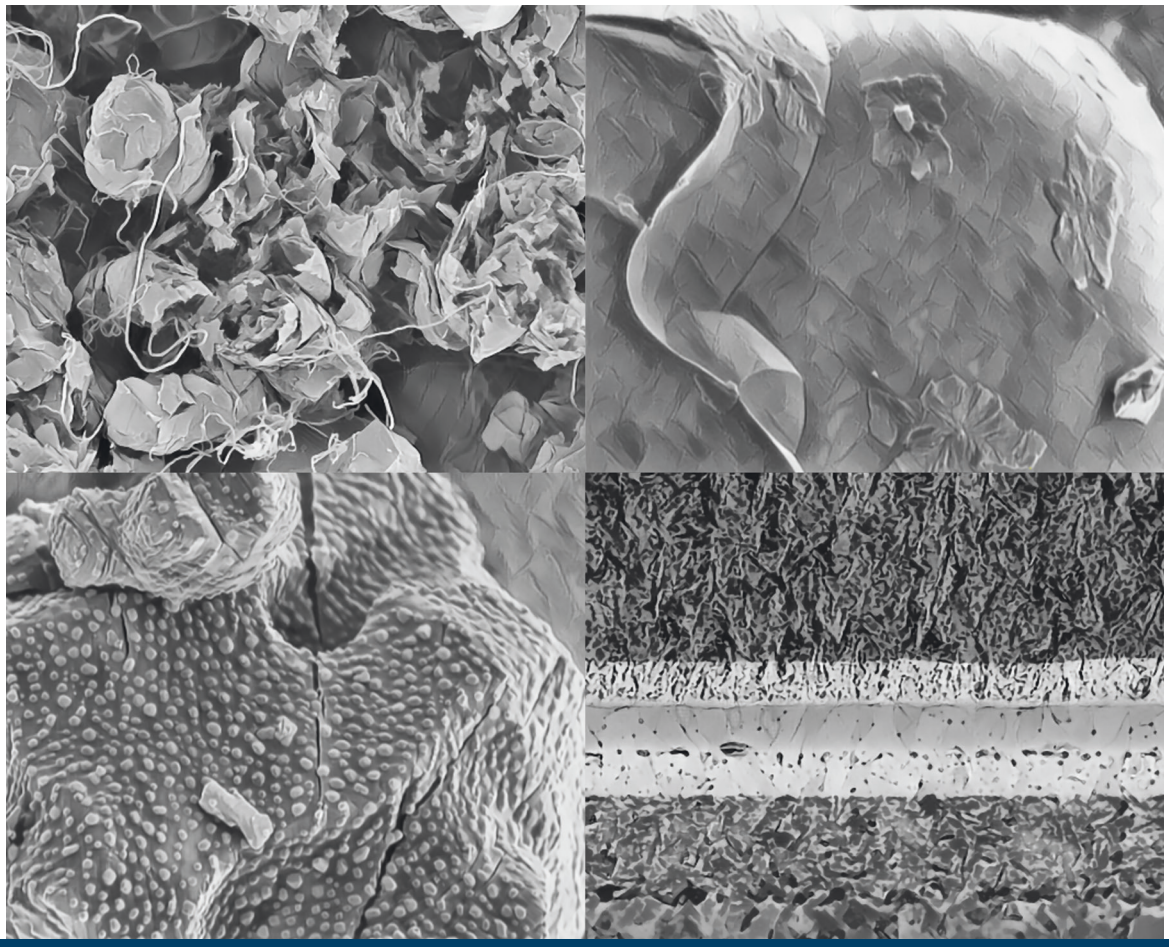

Investigation and implementation of improved and degradation-tolerant fuel electrodes for solid oxide cells

Alexander Schwiers

Energie & Umwelt / Energy & Environment
Band / Volume 634
ISBN 978-3-95806-762-2

Mitglied der Helmholtz-Gemeinschaft

JÜLICH
Forschungszentrum

Schriften des Forschungszentrums Jülich
Reihe Energie & Umwelt / Energy & Environment Band / Volume 634

Forschungszentrum Jülich GmbH
Institut für Energie- und Klimaforschung (IEK)
Werkstoffsynthese und Herstellungsverfahren (IEK-1)

Investigation and implementation of improved and degradation-tolerant fuel electrodes for solid oxide cells

Alexander Schwiers

Schriften des Forschungszentrums Jülich
Reihe Energie & Umwelt / Energy & Environment Band / Volume 634

ISSN 1866-1793 ISBN 978-3-95806-762-2

Bibliografische Information der Deutschen Nationalbibliothek.
Die Deutsche Nationalbibliothek verzeichnet diese Publikation in der
Deutschen Nationalbibliografie; detaillierte Bibliografische Daten
sind im Internet über http://dnb.d-nb.de abrufbar.

Herausgeber und Vertrieb:	Forschungszentrum Jülich GmbH Zentralbibliothek, Verlag 52425 Jülich Tel.: +49 2461 61-5368 Fax: +49 2461 61-6103 zb-publikation@fz-juelich.de www.fz-juelich.de/zb
Umschlaggestaltung:	Grafische Medien, Forschungszentrum Jülich GmbH
Druck:	Grafische Medien, Forschungszentrum Jülich GmbH
Copyright:	Forschungszentrum Jülich 2024

Schriften des Forschungszentrums Jülich
Reihe Energie & Umwelt / Energy & Environment, Band / Volume 634

D 82 (Diss. RWTH Aachen University, 2024)

ISSN 1866-1793
ISBN 978-3-95806-762-2

Vollständig frei verfügbar über das Publikationsportal des Forschungszentrums Jülich (JuSER)
unter www.fz-juelich.de/zb/openaccess.

Abstract

Ni- yttria-stabilized zirconia is commonly used as a fuel electrode cermet in solid oxide cells due to its compelling combination of conductivity, stability, and material compatibility. However, it faces significant degradation when exposed to hydrocarbon-rich fuels, such as tar-containing biogas. Carbon adsorption poisons the Ni component, leading to a decrease in catalytic activity, while the formation of carbon fibers ultimately results in nickel dusting. To address the issue of fuel electrode degradation without the need for fuel pre-treatment, this study investigates two alternative fuel electrode materials. The first material is gadolinia-doped ceria ($Gd_{0.1}Ce_{0.9}O_{2-\delta}$) as a replacement for yttria-stabilized zirconia. Gadolinia-doped ceria possesses mixed electronic and ionic conductivity, allowing it to maintain catalytic activity even when Ni is poisoned. Moreover, it exhibits oxygen storage capacity, potentially aiding in carbon removal. The second candidate is a Ni-exsolution perovskite material, $Sr_{1-x}(Ti_{0.3}Fe_{0.7-y}Ni_y)O_{3-\delta}$. Upon reduction, Ni migrates to the surface, forming nanoparticles that offer a high catalytic surface area. These nanoparticles might be more stable against carbon degradation as they are socketed in the host lattice and can potentially be regenerated through redox-cycling.
One major challenge arises when considering the replacement of the fuel electrode in a specific type of solid oxide cell, namely, the fuel electrode-supported cell. The half cell of this configuration consists of a substrate providing mechanical stability, onto which the fuel electrode and electrolyte are sequentially screen printed and then sintered together at 1400 °C to achieve the desired microstructure and gas-tightness. In state-of-the-art cells, the substrate is composed of NiO- yttria-stabilized zirconia, and the electrolyte is made of yttria-stabilized zirconia. Therefore, high sintering temperatures do not cause interface, structural, or functional degradation. However, if the fuel electrode is modified, interdiffusion can occur. As the sintering temperature cannot be adjusted due to the need for electrolyte gas-tightness, interdiffusion was investigated in symmetrical model cells. The dopant in ceria was changed with the intention of suppressing interdiffusion, resulting in significant but minor changes in the interdiffusion behavior. Additionally, novel sintering techniques and their impact on interdiffusion were explored using compacted powder mixtures. The presence of Ni in the cermet was found to enhance interdiffusion, leading to the formation of Kirkendall voids. These are the primary cause of cell performance degradation, rather than the formation of a mixed phase of ceria and zirconia at the interface. To mitigate porosity, a barrier layer was introduced between the Ni-gadolinia-doped ceria fuel electrode and yttria-stabilized zirconia electrolyte, thereby improving cell performance. Fuel electrode-supported cells with Ni- gadolinia-doped ceria fuel electrodes, with and without the barrier layer, were fabricated and delivered to the Technical University of Munich to assess their performance and degradation tolerance in artificial biogas.

Abstract

The Ni-exsolution material was successfully self-synthesized and investigated in terms of its exsolution behavior, phase stability and carbon degradation tolerance. Although exsolution of nanoparticles was observed, the materials undergo phase transitions at harsher reducing conditions, leading to mechanical instability in compacted pellets. This instability may be attributed to chemical expansion or contraction and secondary phase formation in the presence of H_2O.
Remarkably, when compared to Ni- yttria-stabilized zirconia, $Sr_{1-x}(Ti_{0.3}Fe_{0.7-y}Ni_y)O_{3-\delta}$ exhibited no degradation in terms of carbon deposition or nickel dusting after exposure to tar-containing biogas.

Kurzfassung

Ni- Yttrium-stabilisiertes Zirkoniumoxid wird aufgrund seiner überzeugenden Kombination aus Leitfähigkeit, Stabilität und Materialkompatibilität häufig als Brenngaselektrodenmaterial in Festoxidzellen verwendet. Es leidet jedoch unter erheblicher Degradation, wenn es kohlenwasserstoffhaltigen Brenngasen ausgesetzt ist, wie z.B. teerhaltigem Biogas. Kohlenstoffadsorption vergiftet die Nickelkomponente und führt zu einer verringerten katalytischen Aktivität, während die Bildung von Kohlenstofffasern letztendlich zur Nickelzerstäubung führt. Um das Problem der Brenngaselektrodendegradation ohne die Notwendigkeit einer Brenngasvorbehandlung zu lösen, untersucht diese Arbeit zwei alternative Brenngaselektrodenmaterialien.

Zum einen wurde Gadolinium-dotiertes Ceroxid ($Gd_{0.1}Ce_{0.9}O_{2-\delta}$) als Ersatz für Yttrium-stabilisiertes Zirkoniumoxid untersucht. Gadolinium-dotiertes Ceroxid verfügt über gemischte elektronische und ionische Leitfähigkeit und kann daher selbst bei degradierten Nickelpartikeln die katalytische Aktivität aufrechterhalten. Weiterhin besitzt es eine Sauerstoffspeicherkapazität, die möglicherweise bei der Entfernung von adsorbiertem Kohlenstoff unterstützend wirken kann.

Zum anderen wurde ein „Ni-Exsolution" Perowskit, $Sr_{1-x}(Ti_{0.3}Fe_{0.7-y}Ni_y)O_{3-\delta}$, untersucht. Bei der Reduktion wandert Nickel an die Oberfläche und bildet Nanopartikel, die eine höhere katalytische Oberfläche besitzen. Diese Nanopartikel könnten toleranter gegenüber Kohlenstoffdegradation sein, da sie im Wirtsgitter verankert sind und möglicherweise durch Redoxzyklierung regeneriert werden können.

Eine große Herausforderung stellt der Typ der Festoxidzelle dar, in der die Substitution der Brenngaselektrode vorgenommen werden soll, in diesem Fall in der brenngaselektrodengestützten Zelle. Die Halbzelle dieses Zelltyps besteht aus einem Substrat, das mechanische Stabilität bietet, auf das die Brenngaselektrode und der Elektrolyt nacheinander siebgedruckt und anschließend zusammen bei 1400 °C gesintert werden, um die gewünschte Mikrostruktur und Gasdichtigkeit zu erzielen. In Zellen, die dem heutigen Stand der Technik entsprechen, besteht das Substrat aus NiO- Yttrium-stabilisiertem Zirkoniumoxid und der Elektrolyt besteht aus Yttrium-stabilisiertem Zirkoniumoxid. Daher führen hohe Sintertemperaturen nicht zur Veränderung der Grenzflächeneigenschaften zwischen den einzelnen Schichten und zu einer verringerten Zellleistung. Wenn jedoch die Brenngaselektrode ausgetauscht wird, kann Interdiffusion mit den benachbarten Schichten auftreten. Aufgrund der Notwendigkeit, einen dichten Elektrolyten zu sintern, kann die Sintertemperatur nicht angepasst werden. Deshalb wurde die Interdiffusion in symmetrischen Modellzellen untersucht. Das Dotierkation im Ceroxid wurde mit der Absicht geändert, die Interdiffusion zu unterdrücken. Der Austausch des Dotierkations führt zu signifikanten, aber geringfügigen Änderungen im Interdiffusionsverhalten. Zudem wurden neuartige Sintertechniken und deren

Auswirkungen auf die Interdiffusion in verdichteten Pulvermischungen untersucht. Die Anwesenheit von Nickel in der Brenngaselektrode verstärkt die Interdiffusion und führt zur Bildung von Kirkendall-Poren. Diese Poren sind die Hauptursache für die Leistungsverschlechterung der Zelle, nicht die Bildung einer Cer-Zirkoniumoxidmischphase an der Grenzfläche. Zur Verringerung der Porosität wurde eine Barriereschicht zwischen der Ni- Gadolinium-dotierten Ceroxid Brenngaselektrode und dem Yttrium-stabilisierten Zirkoniumoxid Elektrolyten eingeführt, wodurch die Leistung der Zelle verbessert wurde. Brenngaselektrodengestützte Zellen mit Ni- Gadolinium-dotierten Ceroxid Brenngaselektroden wurden mit und ohne Barriereschicht hergestellt. Diese wurden an die Technischen Universität München gesendet, um hinsichtlich ihrer Leistung und ihrer Toleranz gegenüber künstlichem Biogas untersucht zu werden.
Das „Ni-Exsolutionsmaterial“ wurde erfolgreich selbst synthetisiert und bezüglich seines „Exsolutionsverhaltens“, der Kristallstrukturstabilität und der Kohlenstoffdegradationstoleranz untersucht. Obwohl die Exsolution von Nanopartikeln beobachtet wurde, führen die Materialien bei stark reduzierenden Bedingungen Kristallstrukturübergänge durch, die zu mechanischer Instabilität in verdichteten Tabletten führen. Diese Instabilität kann auf chemische Expansion oder Kontraktion und die Bildung von Sekundärphasen in Gegenwart von Feuchtigkeit oder H_2O zurückzuführen sein.
Bemerkenswerterweise zeigte $Sr_{1-x}(Ti_{0.3}Fe_{0.7-y}Ni_y)O_{3-\delta}$, im Vergleich zu Ni- Yttrium-stabilisiertem Zirkoniumoxid, keine Kohlenstoffablagerungen oder Nickelzerstäubung nach der Exposition gegenüber teerhaltigem Biogas.

Table of contents

Abbreviations

0D	Zero-dimensional
10GDC	Gadolinia-doped ceria / $Gd_{0.1}Ce_{0.9}O_{2-\delta}$
10SDC	Samaria-doped ceria / $Sm_{0.1}Ce_{0.9}O_{2-\delta}$
10XDC	Doped ceria, with 10X = 10 mol% of Y, Gd or Sm
10YDC	Yttria-doped ceria / $Y_{0.1}Ce_{0.9}O_{2-\delta}$
1D	One-dimensional
20GDC	$Gd_{0.2}Ce_{0.8}O_{2-\delta}$
2D	Two-dimensional
3D	Three-dimensional
3ITT	Three interval thixotropy test
3YSZ	3 mol% yttria-stabilized zirconia / $Y_{0.058}Zr_{0.942}O_{1.971}$
8YSZ	8 mol% yttria-stabilized zirconia / $Y_{0.148}Zr_{0.852}O_{1.926}$
ap	As prepared
BE	Backscattered electrons
BET	Brunauer–Emmett–Teller
CHP	Combined heat and power
CPE	Constant phase element
DPB	Double phase boundary
ECM	Equivalent circuit model
EDS	Energy-dispersive X-ray spectroscopy
EIS	Electrochemical impedance spectroscopy
EMF	Electromotive force
ESC	Electrolyte-supported cell
FAST-SPS	Field-Assisted Sintering technique / Spark Plasma Sintering
FC	Full cell
FESC	Fuel electrode-supported cell
FZJ	Forschungszentrum Jülich GmbH
HC	Half cell
HHV	Higher heating value
ICP-OES	Inductively coupled plasma optical emission spectroscopy
IEK	Institute of Energy and Climate Research
IEK-1	Materials Synthesis and Processing
LDS	Laser diffraction spectrometry

LHV	Lower heating value
LSCF	Lanthanum strontium cobalt ferrite / $La_{0.58}Sr_{0.4}Co_{0.2}Fe_{0.8}O_{3-\delta}$
LVE	Linear viscoelastic region
MIEC	Mixed ionic and electronic conductivity
MSC	Metal-supported cell
OCV	Open circuit voltage
PSD	Particle size distribution
PVD	Physical vapor deposition
R-CPE	Resistor in parallel with a constant phase element
red	Reduced
reox	Reoxidized
RP	Ruddlesden-Popper
rSOC	Reversible solid oxide cell
SE	Secondary electrons
SEM	Scanning electron microscopy
SF-P	$SrFe_{12}O_{19}$
SF-RP	$Sr_3Fe_2O_6$
SIMS	Secondary ion mass spectrometry
SOC	Solid oxide cell
SOEC	Solid oxide electrolysis cell
SOFC	Solid oxide fuel cell
SSR	Solid state reaction
sSTFN	A-site substoichiometric Ni-doped strontium titanium ferrite / $Sr_{0.95}Ti_{0.3}Fe_{0.63}Ni_{0.07}O_{3-\delta}$
STF	Strontium titanium ferrite / $SrTi_{0.3}Fe_{0.7}O_{3-\delta}$
STFN	Ni-doped strontium titanium ferrite / $SrTi_{0.3}Fe_{0.63}Ni_{0.07}O_{3-\delta}$
ST-RP	$Sr_4Ti_3O_{10}$, Sr_2TiO_4
TGA	Thermogravimetric analysis
TPB	Triple phase boundary
TUM	Technical University of Munich
UHS	Ultra-fast high temperature sintering
XRD	X-ray diffraction
ZEA-3	Institute for Engineering, Electronics and Analytics 3

1 Introduction

According to the United Nations, climate change is one of the most pressing global issues of our era [1]. Hydrogen, as an energy carrier or as foundational element for Power-to-X processes, is regarded as "the ultimate step on the path away from carbon-based fossil energy" [2]. Ideally, hydrogen is produced from carbon-free, renewable energy sources, such as solar or wind power, which provide energy for the electrolysis of water. During electrolysis, water is split up into hydrogen and oxygen. This process not only circumvents carbon dioxide emissions but also aids in stabilizing the inherent fluctuations of these renewable sources. To meet at least parts of the required demands for hydrogen, Germany recently updated (July 2023) its national hydrogen strategy and plans on establishing up to 10 GW of hydrogen generation capacity by the year 2030 [3].

Solid oxide cells (SOCs) are a key enabler for a successful transition to a mandatory hydrogen-based economy. SOCs fulfill two vital roles: operating as solid oxide electrolysis cells (SOECs) to produce hydrogen from water (or other chemical energy carriers encompassed within Power-to-X technologies [4]), and as solid oxide fuel cells (SOFCs) to generate electricity from hydrogen (or alternative fuels). In the right setup, a SOC can even be operated as both a fuel cell or an electrolysis cell, allowing for a switch between these two modes [5]. Such cells are referred to as reversible solid oxide cells (rSOCs).

Currently, the carbon-free production of green hydrogen constitutes only a minor portion of the total hydrogen output [6]. The ultimate goal is complete reliance on green hydrogen in the future. One potential energy source is the gasification of biomass. The produced biogas can be used as fuel for SOFCs. Nevertheless, being carbon neutral, carbon dioxide is a byproduct of the process [7]. Biogas contains a high share of the hydrocarbon methane and carbon dioxide [8], with only a small amount of hydrogen. SOCs, operating at higher temperatures, can internally reform biogas components like methane into hydrogen and carbon monoxide. The most common reformation process is steam reforming [9]. If the steam to carbon ratio during SOC operation remains sufficiently high, no carbon-related degradation of the fuel electrode is expected [10]. Nonetheless, biogas contains higher hydrocarbons as impurities, such as tars, leading to severe degradation of the commonly used fuel electrodes, composed of a cermet of Ni as a catalyst and electron conductor and 8 mol% yttria-stabilized zirconia ($Y_{0.148}Zr_{0.852}O_{1.926}$, 8YSZ) as an ion conductor [11,12]. Carbon deposition on the Ni-surface blocks active sites for catalysis [13] and the growth of carbon fibers causes Ni-dusting [14,15], ultimately leading to a failure of the cell.

Hence, on the exploration of alternative electrode materials, it is imperative to consider not only performance improvements but also degradation tolerance. This thesis investigates two potential alternatives to the commonly used Ni-8YSZ fuel electrode, which may enhance resistance to carbon deposition and potentially boost

cell performance. The first material is gadolinia-doped ceria ($Gd_{0.1}Ce_{0.9}O_{2-\delta}$, 10GDC), intended to replace 8YSZ in the fuel electrode cermet. The second material is a Ni-doped strontium titanium ferrite perovskite ($SrTi_{0.3}Fe_{0.63}Ni_{0.07}O_{3-\delta}$, STFN) to harness the concept of Ni-exsolution. The primary focus lies on the properties of the materials and interaction with other cell components, particularly during high temperature sintering and reduction processes, as encountered during SOC fabrication and application conditions. These materials are ultimately intended for integration into a fuel electrode-supported cell (FESC). The mechanical stability of this cell type is provided by a porous substrate which consist out of the same material as the fuel electrode, NiO- yttria-stabilized zirconia. Functional layers are typically applied through sequential screen printing and sintering steps. A key advantage of a FESC is the utilization of a thin 8YSZ electrolyte (~10 µm), decreasing ohmic resistance compared to other cell configurations. However, in the fabrication of the thin electrolyte lies also the disadvantage of FESCs. To achieve the desired microstructure of the substrate and the functional layers as well as the gas-tightness of the electrolyte, the half cell (HC), containing the substrate, fuel electrode, and electrolyte, needs to be sintered at high temperatures, in our case 1400 °C. Since conventional FESCs use only NiO and 8YSZ in the HC, high-temperature sintering is unproblematic. However, when substituting the fuel electrode material, interdiffusion and reactions at the adjacent substrate and electrolyte interfaces become inevitable. These processes at the interfaces are undesired and often decrease the cell performance. Therefore, alternative fuel electrode materials need to possess additional properties including material compatibility and stability at the processing temperature of 1400 °C.
In contrast, electrolyte-supported cells (ESCs) gain their mechanical stability from a thicker and sintered electrolyte. This increases the flexibility for alternative electrode materials, as the sintering temperature can be adjusted to match the properties of the chosen materials. Consequently, ESCs are often used to investigate the performance of new materials. In this thesis, ECSs serve as tools to investigate material effects and interactions, circumventing the challenges associated with FESC fabrication.

Outline
This thesis has been organized as follows. Chapter 2 provides a concise overview of the fundamental theories, methodologies, and concepts considered in the thesis.
In Chapter 3 a general introduction along with a brief explanation of the synthesis and characterization methods applied for both materials is given.
Following this, the thesis is divided into two distinct parts. Each part comprises a separate section dedicated to motivation, detailed experimental results, and discussions for (gadolinia-) doped ceria in Chapter 4 and Ni-doped strontium titanium ferrite in Chapter 5.
Finally, Chapter 6 presents an overarching conclusion and summary encompassing both materials and the entire thesis.

2 Fundamental background

This chapter briefly introduces electrochemical principles and devices, mass transport in solids and metal exsolution. Furthermore, (gadolinia-) doped ceria and Ni-doped strontium titanium ferrite are introduced as potential materials for SOC applications, regarding their relevant physical properties.

2.1 Solid oxide cells

SOCs are defined by their solid oxygen-ion conducting electrolyte. They offer the dual functionality of either converting chemical energy to electricity (SOFC) or reversing the process by converting electrical energy into chemical energy (SOEC). In the simplest case, SOFCs convert hydrogen (H_2) and oxygen (O_2) into water (H_2O) and electricity while SOECs convert H_2O into H_2 and O_2 while consuming electrical energy.
As this work is concerned with alternative fuel electrode materials for SOFCs the focus will be on the fundamentals in SOFCs. Since SOECs reverse the reaction of a SOFC, the same holds for the chemical reactions and mechanisms presented in this section.
Basically, an SOFC is a galvanic cell which converts the energy released by a spontaneous redox reaction into electrical energy. The reactions for the simple case of hydrogen as a fuel and oxygen are expressed in Equation (2.1)-(2.3).

$$\begin{aligned} &\text{Anode:} && \mathrm{H_2 \rightarrow 2\,H^+ + 2\,e^-} \\ & && \mathrm{2\,H^+ + O^{2-} \rightarrow H_2O} \end{aligned} \tag{2.1}$$

$$\text{Cathode:} \qquad \mathrm{\frac{1}{2}\,O_2 + 2\,e^- \rightarrow O^{2-}} \tag{2.2}$$

$$\text{Overall:} \qquad \mathrm{H_2 + \frac{1}{2}\,O_2 \rightarrow H_2O} \tag{2.3}$$

The reduction and oxidation reactions proceed in two chambers, which are spatially separated by the electrolyte (galvanic half cells). The current can be directed through an external wire connecting these two half cells, being used as electrical energy. The electrolyte conducts O^{2-} which combine with protons to form water. The whole process is illustrated in Figure 2.1.
The heating value is a measure for available chemical energy contained in a fuel. It corresponds to the reaction enthalpy ΔH_R which is equivalent to the enthalpy of water formation $\Delta H_{f_{\mathrm{H_2O}}}$ (since $\Delta H_{f_{\mathrm{H_2}}} = \Delta H_{f_{\mathrm{O_2}}} = 0$). The heating value is dependent on the formed waters state of aggregation. Therefore, we can distinguish between

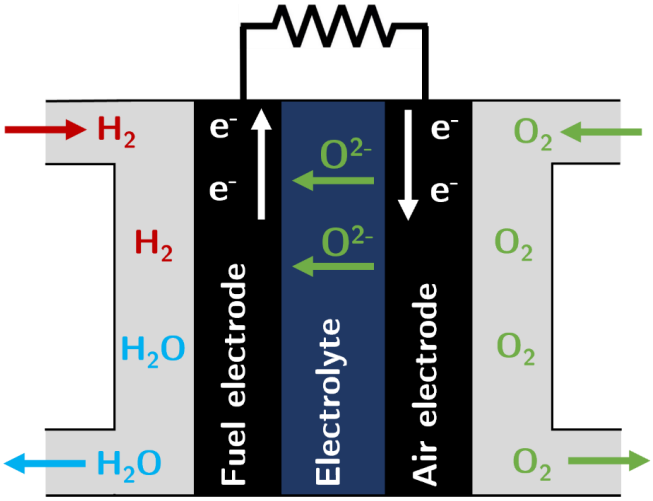

Figure 2.1: Schematic illustration of a SOFC.

the lower heating value (LHV), LHV$= -\Delta H_{f_{\mathrm{H_2O_{(g)}}}} = 241.82\ \frac{\mathrm{kJ}}{\mathrm{mol}}$ corresponding to gaseous water and a higher heating value (HHV), HHV $= -\Delta H_{f_{\mathrm{H_2O_{(l)}}}} = 285.83\ \frac{\mathrm{kJ}}{\mathrm{mol}}$ corresponding to liquid water, at thermodynamic standard conditions, as all thermodynamic potentials are temperature- and pressure-dependent. The difference between the LHV and HHV represents the molar latent heat of water vaporization. The maximal thermodynamic efficiency of a fuel cell is defined by the change in Gibbs free energy of the reaction ΔG_R, which represents the maximum amount of work provided by a thermodynamical system or a chemical reaction at constant pressure p and temperature T, divided by ΔH_R. The efficiency is calculated for the LHV in Equation (2.4) because SOFCs operate at elevated temperatures and the produced water is in gaseous state.

$$\eta = \frac{\Delta G_R}{\Delta H_R} = \frac{\Delta G_{R_{\mathrm{H_2O_{(g)}}}}}{\Delta H_{f_{\mathrm{H_2O_{(g)}}}}} = \frac{-228.57\ \mathrm{kJ/mol}}{-241.82\ \mathrm{kJ/mol}} \approx 94.5\% \tag{2.4}$$

Hence, 94.5 % of the available energy is converted to electricity while the remaining 5.5 % are converted to thermal energy. This divergence arises because some of the available energy to do work is lost in entropy S. Entropy is proportional to temperature. At standard conditions the entropy change of the water formation reaction $\Delta S_{R_{\mathrm{H_2O_{(g)}}}}$ is negative implying the reaction is unfavoured, according to the general drive for an increase in entropy. Since the reaction is exothermic, it is enthalpy-driven, meaning the drive towards lower energy allows the reaction to

proceed, as long as the temperature is sufficiently low and $\Delta G_{R_{H_2O_{(g)}}}$ is negative. Therefore, the theoretical efficiency of a fuel cell decreases with increasing temperature (see Equation (2.5)).

$$\eta = \frac{\Delta G_R}{\Delta H_R} = \frac{\Delta G_{R_{H_2O_{(g)}}}}{\Delta H_{f_{H_2O_{(g)}}}} = \frac{\Delta H_{f_{H_2O_{(g)}}} - T\Delta S_{R_{H_2O_{(g)}}}}{\Delta H_{f_{H_2O_{(g)}}}} = 1 - \frac{T\Delta S_{R_{H_2O_{(g)}}}}{\Delta H_{f_{H_2O_{(g)}}}} \tag{2.5}$$

In theory, if the thermal energy can be fully used to drive a Carnot engine, the efficiency of such a combined system at higher temperatures is comparable to the efficiency of a fuel cell operated at lower temperatures.
There are two common "myths" regarding fuel cell efficiency: i) Fuel cells are not limited by the Carnot efficiency. This is false. For a Carnot engine where the energy for the high temperature reservoir is supplied by the maximum heat generated by the chemical reaction at $\Delta G_R = 0$, the efficiencies of a Carnot engine and a fuel cell are comparable. Nevertheless, in practical application fuel cells do not have to bother about the high temperature of the heat engine.
ii) Fuel cells can achieve efficiencies greater than unity. Depending on the used fuel ΔS_R has a positive value. Due to Equation (2.5), it is often stated in the SOC community that efficiencies of over 100 % are reached if ΔS_R is positive, which is by definition not possible. It is neglected that such reactions absorb heat from the surroundings and convert it to additional electrical energy. If this heat is added to the overall energy input of the system, the efficiencies for reactions with $\Delta S_R > 0$ become unity.[16]
In reality, electrical efficiencies in the range of 45-65 % are typically achieved, also depending on the used fuel. If waste heat is utilized in combined heat and power (CHP) applications, efficiencies exceeding 85 % are achievable.
Therefore, from a thermodynamic perspective, decreasing operating temperature of a single fuel cell system is beneficial. Lower operating temperatures might also aid longevity of the system components due to decreasing degradation rates. In addition, system costs decrease. Cheaper materials could be implemented (especially for interconnects and sealings) as well balance of plant costs (e.g., insulation costs) are reduced. Furthermore, reduced operating temperatures enable alternative applications beyond stationary power generation, also due to more rapid start-up and thermal cycling capabilities. On the contrary, higher operation temperatures facilitate the internal reformation of hydrocarbon based fuels (see Section 2.3) and decrease polarization losses.[17] Polarization losses diminish the theoretical (thermodynamic) electromotive force (EMF) E^0 or reversible open circuit voltage (OCV). E^0 corresponds to the maximum potential difference between the electrodes provided by a chemical reaction when not connected to any circuit or load. E^0 gives the energy provided per unit charge and is linked to ΔG_R, according to the principle of energy conservation (see Equation (2.6)). For the LHV this corresponds to an EMF of:

$$E^0 = \frac{-\Delta G_R}{nF} = \frac{228.571 \text{ kJ/mol}}{2F} = 1.184 \text{ V} \tag{2.6}$$

where F is the Faraday's constant and n the number of exchanged electrons ($n = 2$ for water formation).
E^0 is not only temperature-dependent, but also (partial) pressure-dependent. ΔG_R is linked to the activity a of the educts and products of the reaction according to Equation (2.7), where v_i is the stoichiometric coefficient of component i.

$$\Delta G_R = \Delta G_R^0 - RT \ln \prod_{i=1}^{k} a_i^{v_i} \tag{2.7}$$

By combining Equation (2.6) and (2.7) we get the Nernst equation which shows the voltage dependency on chemical activity (see Equation (2.8)).

$$\Delta E = \Delta E^0 - \frac{RT}{nF} \ln \prod_{i=1}^{k} a_i^{v_i} \tag{2.8}$$

If $a_i = 1$, activity equals concentration c_i. For gases, as used as reactants in fuel cells, the partial pressure p_j is defined as the molar fraction of j x_j times the total pressure of the systems p_0. Therefore, we can rewrite the Nernst equation to express E in terms of its dependence on the partial pressures of gaseous reactants and products, resulting in Equation (2.9), for a fuel cell operated on H_2.

$$\Delta E = \Delta E^0 - \frac{RT}{2F} \ln \frac{p(H_2) p(O_2)^{\frac{1}{2}}}{p(H_2O)} \tag{2.9}$$

Polarization losses
When the electric circuit is closed, ions and electrons start to move, and the kinetics of the electrochemical reaction become relevant, resulting in voltage losses referred to as overpotentials. There are three major losses which result in a decrease in E according to Equation (2.10):

$$\Delta E = \Delta E^0 - (\eta_{a,a} + \eta_{a,c}) - \eta_o - (\eta_{c,a} + \eta_{c,c}) - R_l \tag{2.10}$$

where η_a denotes the activation polarization or overpotential of the electrodes (for both the anode $\eta_{a,a}$ and cathode $\eta_{a,c}$). η_o denotes the ohmic polarization of the fuel cell. Overpotentials caused by mass transport limitations of reactants to the active electrode layers are called concentration polarization losses η_c (anode $\eta_{c,a}$ and cathode $\eta_{c,c}$, respectively). The EMF might further deviate from the thermodynamic equilibrium potential due electron leakage through the electrolyte, resulting in internal currents, or by reactant and gas crossover through the electrolyte as well as

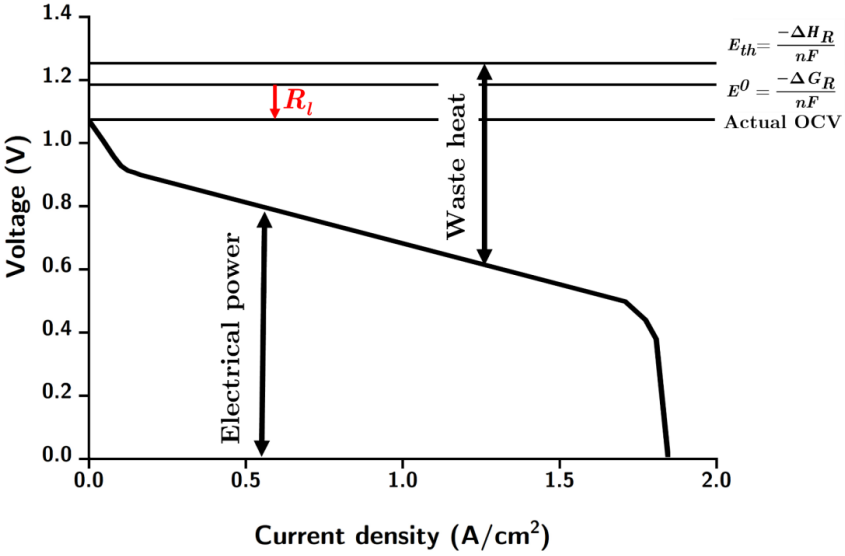

Figure 2.2: Schematic illustration of the voltage-current characteristic of a fuel cell.

impurities in the fuel cell. These losses are summarized in R_l. Figure 2.2 illustrates the characteristic voltage-current relationship of a fuel cell.

Activation polarization

The voltage overpotential caused by the activation polarization is given by the energy barrier for oxidation and reduction at the electrodes. This corresponds to the activation energy required to initiate the electrochemical reaction. A typical fuel electrode consists of an ion-conducting ceramic mixed with an electron-conducting metal, ideally possessing high activity for facilitating the hydrogen oxidation reaction. Catalysts serve as a means to reduce activation energy and enhance reaction rates. Both materials form a metal-ceramic composite, known as cermet, wherein the arrangement of the metal needs to ensure the existence of electronic percolation paths.

The fuel electrode reaction takes place at the interfaces where the ion-conductive ceramic, metal, and a pore volume housing the fuel gas converge. At this juncture, referred to as the triple phase boundary (TPB), hydrogen from the fuel undergoes oxidation, coming into contact with the reduced oxygen generated at the air electrode, forming water. Simultaneously, electrons are generated and subsequently transferred through the external circuit. To overcome the energy barrier at the TPBs of the electrode, preventing a spontaneous reaction, an activation energy is necessary.

The influence of the activation polarization on the current density i is usually described by the Butler-Volmer Equation (see Equation (2.11)):

$$i = i_0 \left(\exp\left(a \frac{nF\eta_{a,el}}{RT} \right) - \exp\left((1-a) \frac{nF\eta_{a,el}}{RT} \right) \right) \tag{2.11}$$

where i denotes the current through the cell and i_0 the exchange current density, which is the rate of exchanged electrons at equilibrium, giving a measure for the performance of an electrode to promote an electrochemical reaction. a is the charge transfer coefficient of the electrode, R is the universal gas constant, and $\eta_{a,el}$ the activation overpotential of the according electrode. If the charge transfer coefficient a differs for the fuel and air electrode (where O_2 is reduced), the activation polarization needs to be calculated separately for each electrode. Activation polarization dominates at low current densities and diminishes with increasing current.
Various factors influence the activation polarization, like reaction mechanism, catalyst type and morphology, operating conditions, and the concentration of the reacting species.[18]

Ohmic polarization
The ohmic overpotential arises from resistances caused by charge transport processes of ions and electrons through the electrodes, electrolyte and the interconnects. It is directly proportional to the current i and follows Ohm's law according to Equation (2.12), where σ and l is the conductivity and thickness of the corresponding layer, respectively.

$$\eta_a = \frac{i_{cell}}{\sigma} l \tag{2.12}$$

Concentration polarization
If the rate of reactant supply to the electrodes is smaller compared to their consumption or the reaction rate, the voltage drops due to concentration overpotential. This is especially the case at high current densities where the reaction rates are elevated. In FESCs the concentration polarization is mainly caused by the microstructure of the substrate layer, limiting gas diffusion.
By combining the Nernst Equation and Fick's law of diffusion, the concentration polarization can be derived using the limiting current density i_l, which describes the current density at which the rate of consumption of the reactants equals the rate of diffusion to the surface. This results in an effective reactant concentration at the electrode of zero. At this point and since fuel cells cannot produce more current than i_l, $i_l = i_{cell}$. The concentration polarization is given by Equation (2.13).[19–21]

$$\eta_c = \frac{RT}{nF} \ln \frac{i_l}{i_l - i_{cell}} \tag{2.13}$$

2.2 Solid oxide cell designs

There exist three main SOC designs: the fuel electrode-supported cell (FESC), the metal-supported cell (MSC), and the electrolyte-supported cell (ESC). They are defined by the layer providing mechanical stability. In the case of FESCs, mechanical support is provided by a porous substrate, typically composed of the same material as the fuel electrode. MSCs share a similar overall configuration with FESC, but the substrate is made of a metal. In ESCs mechanical stability is provided by the electrolyte.
Essential functional layers present in all cell designs include the fuel and steam electrodes. Depending on the used materials, diffusion barrier layers can be implemented to prevent the formation of undesired secondary phases. The different cell designs for planar cells are illustrated in Figure 2.3. In addition to planar configurations there are tubular or roll configurations.[22]
FESCs and MSCs have the advantage of employing thin electrolytes, which leads to reduced ohmic overpotentials and hence promising power densities, especially for stationary applications. Nevertheless, the challenge lies in the fabrication and integration of alternative fuel electrode materials because the electrolyte needs high-temperature sintering for gas-tightness. The composite of substrate, fuel electrode and electrolyte is referred to as a half cell (HC). Since the HC needs to be sintered at high temperatures, interdiffusion at interfaces and constrained sintering takes place between different materials.
In ESCs the electrolyte needs to exhibit a critical thickness to provide mechanical stability but can be sintered as a single layer. Consequently, ESCs are better suited for exploring new potential fuel electrode materials since they can be sintered at lower temperatures.

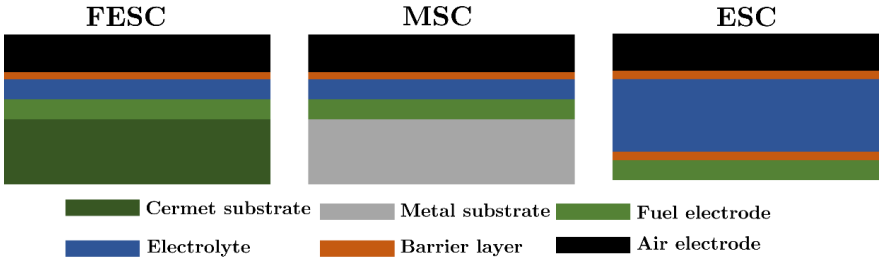

Figure 2.3: Schematic illustration of the three common SOC designs (not to scale).

Some common materials and layer thicknesses applied in SOC manufacturing are listed in Table 2.1.

Table 2.1: Commonly used SOFC materials and layer thicknesses applied by IEK-1.

Layer	**Material**	**Thickness (µm)**
Substrate	Ni-$Y_{0.148}Zr_{0.852}O_{1.926}$	~300
Fuel electrode	Ni-$Y_{0.148}Zr_{0.852}O_{1.926}$	~7
	Ni-$Gd_{0.1}Ce_{0.9}O_{2-\delta}$	~15
Electrolyte	$Y_{0.148}Zr_{0.852}O_{1.926}$	~10
Barrier layer	$Gd_{0.1}Ce_{0.9}O_{2-\delta}$	~6
Steam electrode	$La_{0.58}Sr_{0.4}Co_{0.2}Fe_{0.8}O_{3-\delta}$	~30
	$La_{0.58}Sr_{0.4}CoO_{3-\delta}$	

2.3 Internal reformation and carbon deposition

A notable advantage of SOFCs lies in their fuel flexibility primarily attributed to their elevated operating temperatures enabling the internal reformation of hydrocarbons. Catalytic cracking is an option to produce H_2 as well, but forms solid carbon in the process. It is imperative to prevent the formation of solid carbon within the fuel electrode to maintain the cell's efficiency. The common reformation mechanisms are dry reforming, partial oxidation and steam reforming. They will be explained shortly by taking the example of methane CH_4, a principial component of natural or biogas. Partial oxidation makes direct use of O_2 (I) or CO_2 (II) to convert CH_4 (see Equation (2.14) and (2.15)) while in dry reforming CH_4 reacts solely with CO_2 (see Equation (2.16)). The predominant and highly advantageous internal reformation reaction, however, is steam reforming (see Equation (2.17)), particularly favourable since steam is generated during the fuel cell reaction at the fuel electrode. It is less prone to the formation of solid carbon or carbon deposition on the catalyst surface compared to partial oxidation and dry reforming. Carbon deposition is dependent on the fuel's C:H:O ratio and the operating temperature. Figure 2.4 depicts the ternary C-H-O diagram and its temperature dependency.

$$\text{Partial oxidation (I):} \quad CH_4 + \frac{1}{2}O_2 \rightleftharpoons 2H_2 + CO \tag{2.14}$$

$$\text{Partial oxidation (II):} \quad CH_4 + 2O_2 \rightleftharpoons 2H_2O + CO_2 \tag{2.15}$$

$$\text{Dry reforming:} \quad CH_4 + CO_2 \rightleftharpoons 2H_2 + 2CO \tag{2.16}$$

$$\text{Steam reforming:} \quad CH_4 + H_2O \rightleftharpoons 3H_2 + CO \tag{2.17}$$

$$\text{Water-gas shift reaction:} \quad CO + H_2O \rightleftharpoons H_2 + CO_2 \tag{2.18}$$

With the exception of partial oxidation (II), all of these reactions result in the formation of syngas, a mixture of H_2 and CO in different ratios. The water-gas shift reaction (see Equation (2.18)) further converts syngas to H_2 and CO_2. All these reactions can occur in a SOFC, depending on the ratios of the reactants and temperature. The produced H_2 will further be available as usable fuel.
As mentioned above, carbon deposition on the fuel electrode is a concern when using hydrocarbon fuels. From a purely thermodynamic perspective, adjusting the C:H:O ratio on the fuel side and raising the operating temperature prevents carbon deposition. However, this consideration does not consider the kinetics of the reactions, or non-uniform temperature and partial pressure distributions within the

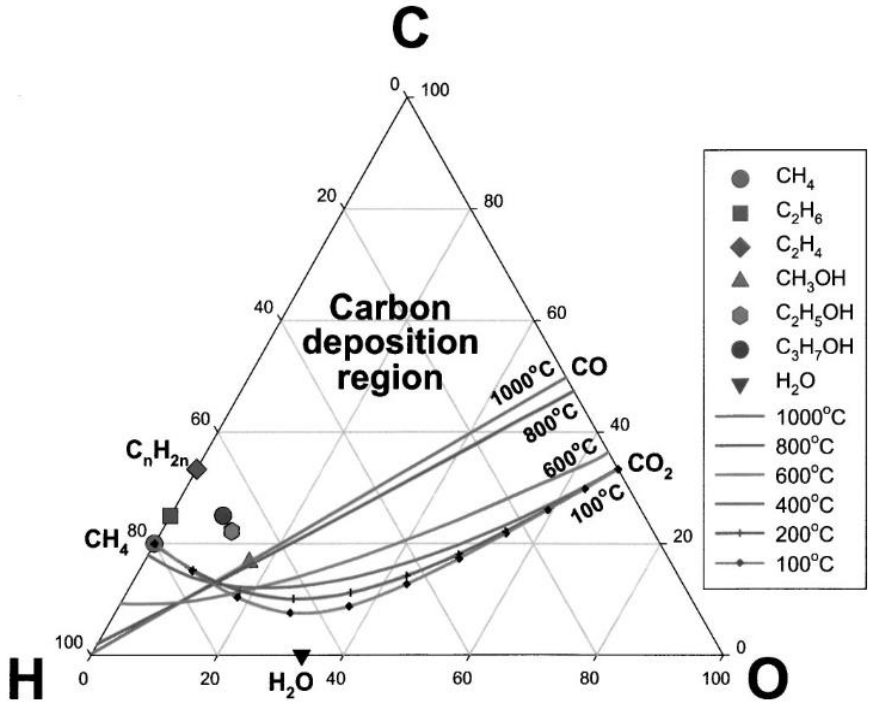

Figure 2.4: Carbon deposition regions and their temperature dependency illustrated in the ternary C:H:O diagram. Figure taken from [23].

SOFC. Consequently, carbon deposition may still occur even if the C:H:O ratio is low.
A severe issue arises from the presence of higher hydrocarbons, such as tars, as impurities in real biogases. This can result in severe carbon deposition within the structure of the fuel electrode. Carbon can be deposited either amorphous or graphitic, often forming an encapsulating film on the catalyst particles. This occurs through the gradual polymerization of hydrocarbon radicals, particularly at lower temperatures. At higher temperatures carbon is deposited on the catalyst surface as pyrolytic carbon through thermal cracking. Both deposition mechanisms block active sites for catalysis and inactivate the catalyst over time.
Occurring at higher temperatures, another deposition mechanism is the growth of carbon whiskers. Carbon is dissolved in the catalyst particle and nucleates while forming a fiber, where the catalyst particle sits at the tip of the fiber. This phenomenon is particularly dominant when nickel (Ni) is employed, as it is commonly used in SOFC fuel electrodes alongside an ion-conducting ceramic. Ultimately, the fibres will grow at the Ni-ceramic interface leading to a loss of contact between the particles and finally to mechanical disintegration of the fuel electrode structure. This process is known as metal- or Ni-dusting.[24–26]

2.4 Ni-doped strontium titanium ferrite

$SrTi_{1-x}Fe_xO_{3-\delta}$ crystallizes in the ABO_3 perovskite structure (see Figure 2.5) where the B-site cation occupies the center of the unit cell and is sixfold coordinated by O^{2-} anions, forming a BO_6 octahedron. Oxygen anions are located at the face-centered sides of the unit cell, while A-cations occupy the corners, being twelvefold coordinated to oxygen. Not directly influencing catalytic properties, A-site cations are responsible for lattice stability since the ratio of the A and B cation radii is a measure for distortion of the crystal lattice (Goldschmidt's tolerance factor). Perovskites exist in various compositions since adjusting their crystal structure is undemanding while maintaining their stability. Transition metal oxides are likely to incorporate defects, distorting the ideal perovskite structure and influencing its properties. Therefore, perovskites can be tailored by adjusting their elemental composition and oxygen stoichiometry, rendering them compelling materials for energy and electrochemical applications [27]. They can exhibit diverse characteristics, such as good oxygen ion conductivity [28], metallic conductivity [29,30] or mixed ionic and electronic conductivity (MIEC) [31]. Controlling the defect structure of materials is a valuable approach to tailor their functional properties.

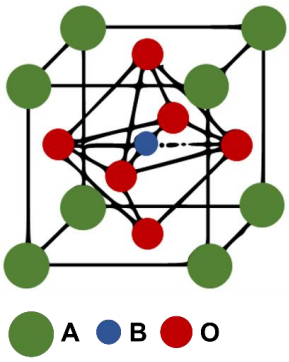

Figure 2.5: Illustration of the (cubic) ABO_3 perovskite unit cell.

Therefore, the theory of defects will be shortly discussed in the following since they fulfil a pivotal role in functional materials.

Defects

Defects are distinguished based on their dimension. Intrinsic point defects, which are zero-dimensional (0D) defects, occur when the crystal periodicity is broken at a single or at some adjacent lattice sites due to cation or oxygen vacancies which are compensated by electronic or ionic defects of opposite charge (Schottky vacancy pair) [32]. Another type of point defects are interstitials, but usually negligible in perovskites due to their high packing density [33]. Point defects can be induced by impurities or deliberately by doping, where a foreign ion is meant to substitutes a regular ion of the material. Increasing point defect density may lead to interaction between the defects.

Defects in materials can extend beyond 0D, encompassing defects of higher dimensions. One-dimensional defects (1D), also known as line defects arise from dislocations that introduce an extra half plane of atoms disordering the regular lattice structure. There are two types of dislocations: edge- and screw dislocations, depending on the angle of the Burger's vector that gives magnitude and direction of the dislocation. If its perpendicular to the dislocation line it is called edge dislocation while for a screw dislocation the vector is parallel to the dislocation line. Atoms can slip along the dislocation lines, impacting the material's properties.

Stacking faults represent two-dimensional (2D) defects where the regular arrangement of atomic planes is interrupted, e.g., by introducing a double layer AO. Another type of 2D defects are grain boundaries forming an interface between grains of different crystallographic orientations.

Three-dimensional (3D) defects comprise secondary phases or other disruptions of the crystal lattice in three-dimensions, like pores and cracks.

Not being directly a defect, surfaces are also interruptions of a periodic lattice. Its properties vary depending on which atomic plane is terminating the surface (AO, BO_2). Oxygen exchange with the surrounding atmosphere is a particularly significant surface property of perovskites in electrochemistry. Further, surface atoms exhibit a lower coordination compared to bulk atoms. Therefore, redistribution of defects, surface reconstruction or cation segregation might be favourable at the surface [34,35].

Acceptor doping $SrTiO_{3-\delta}$ with Fe leads to a deviation from the ideal cubic structure, resulting in a tilt of the BO_6 octahedra and a distortion to crystal structures with lower symmetry (e.g., orthorhombic). The lower valence state of Fe^{3+} compared to Ti^{4+} is compensated by oxygen vacancies to compensate charge, introducing ionic conductivity. The value of ionic conductivity is linked to the oxygen vacancy concentration and their mobility within the material. The mobility is influenced by the symmetry of the unit cell. At high oxygen partial pressures ($p(O_2)$), holes are generated in the valence band instead of oxygen vacancies.

The electrical conductivity of MIEC perovskites like $SrTi_{1-x}Fe_xO_{3-\delta}$ is several orders of magnitude higher compared to the ionic conductivity; e.g., this has been shown experimentally for $SrFeO_{3-\delta}$ [36]. It is assumed to be induced by small polaron hopping along the B-O-B bond in perovskites by interaction of the B-cations' d-orbitals and oxygen ions' 2p-orbitals. A polaron, in contrast to a free moving electron or hole, is a quasi-particle describing a charge coupled to its self-induced lattice distortion, therefore being trapped in a potential well created by its own charge [37,38]. Consequently, transition metals with incompletely filled d-orbitals or cations with mixed valences are advantageous for electronic conductivity. Ionic radii of A- and B-site cations further influence electronic conductivity by lattice distortion and modifying the B-O-B bond.[39] For $SrTi_{1-x}Fe_xO_{3-\delta}$ electrical conductivity increases with a high Fe content [40–42].
Distinct perovskite structures can be observed based on the degree of oxygen and cation non-stoichiometry. For instance, $SrFeO_{3-\delta}$ changes its crystal structure depending on the degree of oxygen non stoichiometry δ: $SrFeO_3$ is cubic, $SrFeO_{2.86}$ adopts a tetragonal structure, $SrFeO_{2.73}$ adopts an orthorhombic, and $SrFeO_{2.5}$ possesses brownmillerite structure [43]. Even Ruddlesden-Popper (RP) $A_{n+1}B_nX_{3n+1}$ structures are possible [44].[45]
Another phenomenon exploited to tailor functional materials is metal exsolution, which will be discussed in the following.

Exsolution
Exsolution is a phenomenon widely observed in geology. Certain thermodynamic conditions create a miscibility gap resulting in the phase separation of solid solutions [46]. Regarding functional oxides this phase separation refers to the reduction of metal cations to their metallic state due to a change in ΔG , resulting in the formation of nanosized particles on the surface [47]. The driving force for exsolution is provided by exposing a material to reducing conditions, causing a release of oxygen from the host lattice [48]. Metal atoms either cluster in the bulk and are subsequently driven to the surface due to lattice strain, or they diffuse to the surface, where they are reduced and form particles through interaction with other metal cations [49]. Several factors govern the exsolution of B-site cations: including the stoichiometric A/B ratio, lattice strain, voltage biasing or polarization, oxygen partial pressure, temperature, phase transitions, defects acting as nucleation sites and topotactic exchange [48,50,51].
The exsolved nanoparticles can be socketed in the host lattice creating a more stable heterogenous metal/oxide(host) interface compared to cermets. This enhanced interaction, when compared to a metal catalyst dispersed in an ion-conducting matrix, may improve stability against metal migration or redox cycling [26,52–54] and improve the carbon degradation tolerance towards metal dusting by supressing the tip-growth of carbon [25]. In fact, nanoparticles might even exhibit self-regeneration capabilities through redox cycling [55,56].

A similar process is segregation of cations to the surface. Opposed to exsolution, segregation refers to an undesired change of material properties and generally occurs in response to an oxidizing treatment. In perovskites segregation of A-site cations to the surface is a common phenomenon [51,57].

2.5 Doped ceria

Cerium dioxide or ceria (CeO_2) crystallizes in the cubic AO_2 fluorite structure (see Figure 2.6). The metal cation A is face centred and eightfold coordinated to oxygen while every oxygen atom is octahedrally coordinated by four metal cations [58,59]. Cerium can be present in two oxidation states either +III or +IV, where the Ce^{4+} electronic configuration ([Xe]$4f^0$) is more stable in comparison to Ce^{3+} ([Xe]$4f^1$) [60]. The Ce^{3+}/Ce^{4+} ratio can be shifted to higher values by introducing oxygen vacancies. The electrons are left behind on the Ce 4f state forming two Ce^{3+} for one oxygen leaving the lattice [58]. The formation of oxygen vacancies is either triggered by reducing conditions, such as low $p(O_2)$-atmospheres, or by doping with aliovalent cations [32]. Doping with aliovalent cations does not induce Ce^{3+}, however. In principle, the general defect compensation mechanism for 0D defects and the principles for defects of higher dimension, as described for perovskites, are similar (*c.f.* **Defects** in Section 2.4). However, fluorite structures offer a greater propensity for Frenkel defects (0D) [61]. Frenkel defects form when a cation vacates its regular lattice site moving to an interstitial site leaving a vacancy behind. An Anti-Frenkel defect involves an anion moving to an interstitial lattice site. In the context of fluorites, this phenomenon is common for oxygen, which can migrate from the smaller tetrahedral gap to the larger octahedral gap. Therefore, in fluorites, an acceptor dopant can be compensated either by a cation interstitial or an oxygen vacancy.

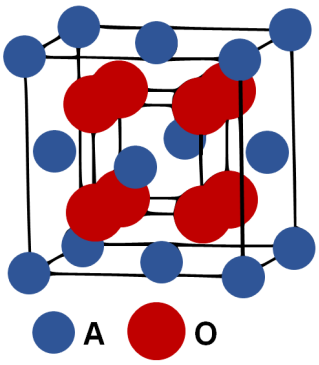

Figure 2.6: Illustration of the (cubic) AO_2 fluorite unit cell.

The fact that fluorite structures like 8 mol% Y_2O_3-doped ZrO_2 (commonly referred to as 8YSZ) are renowned for their high ionic conductivity at elevated temperatures, making them conventional SOFC electrolyte materials, indicates the substantial presence of oxygen vacancies. Although oxygen vacancies can be increased under low $p(O_2)$-conditions in ceria, it is often further acceptor doped to enhance ionic conductivity. The dopant of choice is often Gd. Much like perovskites, the fluorite structure can readily accommodate relatively large amounts of dopants.
Compared to 8YSZ, doped ceria exhibits higher ionic conductivity in the intermediate temperature regime [62], offering the possibility to lower the operating temperature of SOFCs, which may be

beneficial for the whole stack (*c.f.* Section 2.1). Nevertheless, it lacks the redox stability and material compatibility of 8YSZ [63].
The redox couple Ce^{4+}/Ce^{3+} induces electrical conductivity in (doped) ceria. As a MIEC, particularly under low $p(O_2)$, it offers distinct advantages when used in the fuel electrode, serving as a replacement for the purely ionic-conducting 8YSZ. In the case of Ni-8YSZ the reaction takes place at a TPB where several components meet: the electron conductor and catalyst (splitting H_2 and facilitating electron transport to the oxygen electrode), the ionic conductor (providing O^{2-} to form H_2O) and a pore filled with fuel gas. Therefore, a MIEC with catalytic activity forms a double phase boundary (DPB) with the gas molecules, potentially enhancing electrochemical performance of the electrode by extending the active surface area. Moreover, the degradation tolerance of the electrode is potentially increased compared to Ni-8YSZ if the Ni catalyst is deactivated by sulfur poisoning or carbon deposition. Additionally, the oxygen storage capacity of (doped) ceria might aid in the removal of deposited carbon from the surface.[11,12,64–70]
Implementing doped ceria as a fuel electrode cermet into a state-of-the-art FESC is challenging due to material incompatibilities, such as interdiffusion and secondary phase formation during high temperature sintering. Especially the interaction with the 8YSZ electrolyte is concerning. To mitigate these material incompatibilities and guarantee higher ionic conductivities at intermediate temperatures, replacing the 8YSZ electrolyte with a doped ceria one is desired. However, the redox behavior of (doped) ceria induces $p(O_2)$-depended chemo-mechanical stresses in dense doped ceria layers, and can finally lead to cracking of the electrolyte [71].

In a first attempt to introduce 10GDC into the fuel electrode cermet of the state-of-the-art FESC fabricated at Forschungszentrum Jülich GmbH (FZJ), Institute of Energy and Climate Research (IEK) – Materials Synthesis and Processing (IEK-1) the electrochemical performance experienced a substantial decrease. This behavior is not explainable by the formation of a secondary phase alone. Therefore, this thesis investigates differently doped ceria and its interdiffusion behavior with 8YSZ. The objective is to potentially find a doped ceria alternative exhibiting less interdiffusion with 8YSZ, to preserve electrochemical performance of the cell while improving degradation tolerance of the FESC towards carbon deposition from biogas.

2.6 Diffusion and mass transport in solids

Devices such as SOCs are often manufactured to a substantial amount by solid state processing techniques and involving high temperature treatments. Although atom diffusion and mass transport in solids is not just occurring at high temperatures, it is accelerated.
Mass transport is related to a flux of particles J (of a certain species e.g., atoms, ions, point defects, electrons, holes) along a concentration gradient $\partial c/\partial x$. The flux J is proportional to the concentration gradient. The constant of proportionality D is

called diffusivity or diffusion coefficient. This results in Fick's law of diffusion (in a one-dimensional system) according to Equation (2.19).

$$J = -D\frac{\partial c}{\partial x} \tag{2.19}$$

An external driving force may give rise to an additional flux vc, with an average velocity v, which is added to the diffusional flux (see Equation (2.20)). vc is called drift or mass flow.

$$J = -D\frac{\partial c}{\partial x} + vc \tag{2.20}$$

Equation (2.19) and (2.20) are only valid in steady-state, meaning J is time-independent ($J = const.$). If the diffusing species follows a law of conservation, a continuity equation (see Equation (2.21)) can be added to account for material balance or time-dependency.

$$\frac{\partial c}{\partial t} = -\frac{\partial J}{\partial x} \tag{2.21}$$

By combining Equation (2.20) and (2.21) a general diffusion equation is derived, which is a second order differential equation (see Equation (2.22)).

$$\frac{\partial c}{\partial t} = \frac{\partial}{\partial x}\left(D\frac{\partial c}{\partial x}\right) - \frac{\partial}{\partial x}vc \tag{2.22}$$

There are no analytical solutions if Equation (2.22) is dependent on c and t. In the case of systems that remain chemically homogenous (e.g., self-diffusion) D is independent of c, resulting in Equation (2.23).

$$\frac{\partial c}{\partial t} = \left(D\frac{\partial^2 c}{\partial x^2}\right) - \frac{\partial c}{\partial x}v \tag{2.23}$$

If, additionally, the drift is neglected, one achieves Equation (2.24) often referred to as Fick's second law of diffusion.

$$\frac{\partial c}{\partial t} = \left(D\frac{\partial^2 c}{\partial x^2}\right) \tag{2.24}$$

Assuming specific initial and boundary conditions, analytical solutions for Equation (2.23) and (2.24) yielding the form of a concentration profile $c(x,t)$, are calculable. Measuring the concentration profile through a specimen therefore allows the calculation of D. There are several examples for analytical solutions regarding different initial and boundary conditions as *thin layer, constant surface concentration, infinite initial distribution,* the *Boltzmann transformation,*

concentration-dependent diffusion coefficient approximations and for accounting drift the *Nernst-Einstein equation.*
In many practical specimen D is not constant since the composition varies across a wide range of concentrations. Therefore, the *concentration-dependent diffusion coefficient* approach is briefly described, utilizing the *Boltzmann transformation* $\lambda = x/\sqrt{t}$. This change of variables is only valid when the initial and boundary conditions are only functions of λ. Substituting λ into both sides of Fick's second law of diffusion results in Equation (2.25)

$$-\frac{\lambda}{2}\frac{\mathrm{d}c}{\mathrm{d}\lambda} = \frac{\mathrm{d}}{\mathrm{d}\lambda}\left(D\frac{\mathrm{d}c}{\mathrm{d}\lambda}\right) \tag{2.25}$$

which is an ordinary differential equation. To determine D, Equation (2.25) is integrated from one side of the diffusion couple $\lambda = \infty$ to λ or between the concentrations c and c_1 at the positions of interest.

$$-\frac{1}{2}\int_{c_1}^{c}\lambda \mathrm{d}c = D\frac{\mathrm{d}c}{\mathrm{d}\lambda}\Big|_{c} - D\frac{\mathrm{d}c}{\mathrm{d}\lambda}\Big|_{c_1} = D\frac{\mathrm{d}c}{\mathrm{d}\lambda}\Big|_{c} \tag{2.26}$$

At c_1 the concentration gradient is assumed to be zero, leading to Equation (2.27).

$$D = -\frac{1}{2}\frac{\int_{c_1}^{c}\lambda \mathrm{d}c}{(\mathrm{d}c/\mathrm{d}\lambda)_c} \tag{2.27}$$

Transforming back to x and t yields Equation (2.28), known as the Boltzmann-Matano equation.

$$D(c) = -\frac{1}{2t}\frac{\int_{c_1}^{c} x \mathrm{d}c}{(\mathrm{d}c/\mathrm{d}x)_c} \tag{2.28}$$

The Boltzmann-Matano equation is valid for a semi-infinite medium, where the origin of the x-axis is the surface of the medium. The concentration at the surface needs to be constant. Therefore, in a practical diffusion couple, the analyzed species needs to originate from a sufficiently thick layer to ensure a constant concentration at the boundary.
To choose the origin of the x-axis the right-hand side of Equation (2.26) needs to be zero when integrated from c_1 to c_2. Therefore, $\int_{c_1}^{c_2} x \mathrm{d}c = 0$ determines the origin of the x-axis, the so called Matano interface. The Matano interface is the point at which the area under the curve $c(x)$ is equal on the left- and right-hand side. In a physical sense, the Matano interface fixes the plane through which equal amounts of the according species moved in the positive and negative directions.
In a real interdiffusion couple the initial interface is corrected with the Matano interface. Given that different elements exhibit different (inter)diffusion coefficients, the quantity of interdiffused species is not equal. At this point, the Matano interface

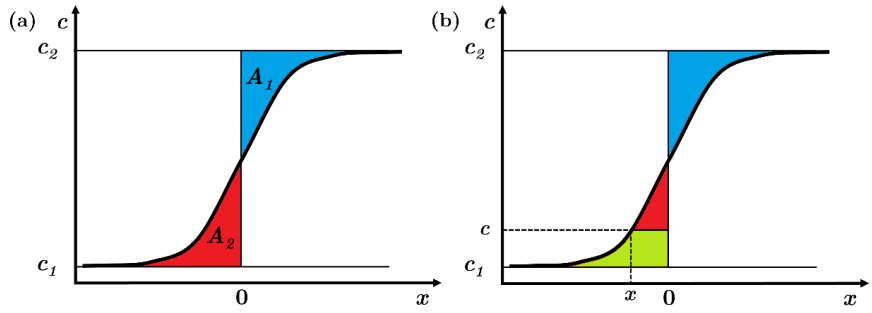

Figure 2.7: Schematic illustration of a sigmoidal diffusion profile. (a) The origin of the Matano interface is determined by the position where $A_1 = A_2$. (b) Calculation of the interdiffusion coefficient at the position x. Figure adapted from [72].

is the position x where the concentration of the respective species becomes similar on the left- and right-hand side of the interface. A schematic (sigmoidal) diffusion profile is illustrated in Figure 2.7, with the position of the Matano interface marked with 0, at the position on the x-axis where $A_1 = A_2$. Figure 2.7(b) shows the calculation of D at the position x.[72]
Different interdiffusion coefficients among cations in a joint diffusion couple lead to the Kirkendall effect [73]. This phenomenon describes the formation of pores at one side of the diffusion couple. This pore formation occurs due to a loss of material or volume in the layer containing cations with the higher interdiffusion coefficient compared to the adjacent layer, which gains volume.

3 Experimental methods

This chapter offers a concise introduction to the methodologies employed for the preparation and characterization of ceramic samples examined in this thesis, along with a discussion of their underlying principles. It encompasses synthesis, processing/shaping and high temperature treatments as well as the fundamental principles of characterization and imaging techniques regarding their interaction with (solid state) matter.
More in-depth experimental details for the preparation and characterization of each individual material investigated are given in the dedicated upcoming sections.

3.1 Synthesis and processing techniques

This section gives a short description of the applied techniques to synthesize the desired materials, the processing and manufacturing of samples for experimental investigation, and subsequent characterization.

3.1.1 Calcination and sintering

Calcination
Calcination is a high temperature treatment applied to solids, with the objective of decomposing or removing (organic) impurities from a material (mixture) and facilitating chemical reactions between solid components to form new materials. Another purpose for calcination is to induce particle growth, allowing for adjustment of the particle size distribution and modification of the sinter activity. Calcination relies on mass transport within solids.
A simple way of synthesizing oxides is the solid state reaction (SSR) route which involves stoichiometric mixing of the precursor materials followed by exposing the mixture to high temperatures at oxidizing conditions. The precursors are decomposed into oxides followed by a transport of the respective elements from one phase to another, originating at the surface of individual grains and progressing until the reaction is complete across the entire grain area.[74]
The SSR route is applied in this thesis to process the exsolution perovskite materials.

Sintering
Sintering is likewise a high temperature treatment of a solid material but with the objective of densification without reaching the melting point. The driving force behind the joining of particles and the reduction of porosity through atomic diffusion is the reduction in surface free energy of the consolidated mass of particles. The joining of particles and grain growth is due to mass transport from the grains to the neck region. Various mass transport mechanisms are involved, including volume,

surface and grain boundary diffusion. Additionally, processes such as evaporation and condensation or plastic flow due to dislocations may also contribute. The processes are depicted in Figure 3.1.
Coarsening, on the other hand, entails a rearrangement of the microstructure by the transfer of matter across a pore's surface, but it does not result necessarily in densification. Coarsening also reduces the surface free energy, thus is a competing mechanism to sintering.
Pre-compacted powder assemblies (green bodies) are used for sintering e.g., by pressing or formulation and applying of a solid suspension.[74,75]
In this thesis, sintering is extensively employed to densify powder compacts or create functional layers with the desired microstructures, often starting from slurries. Simultaneously, the thermal energy provided by the sintering process serves as a means to induce and explore the ongoing interdiffusion processes. Sintering is inherently linked to the diffusion of atoms, and as a result, interdiffusion and densification are interrelated processes. This connection can lead to undesired effects in functional materials, but they cannot be entirely avoided because functionality is tied to specific microstructural characteristics. Some strategies, comprising alternative sintering techniques, to supress interdiffusion while achieving densification will briefly be described in the following.
The conventional sintering process described earlier typically employs furnaces

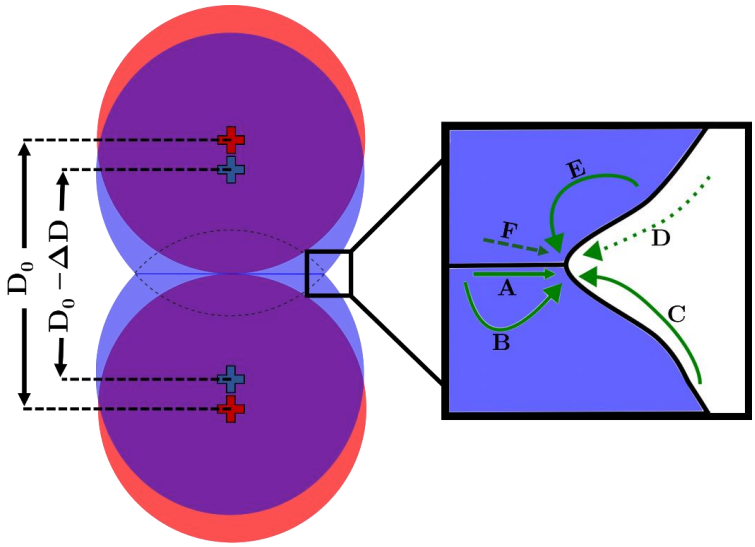

Figure 3.1: Schematic illustration of the sintering process depicted by joining/ grain growth of two adjacent grains. The different mass transport mechanisms decreasing D_0 are depicted where (A) denotes grain boundary diffusion, (B) volume diffusion from grain boundaries, (C) surface diffusion, (D) evaporation and condensation, (E) Volume diffusion from surface, and (F) plastic flow from dislocations. Figure adapted from [75].

equipped with conventional heating elements. Recently, alternative sintering techniques are investigated which share the communality of high heating rates. These elevated heating rates suppress low-temperature-activated processes like grain coarsening or surface diffusion, while promoting densification processes, such as grain boundary and bulk diffusion, occurring at higher temperatures. In the context of this research, three of these innovative techniques were applied to 10GDC and 8YSZ ceramics to analyze their sintering and interdiffusion behavior:

Ultra-fast high temperature sintering
Ultra-fast high temperature sintering (UHS) employs Joule heating to densify a green body. A high current is driven through graphite felts between which the sample is placed. The whole setup is enclosed in an inert atmosphere, typically either a vacuum or a protective gas such as argon. UHS reaches heating rates of ~10^3-10^4 °C/min [76] and temperatures up to ~3000 °C.[77,78]

Field-Assisted Sintering technique / Spark Plasma Sintering
Field-Assisted Sintering technique / Spark Plasma Sintering (FAST-SPS) is a low voltage, pulsed direct current activated, pressure-assisted sintering, and synthesis technique. The powder is compacted in a conductive mechanical loading system (tool). The sintering process is initiated by applying a voltage to the tool. If the sample itself is conductive the energy is directly dissipated in the sample. Otherwise, heat is solely generated within the tool and subsequently transferred to the sample through conduction, similar to the UHS process. Throughout this entire process, uniaxial pressure can be applied to aid densification. The entire setup is maintained within either a vacuum or a protective gas atmosphere. Heating rates reach ~1000 °C/min. Typical graphite tools reach a maximum sintering temperature of up to 2400 °C. For applications involving higher pressures, more mechanically stable tools, such as those made from titanium-zirconium-molybdenum alloys, need to be employed, albeit at the cost of reduced maximum sintering temperature.[79,80]

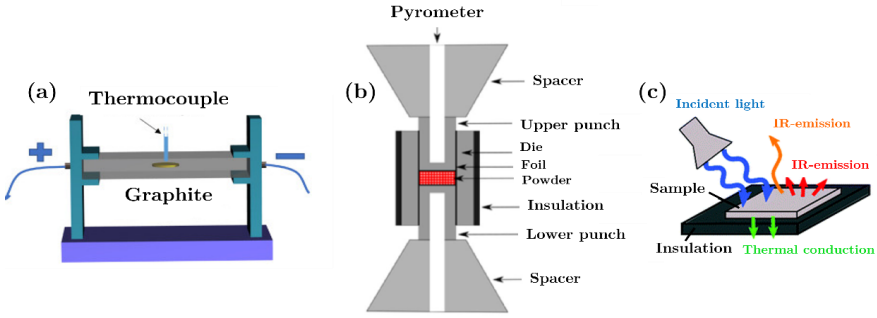

Figure 3.2: Schematic illustration of (a) Ultra-fast high temperature sintering, (b) Field-Assisted Sintering technique / Spark Plasma Sintering, and (c) Blacklight sintering. (a) and (b) are performed in an inert gas atmosphere or vacuum. Figures are taken from (a) [77], (b) [79], and (c) [81].

Blacklight sintering
Blacklight sintering utilizes the temperature-dependent absorption properties of electromagnetic waves in the ultraviolet regime. The temperature of the process stabilizes itself by reaching an equilibrium between absorption of light and emission of thermal radiation. The radiative energy balance is dependent on the spectrum of the light source, absorption properties of the sample material, and its emission characteristics. The bandgap of ceramic oxides diminishes with increasing temperature, enhancing the efficiency of the process. In this study, a multi-pulse Xenon flash lamp (Heraeus Noblelight, Cambridge, United Kingdom) was employed for sintering the samples.[81]

The UHS, FAST-SPS and blacklight sintering setups are illustrated in Figure 3.2.
A common issue of UHS and FAST-SPS techniques is their reducing character. Inert gas atmospheres, reducing the $p(O_2)$, shift the equilibrium of the oxygen non-stoichiometry δ to lower values, thus oxides release oxygen from the lattice [82].
Carbon, being present as electrode material or as tool material, is a potent reducing agent since the entropy change for the formation of CO_2 or CO is small or increasing, respectively. The reducing capability of carbon increases with rising temperature.[83,84] Consequently, many materials tend to undergo reduction in these sintering techniques, which is particularly concerning in the case of ceria due to the loss of oxygen and the resulting valence change of cerium, leading to chemical expansion within the sample. Compared to UHS and FAST-SPS, blacklight sintering can be performed in ambient air, giving rise to higher $p(O_2)$-values.
There are other strategies that can be employed to improve densification or lower the sintering temperature, irrespective of the sintering technique, as briefly described in the following.

Reactive sintering
Reactive sintering is a process where the desired product is formed during the sintering process by chemical reactions between the constituents of the green body. The heat released by the chemical reaction provides additional energy for densification.[85]

Sintering aids
Additives that promote densification and reduce the sintering temperature are referred to as sintering aids. They can achieve this either by facilitating the formation of a liquid phase, enabling rapid material transport, or by introducing dislocations and enhancing diffusion through doping of the host lattice.[86]

3.1.2 Dry pressing

A widely applied forming technique to compact loose powders is dry pressing with the aim to produce (highly) dense green bodies, possessing a desired shape for further

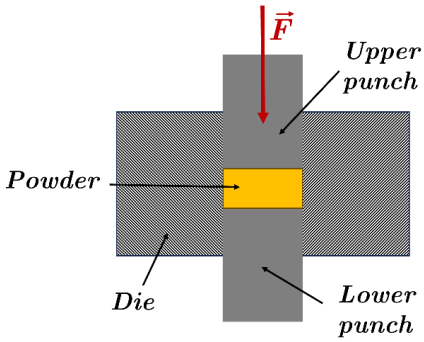

Figure 3.3: Schematic illustration of a pressing die and the uniaxial pressing procedure (cross-section).

manufacturing processes (e.g., sintering). Properties of the green body are defined by the properties of the powder (particle size distribution and morphology), applied pressure, pressing time, and size of the green body. A binder may be added to form more stable green bodies.
Powders were pressed into sinterable green bodies by uniaxial pressing. The force is applied in a single direction through a punch. The powder resides in a pressing die with non-deformable side walls. The pressing process and cross-section of the die is illustrated in Figure 3.3. A common shape produced by uniaxial pressing is a round sample with a fixed diameter (pellet). The pellets can be further compacted by cold-isostatically pressing. In this method, the pre-compacted pellets are placed within a hydraulic vessel, which applies uniform force from all direction onto the sample.[87] Sintered green bodies were used for investigation of crystallographic properties and interdiffusion behavior as well as for investigation of carbon degradation tolerance.

3.1.3 Screen printing

Screen printing involves transferring a printing medium onto a substrate through a fine-meshed fabric (screen), achieved by applying a force with a rubber squeegee. It is widely used since it is simple, efficient, and cheap. The screen printing setup and process are illustrated in Figure 3.4. During this process, the squeegee presses the screen onto the substrate, and as it moves, the printing medium is transported along the substrate and pushed through the screen openings. The distance between the screen and the substrate is referred to as the snap-off distance, and it, along with the tension of the screen, controls the separation of the screen from the printing medium after the squeegee pressure is relieved.
The key parameters for evaluating the quality of the screen printing process encompass printing thickness, thickness uniformity, fine line resolution, and the presence of voids. The number of wire openings in the printing area of the screen

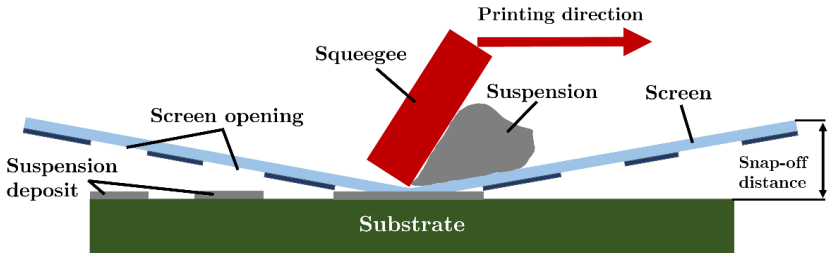

Figure 3.4: Illustration of the screen printing process. The suspension is printed on a substrate by pressing the suspension with a squeegee through a screen. Figure adapted from [88].

respectively the linear distance between two adjacent wires (mesh count number) and mesh material are important factors to control the applied layer thickness. A further crucial parameter affecting layer quality is the open area of the screen. It includes the wire diameter of the screen material and is given by Equation (3.1).

$$\text{Open area} = (1 - \text{mesh count} \times \text{wire diameter})^2 \times 100\% \tag{3.1}$$

Resolution of the screen rises with open area. Additional factors that influence the printing process include wire bias (the angle between the mesh and the substrate), the type of substrate material (which affects the adhesion of the printing medium), and printing parameters such as squeegee pressure and printing speed.
As important as the screen printing materials and process parameters are, the (rheological) characteristics of the printing medium also play a significant role (*c.f.* Section 3.2.8). In terms of SOC manufacturing, screen printing is employed to apply planar functional layers from ceramic powder suspensions, down to thicknesses of a few micrometer.[88,89]
Functional layers for the investigated materials, as well as for the production of SOCs, were applied using a semi-automatic screen printer EKRA-E2 (ASYS Group, Bönnigheim, Germany). The selection of the used meshes was primarily based on achieving the desired layer thicknesses.

3.2 Characterization techniques

Physical and chemical characterization is essential to access and tailor the properties of functional materials to construct performing and durable devices. In addition, it is not only the individual properties of a material that matter but also its interactions with adjacent functional materials and the surrounding atmosphere.

3.2.1 X-ray diffraction

Bragg's law describes the diffraction of waves by periodically ordered, crystallographic planes according to Equation (3.2) where n is the order of diffraction, λ is the wavelength, d is the spacing of the crystallographic planes, and θ is the incident angle of the radiation.

$$n\lambda = 2d\sin(\theta) \tag{3.2}$$

Waves coherently scattered at adjacent crystallographic planes exhibit different phases. Upon interfering with each other, constructive interference results in distinct diffraction signals. The diffraction pattern provides insight into crystallographic structure and lattice spacing, which can be used to derive information about the materials present in the sample and their stoichiometry. To measure crystallographic properties, X-rays are used since their wavelength is in the same order of magnitude as the common lattice spacings in materials. The measurement is depicted in Figure 3.5.

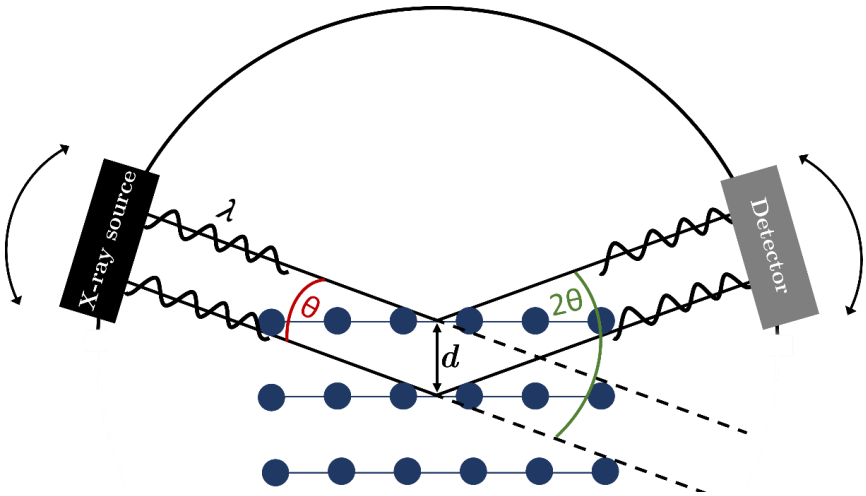

Figure 3.5: Schematic illustration of a X-ray diffraction setup in Bragg-Brentano geometry. This setup offers the possibility to determine the out-of-plane lattice parameter.

X-ray diffraction (XRD) analyses were performed with a Bruker D4 Endeavor X-Ray Diffractometer utilizing a Cu-Kα anode. The crystallographic properties were used to investigate the purity of the synthesized materials, detect the presence of secondary phases and to quantify the extent of interdiffusion in mixtures of different materials following heat treatment. To analyze the phase composition, a polynomial fit was applied to precisely determine the positions of the diffraction lines. Subsequently, the Rietveld refinement method was employed to investigate the phase composition.

3.2.2 Scanning electron microscopy

Scanning electron microscopy (SEM) is a technique to image surfaces down to a nanometer resolution. A focused electron beam scans the sample's surface, generating secondary signals upon interaction, which are then detected. The most common secondary signals are secondary electrons (SE), emitted from the sample due to excitation by the primary electron beam, and backscattered electrons (BE) resulting from elastic scattering of the primary electrons by the nuclei. The interaction volume of the primary electrons with the sample is depicted in Figure 3.6. SE are electrons with an average energy below ~50 eV and originate from the near surface. Therefore,

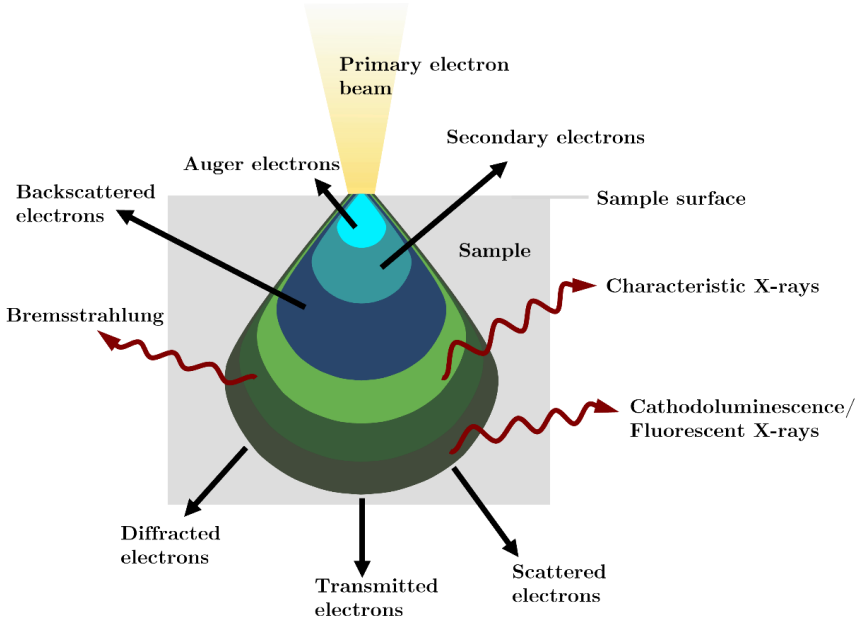

Figure 3.6: Schematic illustration of the excitation bulb and the emitted secondary signals caused by the interaction of a primary electron beam with a sample.

the SE signal includes topographic information and offers higher lateral resolution when compared to BE. In contrast, BE are high-energy electrons that interact with a larger volume within the sample. BE contain chemical information since the portion of primary electrons that are backscattered is proportional to the atomic number Z of the elements in the sample. Another kind of technique employed to gain chemical information about the sample is energy-dispersive X-ray spectroscopy (EDS). The primary electron beam excites an inner shell electron, creating a vacancy that is subsequently filled by a higher shell electron, releasing energy in the process, emitted as characteristic X-rays. Several other kinds of secondary signals may be excited by the primary electron beam, which are also shown in Figure 3.6 but not discussed here, providing further information about the sample.
The penetration depth and resolution depend on factors such as the acceleration voltage and Z or sample density, and the number of scattering events in the sample.[90–92]
For investigation of the samples presented in this thesis primarily SE for imaging, BE for determining interdiffusion lengths in layered samples, and EDS analysis for further chemical analysis are utilized. SEM/EDS analysis were performed either with a GeminiSEM 450 (Carl Zeiss AG, Oberkochen, Germany) equipped with an ULTIMAX 170 EDS detector (Oxford Instruments, Abingdon, Great Britain) or a Zeiss EVO (Carl Zeiss AG, Oberkochen, Germany) equipped with a BE detector and an ULTIMAX 100 EDS detector (Oxford Instruments, Abingdon, Great Britain).

3.2.3 Raman spectroscopy

Not energetic enough to excite core electrons, electromagnetic radiation with wavelengths characteristic for the infrared and visible region excites the vibration of chemical bonds. There are six modes of vibration, subcategorized in valence and

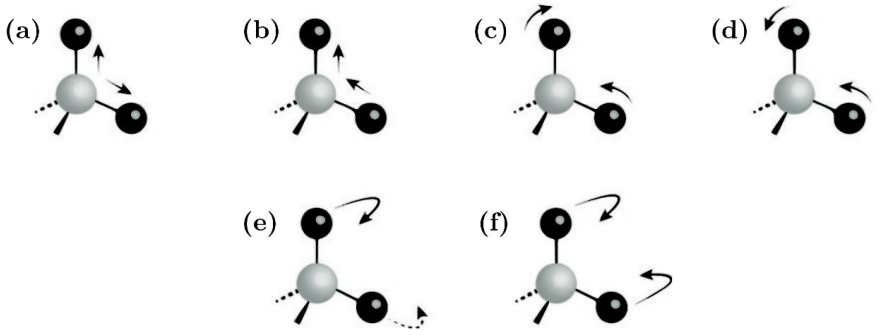

Figure 3.7: Schematic illustration of the six vibrational modes distinguished in valence vibrations: (a) symmetrical, (b) asymmetric stretching, and deformation vibrations: (c) scissoring & bending, (d) rocking, (e) twisting, and (f) wagging. Figure taken from [94].

deformation vibrations. During valence vibrations, the distances between atoms change, including *symmetrical* stretching, which does not alter the dipole moment, and *asymmetrical* stretching, which shifts the "center of charge" and thus changes the dipole moment. Deformation vibrations can even be further distinguished. During in-plane oscillations, the involved atoms remain in the same plane. It can be distinguished between:

— *Scissoring* and *bending,* where atoms move in opposite directions, causing the bond angle to widen or narrow.
— R*ocking*, in which two bonding partners tilt to one side simultaneously without altering the bond angle.

Oscillations involving three-dimensions are called non-planar. Those oscillations comprise:

— *Twisting*, where parts of the molecule twist relative to each other, not changing the bond angle between the involved atoms but to their neighbouring atoms.
— *Wagging,* in which planes of the molecule vibrate relative to each other, without changing the bond angle between the moving atoms.

The six vibration modes are pictured in Figure 3.7.
By means of infrared light or infrared spectroscopy vibrations are detected which alter the dipole moment of a molecule induced by absorption or reflection.
Often called complementary to infrared spectroscopy, Raman spectroscopy detects polarizability changes in the electron cloud of a molecule induced by inelastic

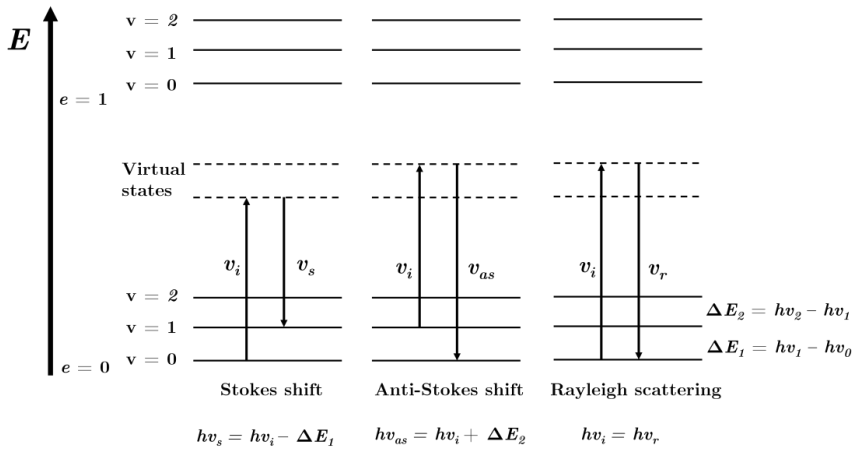

Figure 3.8: Schematic illustration of the energy transitions during scattering , where e denotes electronic states, v denotes vibrational states, v_i the incident beam energy, and v_s, v_as, v_r the scattered beam energy.

scattering of the incident light, a phenomenon known as the Raman effect. Following scattering, the energy difference between the scattered light and the incident beam is termed the Raman shift. A loss in energy is called a Stokes shift, while a gain in energy is an Anti-Stokes shift. Elastic scattering or no change in energy of the radiation is called Rayleigh scattering. In a quantum mechanical sense, during a Stokes shift a molecule is excited by photons from its vibrational ground state to a virtual state and falls back to a higher energy state compared to the ground state, emitting a photon with a lower energy. During an Anti-Stokes shift a molecule already present in an excited vibrational state is excited to a virtual state but falling back to a less energetic vibrational state compared to the initial state. For Rayleigh scattering, the initial state equals the final state after excitation. The energy transitions are illustrated in Figure 3.8.
Therefore, every change in polarizability of a compound is a possible subject for Raman investigation like doping of a material or valence changes.
Raman scattering events are very unlikely compared to Rayleigh scattering with only about $1/10^7$ of Rayleigh scattering events. Therefore, Raman spectroscopy necessitates a monochromatic light source with high intensity, typically employing visible lasers.[93–96]
Although Raman spectroscopy is often used in organic chemistry, it is also suited as a non-destructive analytical technique to investigate inorganic compounds regarding their stoichiometry, composition(al changes) and symmetry. For instance, a perfect cubic perovskite would exhibit no Raman signal, but deviations from ideal symmetry, such as those induced by doping or octahedral tilting, can result in Raman-active modes.
In context of this thesis, Raman spectroscopy was employed to identify materials, examine their stability, investigate the valence state of cerium, and estimate the extent of interdiffusion. Furthermore, Raman spectroscopy is a potent technique to investigate carbon and its deposition within a potential electrode structure.
Raman analysis was conducted using an inVia Qontor distributed by Renishaw (Pliezhausen, Germany) equipped with a 532 nm laser.

3.2.4 Electrochemical impedance spectroscopy

By applying electrochemical impedance spectroscopy (EIS) as a characterization technique, an electrochemical system is perturbed by a sinusoidal current or voltage (*ac*) across a broad frequency spectrum while the sinusoidal response is measured. The system must be linear, time-invariant, and in an equilibrium or steady state. In electrochemical systems, such as SOCs, various processes occur at different time scales, each characterized by its own time constant τ, which is defined as

$$\tau = RC \tag{3.3}$$

where R is the resistance, and C is the capacitance of the according process. By working in the frequency domain, EIS allows the deconvolution of individual processes with different τ, while slow processes respond to lower frequencies and fast processes respond to higher frequencies.
EIS data are evaluated for linearity and time-invariance by the Linear-Kramers-Kronig Transformation [97]. Subsequently, the data is fitted to an equivalent circuit model (ECM) and in many cases visualized in the so-called Nyquist plot. In this representation of the impedance data, the time constant is represented by a semicircle, and the characteristic or peak frequency of a semicircle is determined by Equation (3.4).

$$2\pi f_{max}\,\tau = 1 \tag{3.4}$$

Therefore, to fully separate two semicircles, representing two distinct electrochemical processes, it is crucial to select measurement frequencies that satisfy the condition $2\pi f_{max}\,\tau \gg 1$.
The sinusoidal excitation signal as a function of time is expressed by Equation (3.5)

$$U(t) = U_0 \sin(\omega t) \tag{3.5}$$

while the relationship between the angular frequency ω and the frequency f is:

$$\omega = 2\pi f \tag{3.6}$$

For a linear system, the response I is shifted in phase by an angle φ according to Equation (3.7).

$$I(t) = I_0 \sin(\omega t + \varphi) \tag{3.7}$$

The impedance Z, analogous to resistance in Ohms law for *dc,* is determined by Equation (3.8).

$$Z(t) = \frac{U_0 \sin(\omega t)}{I_0 \sin(\omega t + \varphi)} = Z_0 \frac{\sin(\omega t)}{\sin(\omega t + \varphi)} \tag{3.8}$$

A sinusoidal signal can be represented as a complex number *z:*

$$z = a + jb \tag{3.9}$$

where a is the real part on the x-axis, b is the imaginary part on the y-axis, and j is the imaginary unit, $j^2 = -1$.
Expressed with respect to its magnitude $|z|$ or in the exponential form, utilizing the Euler transformation, z can be represented as shown in Equation (3.10).

$$z = |z|(\cos(\varphi) + j\,\sin(\varphi)) = |z|e^{\varphi j} \tag{3.10}$$

Thus, the impedance, expressed as a complex number, follows Equation (3.11).

$$Z = |Z|(\cos(\varphi) + j\sin(\varphi)) = Z' + jZ'' \tag{3.11}$$

Here, Z' and Z'' denote the real and imaginary part, respectively. The values of φ and $|Z|$ are calculated according to Equation (3.12) and (3.13).[98]

$$\varphi = \tan^{-1}\left(\frac{Z''}{Z'}\right), \tag{3.12}$$

$$|Z| = \sqrt{(Z')^2 + (Z'')^2}, \tag{3.13}$$

Plotting Z'' against Z' generates the Nyquist plot, as illustrated in Figure 3.9, where idealized data are depicted that can be effectively described using a Randles circuit. This circuit serves as an equivalent model for a straightforward system involving an electrode immersed in a liquid electrolyte. The circuit consist of a series or ohmic resistance R_S of the electrolyte, a capacitance resulting from the formed double layer at an electrode C_{dl}, the resistance against the transfer of charges across the electrolyte-electrode interface due to an electrochemical reaction (often referred to as polarization resistance (R_p)) R_{ct}, and the Warburg impedance Z_W modelling slow

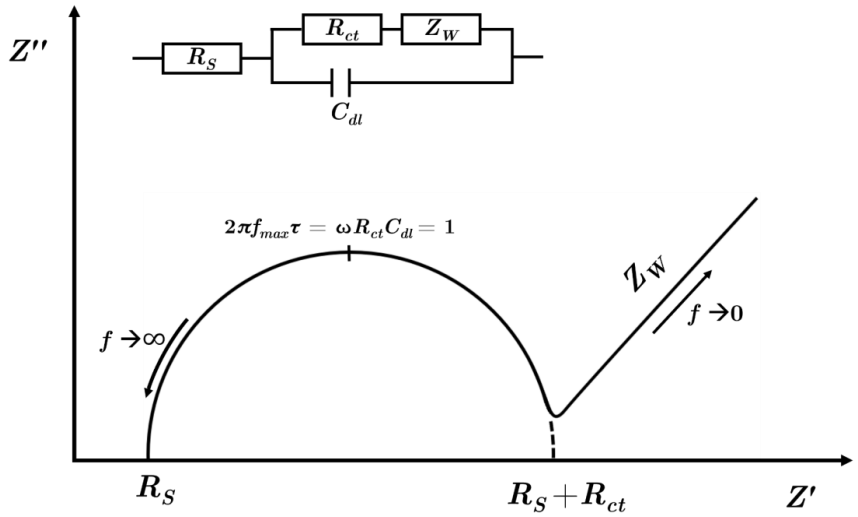

Figure 3.9: Schematic illustration of impedance data in the form of a Nyquist plot and a Randles circuit. R_S is the series or ohmic resistance of the circuit or sample, R_{ct} is the charge transfer resistance (or polarization resistance) of a process, C_{dl} is the capacitance of a double layer arising from a polarisation, and Z_W is the Warburg element which describes a resistance due to diffusion. Measurement frequency increases while approaching the origin.

diffusion processes at the electrode. The Randles circuit is sufficient to describe the impedance behavior of a simple electrochemical cell with a single faradaic process. However, the impedance behavior of a real SOC is more complex due to several physico-chemical charge or mass transport processes. Typical processes occurring in a SOC are: i) Impedance of the test setup's electrical connection, represented by an ideal inductance, predominantly at very high frequencies. ii) Impedance of the cell due to its ionic resistivity, mainly of the electrolyte, described by an ideal resistance which can be considered constant with frequency. iii) Gas diffusion impedance at the fuel and air electrode, occurring at low frequencies and represented by a semi-infinite Warburg element modelling diffusion in porous media. iv) Charge-transfer impedance at both electrodes due to electrochemical reactions, resolvable at high frequencies. In the ideal case it can be modelled by a resistance and capacitance in parallel. However, in real systems semi-circles which arise due to charge-transfer processes are often depressed semi-circles due to a non-ideal capacitive behavior. To account for this behavior, the ideal capacitance is substituted with a constant phase element (CPE) [99]. The impedance of an ideally polarizable electrode in the absence of redox reactions, referred to as blocking or capacitive electrode, can be described by the connection of R_S and C_{dl} in series, according to Equation (3.14).

$$Z = R_S \frac{1}{j\omega C_{dl}} \tag{3.14}$$

At solid electrodes, commonly a capacitance dispersion is observed, thus C_{dl} is replaced by the CPE (see Equation (3.15))

$$Z = R_S \frac{1}{(j\omega)^{\Phi} Q_{dl}} \tag{3.15}$$

where Q_{dl} is the double-layer capacitance parameter (in $Fcm^{-2}s^{\Phi-1}$) and $\Phi \leq 1$ is a dimensionless exponent.[100] For $\Phi = 1$ the system is an ideal capacitor. For $\Phi = 0$ the system is an ideal series resistance. All processes which appear as (depressed) semi-circles are usually modelled by an element containing a resistor R in parallel with a CPE (R-CPE). If the CPE models a non-ideal RC-element, Φ should be in the range of $0.8 < \Phi \leq 1$. When examining real impedance data on a Nyquist plot, it is common to encounter multiple semi-circles, which may partially overlap. Each of these semi-circles corresponds to a distinct charge transfer process and can be represented by an individual R-CPE connected in series. The span of each semi-circle gives the polarization resistance R_p associated with the corresponding charge transfer process.

EIS is utilized to assess the resistance of electrode reaction in electrochemical cells or the resistance against ionic movement within grains or grain boundaries in a ceramic material. Accordingly, R_S quantifies the total ohmic resistance of an electrochemical cell or a ceramic sample.

Impedance measurements were conducted by applying frequencies between 10^6-10^{-1} Hz with a Novocontrol Alpha-A frequency analyzer (NOVOCONTROL

Technologies GmbH & Co. KG, Montabaur, Germany) in a tube furnace. The recorded spectra have been checked for linearity and time-invariance by the Linear-Kramers-Kronig Transformation using the software "Lin-KK" [97]. The data were used for further analysis if the calculated residuals indicated valid spectra. An ECM was used to fit the spectra by using the software ZView (Scribner, LLC, Southern Pines, USA). The used ECMs and the resulting fits do not resemble the real underlying electrochemical processes occurring in the samples but serve as a means to extract the resistances of interest. The processes for the respective ECM-elements (grain, grain boundary, electrode) were identified by determining its capacitance [101]. More information about the measurement conditions and the fitting of the obtained spectra is given in the respective sections.

3.2.5 Thermal analysis

Thermal analysis is a generic term referring to all techniques measuring a physical property of a substance as a function of temperature.

Thermogravimetric analysis
Thermogravimetric analysis (TGA) monitors the mass (change) of a sample as a function of temperature or time. Additionally, the gas atmosphere may be changed to adjust the $p(O_2)$. TGA provides insights into physical phenomena such as phase transitions, thermal decomposition, and adsorption & desorption processes. Especially interesting, when dealing with oxides, is the measurement of oxygen release (reduction) or uptake (oxidation) of the material. The oxygen stoichiometry of transition metal oxides is temperature- and $p(O_2)$-dependent and induces phenomena like valence change of cations, phase transitions and exsolution.[102]
TGA were conducted with a NETZSCH STA 449 F1 Jupiter (NETZSCH-Gerätebau GmbH, Selb, Germany).

Dilatometry
Dilatometry measures the length change of a material as a function of temperature. It is used to gain information about a material's sintering onset, sintering rate, maximum shrinkage of the green body and to determine the coefficient of thermal expansion.[103]
To avoid internal stresses and delamination during the sintering of layered systems, dilatometry measurements were employed to assess the sintering behavior of doped ceria materials used in SOC manufacturing. Dilatometry measurements were carried out with a NETZSCH DIL 402 Expedis Classic (NETZSCH-Gerätebau GmbH, Selb, Germany).

3.2.6 Secondary ion mass spectrometry

As a characterization technique secondary ion mass spectrometry (SIMS) separates ions according to their mass-to-charge ratio (m/z). Therefore, atoms need to be removed (sputtered) from the sample (surface) and ionized. The sputtered secondary ions are separated by electrostatic and/or magnetic analyzers or by their velocity. Basically, every transfer of energy which leads to a sputtering effect on a sample is suitable to generate secondary ions. In the case of this thesis, a primary ion beam is used. The primary ions are accelerated towards the sample, where some are scattered back, but most transfer their kinetic energy to the sample, causing the emission of secondary ions. In addition, electrons, Auger electrons, photons, neutral particles and excited clusters can be generated. The basic equation describing the secondary ion current I_s^x is:

$$I_s^x = I_p c_x S \gamma F \tag{3.16}$$

where I_p is the primary ion current, c_x is the concentration of species x (measured ion count), S is the sputter ion yield, γ is the ionisation efficiency and F is the transmission of the analyzer.
SIMS enables the qualitative analysis of species present in a sample but also a quantitative analysis of these species as a function of position within the sample. Therefore, SIMS is suitable to measure diffusion profiles.[104,105]
Diffusion profiles were measured using positive polarity with a ToF-SIMS (5.NCS, IONTOF GmbH, Münster, Germany). Measurements were performed by the Institute for Engineering, Electronics and Analytics 3 (ZEA-3) at FZJ, Germany.

3.2.7 Inductively coupled plasma optical emission spectroscopy

Inductively coupled plasma optical emission spectroscopy (ICP-OES) is a commonly used technique for analysis of the qualitative and quantitative elemental composition. It can serve as a tool to monitor the elemental composition of samples or synthesized materials, as well as to check for impurities.
The samples are dissolved and injected into the ICP. The ICP is generated from radiofrequency magnetic fields induced by a coil, through which a current passes, lopped around a quartz tube. Ar gas flows through a torch and is ionized by a spark of a tesla coil initiating the plasma. Ar-ions and electrons flow on an annular path due to the magnetic field and collide with further Ar atoms creating a chain reaction of collisional ionization thus increasing the number of ions and electrons in the plasma. Due to the conductive nature of the plasma in the coil region the charged particles are heated up by inductive coupling up to the ionization temperature of the Ar gas (~7000-8000 °C).[106] Samples inside the ICP are atomized, and the atoms' electrons are excited by the plasma. When transitioning back to a lower energy state, the atoms emit energy which is characteristic for each element. The

different wavelengths are separated by a monochromator and detected by a charged coupled device by converting photons to electrons.[107]
ICP-OES was utilized to analyze synthesized or purchased materials for impurities and to check their stoichiometry. Ceramic samples were mixed with lithium borate and chemically digested at 1000 °C for 30 min. The resulting melt was dissolved in hydrochloric acid (5%) with the addition of hydrogen peroxide.
Measurements were performed by ZEA-3 at FZJ, Germany, using an iCAP 7600 ICP-OES analyzer (Thermo Fisher Scientific, Osterode/Harz, Germany).

3.2.8 Rheological characterization

The information presented in this section is taken from [108–111].
Rheology is the science that deals with the deformation- and flow properties of matter. A crucial step in ceramic powder processing is the shaping before sintering. A common shaping technique, which is applied in this thesis to produce functional SOC layers, is screen printing (*c.f.* Section 3.1.3). Screen printing typically involves the use of a powder suspension. Rheological properties of powder suspensions give insight into certain characteristics like dispersion of the powder and the behavior under applied force during shaping. By adjusting rheological properties of the powder suspensions, the quality of the formed green body may be improved.
Rheological properties can be divided in stationary and dynamic properties. Stationary properties include viscosity, thixotropy, and yield stress, while dynamic properties encompass elastic, viscous, and complex moduli.
For measuring rheological properties in a parallel plate setup, the fluid is sheared with a force F between a stationary and a moving plate, with a separation distance x and areas A. It is assumed that the fluid at the top plate moves with velocity v of the plate, while the fluid at the bottom plate remains stationary. The velocity of the fluid decreases linearly from the top to the bottom plate with the assumption that the fluid does not adhere to one of the plates. The process is illustrated in Figure 3.10.
The shear stress σ exerted to the fluid is calculated as follows:

$$\sigma = \frac{F}{A} \tag{3.17}$$

The velocity inside the fluid is referred to as shear rate $\dot{\gamma}$ and defined according to Equation (3.18).

$$\dot{\gamma} = \frac{\mathrm{d}v}{\mathrm{d}x} \tag{3.18}$$

Viscosity describes the flow behavior of fluids (or suspensions or gases) and is a measure of internal friction between two layers of the fluid moving past each other.

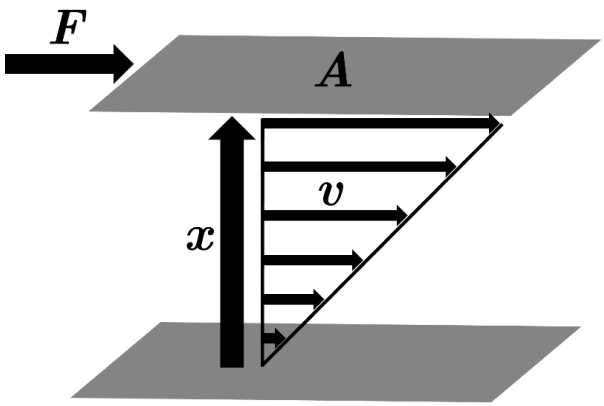

Figure 3.10: Schematic illustration of a rheological measurement.

For Newtonian fluids the shear stress σ is always proportional to the shear rate $\dot{\gamma}$, with viscosity μ being the proportionality constant (see Equation (3.19)).

$$\mu = \frac{\sigma}{\dot{\gamma}} \tag{3.19}$$

Highly loaded suspensions exhibit non-Newtonian behavior, where the proportionality between shear rate and shear stress is not linear, resulting in a change in viscosity or shear stress with shear rate. The viscosity is here termed with apparent viscosity μ_a. If the viscosity decreases with shear rate, the fluid behaves pseudoplastic. If the viscosity increases with shear rate, the fluid behaves dilatant. The relevant apparent viscosity is therefore measured over a wider shear rate range at least up to the shear rate of the applied (shaping) processes. For screen printing of suspensions to form (functional) layers, the suspensions should behave pseudoplastic. Pseudoplasticity allows for shapeability under applied shear stress, while the layers maintain stable in their form when the shear stress is removed. Dilatant suspensions pose the risk of uneven deposition, imposing cracks or defects. The rheological behavior of a suspension is influenced by the powder load, specific surface area, particle size distribution and particle morphology of the powder as well as the kind of additives used in the suspension. Additives can be dispersants which either sterically or electrostatically separate single particles to prevent agglomerations, or binders, which help to build a linked particle network.
The rheological behavior of a suspension can be complex due to interactions between small colloidal particles and their flocking behavior at low shear rates, while the broader end of the particle size distribution dominates the suspension's behavior at high shear rates. Consequently, highly loaded suspensions, where particle

interactions are more pronounced, may exhibit pseudoplastic behavior at low shear rates but become dilatant at higher shear rates.
Viscosity (at a constant shear rate) may exhibit time-dependent behavior, especially for highly loaded suspensions. A decrease in viscosity with time is referred to as thixotropy, while an increase with time is termed rheopexy. Nevertheless, time dependency of viscosity plays a minor role for processes such as screen printing where the shear force is just applied for a short time span.
Particle-particle interactions and yield stress in a suspension are attributed to Van der Waals forces between particles. Yield stress needs to be sufficiently high to prevent sedimentation, but low enough to be overcome by the shaping process. Yield stress serves as a parameter for the particle network strength of the suspension and is measured by determining the point at which the suspension transitions from viscoelastic to fluid-like behavior. Viscoelasticity is a property characterized by the simultaneous presence of elastic and viscous properties in a material. In the case of ideally elastic materials, the application of a constant stress yields a constant strain, resulting in an infinite viscosity. Therefore, viscoelastic systems are often measured applying oscillatory strains or stresses rather than steady flows.
The applied oscillatory strain γ and the resulting stress σ are described according to Equation (3.20) and (3.21) where γ_0 is the maximum strain, σ_0 is the stress amplitude, t is time, ω is the angular velocity, and δ is the phase shift.

$$\gamma(t) = \gamma_0 \sin(\omega t) \tag{3.20}$$

$$\sigma(t) = \sigma_0 \sin(\omega t + \delta) \tag{3.21}$$

The quotient of stress to maximum strain is defined as the complex modulus G^*, describing resistance of the sample against deformation (see Equation (3.22)).

$$G^* = \frac{\sigma_0}{\gamma_0} \tag{3.22}$$

Higher G^* values indicate a more elastic suspension, reducing the likelihood of "ink bleeding" during screen printing.
Viscoelastic properties of a suspension are described by the elastic or storage modulus G' and viscous or loss modulus G''. The elastic modulus represents the storage of energy in the form of deformation and thus the solid-like properties of the suspensions while the viscous modulus describes the liquid-like properties due to dissipation of energy through permanent deformation. The moduli are defined according to Equation (3.23) and (3.24).

$$G' = \frac{\sigma_0}{\gamma_0} \cos(\delta) = G^* \cos(\delta) \tag{3.23}$$

$$G'' = \frac{\sigma_0}{\gamma_0}\sin(\delta) = G^* \sin(\delta) \tag{3.24}$$

A high elastic modulus indicates strong particle network strength, which is beneficial for screen printing but can lead to paste sticking to the squeegee. A high viscous modulus, on the other hand, may result in ink bleeding. The complex modulus can be expressed in terms of the elastic and viscous moduli (see Equation (3.25)).

$$G^* = G' + iG'' \tag{3.25}$$

The magnitude of the full elasticity equals the absolute value of the complex modulus according to Equation (3.26).

$$|G^*| = \sqrt{G'^2 + G''^2} \tag{3.26}$$

The damping factor or phase angle δ gives a measure for the interaction strength of the internal structure and is given by the ratio of elastic and viscous moduli, as shown in Equation (3.27).

$$\delta = \tan^{-1}\left(\frac{G''}{G'}\right) \tag{3.27}$$

For an ideally elastic or solid-like behavior, δ is 0°, and for an ideally viscous or liquid-like behavior, δ is 90°. Thus, all materials with a phase shift in between 0° and 90° are viscoelastic, inhibiting elastic and viscous properties.
The viscoelastic properties of a suspensions offer insight into particle network strength. An important parameter is the linear viscoelastic region (LVE) in which the particle network strength is constant, irrespective of the applied shear stress.
In the LVE the elastic and viscous moduli remain constant, hence no breakdown of the particle network occurs. At a certain shear rate the particle network breaks down, resulting in a sharp decrease of the moduli, giving the yield point. The length of the LVE serves as a measure for particle network strength.
The particle interaction and particle network strength are often modified through additives to achieve the desired properties of the suspension. Suspensions should be pseudoplastic, to facilitate shaping and retain their form after the shaping process. The green body should be organized in a way to achieve the desired microstructure after sintering. Dispersants can be used to modify particle-particle interactions, prevent agglomeration, and enhance the accessibility of the particle surface area to the suspension medium, resulting in a finer and more homogeneous microstructure.
Binders are used to interlink particles in a suspension, thereby increasing particle network strength. Poreformers may also be added to adjust the degree of porosity and pore shape. The density of the produced layers can be influenced by solid loading. Achieving the right balance in suspension content and its rheological

properties is crucial for producing fully or nearly dense layers. At first the powder needs to be well dispersed in a suspension medium. Afterwards, an appropriate amount of binder needs to be added to achieve a printable suspension and a stable green body.
In this thesis, rheology primarily serves to select a suitable dispersant. Lower viscosity of the suspension at rest indicates better dispersion, as low viscosity implies low internal friction between particles. Since viscosity measurement requires the application of a shear rate, which deviates from the "rest state", viscosity at low shear rates is used as a measure of dispersion.
LVE, thixotropy, viscous and elastic moduli as well as phase angle are further measured. While these measurements provide valuable insights, their applicability often lies more in the realm of quality control, as conclusions about these quantities are drawn from the microstructure of the produced layer after sintering.
Rheological measurements were performed with a Physica MCR 301 rheometer (Anton Paar, Graz, Austria) in a plate-plate geometry (PP25/S, 25 mm, serrated) with a shear gap of 0.5 mm at 20 °C. All samples were pre-sheared at shear rates of 0.1 s^{-1} for 2 min followed by a resting phase of 2 min without applying any stress. To measure the dispersion of doped ceria, a constant low shear rate of 0.1 s^{-1} was applied. After 10 s, viscosity was measured and repeated five times, with the average of the five measurements taken as a representative value for the level of dispersion. Flow curves, showing viscosity as a function of shear rate, were measured up to shear rates of 0.1-1000 s^{-1} with a logarithmic slope (22 points per decade) for 5-10 s per measurement point to measure pseudoplastic or dilatant behavior.
To gain insight about the LVE and yield point of the screen printing pastes, the elastic modulus G', viscous modulus G'', and phase angle δ are determined through an oscillatory test. A shear stress of 0.01-1000 Pa with a logarithmic slope (21 points per decade) was applied with an oscillation frequency of 1 Hz. The measurement was stopped when a breakdown of the LVE occurred, indicating the yield point.
To measure thixotropy an oscillatory three interval thixotropy test (3ITT) of the screen printing pastes was performed. In the first interval, the paste was subjected to low shear stresses to simulate resting conditions, with an angular frequency of 10 rad/s imposing a strain of 1 % for 60 s. In the second interval, the paste was exposed to high shear rates to simulate the shaping process, with a shear rate of 3000 s^{-1} applied for 5 s. In the third interval the same measurement parameters as in the first interval were applied to simulate the conditions at rest after the shaping process. The rebuilding of the structure was measured until the moduli reached constant values.

3.2.9 Archimedes' principle and density measurement

The Archimedes' principle was utilized to determine the relative density of a body submerged in a fluid. When a body is partially or fully submerged, it experiences an upward force known as buoyancy that is equal to the weight of the displaced fluid.

If the submerged object's density is less than that of the displaced fluid, it rises, while if the object's density exceeds that of the fluid, it sinks and experiences an apparent mass loss. Therefore, the density of an object submerged in water can be calculated according to Equation (3.28)

$$\frac{\varrho_O}{\varrho_F} = \frac{w_O}{w_f} = \frac{w_O}{w_O - w_{iO}} \tag{3.28}$$

where ϱ_O denotes the density of the object, ϱ_F denotes the density of the fluid, w_O denotes the weight of the object, w_f denotes the weight of the displaced fluid, and w_{iO} denotes the apparent weight of the submerged object.[112]
To investigate the density and open porosity of various samples, the Archimedes' principle was employed in H_2O according to DIN 66137-3, and the density was also analyzed by image analysis of cross-sections using the software Fiji/ImageJ.

3.2.10 Specific surface area measurements

The specific surface area of a material can be determined by measuring the amount of gas adsorbed onto its surface. Physical adsorption occurs due to van der Waals forces, whereas chemical adsorption arises from chemical reactions between the solid and the adsorbate. In this thesis, the specific surface areas of the samples were assessed using Brunauer–Emmett–Teller (BET) analysis. The BET theory assumes physical multilayer adsorption, where all layers are in equilibrium and do not interact with each other, serving solely as adsorption sites for the molecules in the layer above. Accordingly, the single layers follow the Langmuir equation for adsorption. The BET theory leads to Equation (3.29):

$$\frac{p/p_0}{n(1-p/p_0)} = \frac{1}{n_m C} + \frac{C-1}{n_m C}(p/p_0) \tag{3.29}$$

where n denotes the specific amount of adsorbed gas, p is pressure, p_0 is the saturation pressure of the adsorbate at the adsorption temperature, n_m denotes the monolayer capacity, and C is the BET constant, which exhibits an exponential relationship with the monolayer adsorption energy. From the measured adsorption isotherm, which gives the adsorbed gas volume as a function of the relative pressure, a BET transform plot is generated, where $(p/p_0)/(n(1-p/p_0))$ is plotted versus p/p_0, obtaining a linear plot, with $C - 1/n_m C$ being the slope S and $1/n_m C$ being the y-axis intercept I. With the help of S and I, the monolayer capacity and the BET constant are calculated according to Equations (3.30) and (3.31).

$$n_m = \frac{1}{S + I} \tag{3.30}$$

$$C = 1 + \frac{S}{I} \tag{3.31}$$

Knowing n_m, the BET surface area per unit mass of the sample A_{BET} is calculated according to Equation (3.32):

$$A_{BET} = \frac{n_m L \sigma_m}{V_0 m} \tag{3.32}$$

where L is the Avogadro constant, σ_m denotes the molecular cross sectional area of the adsorbate, m denotes the sample mass, and V_0 denotes the molar gas volume of the adsorbate at standard conditions.[113,114]
The specific surface areas for samples in this thesis were determined by measuring N_2 (σ_m = 0.162 nm^2) adsorption isotherms using an areameter (Jung Instruments Areamat) and subsequently performing BET analysis on the resulting data.

3.2.11 Laser diffraction spectrometry / particle size distribution analysis

To gain insight into the particle size distribution (PSD) of an accumulation of particles, laser diffraction spectrometry (LDS) is a convenient technique. Light is scattered by passing through a system of dispersed particles. The particle size distribution can be calculated from the emerging light-intensity diffraction pattern. However, for particles that are large in relation to the wavelength of the incident beam, the Lorenz-Mie theory must be applied to derive the PSD from the diffraction pattern. This theory, which is based on Maxwell's equations, provides a description of the electromagnetic field after it has interacted with a spherical, homogeneous particle, taking into account not only diffraction at the particle's edges but also absorption, refraction, and reflection occurring at the particle's surface and within the particle. For further information, see [115–117].
Particle sizes were measured in ethanol using a laser scattering particle size distribution analyser (Partica LA-950V2 by Retsch Technology). Initially, an ultrasonic treatment was used to break loose agglomerates and disperse the particles.

4 Doped ceria and its interdiffusion with 8YSZ in SOC manufacturing

This chapter addresses doped ceria as potential substituent for 8YSZ in the fuel electrode of a SOFC. Initially, a series of foundational experiments was conducted to understand the interdiffusion behavior between Y-, Gd-, and Sm-doped ceria and an 8YSZ electrolyte. These experiments comprised the analysis of phase formation within powder mixtures, the determination of interdiffusion lengths in layered diffusion couples, and the assessment of impedance responses in symmetrical cells. In a second step, the process of integrating doped ceria into an actual FESC is described. The electrochemical performance and carbon degradation tolerance of these cells is tested at the Technical University of Munich (TUM), Chair of Energy Systems.
In addition, alternative sintering strategies were examined to investigate their applicability and impact on interdiffusion.
Part of this chapter has been published in the *Journal of the European Ceramic Society* [118].

4.1 Interdiffusion experiments

Motivation
Owing to its compelling combination of conductivity, stability, and material compatibility, 8YSZ is the preferred material for electrolytes and fuel electrodes in FESCs. Mainly used in stationary applications at higher operating temperatures, FESC exhibit promising power densities, utilizing a thin electrolyte. However, lowering the operating temperature might allow applications beyond stationary power generation. In comparison to 8YSZ, doped ceria shows higher ionic conductivities in the intermediate temperature range. A further concerning disadvantage of Ni-8YSZ fuel electrode cermets is their severe degradation during internal reforming of higher hydrocarbons. Although the main degradation is related to the Ni catalyst, the fuel electrode is nevertheless deactivated or disintegrates due to Ni-dusting [11,14,119–121].
Doped ceria is regarded as a promising alternative in the fuel electrode cermet, as it tends to show improved performance compared to Ni-8YSZ fuel electrodes [122–124]. This performance increase is attributed to doped ceria's higher ionic conductivity in the intermediate temperature range (500-700 °C) [62] and its ($p(O_2)$-dependent) redox and MIEC behavior, enabling catalytic activity and forming DPBs with the fuel gas phase [125,126]. Basically, doped ceria can also fulfil the role of the Ni-catalyst. Therefore, studies showed the improved degradation tolerance of doped ceria [12,65,66,69,127], where one reason might be that doped ceria can take over the role of the Ni catalyst, if it is deactivated, which is not the case for 8YSZ. For

this reason, fuel electrodes just made of doped ceria have been explored, but their performance is worse than that of a Ni-doped ceria cermet [128]. Presumably, due to the lower electronic conductivity and catalytic activity of doped ceria in comparison to Ni.

Obstacles

The obstacle to replace 8YSZ with doped ceria lies in the fabrication process of FESCs. In the case of the FESCs manufactured at IEK-1, FZJ a cofiring of the HC layers (substrate|fuel electrode|electrolyte) at 1400 °C is necessary to achieve the desired microstructures [129]. The high-temperature sintering of layered systems inevitably leads to interdiffusion between the layers and may compromise their functional behavior, in the present case between 10GDC and 8YSZ. The interdiffusion process between GDC and 8YSZ is well investigated on the air side of the FESC between the GDC diffusion barrier layer and the 8YSZ electrolyte [130–135]. The formed $ZrCeO_2$ mixed phase exhibits lower conductivity [136–139], but is nevertheless beneficial because it plays a significant role in preventing $SrZrO_3$ formation at the electrolyte interface during air electrode sintering, which is even more insulating [140]. The sintering temperature of the GDC barrier should be at least 1300 °C to form a sufficiently dense $ZrCeO_2$ layer [141], which is 100 °C lower than the sintering temperature of the Ni-10GDC/8YSZ layer composite on the fuel side. As the temperature dependency of diffusion follows an Arrhenius law, the difference in sintering temperature might significantly enhance interdiffusion. In addition, NiO is present on the fuel side. At IEK-1, FZJ a FESC was manufactured, where 8YSZ in the fuel electrode was replaced with 10GDC. However, this replacement led to a performance degradation that cannot be explained by the formation of a mixed phase alone [142].

Experimental design

Therefore, this thesis investigates the interdiffusion behavior between doped ceria and 8YSZ in the context of SOC manufacturing. One strategy to influence diffusion in solids involves the modification of the crystal lattice by doping it with foreign cations of varying ionic radii or valence charges. Dopants impose strain, alter electrostatic interactions (such as dopant-vacancy interactions), influence segregation behavior and affect the solute drag at the grain boundaries, which potentially influences the diffusion of cations and anions through the crystal lattice and the grain growth in polycrystalline materials. In the case of ceria, reduction induces "self-doping" through the valence change of Ce^{4+} to Ce^{3+}. Different acceptor dopants with an average valence of +III were chosen to investigate the influence

Table 4.1: Ionic radii for Ce, Y, Gd, and Sm summarized by Shannon for a coordination number of VIII. Values determined by r^3 vs V plots.[143]

Ion	Ionic radius (Å)
Ce^{4+}	0.97
Ce^{3+}	1.143
Y^{3+}	1.019
Gd^{3+}	1.053
Sm^{3+}	1.079

of the ionic radii on the interdiffusion with 8YSZ. The dopants of choice are listed in increasing order of their radii: Y>Gd>Sm. Table 4.1 displays the values of the ionic radii in comparison with Ce for a coordination number of VIII [143].
Gd is the most common atom ceria is doped with to enhance ionic conductivity, although Sm as a dopant seems to enhance ionic conductivity slightly more than Gd [144,145]. Y as a dopant may decrease the chemical concentration gradient with the adjacent 8YSZ layer and reduce interdiffusion of the Y dopant from both layers.
To investigate the interdiffusion behavior and its impact on material properties, several experiments were carried out: i) Analysis of the relative phase formation in compacted powder mixtures. ii) Ionic conductivity measurements of the materials and formed secondary phases. iii) TGA of the materials and formed secondary phases. iv) Determination of the interdiffusion lengths in diffusion couples. v) Investigation of the interdiffusion on the impedance response of symmetrical cells. In addition, novel sintering techniques such as UHS, FAST-SPS, and blacklight sintering were performed on compacted powder mixtures to compare their influence on interdiffusion and secondary phase formation with conventional sintering. Reactive sintering of the 8YSZ electrolyte was explored to lower the sintering temperature.
For sample preparation, commercially available powders were used: yttria-stabilized zirconia $Y_{0.148}Zr_{0.852}O_{1.926}$ (8YSZ, TZ-8Y, Tosoh, Japan), gadolinia-doped ceria $Gd_{0.1}Ce_{0.9}O_{2-\delta}$ (10GDC, Fuelcellmaterials, USA), yttria-doped ceria $Y_{0.1}Ce_{0.9}O_{2-\delta}$ (10YDC, Cerpotech, Norway), samaria-doped ceria $Sm_{0.1}Ce_{0.9}O_{2-\delta}$ (10SDC, Kceracell, Republic of Korea), and nickel oxide NiO (Vogler, The Netherlands).
At first the starting powders were characterized regarding their PSD, particle morphology, and specific surface area.

Particle size distribution & specific surface area
PSD and specific surface areas of the starting powders are given in Table 4.2.
PSD of the doped ceria powders (10XDC, 10X = 10 mol% Y, Gd or Sm) are comparable, except for the d_{90} of 10YDC which is approximately 5 times higher compared to 10GDC and 10SDC. Considering the higher specific surface area of 10YDC, it is probable that the ultrasonic treatment applied before particle size analysis was unable to break all agglomerates. However, it can be assumed that

Table 4.2: Particle size distribution and specific surface area of the starting powders 8YSZ, 10YDC, 10GDC, 10SDC, and NiO.

Material	**d_{10} (µm)**	**d_{50} (µm)**	**d_{90} (µm)**	**SSA (m^2/g)**
10YDC	0.07	0.11	1.10	16.2
10GDC	0.07	0.11	0.23	12.1
10SDC	0.07	0.10	0.19	10.5
8YSZ	0.16	0.54	1.51	13.2
NiO	0.40	0.66	1.19	4.8

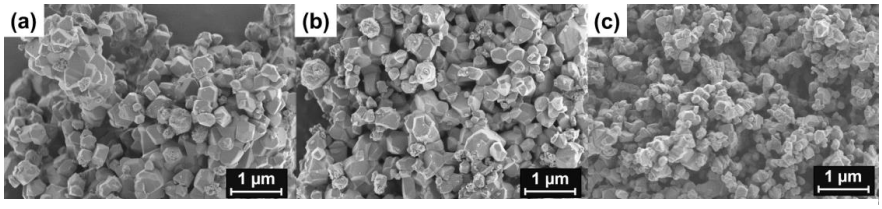

Figure 4.1: Powder morphologies and particle sizes analyzed by SEM for (a) 10YDC, (b) 10GDC, and (c) 10SDC.

these agglomerates have been effectively broken up due to the ball milling process, which was carried out before using these powders for pellet or slurry fabrication.
The particle morphology of the 10XDC powders was investigated by SEM (see Figure 4.1). The particle shapes are similar, while all powders tend to agglomerate. On average, the powders are similar enough to assume that individual powder properties, especially the contact area with 8YSZ particles, do not influence the interdiffusion behavior to a substantial degree, thus individual processing steps do not have to be adapted for each one.

4.1.1 Interdiffusion in powder mixtures

The relative formation of secondary phases (here referred to as mixed phases) in the powder mixtures after heat treatment was utilized as an indirect measure of the influence of the dopant in ceria on interdiffusion with 8YSZ. For sample preparation, 58 mol% of 10XDC and 42 mol% of 8YSZ were mixed and ball milled with 3 mm ZrO_2 milling balls to ensure homogenization and break up agglomerates. The dried powder mixtures were pressed into pellets with a diameter of 20 mm by applying a uniaxial pressure of approximately 35 MPa. Subsequently, the pellets were cold isostatically pressed at a pressure of 400 MPa. Sintering was carried out for 5 h at temperatures between 1000-1400 °C in ambient air, with an increment of 100 °C. Afterwards, the pellets were ground, and XRD analysis along with Rietveld refinement were performed to analyze the relative phase distribution. Furthermore, TGA and ionic conductivity measurements were conducted on the pellets sintered at 1400 °C. In addition, microstructure analyses were performed on thermally etched (1300 °C for 0.5 h) cross-sections.

Microstructure of the sintered pellets
In general, the microstructure of the sintered 8YSZ/10XDC pellets (shown in Figure 4.2) is comparable. 8YSZ/10GDC shows a slightly larger average grain size compared to 8YSZ/10YDC and 8YSZ/10SDC pellets (see Table 4.3), indicating slightly higher cation mobility. The grain size for Y or Sm as a dopant in ceria in the mixture with 8YSZ does not differ. The density of the 8YSZ/10XDC pellets is comparable, yielding approximately above 96% of the theoretical density, as shown

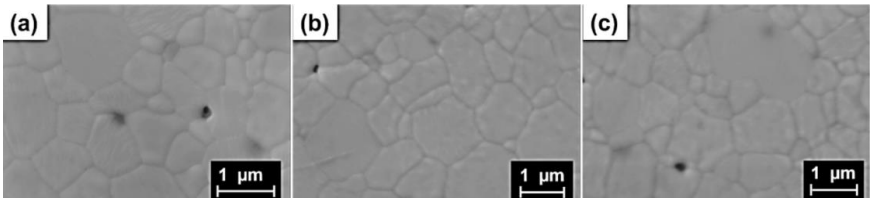

Figure 4.2: Microstructures of (a) 8YSZ/10YDC, (b) 8YSZ/10GDC, and (c) 8YSZ/10SDC pellets sintered at 1400 °C for 5 h and subsequently thermally etched at 1300 °C for 0.5 h.

in Table 4.3.

XRD analysis of the relative phase formation

The complete miscibility of zirconia and ceria and the interdiffusion during high temperature treatment is well documented [130,146–150]. Since interdiffusion kinetics depend on the contact area between particles, powders with similar particle size distributions and shapes have been chosen for the different dopants in 10XDC. Although, a certain similarity of the used powders is given, the obtained results are dependent on the properties of the used powders and its influence cannot fully be separated from the influence of the dopant.

The other parameters that influence interdiffusion are temperature and time. Therefore, the phase formation and content inside the mixed 8YSZ/10XDC pellets were analyzed as a function of temperature while the sintering time has been held constant (5 h).

Figure 4.3(a–c) shows the diffraction patterns of 8YSZ/10XDC pellets after sintering at different temperatures. The Bragg reflections of the (111) crystallographic plane of 8YSZ and 10XDC are indicated with a black line and a black dashed line, respectively. No additional phases are visible apart from 8YSZ, 10XDC and their intermixing phases.

No intermixing is apparent after sintering at 1000 °C. With rising sintering temperature, the diffraction patterns show a shift in the position of the (111) diffraction line to higher 2Θ angles for 8YSZ and to lower 2Θ angles for 10XDC, respectively, indicating intermixing.

The 8YSZ lattice expands due to an increasing amount of Ce and the respective dopant X dissolving into it, leading to a shift of the reflections to lower 2Θ angles according to Bragg's law ($\sin(\Theta) \sim 1/a$). On the other hand, the XDC lattice

Table 4.3: Average grain sizes and relative densities for the 8YSZ/10XDC pellets sintered at 1400 °C for 5 h and subsequently thermally etched at 1300 °C for 0.5 h.

Material	Average grain size (µm)	Relative density (%)
8YSZ/10YDC	0.65 ± 0.09	97 ± 2
8YSZ/10GDC	0.88 ± 0.12	96 ± 2
8YSZ/10SDC	0.65 ± 0.08	98 ± 1

contracts with increasing Zr and Y content shifting the reflections to higher 2Θ angles. These phases are denoted as YSZ_$_{XDC}$ and XDC_$_{YSZ}$, respectively.
After sintering at 1300 °C, only one single fluorite phase is visible for all dopants. They differ in the full width at half maximum (FWHM) of the reflections for the different dopants, indicating differences in lattice disorder and different amounts of fully intermixed phases. The FWHM is highest for Sm, followed by Y, and lowest for Gd, indicating a higher amount of lattice order and intermixing for 10GDC followed by 10YDC and 10SDC.
For all dopants, the FWHM decreases again when increasing the sintering temperature to 1400 °C, indicating larger crystallites and less strain in the lattice.
To analyze the relative phase content and its development, a Rietveld analysis was performed (the error is estimated to be about ~1%). Since the solid solutions follow Vegard's law, meaning a linear relationship between lattice parameter and stoichiometry (see Figure A.1, Appendix A), it is possible to determine the lattice parameter of each phase, calculate the stoichiometry of the phases, and then determine the relative phase content. Note that for the purpose of this analysis, the stoichiometry of the parent compounds and the fully intermixed phase are fixed, whereas the intermediate phases YSZ_$_{XDC}$ and XDC_$_{YSZ}$ have a varying stoichiometry over the temperature range. This is necessary since the interdiffusion is a continuous process, meaning that the only defined stoichiometries are the starting compounds and the fully intermixed result.
Figure 4.3(d–f) shows the results of the Rietveld refinement for 8YSZ/10XDC powder mixtures. Discrete data points are shown, the lines are a guide to the eye.
In general, the amounts of the pure 10XDC-phases decrease faster than the pure 8YSZ phase independent of the dopant in ceria. The YSZ-rich mixed phases (YSZ_$_{XDC}$) increase faster in amount than the 10XDC rich mixed phases (XDC_$_{YSZ}$) indicating a higher interdiffusion coefficient for Ce and the respective dopant X compared to Zr and Y.
Considering the dopant in ceria and its influence on the interdiffusion behavior with 8YSZ, changes in the relative phase distribution are observable. The YSZ_$_{GDC}$ and GDC_$_{YSZ}$ phases form at lower temperatures and in higher amounts compared to Y and Sm doped ceria. Also, the mixed phase forms at temperatures between 1200 and 1300 °C. For 8YSZ/10YDC mixtures, the mixed phase forms at higher temperatures between 1300 and 1400 °C. For 8YSZ/10SDC mixtures, no completely mixed phase is formed up to 1400 °C and the amount of YSZ_$_{SDC}$ and SDC_$_{YSZ}$ is lower at all given temperatures compared to YSZ_$_{GDC}$, GDC_$_{YSZ}$ and YSZ_$_{YDC}$ and YDC_$_{YSZ}$. Also, for 8YSZ/10SDC two YSZ rich mixed phase were observed (YSZ1_$_{SDC}$ and YSZ2_$_{SDC}$) and no formation of a fully intermixed phase.
This may indicate an influence of the dopant or dopant radius on the interdiffusion kinetics and the formation of mixing phases in powder mixtures with 8YSZ.
The intermediate phases are kinetically stabilized phases, since the system has not had sufficient time to fully intermix. In this investigation, we intentionally limited

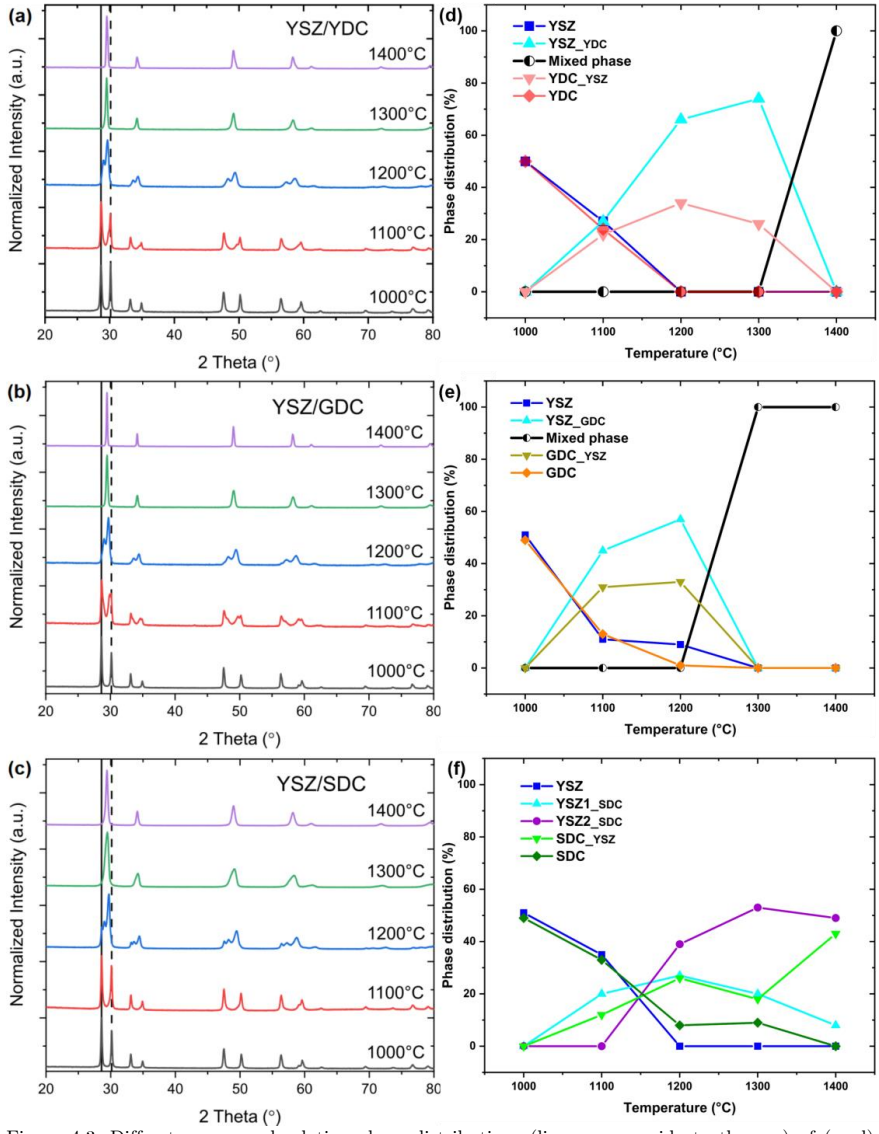

Figure 4.3: Diffractograms and relative phase distributions (lines are a guide to the eye) of (a, d) 8YSZ/10YDC, (b, e) 8YSZ/10GDC, and (c, f) 8YSZ/10SDC powder mixtures sintered in ambient air at temperatures between 1000 and 1400 °C for 5 h. Black and dashed black vertical lines represent the position of the (111) 8YSZ and 10GDC reflections, respectively.

the sintering time to 5 hours in order to determine the degree of intermixing that can be expected during sintering of the fuel electrode-supported HF.

Phase formation in Ar/H_2 and O_2

The experiment was repeated but with pellets sintered in a saturated Ar/ 3 % H_2 or O_2 atmosphere. The sample preparation, sintering, and data evaluation were similar to those described above for samples sintered in ambient air.

The resulting diffractograms and calculated relative phase distributions can be found

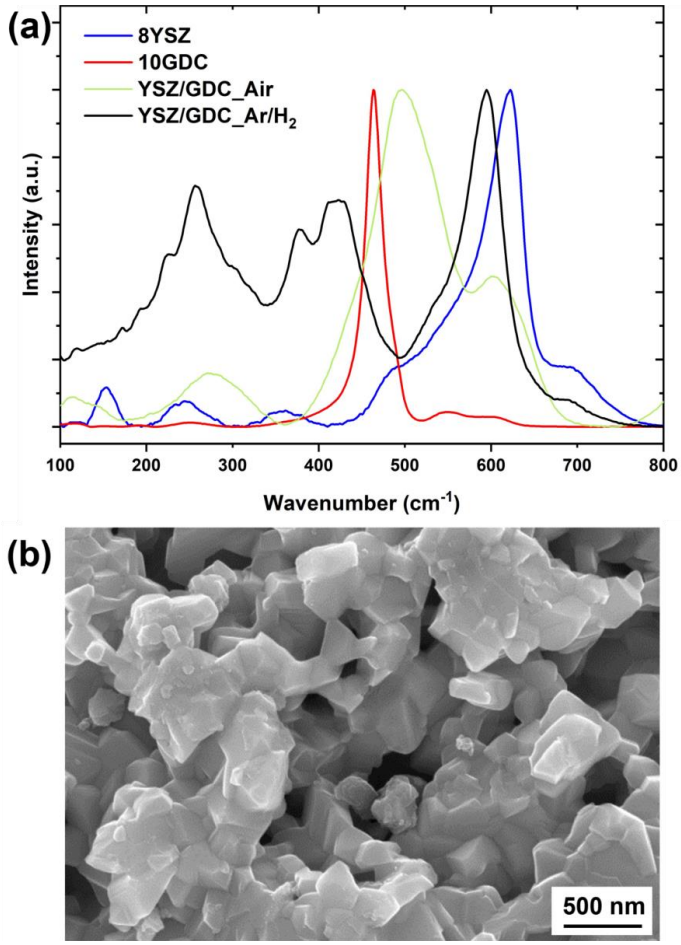

Figure 4.4: (a) Raman spectra of 8YSZ, 10GDC, and 8YSZ/10GDC sintered at 1400 °C for 5 h either in air or Ar/ 3 % H_2. (b) SEM micrograph of a pellet sintered at 1400 °C for 5 h in Ar/ 3 % H_2.

in Appendix A, with Figure A.2, illustrating the outcomes for samples sintered in Ar/ 3 % H_2, and Figure A.3, for those sintered in O_2.
It appears that an O_2 atmosphere slightly suppresses mixed phase formation. In the cases of 8YSZ/10YDC and 8YSZ/10GDC, the mixed phase formation decreases, albeit it starts at lower temperatures for 8YSZ/10YDC. Meanwhile, for 8YSZ/10SDC, the results are comparable to samples sintered in ambient air.
For samples sintered in an Ar/ 3 % H_2 atmosphere, the interdiffusion of the cations is enhanced, as mixed phase formation starts at 1000 °C. Additionally, the formation of a pyrochlore phase, and a color change of the samples from white/yellow to dark blue /black is observable, starting between 1000-1100 °C, indicating reduction of the materials [151]. The reduction of Ce induces porosity inside the samples owing to chemical expansion. Raman spectroscopy confirms the formation of a new phase. Some characteristic Raman signals for the pyrochlore phase are around 300, 400 and 600 cm^{-1} [141]. One characteristic ceria signal is around 466 cm^{-1}, and the characteristic 8YSZ signal is around 620 cm^{-1} [152]. In comparison to the fluorite phase, Raman spectra, alongside with a SEM micrograph of 8YSZ/10GDC sintered in Ar/ 3 % H_2 at 1400 °C for 5 h, are shown in Figure 4.4. It is important to note that due to potential local stoichiometry and phase composition variations within the sample, Raman signals may appear broad and shifted.

4.1.2 Alternative sintering of 8YSZ/10GDC powder mixtures

UHS, FAST-SPS, and blacklight sintering techniques were employed on 8YSZ/10GDC powder mixtures to assess the extent of mixed phase formation in comparison to conventional sintering.
The preparation of the powders involved mixing and ball milling, following the procedures outlined in Section 4.1.1 , which were similar to those employed for conventional sintering. As mentioned in Section 3.1.1, the common issue of UHS and FAST-SPS is their reducing character, which is especially challenging for the sintering of ceria due to its redox behavior. Although blacklight sintering and its setup are not reducing in nature, the high sintering temperature might alter the temperature-dependent oxygen non-stoichiometry of the materials. Initial experiments posed a challenge, as the inherently reducing nature of these sintering methods led to the formation of a pyrochlore phase, rendering a meaningful comparison unfeasible. The appearance of the pyrochlore phase was also visually evident, with the samples transitioning from a white/yellow to a dark blue /black color, resembling conventionally sintered samples in Ar/H_2 (as elaborated in Section 4.1.1). Therefore, to identify whether the respective sintering experiment reduced the 8YSZ/10GDC sample, the XRD and Raman data were compared with those of samples conventionally sintered in Ar/H_2. The primary objective of further experiments was to prevent reduction of ceria and pyrochlore phase formation, allowing for a meaningful comparison of the extent of relative phase formation with conventionally sintered samples. The high heating rates achievable with all these

Table 4.4: Sintering parameters and porosity values of the UHS1-6 samples.

UHS sample/ parameter	UHS1	UHS2	UHS3	UHS4	UHS5	UHS6
Current (A)	14	16	18	24	20	24
Sintering time (s)	10	10	10	10	10	10
Atmosphere	Vacuum	Vacuum	Vacuum	Vacuum	Vacuum	Vacuum
Coverage	/	/	/	/	/	/
Temperature (°C)	/	/	/	/	/	/
Porosity (%)	42	37	24	25	9	8

techniques might decrease interdiffusion, as they might suppress diffusion mechanisms occurring at lower temperatures, such as surface diffusion.

UHS

For UHS, pellets with a diameter of 8 mm were pressed by applying a uniaxial pressure of approximately ~120 MPa. Subsequently, the pellets were cold isostatically pressed with a pressure of 400 MPa. In a first set of experiments, all samples were positioned between a graphite felt and sintered in a vacuum environment with a current of 14-24 A (UHS1-6) gradually increasing by 2 A increments for 10 s each. In a second set of experiments, the samples were encapsulated in a 25 µm thick tantalum foil to prevent direct contact to the graphite felt electrodes. The encapsulation was not gastight. Additionally, the sintering atmosphere was changed to Argon. A current of 24 A was applied for 10 s, 30 s, 40 s or 60 s, respectively. Another sample was sintered at 20 A for 30 s (UHS7-11). For the sample UHS7-11 the temperature next to the sample was measured with a pyrometer. Relative density or porosity was estimated applying the Archimedes' method in water. Porosity values and sintering parameter are summarized in Table 4.4 and Table 4.5.

Table 4.5: Sintering parameters, temperatures, and porosity values of the UHS7-11 samples.

UHS sample /parameter	UHS7	UHS8	UHS9	UHS10	UHS11
Current (A)	24	24	24	24	20
Sintering time (s)	10	30	40	60	30
Atmosphere	Argon	Argon	Argon	Argon	Argon
Coverage	Ta	Ta	Ta	Ta	Ta
Temperature (°C)	1196	928	980	1237	906
Porosity (%)	9	34	20	13	25

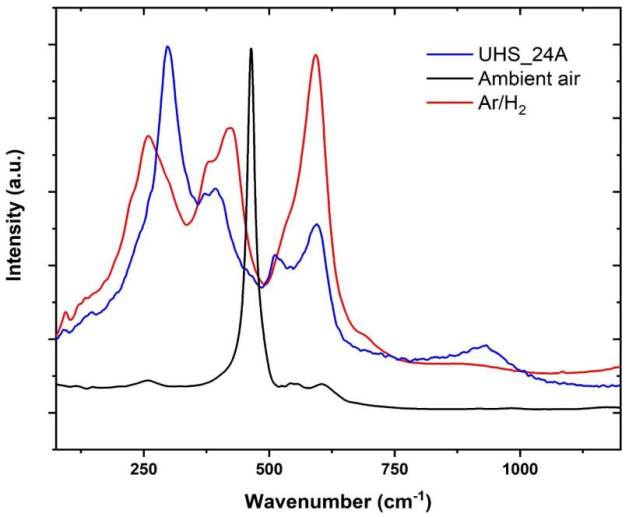

Figure 4.5: Raman spectra of 8YSZ/10GDC powder mixtures sintered in ambient air or Ar/H_2 at 1400 °C for 5 h or with UHS at 24 A for 10 s.

For samples sintered without tantalum foil and in vacuum (UHS1-6) porosity decreases from a state of barely sintered at 14 A (UHS1) to ~8 % when sintered with a current of 24 A (UHS6). An alteration in sample color is notable, commencing at 16 A and transitioning to a dark blue /black color by 18 A. Raman analysis for UHS6 (see Figure 4.5) indicates a resemblance to 8YSZ/10GDC samples sintered in an Ar/H_2 atmosphere, suggesting the emergence of the pyrochlore phase (as shown in Section 4.1.1 and Figure 4.4). Therefore, the dark blue /black color transformation serves as an initial indicator of reduction.

Diffractograms, along with the calculated relative phase distributions (see Figure 4.6(a,b)), reveal gradual intermixing starting at 14 A, with about 10 % of the initial 10GDC phase and 35 % of the initial 8YSZ phase still present. Intermixing increased at 16 A, and at 18 A, a predominantly fully intermixed phase formed. Increasing the current further results in the coexistence of the pyrochlore phase alongside with the fluorite mixed phase. As the current increases, the pyrochlore phase content rises, while the amount of the fluorite mixed phase diminishes, indicating enhanced reduction of the materials. Consequently, in the subsequent series of experiments, the samples were enveloped in a tantalum foil to reduce the extent of reduction by preventing direct contact with the graphite electrodes. Additionally, the atmospheric environment was switched to argon.

2Θ-angle position of the mixed phase reflections in the sample were compared to the position of the 2Θ-angles for the mixed phases formed in conventionally sintered 8YSZ/10GDC samples in ambient air or Ar/H_2 environments. For samples labelled as UHS7-10, sintered at 24 A, an increase in sintering time leads to a shift of the mixed phase reflections towards the pyrochlore phase. Despite UHS7 exhibiting the

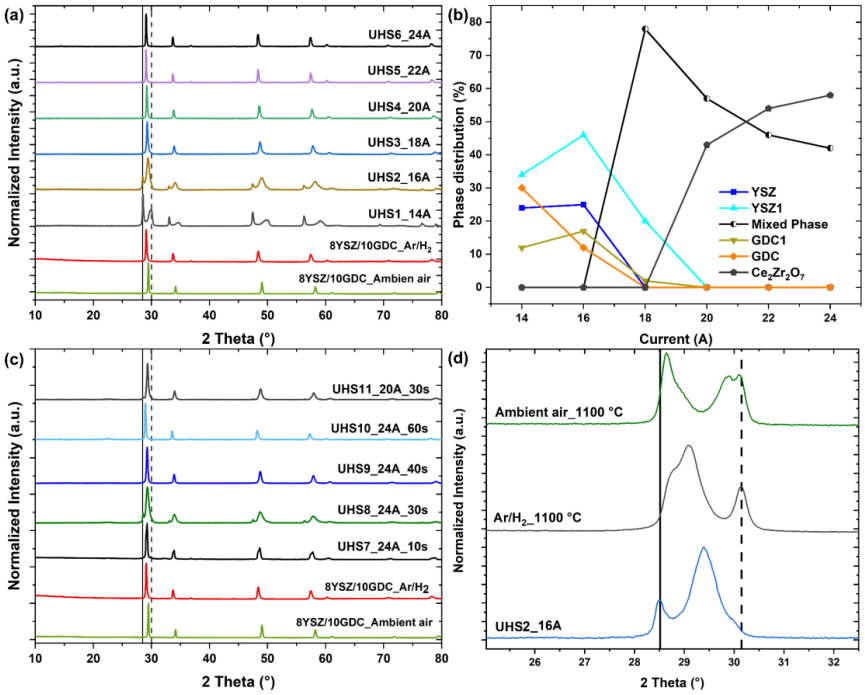

Figure 4.6: (a) Diffractograms of UHS1-6, (b) calculated relative phase distributions (lines are a guide to the eye) from (a) for UHS1-6 sintered at 14-24 A, (c) diffractograms of UHS7-11, (d) (111) reflections of 10GDC (solid line) and 8YSZ (dashed line) and their intermixing phases. (a, c) show additionally diffractograms of 8YSZ/10GDC sintered in ambient air and Ar/H_2 sintered at 1400 °C for 5 h to analyze if the fluorite mixed phase or the pyrochlore phase was formed in UHS samples. Black and dashed black vertical lines represent the position of the (111) 8YSZ and 10GDC reflections, respectively.

shortest sintering time (10 s), its corresponding reflections display a more pronounced shift towards the pyrochlore phase when compared to UHS8 and UHS9. In the case of UHS8, the reflection of the original 10GDC phase remains visible. Furthermore, reducing the sintering current to 20 A (UHS11) results in the persistence of residual 10GDC phases and a higher quantity of the fluorite mixed phase.

The samples themselves exhibit color gradients, suggesting a significant degree of inhomogeneity. The corresponding Raman spectra display broad and overlapping peaks, reflecting the presence of both the fluorite and pyrochlore mixed phases, as well as remnants of the precursor materials. Therefore, the Raman signal around 2100-2150 cm^{-1} which is attributed to Ce^{3+} is used as means to identify if the sample is partially reduced [153]. UHS10 and UHS11 samples exhibit distinct bright (UHSX_b) and dark (UHSX_d) regions, which were investigated separately.

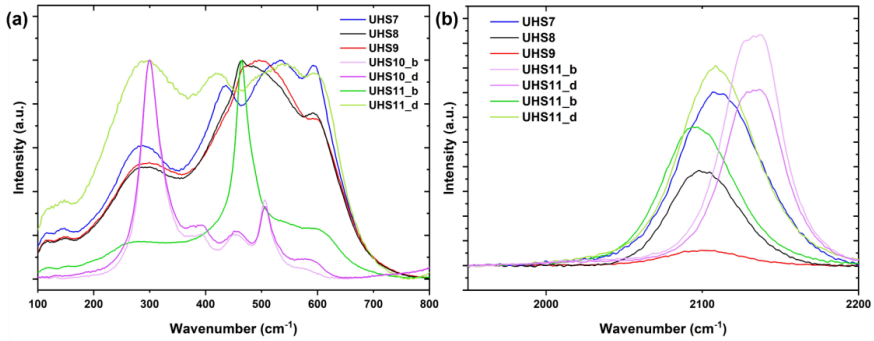

Figure 4.7: Raman spectra of UHS1-7 for a wavenumber range of (a) 100-800 cm^{-1} and (b) 1950-2200 cm^{-1}.

In general, the Raman spectra resemble the indications from the XRD data (see Figure 4.7). UHS7 indicates the pyrochlore phase, while UHS8-9 show additional signals for 10GDC and the fluorite mixed phase. Both UHS10_b and UHS10_d reveal similar spectra, predominantly indicating the pyrochlore phase. UHS11_d also indicates the pyrochlore phase but with broader signals. In contrast, UHS11_b shows a high amount of the original 10GDC phase, but with Ce^{3+} present. All samples exhibit at least a weak signal around 2100-2150 cm^{-1}, indicating the presence of Ce^{3+} (see Figure 4.7(b)). In general, low $p(O_2)$-atmospheres decrease the onset for thermal reduction of ceria substantially; e.g., at a ~$p(O_2) = 10^{-8}$ bar, reduction of $CeO_{1.95}$ starts at around 500 °C [154]. The presence of ZrO_2 enhances reducibility of ceria [155]. Therefore, mitigating the presence of carbon in a low $p(O_2)$ sintering setup might not be sufficient to prevent the pyrochlore phase formation in ceria-zirconia compounds. Due to its novelty, the UHS setup is susceptible to fluctuations during the sintering process, as indicated by temperature measurements from the pyrometer. Although UHS7-10 were sintered at the same current of 24 A, the sintering temperature deviates from 928 °C up to 1237 °C. When the temperature exceeds about 980 °C, as seen in UHS9, the formation of the pyrochlore phase and possibly reduction appears to be significantly enhanced. But samples with a sintering temperature below <~1000 °C lack density, reaching a maximum relative density of 80 %. It is possible that increasing the sintering time further might reduce porosity. If the sintering temperature exceeds approximately 1000 °C, samples reach up to ~90 % relative density. This has also been observed for 8YSZ/10GDC powder mixtures conventionally sintered in Ar/H_2. The extensive reduction of cerium and the resulting chemical expansion may induce porosity in the sample, reaching around 10 % of the bulk sample.

Shielding the sample from carbon exposure during sintering through the use of a conductive foil effectively mitigates carbothermal reduction. Nevertheless, high

sintering temperatures in a low $p(O_2)$-environment still lead to the inherent reduction of ceria.
Interestingly, contradictory to conventionally sintered 8YSZ/10GDC samples, during the UHS process the reflection of the 8YSZ shifts earlier compared to the 10GDC reflection. This shift indicates higher cation mobility of Zr and/or Y compared to Ce and/or Gd during the UHS process (see Figure 4.6(d)). The underlying causes for this behavior need further investigation.

FAST-SPS

For FAST-SPS experiments, the powders were loosely pressed into a graphite tool. During the sintering process a uniaxial pressure of 50 MPa was applied. In contrast to UHS, the setup allows precise control of heating rates and sintering temperature. Sintering temperature was set to 1400 °C. Heating and cooling rates were set to 100 °C/min. Sintering time was 10 min for FAST1-3 and 5 min for FAST4. FAST1 was sintered in a vacuum, whereas atmosphere was switched to argon for FAST2-4. For the sintering of FAST4 tantalum powder was pressed on top and bottom of the sample pellet to prevent contact with the tool. However, the edges of FAST4 still came into contact with the tool. The sintering parameters alongside with the porosity values are summarized in Table 4.6.

During the sintering process, FAST1-3 displayed a transformation, with their top and bottom surfaces turning dark blue /black, indicating the formation of the pyrochlore phase and material reduction. Interestingly, the central regions of these samples exhibited less alteration and retained a more white/yellow color. FAST1 sintered in a vacuum environment exhibited a porosity of approximately 15 %, but when the atmosphere was switched to argon, there was a slight reduction in porosity to around 9 % for FAST2 and 13 % for FAST3. This residual porosity is attributed

Table 4.6: Sintering parameters and porosity values of FAST1-4 samples.

FAST sample/ parameter	**1**	**2**	**3**	**4**
Temperature (°C)	1400	1400	1400	1400
Sintering time (min)	10	10	10	5
Heating rate (K/min)	100	100	100	100
Cooling rate (K/min)	100	100	100	100
Pressure (MPa)	50	50	50	50
Coverage	Graphite	Graphite	Graphite	Tantalum
Atmosphere	Vacuum	Argon	Argon	Argon
Porosity (%)	15	9	13	/

to cerium reduction, once again nearing the critical threshold of 90% relative density. XRD measurements of the entire samples were taken (see Figure 4.8). Position of the (111) reflection for FAST1-3 is similar compared to 8YSZ/10GDC samples conventionally sintered in Ar/H_2. In the case of FAST4, the application of a tantalum cover to prevent contact with the graphite tool resulted in a reduced color change, with the sample predominantly retaining its yellow color. The reflection of the mixed phase for FAST4 is slightly shifted to the position of sample 8YSZ/10GDC samples conventionally sintered in ambient air and exhibit a shoulder in this direction, indicating less reduction and pyrochlore phase formation in FAST4. Since the edges of the sample were in contact with the graphite tool carbothermal reduction was not prevented fully. Furthermore, the samples were not properly sintered, coming out brittle out of the tool, not allowing a density determination. Sintering temperature is even higher compared to UHS, potentially leading to an increased level of thermal reduction. Similar to the UHS process, the reduction of cerium and pyrochlore phase formation could not be prevented.
First experiments using a titanium-zirconium-molybdenum alloy tool were conducted ($T = 900$ °C and $p = 150$ MPa) but the samples turned out dark blue /black, nevertheless.

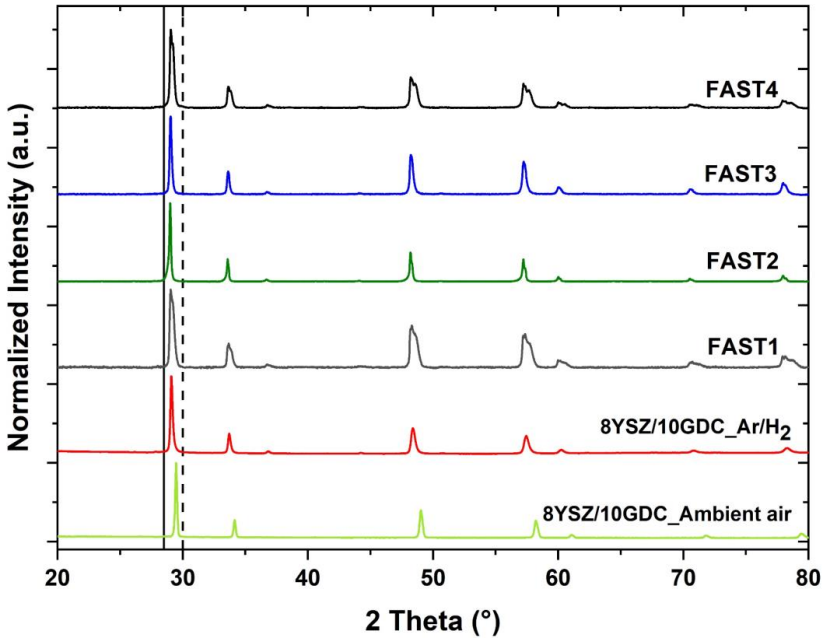

Figure 4.8: Diffractograms of FAST 1-4. Black and dashed black vertical lines represent the position of the (111) 8YSZ and 10GDC reflections, respectively.

Table 4.7: Sintering parameters and porosity values of BL1-6.

BL sample/ parameter	Voltage (V)	Pulse duration (ms)	Frequency (Hz)	Number of pulses	Time (s)	Porosity (%)
1	220	1	60	600	10	19
		1.8	60	1200	20	
		0.5	60	600	10	
2	220	1	60	600	10	9
		1.8	60	1500	25	
		0.5	60	600	10	
3	Analogous to 2					4
4						8
5						16
6						13

Blacklight sintering

8YSZ/10GDC samples were prepared in a similar way to UHS samples. The samples were sintered with two different numbers of pulses where the sintering was reproduced for the second number of pulses for four times (BL2-6). The pulses were divided into three segments, each with a different pulse duration. The sintering parameters, in addition to the porosity values, are presented in Table 4.7.

Increasing the number of pulses in the second segment by 300 decreases overall porosity from 19 % to 10 $\pm$ 5 %. Diffractograms, shown in Figure 4.9, reveal a reflection indicating the presence of the fluorite mixed phase, along with a shoulder pointing towards the pyrochlore phase. Raman spectra for BL3 are shown in Figure 4.10(a-b), accompanied by a cross-sectional micrograph of BL3 (see Figure 4.10(c)). This sample exhibited a highly graded microstructure from top to bottom, roughly divided into four distinct regions. (It should be noted that the other BL samples exhibited similar graded microstructures but were not further examined via Raman spectroscopy.) In Region 4, illuminated by the Xenon flash lamp, the sample exhibited high density, while it shows a gradient towards higher porosity in the direction of Region 1. Moreover, Regions 2-4 displayed a dark color change, while Region 1 maintained a white/yellow color. Raman spectra of the four regions reveal broad signals suggesting the presence of the fluorite and pyrochlore mixed phase. Region 2-4 exhibit the presence of Ce^{3+}, which is absent in Region 1. Overall, the BL samples displayed only slight reduction compared to the UHS and FAST-SPS methods.

Blacklight sintering from one side of the sample likely leads to a temperature gradient across the sample, resulting in different degrees of sintering and cerium reduction. Interestingly, Region 4 is highly dense. A residual bulk porosity of about 10 % could not be overcome which is attributed to the gradient in sintering. Since

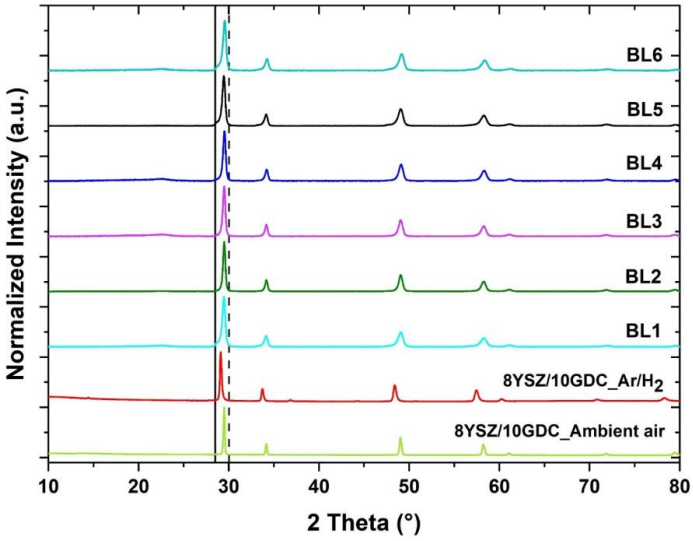

Figure 4.9: Diffractograms of BL1-6. Black and dashed black vertical lines represent the position of the (111) 8YSZ and 10GDC reflections, respectively.

Region 4 is almost fully dense, it might be possible to sinter fully dense samples by fine-tuning the sintering parameters. The lower degree of thermal reduction probably due to higher $p(O_2)$-atmospheres compared to UHS and FAST-SPS, might prevent the induced porosity by chemical expansion of cerium. Nevertheless, mixed phase formation was still evident during blacklight sintering.

Overall conclusion

The purpose of exploring alternative sintering techniques was to investigate whether high heating rates could mitigate the mixed phase formation of 8YSZ with 10GDC. Unfortunately, the inherently reducing nature of UHS and FAST-SPS, leading to the formation of a pyrochlore mixed phase, precludes a direct comparison with samples sintered using conventional methods in ambient air. As shown in Section 4.1.1, reducing atmospheres enhance cation mobility in 8YSZ/10GDC mixtures, probably induced by self-doping through the reduction of Ce^{4+} to Ce^{3+}. Furthermore, sintering in reducing atmospheres tends to result in residual porosity in 8YSZ/10GDC powder mixtures. While some partial thermal reduction of cerium occurs in ambient air or higher $p(O_2)$-atmospheres (as compared to vacuum or argon), it does not impede the densification process. Blacklight sintering experiments indicated that sintering techniques employing high heating rates could be a viable option for ceria-containing compounds, provided that sintering temperature is well-controlled, and the atmosphere is non-reducing. Nonetheless, mixed phase formation

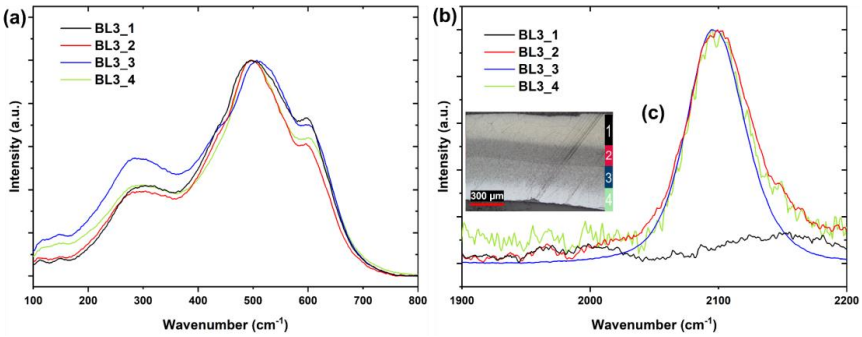

Figure 4.10: Raman spectra of the four regions of BL3 for (a) wavenumbers of (a) 100-800 cm^{-1} and (b) 1900-2200 cm^{-1}. (c) shows the cross-section of BL3 where the four different regions are marked.

and interdiffusion remained unavoidable. Therefore, it is advisable to avoid sintering of ceria containing compounds in reducing atmospheres.

4.1.3 Thermogravimetric analysis of sintered powder mixtures

To access the oxygen loss and therefore reducibility of the mixed 8YSZ/10XDC phases, TGA analyses were performed on the pellets sintered in ambient air at 1400 °C for 5 h. The samples were heated up to a temperature of 1100 °C for 2 h with 5 °C/min in ambient air to remove organic impurities. Afterwards, the temperature was decreased to 900 °C with 5 °C/min and held for 15 h in ambient air. Subsequently, the samples were reduced in Ar/ 3 % H_2 for 24 h. Finally, the atmosphere was switched back to ambient air and the samples were oxidized for 5 h. The samples were cooled down to room temperature with ~5 °C/min.

It is proposed that the presence of ZrO_2 enhances the reducibility of ceria [156], while dopants with a smaller ionic radius tend to decrease reducibility [157]. The TGA data, illustrated in Figure 4.11, reveal a similar mass loss of about ~1.5-1.7 % for the differently doped samples. Uncertainties and drifts in the recorded measurement data, probably caused by artifacts like buoyancy or an unsteady gas atmosphere, make it challenging to discern the precise influence of the dopant on mass loss, particularly when dealing with minor variations. Equilibration time at 900 °C after removal of organics (at 1100 °C) and after reduction might be too short.
Hence, based on the data currently available, it can be reasonably concluded that dopants in ceria do not exert a significant impact on mass loss or reducibility. Any potential changes in reducibility that may exist, likely below the threshold of approximately 0.2 wt%, fall within the margin of inaccuracy in the measurements presented. As such, it is reasonable to assume that altering the dopant in ceria will

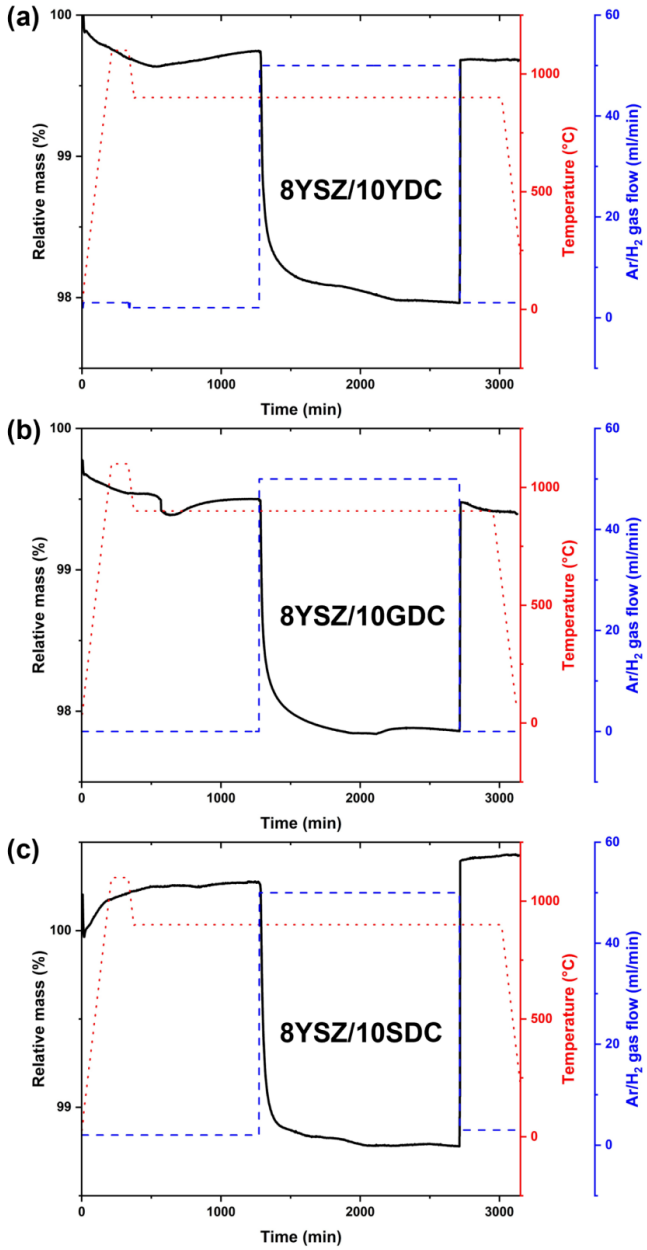

Figure 4.11: TGA measurements of 8YSZ/10XDC in ambient air and reduced in Ar/ 3 % H_2. Samples were pre-sintered at 1400 °C for 5 h in ambient air.

not substantially affect the reduction properties of the mixed phase, to the extent that it would impact the operation or manufacturing of SOCs.

4.1.4 Ionic conductivity of 8YSZ/10XDC mixed phases

The ionic conductivities of 8YSZ/10XDC pellets sintered at 1400 °C for 5 h were measured between 500–900 °C in ambient air using impedance spectroscopy. The grain and grain boundary impedances were added up to the total ionic impedance of the ceramic using the brick-layer model [158–160]. The spectra were fitted with an ECM of two R-CPE elements in series. For evaluation of the resistances, a series resistance was added. The two R-CPE circuits describe the grain and grain boundary processes, respectively. Platinum paste was applied on the top and bottom of the samples to improve the contact to the platinum electrodes of the potentiostat. The impedance response of the Pt electrode occurs at lower frequencies than the ionic conductor. The electrode impedance was removed from the spectra since it substantially increased the error of the fit.

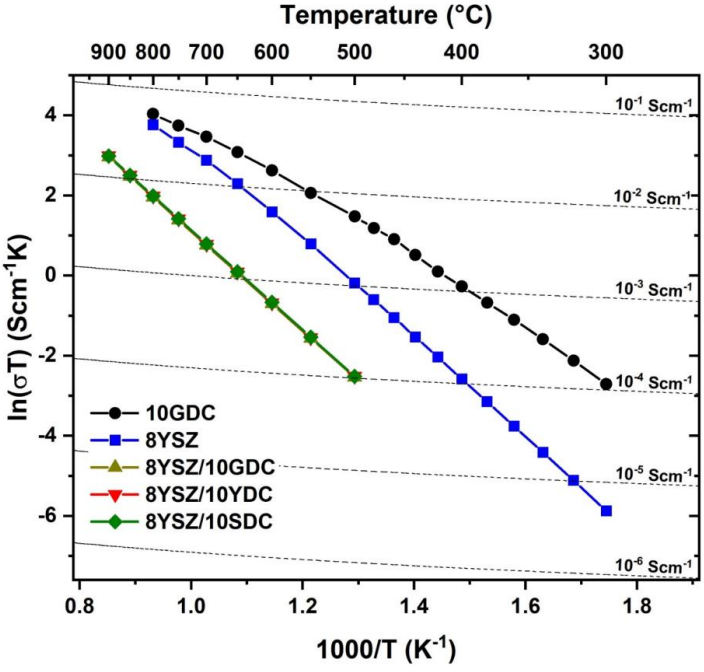

Figure 4.12: Arrhenius plot of the ionic conductivities of 8YSZ/10XDC pellets sintered at 1400 °C for 5 h in ambient air, compared to the conductivities of dense 8YSZ and 10GDC samples.

The total ionic conductivity of 8YSZ/10XDC pellets is shown in Figure 4.12. The nominal stoichiometry of the YDC/YSZ and GDC/YSZ samples according to Rietveld refinement is: $Y_{0.127}Zr_{0.487}Ce_{0.387}O_{2-\delta}$ and $Y_{0.084}Zr_{0.487}Gd_{0.043}Ce_{0.387}O_{2-\delta}$, respectively. The 8YSZ/10SDC sample contains three phases: $Y_{0.105}Zr_{0.605}Sm_{0.029}Ce_{0.261}O_{2-\delta}$, $Y_{0.090}Zr_{0.520}Sm_{0.039}Ce_{0.351}O_{2-\delta}$ and $Y_{0.078}Zr_{0.452}Sm_{0.047}Ce_{0.423}O_{2-\delta}$. The ionic conductivities are compared to dense 8YSZ and 10GDC ceramics. The 8YSZ/10XDC pellets possess ionic conductivities which are about one order of magnitude lower compared to 8YSZ. The values are in agreement with the conductivity values determined in literature for 8YSZ/10GDC and their solid solutions and it is reported that YSZ and GDC/SDC mixtures possess the lowest ionic conductivity when they form a mixed phase with a stoichiometry of $8YSZ_{0.5}$-$YDC_{0.5}$/$GDC_{0.5}$/$SDC_{0.5}$ [146,150,161,162]. It was shown that this is due to the lower mobility of the charge carriers compared to the pure material, which is likely a result of the increasing lattice disorder in the intermixed phases [142]. Nevertheless, there is no significant difference in the ionic conductivities for the different dopants in ceria within the accuracy of the measurement and the applied fit. Comparing 8YSZ/10YDC and 8YSZ/10GDC regarding the calculated phase distribution, no difference in ionic conductivity is expectable, except the influence of the dopant on conductivity. Although, 8YSZ/10SDC do not form a fully intermixed phase, no change in ionic conductivity is observable. Hence, the lower degree of mixed phase formation shows no impact on ionic conductivity in bulk material. Furthermore, the dopant does not alter the ionic conductivity in densely sintered mixed 8YSZ/10XDC pellets, although 10SDC exhibits slightly higher ionic conductivity compared to 10GDC [145,163].

The total ionic conductivity for 8YSZ/10XDC pellets sintered in Ar/H_2 and O_2 atmosphere at 1400 °C for 5 h were measured. The results are shown in the Appendix A, Figure A.4. Ionic conductivity for samples sintered in O_2 is similar to samples sintered in ambient air. No influence of the dopant on ionic conductivity in O_2 atmosphere sintered samples is measurable, just at lower temperatures ($\lesssim$ 400 °C) ionic conductivity tends to be influenced slightly by the dopant. Sm as a dopant exhibits highest conductivity followed by Y and Gd.

Conversely, 8YSZ/10XDC powder mixtures sintered in an Ar/H_2 environment exhibit approximately one order of magnitude lower conductivity compared to samples sintered in ambient air, while the conductivity loss at lower temperatures is steeper. Once again, at lower temperatures, the dopants appear to influence conductivity, with Y demonstrating the highest conductivity, followed by Gd and Sm. As the samples sintered in Ar/H_2 are porous induced by the reduction of cerium, it is not clear if the loss in conductivity is attributed to the formation of the mixed and pyrochlore phase or due to microstructural changes.

4.1.5 Interdiffusion in layered systems

FESCs are manufactured through the sequential sintering of functional layers. After investigating the influence of the dopant, atmospheric conditions, and the sintering technique on the interdiffusion behavior between 8YSZ and 10XDC in homogenously distributed systems, the next experiments target the interdiffusion behavior in layered structures with chemical gradients.
The utilization of alternative sintering techniques and reducing atmospheres was revealed to be counterproductive in the manufacturing of SOCs that incorporate ceria compounds. Hence, this section's primary focus is on examining interdiffusion in layered systems that are traditionally sintered in ambient air.

Interdiffusion in model systems - SIMS
To determine interdiffusion coefficients, SIMS measurements were performed. Initially, physical vapor deposition (PVD) of 10YDC layers on dense ~200 µm thick 8YSZ substrates (Kerafol, Germany) was conducted. The system was annealed at 1400 °C for 5 h. The SIMS data exhibited high fluctuations and unsteady signals, primarily attributed to the high roughness of the deposited layer relative to its thickness.
In an attempt to mitigate layer roughness, a 10YDC layer was deposited onto a (110) YSZ single crystal, followed by annealing at 1400°C for 5 hours. Nonetheless, the data displayed some fluctuations, particularly in the regions of the layers that extended beyond the interdiffusion zone where the concentration of the according species is supposed to be constant. These fluctuations might be caused by inhomogeneities of the layers, e.g., due to microstructural features such as pores. Furthermore, an increase in intensity at the interface, which is especially sharp for the Ce^{+} signal, indicates a certain interface roughness [164]. Both aspects render the

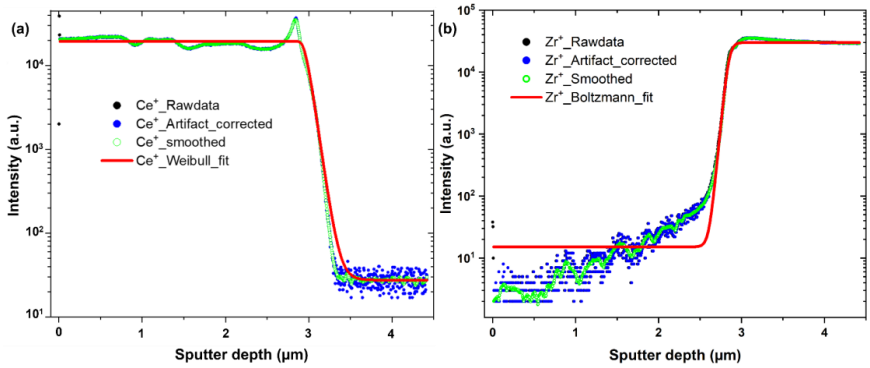

Figure 4.13: Fitted SIMS data of Zr^{+} and Ce^{+} measured in an 8YSZ/10YDC diffusion couple annealed at 1400 °C for 5 h in ambient air.

data suboptimal for further analysis, especially decreasing the quality of a sigmoidal fit.
To provide a rough estimation of the order of magnitude for the interdiffusion lengths of Ce and Zr in 8YSZ/10XDC layered systems, the Ce^+ and Zr^+ signals were extracted from the data, while the Y^+ signal, which exhibited considerable fluctuations in the deposited 10YDC, was excluded from the analysis. The extracted data were subjected to artifact correction and smoothed using a Savitzky-Golay filter. Subsequently, the data was subjected to a sigmoidal function fit (using a Weibull fit for the Ce^+ signal and a Boltzmann fit for the Zr^+) for the numerical determination of the interdiffusion coefficients utilizing the Boltzmann-Matano analysis. The diffusion coefficient was calculated at every position x where the change in the measured intensity was attributed to a real change in concentration. Afterwards, the calculated values were averaged. The data and its analysis are presented in Figure 4.13.

The calculated average diffusion coefficients for Ce and Zr are $\breve{D}_{Ce} = 7.34 \cdot 10^{-17}$ m²/s and $\breve{D}_{Zr} = 3.36 \cdot 10^{-17}$ m²/s. Using these values to calculate the diffusion length ($L = \sqrt{Dt}$) of Ce and Zr in an 8YSZ/10YDC diffusion couple annealed at 1400 °C for 5 h yields diffusion lengths of 1.15 µm and 0.78 µm, respectively. This is consistent with results obtained on 8YSZ/10YDC powder mixtures in Section 4.1.1 which revealed a lower activation energy for Ce diffusion compared to Zr.

Interdiffusion in screen-printed systems – SEM
To determine interdiffusion lengths in layered screen-printed systems, pre-suspensions were prepared containing 64.10 wt% of XDC, 33.34 wt% of terpineol, 2.56 wt% Disperbyk P-104 (BYK-Chemie GmbH, Wesel, Germany) dispersant and were mixed with 3 mm zirconia grinding balls (the weight ratio of grinding balls to pre-suspension was approximately ~4:1) using a tumbling mixer for 24 h. Afterwards, a slurry was formed by adding 16 wt% of a transport agent (15 wt% ethyl cellulose [10cps] (Sigma-Aldrich, St. Louis, USA) dissolved in 85 wt% terpineol) to the pre-suspension.
The layers were printed on dense, ~200 µm thick 8YSZ substrates (Kerafol, Germany) using a semi-automatic screen printer. The mesh used leads to a layer of about ~5-8 µm after sintering at 1400 °C for 5 h (according to FES-HC sintering conditions).
To analyze the degree of interdiffusion in layered systems, BE imaging is used instead of EDS mapping. BE enable a better spatial resolution due to the much smaller scattering volume compared to the excitation volume of EDS (which is ~1 µm and is in the range of the measured interdiffusion lengths). The BE coefficient η is depended on the atomic number Z resulting in different intensities and contrasts in the recorded BE image (Z-contrast). Since in polyphase specimens Z varies, the BE image contains different contrasts. The higher Z the brighter the phase appears. Therefore, the material contrast is suitable to resolve the original 8YSZ and 10XDC

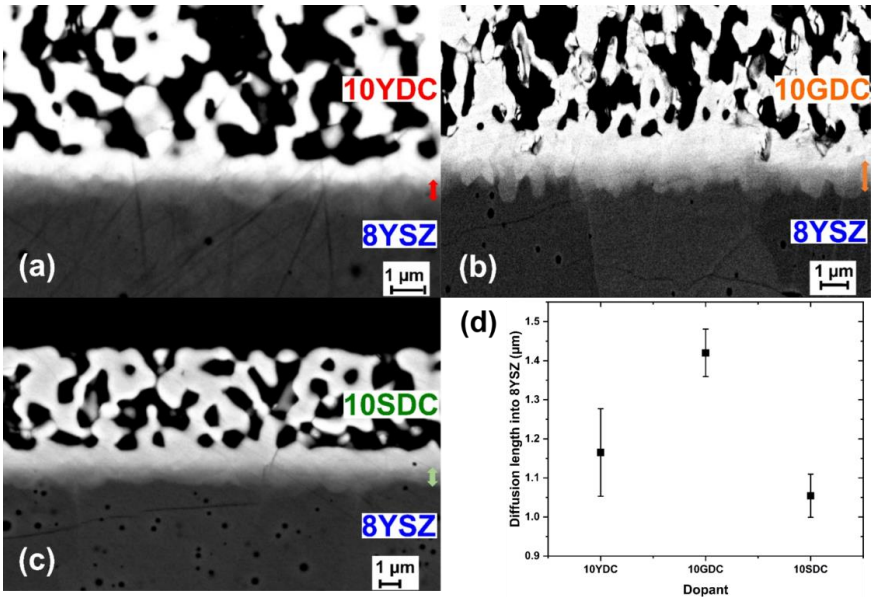

Figure 4.14: BE micrographs of polished cross-sections of screen-printed doped ceria layers (porous light layer on top) on dense 8YSZ substrates (bottom dark layer) for (a) 8YSZ/10YDC, (b) 8YSZ/10GDC, and (c) 8YSZ/10SDC sintered at 1400 °C for 5 h. (d) Diffusion lengths of the cations Ce and X of screen-printed 10XDC layers into dense 8YSZ sintered at 1400 °C for 5 h estimated by material contrast.

phases as well as their intermixing phases, since they significantly vary in Z [165]. Furthermore, the process of using material contrast is common practice in the solid oxide cell (SOC) community and was evaluated for the air side of a SOC by Wankmüller et al. [166]. To resolve the interdiffusion length of Ce and X into the dense 8YSZ substrate, the variation in material contrast was investigated across the interdiffusion zone.

An exemplary SEM picture of the analyzed cross-sections for every dopant is shown in Figure 4.14(a–c). Since the interface shifts during sintering due to the difference in diffusion coefficients, the position of the interface has been estimated using material contrast. The printed layers are porous but the interface is homogenously covered with XDC. The interdiffusion zone shows no clear horizontal border but a wavelike form. This might be due to statistical effects or a gradient in chemical potential.

The interdiffusion lengths have been estimated up to the furthest point of the contrasted zone. The average grey value of the boundaries of the 10XDC and 8YSZ layers were measured using the software Fiji by utilizing data points which are located outside of the interdiffusion zone. The length of the interdiffusion zone was then measured by drawing a straight line between the boundaries of the 10XDC and

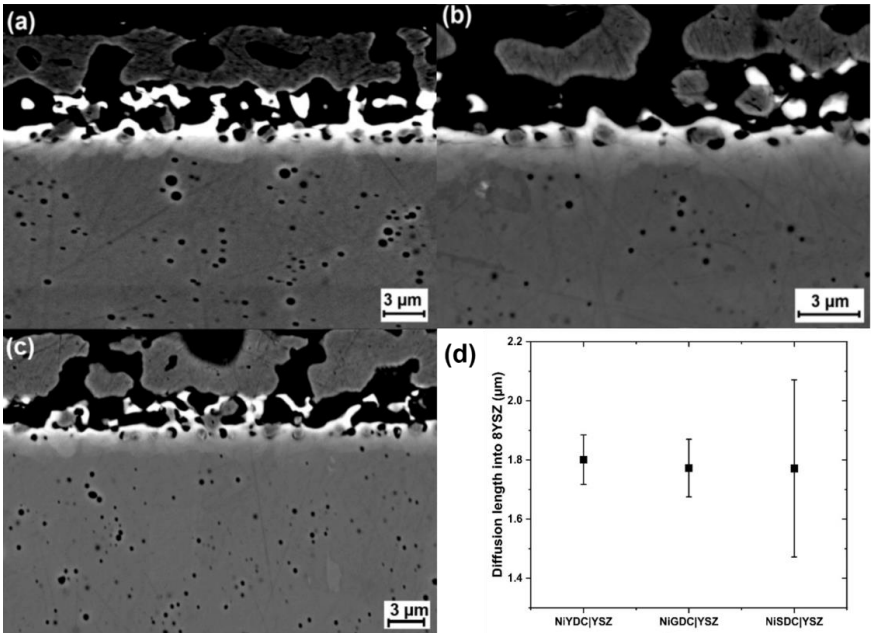

Figure 4.15: BE images of cross-sections of symmetrical (a) Ni/Ni-10YDC/8YSZ cells, (b) Ni/Ni-10GDC/8YSZ, and (c) Ni/Ni-10SDC/8YSZ cells sintered at 1400 °C for 5 h. (These cells were used for impedance measurements in Section 4.1.6). (d) Diffusion lengths of Ce and X into 8YSZ in Ni-10XDC symmetrical cells estimated by material contrast.

8YSZ grey value. Error bars show the standard deviation of at least seven evaluated pictures. The estimated diffusion lengths are plotted in Figure 4.14(d). A slight change in the diffusion length is observable for Gd (1.42 ± 0.06 µm) into 8YSZ compared to Y (1.17 ± 0.11 µm) and Sm (1.05 ± 0.06 µm) as dopant in the 8YSZ/10XDC diffusion couples. The obtained diffusion length for Ce into 8YSZ in an 8YSZ/10YDC diffusion couple are in good agreement with the data obtained by SIMS. Furthermore, the results are consistent with the obtained phase distribution in powder mixtures, where 10GDC shows the highest amount of interdiffusion. This also indicates a slight influence of the dopant size on the diffusion coefficient of the respective cations. The results are similar compared to the measured diffusion lengths by Ozawa et al. for YSZ and CeO_2 diffusion couples [167].
The difference in material contrast indicates the formation of a mixed phase which is known to be less conductive than 8YSZ and 10XDC and may limit the performance of a FESC.

Interdiffusion in the presence of NiO
NiO is typically part of fuel electrodes to guarantee sufficient electrical conductivity and catalytic properties. We observed an enhancement of the cation diffusion in

fluorite structures in the presence of NiO. Additionally, porosity was formed at the interface of symmetrical Ni-10XDC cells with an 8YSZ electrolyte. Cross-sections of the cells after impedance measurements are shown in Figure 4.15(a–c). The diffusion lengths of Ce and X into 8YSZ increased for all samples, independent of the dopant, while the presence of NiO seems to neutralize the impact of X on the diffusion process (see Figure 4.15(d)).
In addition, EDS line scans and maps were performed to confirm the results and to measure the interdiffusion of Ni in symmetrical cells since its material contrast is similar to 8YSZ. The diffusion lengths of Ni are similar or slightly shorter compared to Ce and X meanwhile enhancing their interdiffusion kinetics. This information is not shown here but in the Appendix A, Figure A.5 - Figure A.10.

4.1.6 Impedance response of symmetrical cells

In this section the influence of the dopant on the electrochemical performance of a Ni-10XDC symmetrical cell is investigated. To analyze the impedance response of symmetrical cells, pre-suspensions containing 35.13 wt% of 10XDC, 32.42 wt% of NiO, 29.55 wt% of terpineol, 2.90 wt% Disperbyk P-104 were prepared. To form a slurry, 16 wt% of a transport agent (15 wt% ethyl cellulose [10cps] dissolved in 85 wt% terpineol) was added to the pre-suspension. The layers were symmetrically screen printed on ~200 µm thick 8YSZ electrolyte substrates. The layers were sintered at 1400 °C for 5 h. In the first part of this section the influence of different contact layers on the impedance response is investigated. Sputtered Pt-layers, sputtered Pt-layers with a brushed Ag-paste layer and a brushed NiO layer were compared. The cells were reduced in situ at 900 °C for 3 h in Ar/ 3 % H_2. Impedance measurements were conducted in Ar/ 3 % H_2 at temperatures between 200-400 °C and 600-900 °C. The spectra were fitted with an ECM containing R-CPE elements in series. For evaluation of the polarization resistances a series resistance was added. Subsequently, the polarization resistance (R_{pol}) at higher temperatures (600-900 °C) and the characteristic frequencies (f_max) of the respective R-CPE elements and the ohmic resistance (R_{ohm}) of the electrolyte at lower temperatures (200-400 °C) were calculated. For the evaluation of f_max and R_{ohm}, the electrode impedance was removed from the spectra since it substantially increased the error of the fit. Φ was typically in the range of 0.86-0.99 in this analysis.

Influence of different contact layers
The quality of the contacted layers is a critical factor in obtaining reliable spectra, especially when the contact between the sample and the Pt-mesh electrodes of the potentiostat is not optimal. In the symmetrical cells used in this study, which contain 50 vol% NiO, the ohmic resistance of the electrodes is negligible. Therefore, the ohmic resistance of the ionic conductor can be estimated by analyzing the high-frequency intercept with the x-axis. Even though the ohmic resistance of the

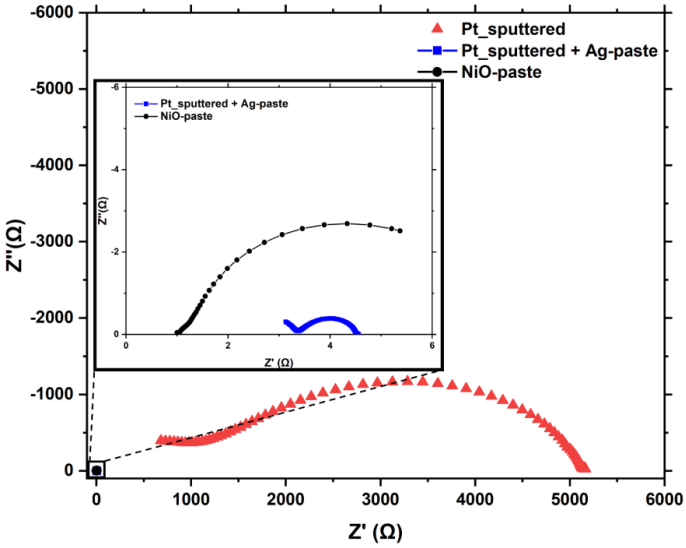

Figure 4.16: Impedance data in the form of a Nyquist plot of different contact layers.

electrodes is negligible, the ohmic resistance of the samples remained relatively high, resulting in spectra with insufficient quality. What proves crucial is the lateral conductivity of the contacting layer. If the lateral conductivity is insufficient, it can lead to incomplete contact across the full electrode area, making it challenging to estimate the contacted area accurately based on its geometry, which, in turn, can yield inaccurate results. To address this issue, the lateral conductivity needs to be higher than the medial conductivity, with lateral resistance ideally below 0.5 Ωcm^2. To assess the quality of different contact layers, testing was conducted at 700 °C, where the area-specific ohmic resistance of a ~200 µm 8YSZ layer is approximately 1.1 Ωcm^2. Three different types of contact layers were examined: i) a Pt-sputtered layer, ii) a Pt-sputtered layer with a brushed Ag layer applied from a paste, and iii) a brushed NiO layer from a paste. The impedance data are presented in Figure 4.16. For the Pt-sputtered layer alone, there is no observable intercept with the x-axis, and a very high polarization resistance of around ~4000 Ωcm^2 is noted. By adding an Ag-layer on top of the Pt-layer, the ohmic resistance decreases to about 2.5-3 Ωcm^2, and the polarization resistance substantially drops to approximately 1 Ωcm^2. When a NiO contact layer is employed, the estimated ohmic resistance of the 8YSZ electrolyte is achieved, approximately 1 Ωcm^2. However, an increase in polarization resistance is observed.

In the case of the Ag-layer, the high ohmic resistance and lower polarization resistance suggest an infiltration of the electrode by the very fluid Ag-paste. This infiltration likely results in a surface depleted of Ag, altering the catalytic activity of the electrode structure. Conversely, for a NiO contact layer, even if it infiltrates

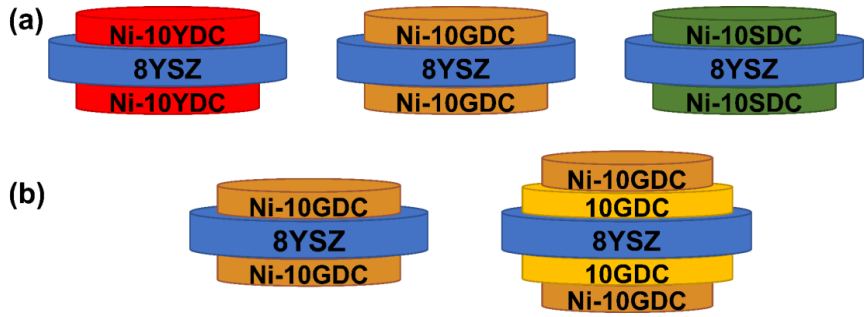

Figure 4.17: Illustration of the symmetrical Ni-10XDC cells used for impedance spectroscopy and SEM-analysis to investigate (a) the dopant influence and (b) the influence of porosity at the interface with 8YSZ.

the electrode, its catalytic activity is only slightly affected, as the catalyst of the electrode itself is also Ni. Furthermore, the NiO paste is more viscous, which hinders infiltration compared to the Ag-paste.
Given that the NiO contact layer provides the correct ohmic resistance for the 8YSZ electrolyte in the impedance data, it was selected as the contact layer for further experiments.

Dopant influence in symmetrical cells
Symmetrical cells with Ni-10XDC layers were investigated with impedance spectroscopy. An illustration of the symmetrical cells investigated in this subsection

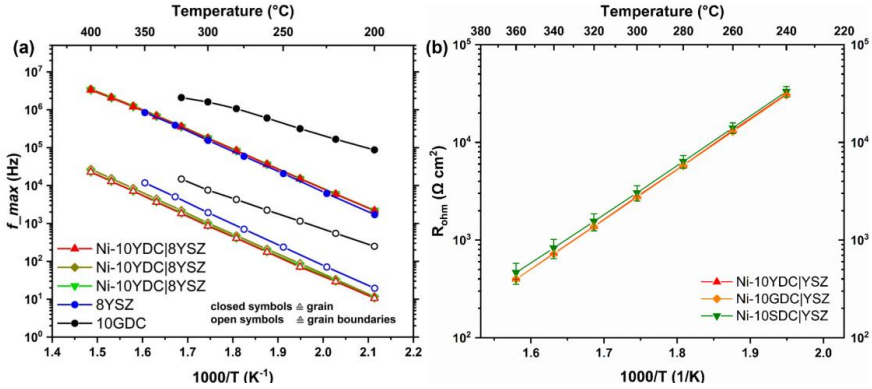

Figure 4.18: (a) Arrhenius-type plot of the characteristic frequencies f_max for differently doped ceria symmetrical cells (Ni-10XDC|8YSZ|Ni-10XDC) and dense 8YSZ and 10GDC ceramics for grain and grain boundary response. (b) Ohmic resistances of differently doped symmetrical Ni-10XDC cells on 8YSZ electrolyte. Lines are a guide to the eye.

and of the symmetrical cells investigated in the next subsection - **Influence of porosity at the electrode/electrolyte interface** – is shown in Figure 4.17.
The characteristic frequencies for grains f_max(g) and grain boundaries f_max(gb) were compared to dense bulk 8YSZ and 10GDC ceramics.
The results for f_max are plotted in Figure 4.18(a) in an Arrhenius plot for the symmetrical Ni-10XDC cells and for dense 8YSZ and GDC ceramics. The results show a change in the grain boundary response f_max(gb) for the symmetrical Ni-10XDC cells compared to dense 8YSZ and 10GDC ceramics. For grains f_max(g) no significant difference compared to the 8YSZ ceramic is observable. This change in f_max(gb) is attributed to the interdiffusion between the Ni-10XDC layer and the 8YSZ substrate although it shows no influence on cell performance. Since dopants prefer to segregate at grain boundaries [168–172] this might be the reason for the change of f_max(gb) compared to f_max(g). Since no difference in the interdiffusion lengths in symmetrical cells is observed, the lack of change of f_max(g) is comprehensible. On the other hand, a lower amount of mixed phase formation at the interface for Sm doped cells is assumable.
Comparing the f_max for the differently doped symmetrical cells, no significant change in f_max is observed for Ni-10YDC, Ni-10GDC and Ni-10SDC cells.
The ohmic resistance of the Ni-10XDC cells also shows no significant difference (see Figure 4.18(b)).

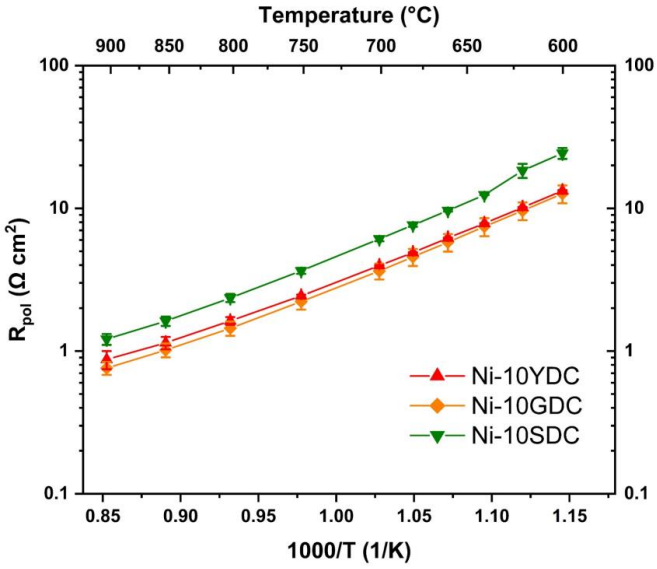

Figure 4.19: Polarization resistances of Ni-10XDC symmetrical cells measured at temperatures between 600-900 °C in Ar/ 3 % H_2. Lines are a guide to the eye.

The polarization resistances of the Ni-10XDC cells (cross-sections are shown in Figure 4.15(a-c)) are shown in Figure 4.19. Error bars show the standard deviation of three samples. The results show no significant difference between Gd- and Y-doped electrodes and a higher polarization resistance for Sm-doped electrodes. On the one hand, this result is counterintuitive since Sm-doped ceria possesses the highest ionic conductivity. On the other hand, ceria with Sm as a dopant exhibits lower reducibility [173]. Although all cells have been prepared in the same way, microstructural features could influence the performance of the electrode since the starting powders are not fully alike. Especially the specific surface area of 10SDC is lower compared to 10GDC and 10YDC. Therefore, the higher polarization resistance of Ni-10SDC is likely a result of microstructural differences.
These results indicate that the differences in interdiffusion between the three ceria phases have a negligible influence on the polarization resistance.

Influence of porosity at the electrode/electrolyte interface
As has been shown in Section 4.1.5, NiO enhances the interdiffusion between 8YSZ and 10XDC and leads to the formation of porosity at the electrode/electrolyte interface. To analyze the influence of porosity at the electrode/electrolyte interface, the impedance response of symmetrical cells with Ni-10GDC electrodes with and without a 10GDC barrier layer were measured. In addition, the influence of sequential- or co-sintering of the barrier layer on cell performance was investigated. Cross-sections of the symmetrical cells are shown in Figure 4.20(a–c). It is clearly visible again that incorporation of NiO into a doped ceria layer which is in direct contact with the 8YSZ interface leads to emerging porosity in the most electrochemically active area, while a doped ceria barrier layer prevents the forming of porosity at the 8YSZ interface during sintering. The diffusion lengths of Ce and Gd into the 8YSZ electrolyte are shown in Figure 4.20(d). Diffusion lengths of Ce and X are slightly longer if NiO is present in the layer adjacent to the 8YSZ electrolyte. If the barrier is co-sintered with the electrode, diffusion lengths are about 1 µm shorter compared to sequentially sintered barrier and electrode layer. The polarization resistances of cells without barrier layer, co-sintered electrode/barrier layers and sequentially sintered electrode and barrier layers are shown in Figure 4.20(e). Error bars show the standard deviation of three samples. Symmetrical cells without a barrier layer show significantly higher polarization resistances compared to cells with a barrier layer. Interestingly, whether the electrode and barrier layers were co-sintered or sequentially sintered does not influence the polarization resistance, although two sintering steps increase the length of interdiffusion of Ce and Gd into 8YSZ significantly.
In Figure 4.21 the ohmic resistance of the 8YSZ electrolyte and (if present) additionally the 10GDC barrier is shown. The ohmic resistance for cells with barrier layer is slightly but significantly higher compared to cells without barrier. Cells with co-sintered and sequentially sintered layers do not vary in ohmic resistance at temperatures between 340–280 °C. At lower temperatures the cells with co-sintered

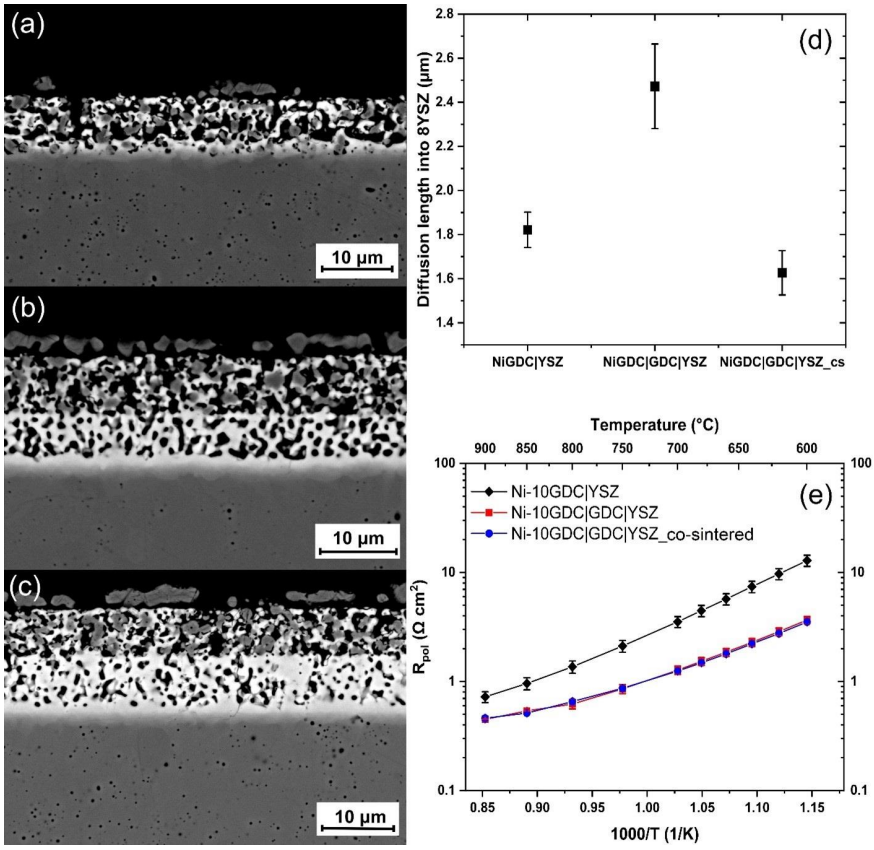

Figure 4.20: BE images of cross-sections of symmetrical Ni-10GDC cells (a) without a 10GDC barrier layer, (b) with a sequentially sintered 10GDC barrier layer, and (c) with a co-sintered 10GDC barrier layer. (d) Diffusion lengths of Ce and Gd into 8YSZ of Ni-10GDC symmetrical cells with (sequentially- and co-sintered) and without barrier layer. (e) Polarization resistances of Ni-10GDC symmetrical cells with (sequentially and co-sintered) and without barrier layer measured at temperatures between 600-900 °C in Ar/ 3% H_2; lines are a guide to the eye.

layers show slightly higher ohmic resistance. The co-sintered cells show significantly shorter interdiffusion lengths, leading to the conclusion that the influence of a mixed phase with reduced conductivity on the total ionic conductivity is negligible in these systems, while the polarization resistance is dependent on the microstructure at the interface.

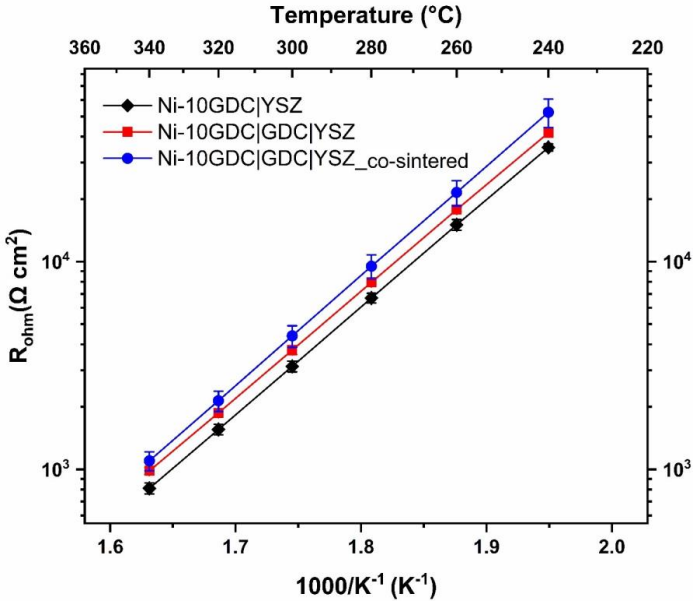

Figure 4.21: Ohmic resistances of symmetrical Ni-10GDC cells and cells with 10GDC barrier layer (sequentially- or co-sintered with the electrode) measured at temperatures between 240-340 °C in Ar/ 3 % H_2. Lines are a guide to the eye.

4.1.7 Discussion

The results on the interdiffusion behavior between 8YSZ and 10XDC presented in Section 4.1 - **Interdiffusion experiments** will primarily be discussed regarding their impact on FESC manufacturing and cell performance. Although the dopant in ceria shows an influence on the interdiffusion behavior with 8YSZ, the influence is too marginal to show a significant impact during FESC manufacturing or on cell performance. The reduction behavior of 8YSZ/10XDC and sintering of 8YSZ/10GDC in reducing atmospheres or alternative sintering techniques like UHS, FAST-SPS and blacklight sintering showed no promising results in this regard. Reducing atmospheres and the accompanied self-doping of ceria by the reduction of Ce^{4+} to Ce^{3+} enhances interdiffusion with 8YSZ and is disadvantageous for the manufacturing of layered functional structures. Furthermore, the reduction of cerium complicates densification of ceria-containing compounds due to chemical expansion of ceria. Redox-cycling of ceria-containing layers might induce cracks, especially in dense layers. The precise control of oxidation and reduction during sintering of ceria might help to lower the sintering temperature and achieve full densification.

Consequences of interdiffusion

The suppression of interdiffusion between two functional layers is generally desirable. But if high temperature manufacturing steps are involved, interdiffusion seems to be inevitable. There are two consequences of interdiffusion in the manufacturing process of a common FESC with a Ni-10XDC fuel electrode and an 8YSZ electrolyte layer: The formation of a mixed phase with reduced conductivity, and microstructural changes in terms of porosity at the electrode/electrolyte interface. Regarding the formation of the mixed phase, shorter diffusion lengths should be beneficial since less amount of mixed phase is formed.

A fully intermixed 8YSZ/10XDC phase exhibits the lowest ionic conductivity, but in practice a gradient in stoichiometry is present which leads to a gradient in ionic conductivity in the interdiffusion zone (which was also confirmed by EDS line scans; see Figure A.5 - Figure A.7, Appendix A). Symmetrical cells with sequentially sintered barrier and electrode show significantly longer interdiffusion lengths of Ce and Gd into the 8YSZ electrolyte compared to co-sintered cells but no difference in ionic conductivity. Whereas increasing the electrolyte thickness by adding a porous barrier increases ionic conductivity measurably. Therefore, if the electrolyte has a certain thickness (here ~200 µm) a narrow and graded interdiffusion zone shows no significant influence on ionic conductivity of the electrolyte. In FESC a thinner electrolyte of about 10 µm is present. In this case the ratio of electrolyte thickness to the length of the interdiffusion zone changes from about 133 to 7, which might lead to a more significant influence on ionic conductivity and cell performance.

Porosity at the electrode/electrolyte interface as a consequence of interdiffusion shows a severe influence on the polarization resistance, where cells with porous interfaces have drastically higher values. The reason could be an inferior contact between the fuel electrode and electrolyte layer. Porosity at the interface might also lead to less electrochemically active area at the interface. In general, if there is no contact between the fuel electrode and the electrolyte, the flow of O^{2-} from the electrolyte to the fuel electrode is prevented. This would also be the case in an actual FESC. Therefore, also in case of a thinner electrolyte, prevention of porosity at the electrode/electrolyte interface has a more beneficial impact on cell performance than prevention of a mixed phase with lower conductivity.

Nenning et al. showed that a more homogeneous and adhesive contact at the direct electrolyte interface improves polarization resistance. The improved contact was realized by adding a 10GDC layer between the 8YSZ electrolyte and Ni-10GDC electrode. The cells without barrier are just connected to the electrolyte by some sintering necks. Although no porosity was found (likely due to the lower sintering temperature of 1100 °C) this study also indicates that less contact area at the direct electrolyte interface increases polarization resistance of the electrode, similar to this study [174].

Although the dopant modifies the interdiffusion kinetics slightly, it cannot prevent formation of porosity at the interface while porosity is not formed in the absence of NiO.

It is interesting to compare these findings regarding the effectiveness of a 10GDC barrier layer between 8YSZ and NiO-10GDC to the barrier layers commonly applied on the air side of a cell.
It has been shown that an interdiffusion zone between 10GDC and 8YSZ is the key to prevent the formation of insulating $SrZrO_3$, whereas the decrease in ionic conductivity in the interdiffusion layer has a negligible impact on cell performance. Contrary to our findings on the fuel side, co-sintering of the GDC barrier with a lanthanum strontium cobalt ferrite ($La_{0.58}Sr_{0.4}Co_{0.2}Fe_{0.8}O_{3-\delta}$, LSCF) electrode on the air side has tremendously negative effects on cell performance. The difference is likely the transport mechanism of Sr during electrode sintering, where there are strong indications for gas-phase transport of the Sr species to the electrolyte interface. Therefore, the barrier on the air side has to be sintered sequentially, and at higher temperatures of at least 1300 °C to form a sufficiently dense interdiffusion layer [141].
Since the interdiffusion processes on the fuel side is driven mainly by bulk and surface diffusion, co-sintering does not affect performance since the NiO is much slower to arrive at the interface compared to gaseous Sr-(hydr)oxides.
Hence, the prevention of porosity at the electrolyte interface on the fuel side has the most beneficial impact on polarization resistance and overall cell performance, and the additional 10GDC barrier layer is crucial if porosity cannot be prevented otherwise.

Possible reasons for porosity formation
The formation of porosity at an interface due to diffusion is known as Kirkendall porosity. If the cations of the adjacent layers possess sufficiently different diffusion coefficients, more cations diffuse from one layer into the other than vice versa. This leads to material depletion in the layer where the cations possess the higher interdiffusion coefficient, and thus to the formation of Kirkendall voids in the vicinity of the interface. Normally, the formation of Kirkendall voids can be expected on the XDC side at the interface since more Ce and X atoms diffuse into 8YSZ compared to Zr and Y atom diffusion into XDC in a given time frame [136,138,175]. Interestingly, Kirkendall voids were not observed in the layered structures when NiO was absent. The addition of NiO to the electrode cermet seems to enhance the interdiffusion coefficient of Ce and X into 8YSZ. This leads to an increase in the difference of the interdiffusion coefficients of Zr and Y compared to Ce and X which is then sufficiently high to generate porosity. In former experiments, Lenser et al. [142] observed the enhancement of interdiffusion in the presence of NiO between 8YSZ and 10GDC in powder mixtures whereas Tsoga et al. [138] report a suppression of Ce into a YSZ lattice.
Smaller amounts of NiO, below the solubility limit, are observed to enhance the sinterability of 8YSZ and 10GDC. Presumably, doping the host lattice with Ni increases volume diffusion. Below the solubility limit, the grain boundary diffusion seems not to be influenced (just if some decomposition reaction of NiO precursors

take place in the initial state of sintering). Above the solubility limit, NiO tends to segregate at grain boundaries and decreases the sinterability due to pinning effects [176,177].
It should be added that it is also proposed that sinterability might be increased due to promoted grain boundary mobility as a result of the distortion of the surrounding lattice by Ni [178]. Ni diffuses during sintering of Ni-GDC|GDC layered system and causes microstructural modifications which is believed to be due to the formation of Ni interstitials and oxygen vacancies resulting in defect clusters and inhomogeneous microstructures due to altered ion diffusion [179].
Furthermore, the influence of NiO as sintering aid in the fabrication of proton conducting $Ba(Zr,Ce,Y)O_{3-\delta}$ has been reported. Although not possessing the fluorite crystal structure but the perovskite structure, some of the proposed mechanisms should be mentioned here, since some of the NiO-induced modifications might be similar. By doping the host lattice with Ni, cation defects, oxygen vacancies as well as electronic defects are created which accelerate phase transitions and sintering. The prevention of $BaZrO_{3-\delta}$ seems to be of importance. It was shown that using sintering aids with a similar ionic radius to Zr^{4+} and a valence of +II promotes sintering the most [180]. However, if the NiO fraction is too large it tends to aggregate [181]. Another possible mechanism is the formation of a transient liquid phase or occurrence of liquid flow which accelerates cation diffusion and thus sintering [182].
Based on the suggested mechanisms in literature and the findings in this study, a plausible hypothesis would be the doping of the 10GDC grains by adjacent NiO grains during sintering. The doping with Ni would lead to cationic defects (Ni might be located on a regular lattice site or an interstitial site) and to the formation of oxygen vacancies which would affect volume diffusion. This would be coherent with the data presented in the former sections, where it was shown that the dopant radius in ceria influences the interdiffusion with 8YSZ, whereas Ni even possess a lower average oxidation number of +II. This might lead to an even enhanced interdiffusion at the interface.

4.1.8 Conclusion

The influence of the dopant in ceria (Y, Gd, Sm) on the interdiffusion kinetics with 8YSZ was investigated in terms of powder mixtures, layered systems, and symmetrical cells. The size of the dopant shows an influence on the interdiffusion behavior in terms of phase formation in thermodynamically driven systems. Reducing sintering atmospheres enhance interdiffusion and induce porosity in the samples by the reduction of cerium.
A slight change in the interdiffusion length at the interface of doped ceria layers and 8YSZ substrates was observed. The formation of Kirkendall voids was not observed. Therefore, the size of the dopant in ceria appears to modify the overall interdiffusion kinetics with 8YSZ in the following order: Sm<Y<Gd.

No significant difference in ionic conductivity was measured for 8YSZ and differently doped ceria mixtures.
Furthermore, the influence of the dopant in symmetrical cells was investigated. Sm as a dopant in Ni-doped ceria electrodes shows a higher polarization resistance compared to Y and Gd, but microstructural influences cannot be excluded. The dopants and its interdiffusion behavior show no influence on the ohmic resistance of the electrolyte.
Sintering a cermet of NiO and doped ceria with an 8YSZ electrolyte leads to the formation of Kirkendall voids (porosity) at the electrochemical interface. Symmetrical cells with porosity at the interface show significantly higher polarization resistances compared to cells where the formation of porosity was prevented by adding a Gd-doped ceria barrier layer between electrode and electrolyte. Co-sintering of the barrier layer with the electrode compared to sequential sintering of the layers shows no difference in polarization resistance. The added electrolyte thickness by a porous barrier layer adds more ohmic resistance to the electrolyte than a larger interdiffusion zone, indicating a negligible effect of the interdiffusion zone but a significant effect of the barrier layer on the ohmic resistance. However, the prevention of porosity at the interface in the investigated systems is more important for total cell impedance.
It is not possible to prevent the formation of porosity at the electrochemical interface in the presence of NiO by modifying the dopant in ceria. Additionally, the choice of the dopant in the electrode does not alter the ohmic resistance after interdiffusion. Therefore, it is crucial to implement a doped ceria barrier layer between a cermet electrode consisting of NiO and doped ceria and an 8YSZ electrolyte to decrease polarization resistance significantly.

4.2 Integration of doped ceria into a FESC

In the preceding section, it was established that the dopant in ceria has no significant impact on cell manufacturing and performance in ESCs. However, it became evident that the formation of porosity at the interface between the fuel electrode and electrolyte plays a pivotal role. Consequently, the commonly used dopant, Gd, was selected as the candidate for developing and optimizing a screen printing paste for the Ni-10GDC fuel electrode in FESC manufacturing. The same strategies were adapted for 10SDC to explore potential variations in performance or degradation tolerance in FESC.
This section focuses on the sintering behavior of doped ceria and its alignment with the 8YSZ electrolyte layer. The development of a screen printing paste, followed by an evaluation of its formulation through rheological measurements is presented. The layers applied are examined via cross-sectional SEM imaging.

In initial trials, the state-of-the-art fuel electrode paste recipe from IEK-1, FZJ (based on NiO-8YSZ) to create a NiO (Vogler, The Netherlands) and 10GDC

(Fuelcellmaterials, USA) or 10SDC (Kceracell, Republic of Korea) paste was applied. This recipe involved the use of terpineol (Sigma-Aldrich, St. Louis, USA) as a suspension medium, Disperbyk P 104 (BYK-Chemie GmbH, Wesel, Germany) as a dispersant, and ethylcellulose [10cps] (Sigma-Aldrich, St. Louis, USA) as a binder. If not stated otherwise the same chemicals were used for formulation of screen printing pastes as described here in Section 4.2. Furthermore, adjustments were made to the quantities of the individual chemicals. However, challenges emerged during the sintering process of the HC when using these formulations for doped ceria fuel electrodes. Several dark spots referred to as defects on the surface of the HC were observable. These defects became more pronounced when the top layer contained doped ceria instead of 8YSZ. Therefore, it was assumed that the origin of these defects was primarily associated with the substitution of 8YSZ with 10GDC in FESC manufacturing. The exact causes of these defects remain unknown, but several factors were assumed to contribute. Some of these defects are just holes while other holes contain a larger particle indicating agglomerates of either the powder or the binder. Additionally, the solid content of the green body or the screen printing paste may have been too low. The constrained sintering of doped ceria layers, stemming from the higher sintering activity of doped ceria powders, could have resulted in internal stresses within the layer. This was observable in a HC that curled up during sintering. Furthermore, the roughness or unevenness of the NiO- yttria-stabilized zirconia substrate used might have led to irregularities in the relatively thin layers. Another possible explanation was contamination originating from the furnace, particularly silicon (Si) likely originating from the SiC sintering and covering plates, which could react with gadolinium to form gadolinium silicates [183]. To address these issues, various measures were implemented, such as adapting the sintering behavior of doped ceria to align with the commonly used 8YSZ, optimizing the dispersion of ceria, increasing the solid content of the screen printing pastes, and taking steps to prevent contamination from the furnace.
Laser microscope and SEM micrographs supporting all these observations are shown in Appendix A, Figure A.11 and Figure A.12.
The foundation for FESC manufacturing in this thesis is based on a ~300 µm thick NiO-3 mol% yttria-stabilized zirconia ($Y_{0.058}Zr_{0.942}O_{1.971,}$ 3YSZ) substrate manufactured by CeramTec, Plochingen, Germany. All screen printing pastes were applied with a semi-automatic screen printer EKRA E-2 (ASYS Automatisierungssysteme GmbH, Dornstadt, Germany).

4.2.1 Reactive sintering of an 8YSZ electrolyte

Lowering the sintering temperature has a direct impact on minimizing interdiffusion, offering the potential to mitigate unwanted processes. The concept of reactive sintering (or reaction sintering) is employed to sinter a dense 8YSZ electrolyte from the precursor materials Y_2O_3 (Treibacher Industrie AG, Althofen, Germany) and ZrO_2 (Tosoh, Japan). The green body was formed by applying a paste onto pre-

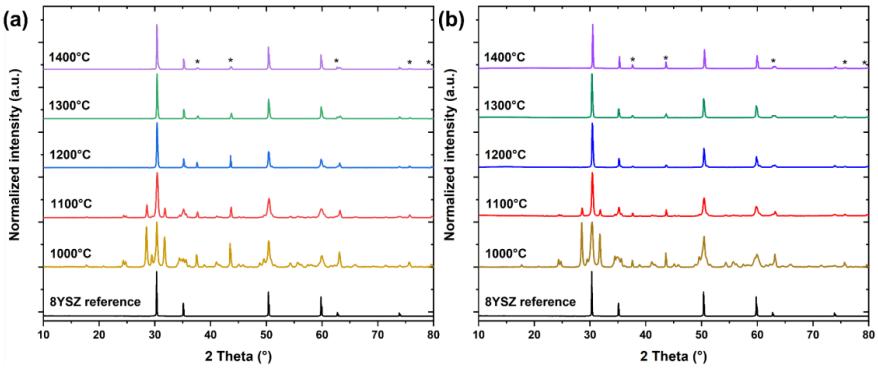

Figure 4.22: Diffractograms of the surface of (a) reactive sintered 8YSZ layers and (b) reactive sintered 8YSZ layers with 1 mol% of NiO added as sintering aid. Stars denote NiO reflections, primarily caused by the NiO-3YSZ substrate.

sintered NiO-3YSZ substrates by screen printing. The precursors were mixed in the desired molar ratio and ball milled with 3 mm zirconia milling balls for 24 h in ethanol. Subsequently, the powder mixture was dried. To form a pre-suspension, 70.0 wt% of the mixed powders, 29.5 wt% terpineol and 0.5 wt% dispersant Disperbyk P-104 were mixed with 3 mm zirconia grinding balls (the weight ratio of grinding balls to pre-suspension was approximately ~4:1) using a tumbling mixer for 24 h. Afterwards, a slurry was formed by adding 16 wt% of a transport agent (15 wt% ethyl cellulose [10cps] dissolved in 85 wt% terpineol) to the pre-suspension. A second paste was prepared by substituting 1 mol% of the powder mixture with NiO, serving as a sintering aid. The pastes were applied via screen printing. Subsequently, they were dried and sintered at temperatures between 1000-1400 °C for 5 h in ambient air. The surfaces of the sintered layers were examined with XRD and polished cross-sections were investigated by SEM.

The diffractograms are shown in Figure 4.22. Stars denote NiO reflections of the NiO-3YSZ substrate. Commencing at 1200 °C, the reflections linked to the precursor materials are absent, indicating complete formation of 8YSZ. The primary reflections exhibit peak splitting, indicating the presence of both tetragonal and monoclinic crystal structures which might be caused by diffraction of the NiO-3YSZ substrate. The addition of NiO does not affect the formation temperature for 8YSZ within the examined temperature range or at the distinct 100 °C intervals. Additionally, the reflections exhibit comparable width and shape. Nevertheless, the introduction of NiO aids the densification of the reactively sintered 8YSZ layer. Figure 4.23 depicts cross-sections of the sintered layers for temperatures ranging from 1000 °C to 1400 °C. Hardly any sintering takes place before 1200 °C, resulting in porous layers. At 1400 °C, a reasonably dense layer emerges, exhibiting worm-like pores, indicating that the layer might not be gastight.

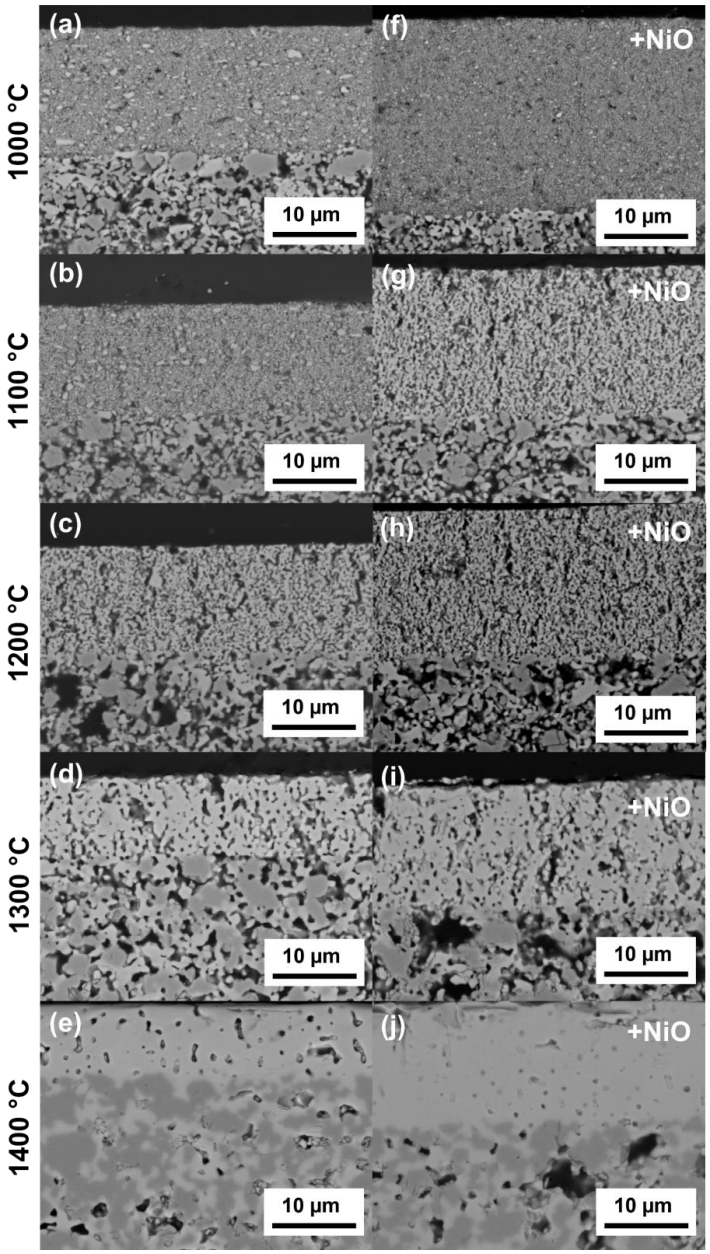

Figure 4.23: (a-e) Reactive sintered 8YSZ layers (1000-1400 °C for 5 h) screen-printed on NiO-3YSZ substrates. (f-j) Reactive sintered 8YSZ layers (1000-1400 °C for 5 h) with addition of 1 mol% NiO, screen-printed on NiO-3YSZ substrates.

With the addition of NiO as a sintering aid, densification is improved, resulting in a denser layer with just some residual round-shaped pores at a sintering temperature of 1400 °C. Although 8YSZ can be formed at 1200°C, achieving densification in a screen-printed layer necessitates a temperature of 1400°C. Consequently, the reactive sintering of an 8YSZ electrolyte layer does not offer significant reduction potential in sintering temperature. It is plausible that further optimization of the sintering process could yield a denser layer at lower sintering temperatures. Nonetheless, the sintering temperature for the NiO- yttria-stabilized zirconia substrate must remain sufficiently high to attain the desired microstructure and functionality.
In the case of the NiO-3YSZ substrate utilized in the fabrication of FESCs in this thesis, the required sintering temperature is also around 1400°C to establish sufficient percolation of the NiO phase. Therefore, lowering the sintering temperature of the HC is only feasible if the microstructure evolution of the substrate remains adequate at the given temperature.

4.2.2 Sintering onset of doped ceria

To ensure sintering compatibility with the pre-calcined yttria-stabilized zirconia in the substrate, the 8YSZ in the state-of-the-art fuel electrode and electrolyte is pre-calcined at 1230 °C for 3 h. This pre-calcination is carried out to mitigate the impact of constrained sintering. To address the issue of constrained sintering resulting from the substitution of 8YSZ with doped ceria in the fuel electrode, Gd- and Sm-doped ceria materials were pre-calcined at different temperatures. This step is taken to reduce sintering activity and align the sintering onset with that of the pre-calcined yttria-stabilized zirconia.
10GDC and 10SDC were calcined at different temperatures (1230 °C, 1250 °C and 1280 °C) for 3 h with a heating rate of 3 °C/min and a cooling rate of 5 °C/min until their sintering onset matched the sintering onset of the pre-calcined 8YSZ powder.

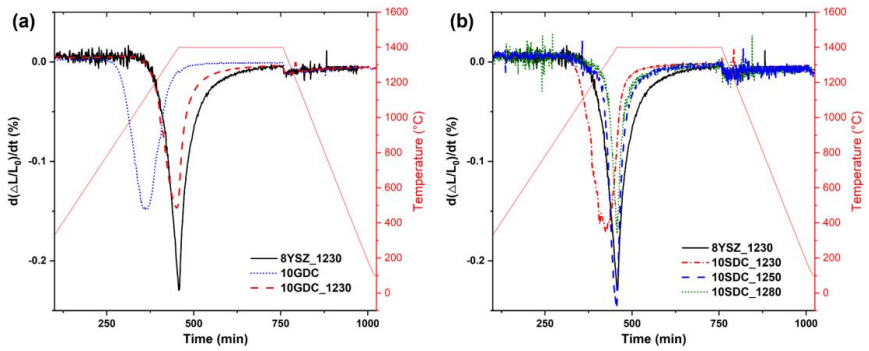

Figure 4.24: First derivative of the sinter shrinkage at 1400 °C for 5 h for 10GDC and 10SDC untreated and calcined at different temperatures. Heating rate was set to 3 °C/min and cooling rate to 5 °C/min.

Table 4.8: Sinter onset of 8YSZ, 10GDC, and 10SDC uncalcined or calcined at different temperatures for 3 h.

Material	Calcination temperature (°C)	Sinter onset (°C)
8YSZ	/	1132
8YSZ	1230	1249
10GDC	/	966
10GDC	1230	1234
10SDC	/	1048
10SDC	1230	1143
10SDC	1250	1297
10SDC	1280	1307

The calcined powders were uniaxially pressed into pellets with a diameter of 8 mm. Sinter shrinkage was measured at a sintering temperature of 1400 °C for 5 h, using a heating rate of 3 °C/min and a cooling rate of 5 °C/min.

Figure 4.24 shows the first derivative of the sintering shrinkage and the onset temperatures are provided in Table 4.8.
When 10GDC is pre-calcined at 1230 °C and 10SDC at 1250 °C, their sintering onset temperatures adequately match those of the 8YSZ pre-calcined at 1230 °C. Consequently, 10GDC and 10SDC powders were pre-calcined at 1230 °C and 1250 °C, respectively, for further optimization of the screen printing pastes. After calcination, the powders were ball-milled in ethanol to break large agglomerates.

4.2.3 Dispersant evaluation for ceria

In the process of formulating an appropriate screen printing paste, the initial step involves selecting a suitable dispersant for the specific material in use. This dispersant should effectively separate individual particles through either steric or electrostatic interactions. The dispersant must be soluble in the desired suspension medium and the amount of dispersant must be tailored to the specific surface area of the powder at hand.
Analogous to the state-of-the-art formulation for Ni-8YSZ fuel electrode pastes at IEK-1, FZJ, terpineol was chosen as a suspension medium. Nine different dispersants were considered, as listed in Table 4.9. Disperbyk dispersants were bought from the company BYK-Chemie GmbH, Wesel, Germany, while Hypermer dispersants were bought from the company Croda, East Yorkshire, United Kingdom. As ceria acts as a Lewis acid [184], acidic dispersants were preferred. However, as these dispersants are commercially available products, their precise chemical composition is not known.
At first the complete miscibility of each dispersant with terpineol was investigated. The dispersants were mixed with terpineol at room temperature and mixed and

Table 4.9: Investigated dispersants and their chemical notation.

Dispersant	Abbreviation	Chemical notation
Hypermer KD2	HKD2	Polyoxyalkyleneamine derivative
Hypermer KD6	HKD6	No specification
Hypermer KD73	HKD73	Carboxylic acid functionalized methyl polyethylene glycol
Hypermer KD77	HKD77	Carboxylic acid functionalized methyl polyethylene glycol
Disperbyk 101N	B101	Salt of a polyamine amide and a polar acidic ester
Disperbyk 102	B102	Phosphoric ester
Disperbyk P 104	BP104	Unsaturated polycarboxylic acid
Disperbyk 2081	B2081	Salt of a polycarboxylic acid
Disperbyk Anti-Terra U	BAntiT.U	Salt of a polyaminamide and an acidic ester

heated up to 60 °C in a weight ratio of 1:3. If the dispersant separated from terpineol after 24 h it was excluded from further investigation. Pictures of the respective mixtures are shown in Appendix A, Figure A.13

Among the dispersants, HKD6 and B2081 were found to be immiscible at both room temperature and 60 °C, while HKD77 exhibited miscibility only at 60 °C. All other dispersants showed full miscibility at room temperature and were subsequently assessed for their viscosity at low shear rates in a suspension containing 10GDC. These suspensions consisted of 75 wt% 10GDC, with either 1 wt% or 3 wt% of

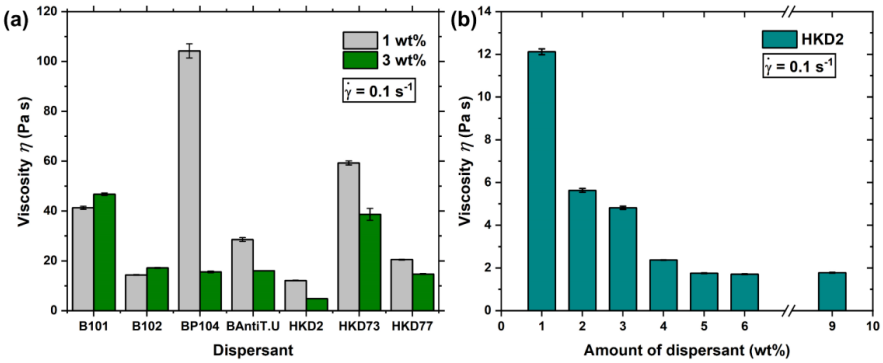

Figure 4.25: (a) Viscosity at low shear rate of 0.1 s^{-1} for 10GDC (75 wt%) suspensions with various dispersants (Left pillar shows results for 1 wt% dispersant and 24 wt% terpineol, right pillar for 3 wt% dispersant and 22 wt% terpineol in the mixture). (b) Viscosity at a low shear rate of 0.1 s^{-1} for 10GDC (75 wt%) suspensions with different amounts of HKD2 dispersant (1-9 wt%; the amount of terpineol was accordingly lowered).

dispersant and 24 wt% or 22 wt% of terpineol, respectively. The results are shown in Figure 4.25(a). HKD2 emerged as the dispersant with the lowest viscosity and was therefore subjected to further investigation regarding the optimal dispersant concentration. Viscosity at low shear reates for 10GDC suspensions with different amounts of HKD2 are shwon in Figure 4.25(b). The amount of HKD2 in the suspensions, which contained 75 wt% 10GDC, was adjusted within the range of 1-6 wt% and 9 wt%, along with corresponding variations in terpineol content (from 24-19 wt% and 16 wt%, respectively). The viscosioty decreases with an increase in the amount of HKD2, reaching an optimum at 6 wt%. Beyond this concentration, viscosity slightly increased with 9 wt% HKD2 in the suspension. Consequently, the selected amount of HKD2 dispersant for doped ceria pre-suspensions, used in the fabrication of screen printing pastes, was fixed at 6 wt%.

4.2.4 Screen printing paste formulation and rheological characterization

To manufacture FESCs with a Ni-doped ceria fuel electrode, a screen printing paste for the electrode needs to be formulated. This process starts with a pre-suspension containing 10GDC (or 10SDC). By using BP104 as a dispersant, the maximum powder load achievable in the pre-suspension is approximately 70 wt% to ensure a processable suspension. Substituting BP104 with HKD2 increases the maximum powder load to 75 wt% in the pre-suspension and also improves dispersion, as shown in Section 4.2.3. The powder load was fixed to 75 wt% for further screen printing paste formulation, with the addition of 19 wt% terpineol and 6 wt% HKD2. Further optimization may allow for even higher powder loads. In addition, a NiO pre-suspension was formulated containing 72.0 wt% NiO, 27 wt% terpineol and 1 wt% HKD2. Both pre-suspensions were mixed in different ratios to yield fuel electrodes with Ni:10XDC (X= Gd or Sm) ratios of either ~50:50 vol% or ~38-40:60-62 vol% after binder burn out, sintering and reduction of NiO to Ni. To create a screen printing paste for the fuel electrodes, 15 wt% of a transport suspension containing 15 wt% ethyl cellulose [10cps] dissolved in 85 wt% terpineol was added to the pre-suspension.
In Section 4.1.6, it was demonstrated that a barrier layer is necessary between the Ni-10GDC electrode and the 8YSZ electrolyte to prevent performance degradation. To investigate the influence of a barrier layer between the Ni-10XDC fuel electrode and the 8YSZ electrolyte in FESCs, FESCs were manufactured both with and without a 10XDC barrier layer between the fuel electrode and the electrolyte. Two different types of barrier layers were investigated. On the one hand, the state-of-the-art 20GDC barrier layer, commonly applied at IEK-1, FZJ between the LSCF air electrode and the 8YSZ electrolyte, containing 72 wt% $Gd_{0.2}Ce_{0.8}O_{2-\delta}$ (20GDC, Treibacher Industrie AG, Althofen, Germany), 27.1 wt% terpineol and 0.9 wt% BP104. To form a screen printing paste 15 wt% of a transport suspension was added to the pre-suspension containing 15 wt% ethyl cellulose [10cps] dissolved in 85 wt%

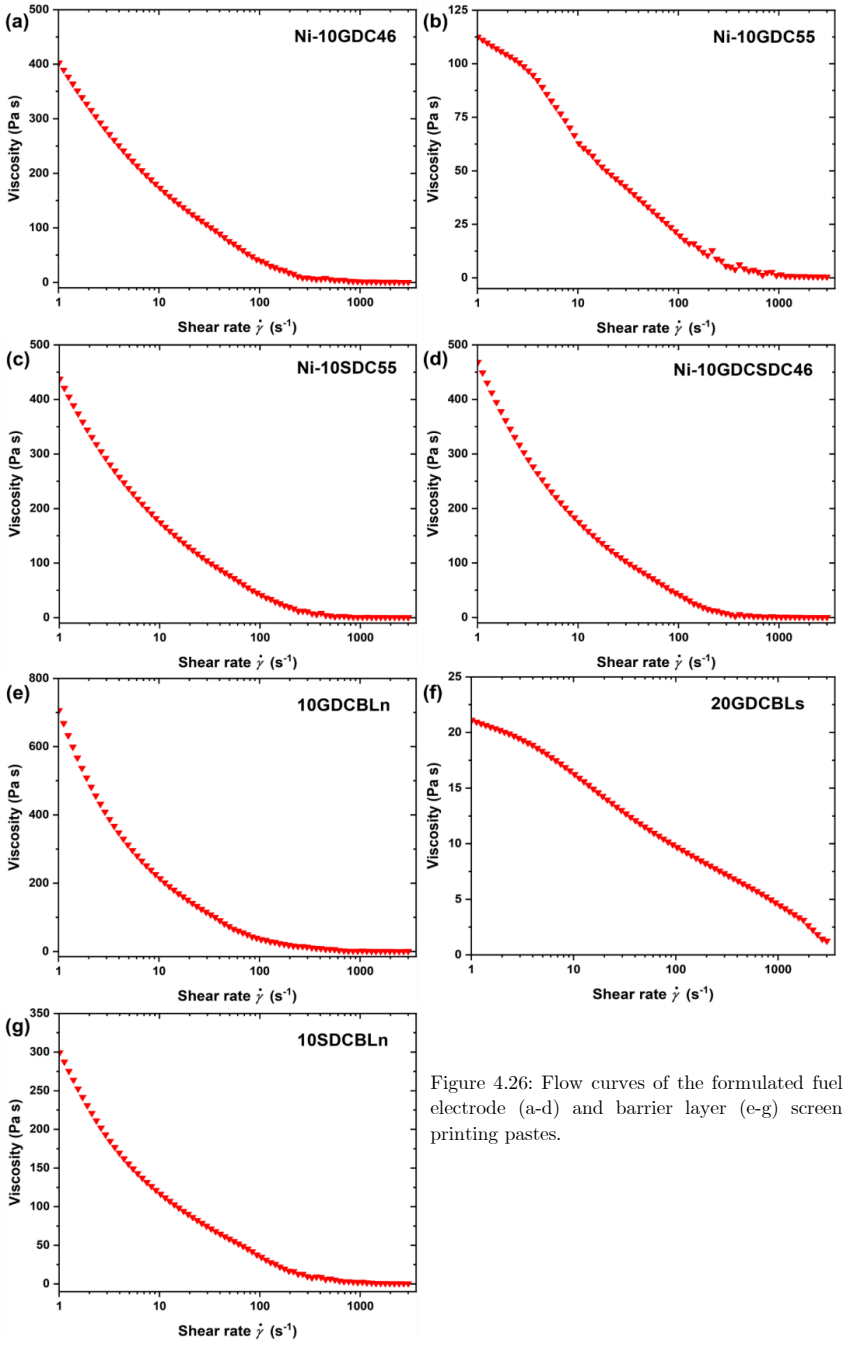

Figure 4.26: Flow curves of the formulated fuel electrode (a-d) and barrier layer (e-g) screen printing pastes.

terpineol. For the new barrier layer formulation, the same 10XDC pre-suspensions as for the Ni-doped ceria fuel electrodes was used where 15 wt% of a transport suspension was added to the pre-suspension containing 20 wt% ethyl cellulose [45cps] dissolved in 80 wt% terpineol. Fuel electrode pastes with either Gd or Sm, resulting in fuel electrodes with a ratio of Ni:10XDC of ~50:50 vol% (referred to as Ni-10GDC55 or Ni-10SDC55) or ~40:60 vol% (referred to as Ni-10GDC46 or Ni-10SDC46), a Gd and Sm mixed fuel electrode with a Ni:10GDC:10SDC ratio of ~40:30:30 vol% (referred to as Ni-10GDCSDC46) and barrier layer pastes of either 10GDC or 10SDC (referred to as 10GDCBLn or 10SDCBLn) were formulated and characterized by rheological methods. For comparison, the state-of the-art 20GDC barrier layer (referred to as 20GDCBLs) was measured. For Ni-10SDC46 no paste remained for characterization after FESC manufacturing.
Flow curves, LVE regions, and thixotropic behavior for the formulated fuel electrode and barrier layer pastes are shown in Figure 4.26, Figure 4.27, and Figure 4.28, respectively. The measurements were adapted to the screen printing process. Although shear rates during the process are not precisely known, they could easily exceed 1000 s^{-1}. Therefore, flow curves were measured up to a shear rate of 3000 s^{-1}. The printing process itself, and thus the exertion of force on the paste, lasts around 5 s. Consequently, the thixotropic behavior was measured after the structure was destroyed for 5 s at a shear rate of 3000 s^{-1}. The LVE region is tested until the structure breaks down and the paste transitions from solid to liquid-like behavior. Not much is reported in literature regarding appropriate rheological characteristics for SOC screen printing pastes. It is reported that appropriate viscosity for YSZ pastes at a shear rate of 100 s^{-1} is around 4-45 Pa s [109]. Ultimately, the pastes need to be printable, and the applied layers must exhibit the desired microstructures after sintering. In addition, rheological behavior changes with material's chemistry. Therefore, it is proposed to use rheology as a tool to monitor the quality of screen printing pastes if the paste results in layers exhibiting the desired properties. Nevertheless, some basic conclusions can be drawn from the rheological data.

All pastes exhibit shear-thinning behavior, a crucial characteristic for the printing process. The viscosity at 1000 s^{-1} is below 5 Pa s and below 45 Pa s at 100 s^{-1} for all pastes, indicating sufficient shapeability during the screen printing process. The Ni-10XDC fuel electrodes demonstrate lower viscosities at low shear rates compared to the newly formulated barrier layers (10XDCBLn), primarily due to their higher binder content. The state-of-the-art barrier layer, 20GDCBLs, exhibits very low viscosity at low shear rates, indicating a highly liquid-like behavior.
Interestingly, all screen printing pastes exhibit higher loss modulus than storage modulus at every measured strain, indicating more liquid than solid-like properties. This observation is reinforced by the phase angle, which is around 65° for the fuel electrode pastes. In contrast, the newly formulated 10GDCBLn barrier layer, with a higher binder content, shows a phase angle of 60°, indicating more solid-like behavior compared to the fuel electrode pastes. Specifically, 10SDCBLn and 20GDCBLs

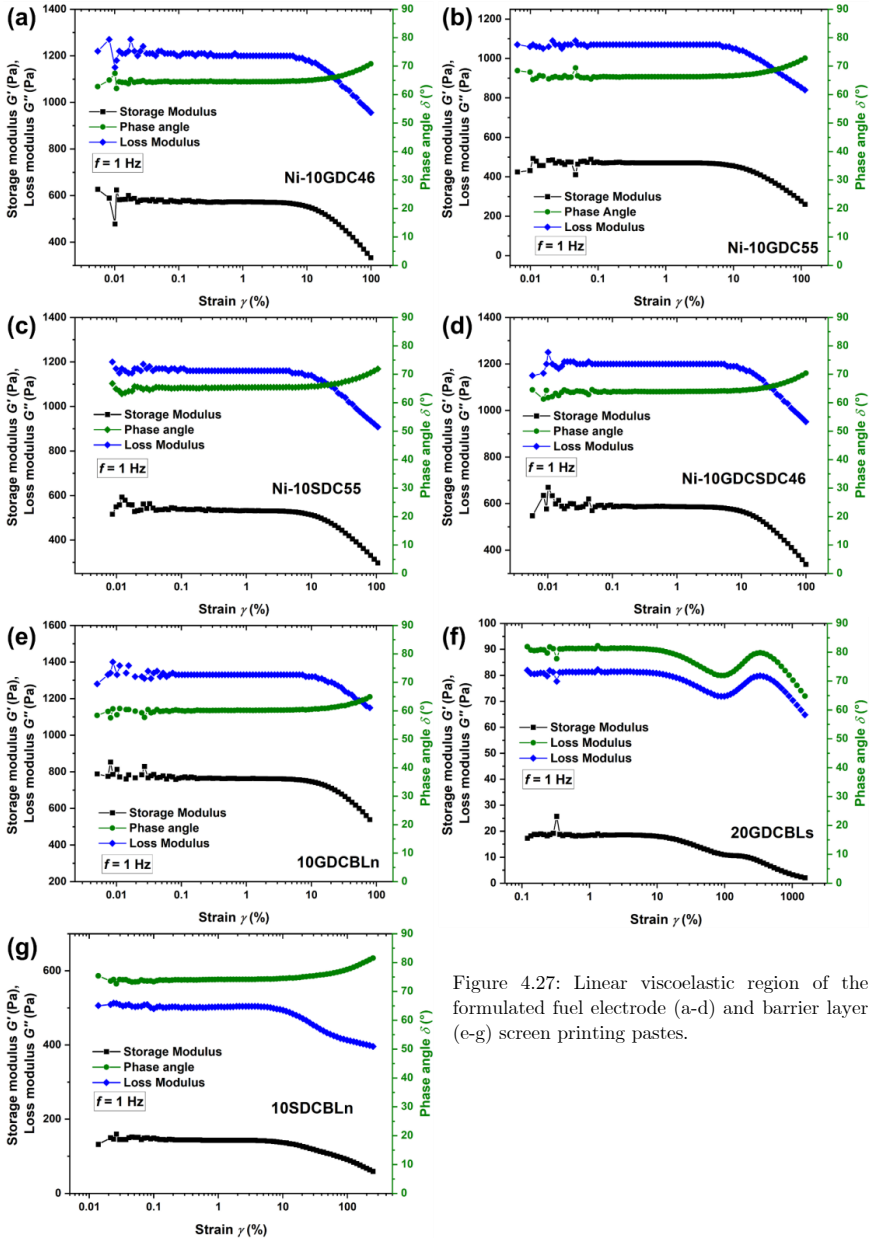

Figure 4.27: Linear viscoelastic region of the formulated fuel electrode (a-d) and barrier layer (e-g) screen printing pastes.

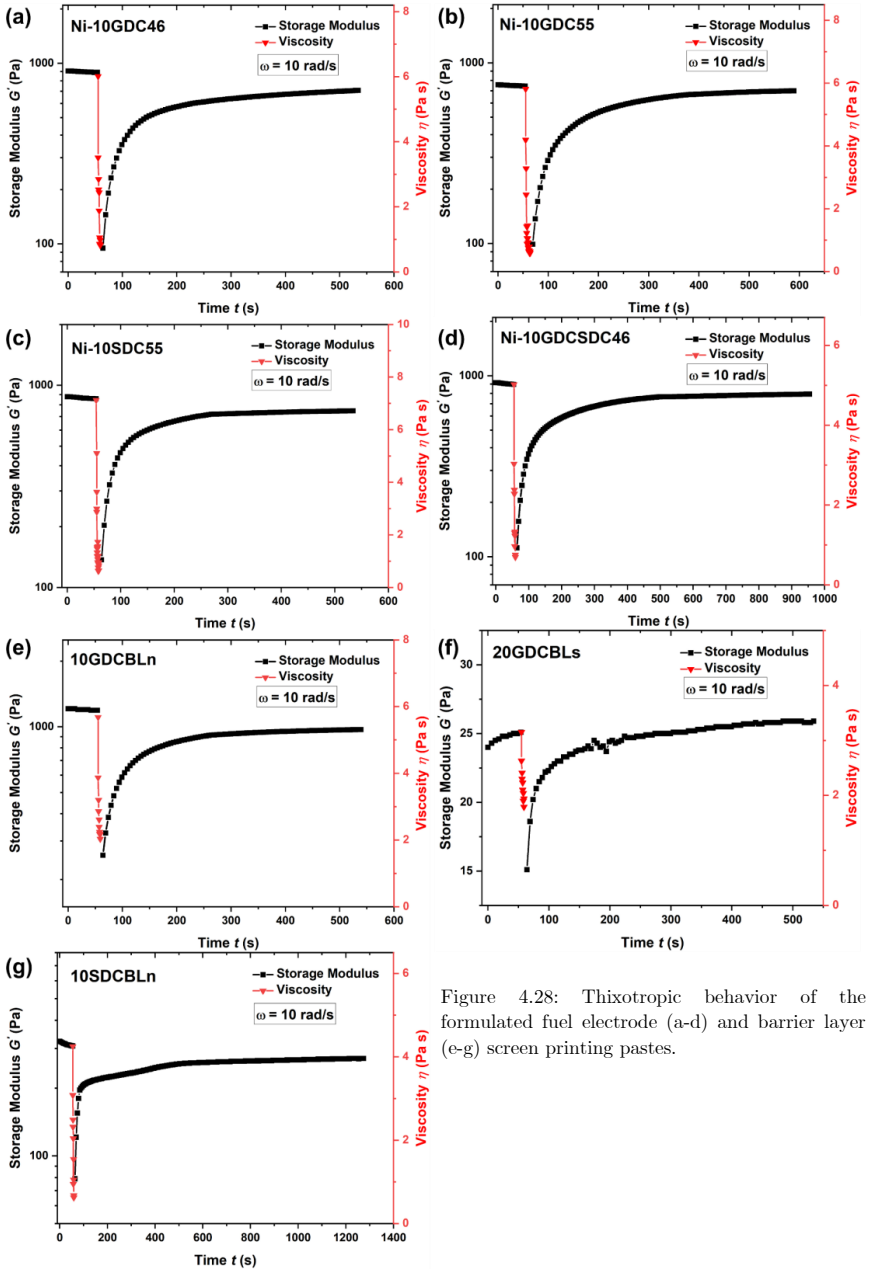

Figure 4.28: Thixotropic behavior of the formulated fuel electrode (a-d) and barrier layer (e-g) screen printing pastes.

exhibit phase angles of 74° and 81°, indicating even more pronounced liquid-like behavior in comparison to the fuel electrodes. Remarkably, regardless of the binder content, the presence of dopants in ceria, or the presence of NiO, all pastes exhibit similar yield points at strains around 6-10 %, implying comparable lengths of the LVE. Since the screen printing pastes exhibit phase angles above 45°, indicating pronounced liquid-like behavior, ink bleeding or sedimentation of the pastes might occur. To evaluate thixotropy, the recovery of the storage modulus in region three was compared to the initial value in region one. The storage modulus was compared after a 20 s recovery time, offering insights into the crucial rapid structural recovery of screen printing pastes to prevent ink bleeding. A second comparison was conducted after around 440 s to observe the extent of recovery of the paste's initial properties. The results are summarized in Table 4.10.

Fuel electrode pastes exhibit lower total recovery after 440 s compared to the newly formulated barrier layer pastes, which can be attributed to their higher binder content. However, they recover their storage modulus faster after 20 s.

Pastes containing 10SDC outperform those with 10GDC in terms of recovery rates and total recovery. The state-of-the-art barrier layer 20GDCBLs demonstrate the best thixotropic behavior in these measurements but display a higher tendency for ink bleeding after the screen printing process due to their very low storage modulus, indicative of more liquid-like behavior. Although all pastes show more liquid-like behavior in the LVE test and the 3ITT test for thixotropy indicates worse recovery compared to 20GDCBLs, with no total recovery even after 440 s and less than 50 % recovery (except 10SDCBLn exhibiting 64 % recovery) after 20 s, the fuel electrode pastes showed good printability, maintained shape, and showed no ink bleeding. The newly formulated barrier layer pastes were printable and showed no ink bleeding, but they tend to be somewhat tacky, adhering to the squeegee and screen, which could lead to incomplete printing of the layers. This tackiness is attributed to the higher binder content and the longer chain length of the ethylcellulose used in these pastes.

Considering just a rheological point of view, the fuel electrode and newly formulated barrier layer pastes show sufficient shear-thinning behavior but possess a higher loss modulus than storage modulus, indicating a lack of solid-like behavior, which is

Table 4.10: Thixotropic behavior or recovery of the storage modulus of the formulated fuel electrode and barrier layer screen printing pastes after 20 s and 440 s recovery time.

Paste	Recovery of the storage modulus (%) after	
	20 s	440 s
Ni-10GDC46	34	78
Ni-10GDC55	36	92
Ni-10SDC55	47	73
Ni-10GDCSDC46	35	85
10GDCBLn	44	81
20GDCBLs	88	100
10SDCBLn	64	82

generally undesirable. Nevertheless, from a practical screen printing point of view, the layers are applicable and maintain shape. If the sintered layers show the desired microstructural properties (investigated in the next Section 4.2.5), the measured rheological properties can serve as a tool for quality control of the screen printing pastes.

4.2.5 FESC manufacturing with Ni-doped ceria fuel electrodes

The screen printing pastes, formulated and investigated in Section 4.2.4, were implemented into the state-of-the-art FESC cell concept at IEK-1, FZJ. The functional layers are screen printed onto a NiO-3YSZ substrate and sintered. FESCs with and without an XDC barrier layer between the Ni-10XDC fuel electrode and the 8YSZ electrolyte are compared. At first, the Ni-10XDC fuel electrodes are printed two times (the second layer is applied on top of the first layer after drying) and were pre-sintered at 1000 °C for 1 h applying a heating rate of 3 °C/min and a cooling rate of 5 °C/min. When employing an XDC barrier layer between the fuel electrode and the electrolyte, these barrier layers are either pre-sintered at 1000 °C for 1 h, applying a heating rate of 3 °C/min and a cooling rate of 5 °C/min or simply dried before applying the 8YSZ electrolyte. The 8YSZ electrolyte and the LSCF air electrode were formulated according to the state-of-the-art recipes developed by IEK-1, FZJ. The electrolyte was sintered at 1400 °C for 5 h and the air electrode at 1080 °C for 3 h, for both a heating rate of 3 °C/min and a cooling rate of 5 °C/min was applied. Additionally, between the 8YSZ electrolyte and the LSCF air electrode, a state-of-the-art 20GDC barrier layer derived from the 20GDCBLs screen printing paste is applied and sintered at 1300 °C for 3 h, employing a heating rate of 3 °C/min and a cooling rate of 5 °C/min.
Details regarding sample names and configurations for the various FESC setups can be found in Table 4.11. Illustrations of the different FESC design are shown in Figure 4.29. All cells were investigated after manufacturing of the HC. In addition, for Ni-10GDC46BLn and Ni-10GDC55BLs_ps full cells (FC) were examined. Cross-

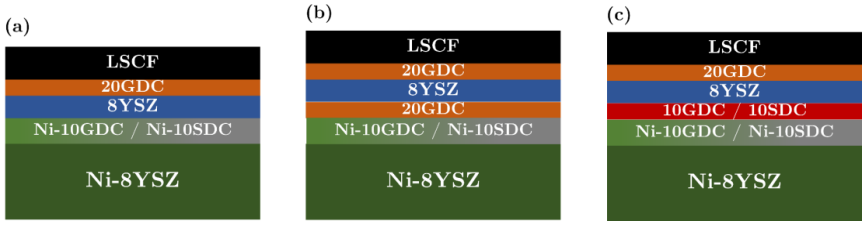

Figure 4.29: Illustration of the manufactured FESCs with a Ni-10XDC fuel electrode. (a) FESC without a barrier between the fuel electrode and 8YSZ electrolyte. (b) FESC with a state-of-the-art 20GDC barrier layer either pre-sintered or just dried between the fuel electrode and electrolyte. (c) FESC with a new 10GDC barrier layer formulation (just dried) between the fuel electrode and electrolyte.

Table 4.11: Notations and processing procedures of the FESCs manufactured in this thesis. All FESC contain a state-of-the-art 8YSZ electrolyte sintered at 1400 °C for 5 h and a LSCF air elecotrode sintered at 1080 °C for 3 h separated by a 20GDC barrier layer sintered at 1300 °C for 3 h. 46 or 55 denotes fuel electrodes with a Ni:10XDC vol% ratio of 40:60 or 50:50, respectively. All fuel electrodes were pre-sintered sintered at 1000 °C for 1 h. Barrier layer between fuel electrode and electrolyte (if present) were either pre-sintered in a separate step at (1000 °C for 1 h) or co-sintered with the electrolyte.

Sample	**Ni:10XDC (vol%) (X=Gd, Sm)**	**Barrier layer between fuel electrode and electrolyte?**	**Barrier layer composition**	**Pre-sintered Barrier layer?**
Ni-10GDC46	40:60	No	/	/
Ni-10GDC55	50:50	No	/	/
Ni-10GDC46BLn	40:60	Yes	New formulation	No
Ni-10GDC46BL_s_ps	40:60	Yes	State-of-the-art	Yes
Ni-10GDC55_BLn	50:50	Yes	New formulation	No
Ni-10GDC55_BLs	50:50	Yes	State-of-the-art	No
Ni-10GDC55_BLs_ps	50:50	Yes	State-of-the-art	Yes
Ni-10SDC55	50:50	No	/	/
Ni-10SDC55_BLn	50:50	Yes	New formulation	No
Ni-10GDCSDC46_BLn	40:60 GDC:SDC=50:50	Yes	New formulation	No

sections of the manufactured fuel electrode-supported HCs or fuel electrode-supported FCs were investigated by SEM. Furthermore, the interdiffusion behavior of the doped ceria fuel electrodes or the doped ceria barrier layers with the 8YSZ electrolyte is measured.

Microstructure of the Ni-10XDC fuel electrodes and 10XDC barrier layers

SEM micrographs of polished cross-sections for HCs and FCs are shown in Figure 4.30. Layer thicknesses and layer porosities were estimated through image analysis, employing the Fiji software, and the resulting values can be found in Table 4.12. Ni-10GDC fuel electrodes exhibit layer thicknesses ranging from approximately 13.5 to 18.6 µm, while Ni-10SDC and Ni-10GDCSDC electrodes are notably thicker, measuring around 20.6 to 23.4 µm. In contrast, the 10XDCBLn and 20GDCBLs barrier layers have thicknesses of approximately 5.9 to 7.2 µm, with 10SDCBLn being slightly thicker at around 8.1 to 8.4 µm. These findings suggest that 10SDC screen printing pastes yield thicker layers compared to their 10GDC counterparts. The 8YSZ electrolyte exhibits an average layer thickness of 7.3 ± 0.7 µm and a residual porosity of 2.9 ± 1.5 %. The LSCF air electrode exhibits an average layer thickness of 31.9 µm and a residual porosity of 40.5 %.

All Ni-10XDC fuel electrodes show a residual porosity of around 5-10 %. Interestingly, no discernible porosity trend is evident concerning the Ni:10XDC ratio

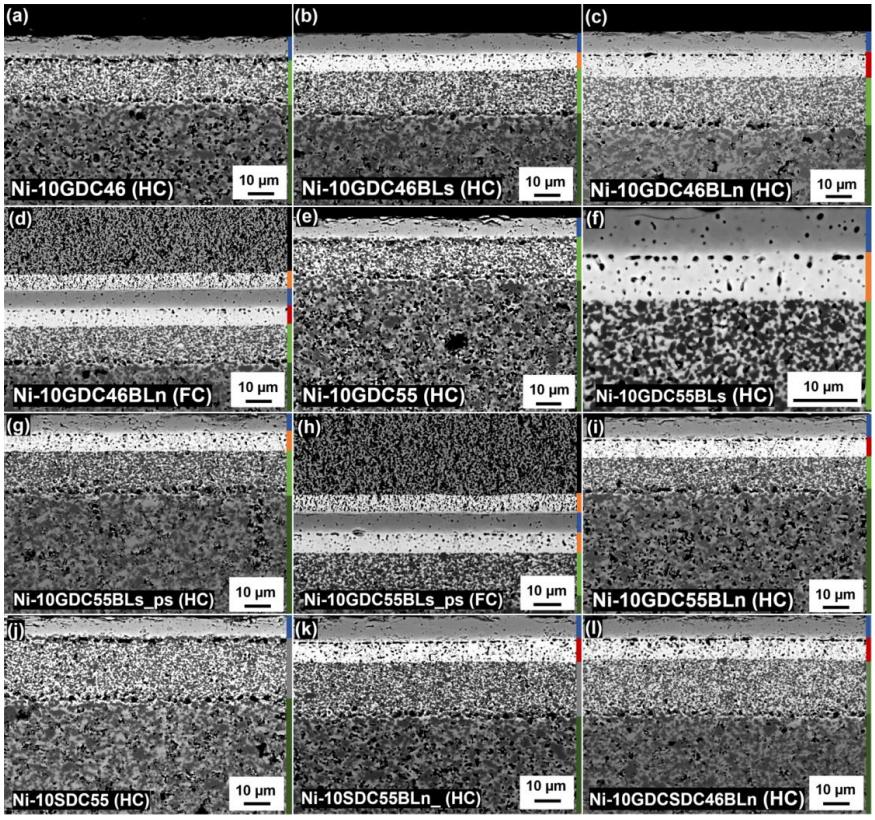

Figure 4.30: FESCs with (a-d) Ni-10GDC46, (e-i) Ni-10GDC55, (j-k) Ni-10SDC55, and (l) Ni-10GDCSDC46 fuel electrodes. (b, f, g, h) contain barrier layers from the state-of-the-art barrier layer paste while (c, d, i, k, l) possess barrier layers with newly formulated barrier layer pastes between the fuel electrode and the 8YSZ electrolyte. (g-h) contain pre-sintered barrier layers; HC = half cell, FC = full cell. Dark green bar denotes the NiO-3YSZ substrate, green or grey the Ni-10XDC fuel electrode, red newly formulated 10XDCBLn barrier layers, blue the 8YSZ electrolyte, orange the state-of-the-art 20GDCBLs barrier layer, and black the LSCF air electrode.

or the number of sintering steps (HC or FC). Similar to the observation in ESCs (see Section 4.1.5), porosity is noticeable at the interfaces with the NiO-3YSZ substrate and in cases where no barrier layer is present between the fuel electrode and the 8YSZ electrolyte. In fact, roughly half of the overall porosity for every fuel electrode (1-5 %) is concentrated at these interfaces.
The NiO-3YSZ substrate shows enhanced densification at the interface with the Ni-10XDC fuel electrodes. The newly formulated barrier layers (10XDCBLn) exhibit a comparable porosity, averaging 10.6 ± 3.0 %, when compared to the state-of-the-art barrier layer paste (20GDCBLs) with 9.2 ± 2.1 %. Again, nearly half of the porosity

Table 4.12: Layer thicknesses, layer porosities, and amount of layer porosity at the interface for the manufactured FESCs with Ni-10XDC fuel electrode with and without XDC barrier layer between fuel electrode and electrolyte.

FESC	Layer thickness (µm) / Porosity [Interface porosity] (%)				
	Fuel electrode (Ni-10XDC)	Barrier layer (10XDCBLn)	Electrolyte (8YSZ)	Barrier layer (20GDCBLs)	Air electrode (LSCF)
Ni-10GDC46 (HC)	18.6 / 8.4 [4.9]	/	6.6 / 2.5	/	/
Ni-10GDC46BLs (HC)	15.2 /7.5 [3.7]	6.5 / 10.0 [5.7]	7.5 / 2.0	/	/
Ni-10GDC46BLn (HC)	16.1 /4.5 [1.5]	7.8 /7.3 [4.6]	6.9 / 1.5	/	/
Ni-10GDC46BLn (FC)	14.3 / 6.9 [5.6]	6.6 / 8.0 [4.8]	6.6 /2.5	5.9 /25.0	31.7 / 38
Ni-10GDC55 (HC)	16.3 / 9.2 [4.3]	/	6.8 / 5.0	/	/
Ni-10GDC55BLs (HC)	16.1 / 3.8 [1.9]	6.9 / 8.2 [4.3]	6.8 / 1.8	/	/
Ni-10GDC55BLs_ps (HC)	16.6 / 10.8 [4.2]	7.2 / 15.0 [4.0]	6.6 / 7.0	/	/
Ni-10GDC55BLs_ps (FC)	16.7 / 7.0 [3.7]	7.0 /9.3 [2.9]	6.7 /2.6	6.3 /27.0	32.0 / 43
Ni-10GDC55BLn (HC)	13.5 / 7.6 [3.1]	6.6 / 8.1 [4.0]	7.7 / 2.9	/	/
Ni-10SDC55 (HC)	23.4 / 10.0 [4.2]	/	8.5 / 1.9	/	/
Ni-10SDC55BLn (HC)	20.6 / 8.1 [4.8]	8.4 /10.5 [1.8]	8.5 / 2.4	/	/
Ni-10GDCSDC46BLn (HC)	20.9 /6.3 [4.0]	8.1 /12.2 [2.7]	8.0 /3.0	/	/

is found at the interface with the 8YSZ electrolyte. Pre-sintering of the barrier layers has no discernible impact on porosity, suggesting that densification primarily occurs during electrolyte sintering at 1400 °C. Interestingly, there is no porosity at the interface between the Ni-10XDC fuel electrodes and the XDC barrier layers. This suggests different interdiffusion coefficients for cerium and X compared to zirconium and yttrium, potentially leading to the formation of Kirkendall voids, as observed in ESCs (see Section 4.1.5). Furthermore, and in contrast to ESCs, Kirkendall porosity develops in the absence of NiO between the XDC barrier layers and the 8YSZ electrolyte when sintered at 1400 °C. If the air electrode barrier layer is applied from a paste on the sintered 8YSZ electrolyte, no Kirkendall porosity is present on this side of the electrolyte interface. This could be attributed to the lower sintering temperature of 1300°C, or it might be a result that both layers the Ni-10XDC fuel electrodes or the XDC barrier layers and the 8YSZ electrolyte are just present in a debindered (green body) or pre-sintered state, possibly offering improved contact between the particles or diffusion paths during electrolyte sintering.
When the 20GDC barrier layer (positioned between the electrolyte and the air electrode) is subjected to constrained sintering at just 1300 °C for 3 h, it exhibits a residual porosity of approximately 26 %.

Interdiffusion lengths in FESCs

The diffusion lengths of Ce and X between the Ni-10XDC fuel electrodes and the XDC barrier layers into the 8YSZ electrolyte were investigated utilizing material contrast. The results are summarized in Table 4.13. Unfortunately, some of the prepared cross-sections possessed insufficient quality to conduct the analysis. For the diffusion lengths from a Ni-10GDC46 fuel electrode into the 8YSZ electrolyte during its sintering from a green body, a slight enhancement is observed compared to ESCs with 2.58 ± 0.26 µm versus 1.82 ± 0.08 µm. The diffusion lengths from

Table 4.13: Diffusion length of Ce and Gd or Sm into 8YSZ during FESC manufacturing. FE = Fuel electrode (Ni-10XDC), EL = Electrolyte (8YSZ), BL = Barrier layer (XDCBL).

FESC	Diffusion length (µm)	Interface	
		FE-EL	BL-EL
Ni-10GDC46 (HC)	2.58 ± 0.26	x	
Ni-10GDC46BLs (HC)	1.89 ± 0.30		x
Ni-10GDC46BLn (HC)	/		
Ni-10GDC46BLn (FC)	2.27 ± 0.14		x
Ni-10GDC55 (HC)	/		
Ni-10GDC55BLs (HC)	1.69 ± 0.02		x
Ni-10GDC55BLs_ps (HC)	1.76 ± 0.05		x
Ni-10GDC55BLs_ps (FC)	2.36 ± 0.31		x
Ni-10GDC55BLn (HC)	1.88 ± 0.27		x
Ni-10SDC55 (HC)	/		
Ni-10SDC55BLn (HC)	1.85 ± 0.35		x
Ni-10GDCSDC46BLn (HC)	/		

XDC barrier layers into the 8YSZ are generally consistent with those observed in ESCs when subjected to either one sintering step at 1400 °C or two sintering steps at 1400 °C and 1300 °C.
Additionally, an EDS map and EDS line scans were performed which are not shown here but in the Appendix A, Figure A.14 and Figure A.15. The line scans show on average longer diffusion lengths of 3.6-5 µm. The EDS map reveals Sr movement from the LSCF air electrode to the interface and into the 8YSZ electrolyte. The LSCF air electrode contains small amounts of Y. A contamination of the used 8YSZ and LSCF with Si is observable, while all layers show traces of Al contamination.

Performance evaluation & Carbon degradation tests
All the FESCs shown in this section are currently (December 2023) under investigation in terms of their performance and carbon degradation behavior at the Chair of Energy Systems, TUM.

4.2.6 Discussion

Although rheology indicates suboptimal properties of the Ni-10XDC fuel electrode and XDC barrier layer screen printing pastes, FESCs were successfully manufactured. The Ni-10XDC fuel electrodes show an appropriate microstructure, and by printing two times an optimal layer thickness was achieved, since the reaction zone in GDC is extended. Therefore, an ideal layer thickness for a GDC containing fuel electrode is around 15-20 µm [185–187] compared to 8YSZ with around 7 µm [188].
If a two-step printing process is to be avoided, the use of a screen providing a thicker green layer thickness becomes necessary.

The XDC barrier layers, on average, displayed a residual bulk porosity below 10 %. The lowest observed porosity value was 2.7 % for 10GDCBLn sintered at 1400 °C for 5 h. The porosity emerging at the interface of ceria-containing layers with an 8YSZ layer sintered at 1400 °C for 5 h is likely attributed to interdiffusion and may prove challenging to eliminate through paste rheology optimization or alterations in the sintering strategy.
In comparison to ESCs, porosity also emerged at the XDC/8YSZ interfaces without NiO being present in the XDC layer. In ESCs, the 8YSZ layer is fully sintered and dense, while in the FESC concept, the 8YSZ layer is sintered from a paste on top of pre-sintered or (NiO-)XDC green bodies. This might foster better contact between the layers and potentially create diffusion paths.
However, optical investigation suggests that, at least, the investigated sections of the XDC barrier layers between the fuel electrode and the electrolyte are gastight. Furthermore, the 8YSZ electrolyte appears to be gastight, with a closed porosity of 2.9 ± 1.6 %. The air electrode barrier layer and the air electrode exhibit the usual microstructure. Therefore, if layers, exhibiting properties as shown in Section 4.2.5, are to be fabricated, the rheological data provided in Section 4.2.4 may serve as a tool for quality control and reproducibility. HKD2 was shown to be a suitable dispersant for doped ceria.
The reactive sintering of an 8YSZ electrolyte is indeed possible, but achieving nearly full densification requires a sintering temperature of 1400 °C, making it an impractical alternative in FESC manufacturing.
As established in Section 4.1, preventing porosity at the fuel electrode /electrolyte interface is crucial, and interdiffusion is an inevitable factor. In Section 4.2.5, it was observed that no porosity emerged at the NiO-10XDC/XDC interface but at every Ni-10XDC/8YSZ or XDC/8YSZ interface when sintered at 1400 °C. To implement a Ni-doped ceria fuel electrode in a FESC concept, the following manufacturing strategy may be viable: To prevent porosity and interdiffusion at the fuel electrode-electrolyte interface when using a Ni-10XDC fuel electrode, it should be followed by a dense 10XDC layer serving as the main electrolyte. This could be achieved by sintering the Ni-10XDC fuel electrode and XDCBL (now serving as the electrolyte) at sufficiently high temperatures to achieve gas-tightness and (almost) full densification. Some residual porosity might be tolerable, as in the case of the 8YSZ state-of-the-art electrolyte. Optimization of the XDCBL pastes or the sintering strategy may aid in densification.
On top of the XDC electrolyte, a dense and ideally very thin 8YSZ layer needs to be applied to block electron leakage induced by the reduction of ceria during FESC operation. This needs to be followed by a doped ceria air electrode barrier layer to prevent the formation of insulating $SrZrO_{3-\delta}$ at the 8YSZ electrolyte interface during sintering of Sr-containing air electrodes.[71] For this purpose, a small and dense $ZrCeO_{2-\delta}$ mixed phase layer is sufficient [141].

4.2.7 Conclusion

FESCs featuring Ni-10XDC fuel electrodes, both with and without an XDC barrier layer positioned between the fuel electrode and the 8YSZ electrolyte, were successfully fabricated. The screen printing pastes developed for this purpose were evaluated, focusing on their rheological properties such as flow curves, linear viscoelastic regions, and thixotropy. Furthermore, the produced layers exhibited satisfactory microstructural characteristics after sintering, thereby affirming that rheological data can be effectively utilized as a tool for the reproducible production of the fabricated layers.
However, during the manufacturing of FESCs, porosity was observed at the interface between Ni-10XDC and 8YSZ, and this issue persisted despite the implementation of an XDC barrier layer. In contrast, no porosity was evident between Ni-10XDC and 10XDC layers after sintering.
This highlights the importance of incorporating a dense XDC electrolyte when employing a Ni-10XDC fuel electrode in a FESC concept. This strategic choice is crucial for preventing performance degradation resulting from the porosity observed at the fuel electrode /electrolyte interface, as previously demonstrated in ESC experiments.

5 Ni-Exsolution electrode material

This chapter covers the investigation and discussion of $Sr_{1-x}(Ti_{0.3}Fe_{0.7-y}Ni_y)O_{3-\delta}$ as a potential Ni-exsolution fuel electrode material. The exsolution behavior and phase stability of bulk $Sr_{1-x}(Ti_{0.3}Fe_{0.7-y}Ni_y)O_{3-\delta}$ ceramics were analyzed at various temperatures and atmospheres. The tolerance to carbon deposition of $Sr_{1-x}(Ti_{0.3}Fe_{0.7-y}Ni_y)O_{3-\delta}$ was compared with that of commonly used Ni-3YSZ materials in the presence of tar-containing biogas.
This chapter has been published in the *Journal of Materials Chemistry A* [189].

5.1 Motivation and obstacles

Exsolution is defined as the phase separation of a solid solution due to a miscibility gap under specific conditions [46]. In the context of catalysis, exsolution refers to the reduction of metal cations to the metallic state, forming nanosized particles on the surface [47]. This process is initiated by exposing the material to reducing conditions, resulting in the release of oxygen from the host lattice and thus providing the driving force to exsolve certain cations [48]. Perovskite materials are very popular in this field due to the possibility to be doped with various exsolvable cations, since adjusting their crystal structure is undemanding while preserving stability [190].
For electrochemical applications such as SOCs, the general approach is to exsolve a catalytically active metal from its host lattice to achieve enhanced catalytic activity and high resistance to degradation due to the higher surface-to-volume ratio and socketing of the nanoparticles in the host lattice.
State-of-the-art fuel electrode cermets in SOCs, which consist of an oxygen ion conductor (e.g., 8YSZ or 10GDC) and Ni, suffer from significant degradation when exposed to fuels containing higher hydrocarbons and sulfur species [11,68,69]. The Ni surface can be poisoned, leading to a loss of catalytic activity, or carbon deposition can result in metal dusting. Another concern is the migration of Ni, especially during electrolysis [54]. Exsolved and socketed nanoparticles might be more stable against migration and redox cycling compared to Ni particles distributed in an ion conducting ceramic (although they may suffer from Ostwald ripening and agglomeration) [26,52,53]. Redox cycling of exsolved nanoparticles might be an option to self-regenerate degraded catalyst particles [55,56].
In the case of SOCs, a MIEC is doped with a metal that shows activity towards hydrogen oxidation or water splitting. Using a single material instead of a cermet increases the reaction zone as the material forms a DPB with the gas molecules (compared to the active TPB – pores, oxygen ion-conducting phase, electron-conducting phase – in cermets). However, despite possessing a certain catalytic activity, they often cannot match the performance of a typical Ni-containing cermet

[63]. Furthermore, their electronic conductivity may not be sufficient for practical operation [40].
In this context, the properties of the oxide host lattice after exsolution are insufficiently investigated. Since the exsolved nanoparticles are not percolated, their function is very different from that of a percolated Ni network and the electrode performance will strongly depend on the properties of the oxide backbone. The phase stability of the oxide during the exsolution process and its influence on mechanical stability of the perovskite backbone is not well investigated. It is therefore important to understand how the loss of a significant amount of B-site cations influences the physical properties of the oxide.
$Sr_{1-x}(Ti_{0.3}Fe_{0.7-y}Ni_y)O_{3-\delta}$ was selected as a SOC electrode material to investigate its overall phase stability and exsolution behavior, as well as its tolerance to degradation from carbon deposition in tar-containing biogas. To enhance catalytic activity, Ni was added to the B-site to induce exsolution. To potentially address the problem of limiting electronic conductivity, particularly in the case of $Sr(Ti_{1-y}Fe_y)O_{3-\delta}$, the Fe to Ti ratio needs to be high [191,192].
Based on these considerations, we utilized the stoichiometry (STF) and the Ni co-doped stoichiometries $SrTi_{0.3}Fe_{0.63}Ni_{0.07}O_{3-\delta}$ (STFN) and A-site substoichiometric $Sr_{0.95}Ti_{0.3}Fe_{0.63}Ni_{0.07}O_{3-\delta}$ (sSTFN). These were also investigated by, e.g., Zhu et al. [193] and Santaya et al. [194], respectively, reporting promising electrochemical properties.
The focus lies on characterizing the phase formation in STF, STFN and sSTFN and its influence on mechanical stability during reduction in the temperature range of 710 °C to 900 °C. Additionally, the carbon deposition tolerance in tar-containing biogas was compared to a Ni-3YSZ cermet.

5.2 Materials synthesis and characterization

Commercially available powders purchased from Sigma-Aldrich (St. Louis, USA) were used as precursors: $SrCO_3$, TiO_2, Fe_2O_3 and NiO. The purity of the powders was measured by ICP-OES. On average the powders show only minor impurities $< \sim 0.05$ wt% (see Table B.1, Appendix B). Notable is a 2.78 ± 0.15 wt% Si contamination in NiO and a 0.67 ± 0.03 wt% Mn contamination in Fe_2O_3.
STF, STFN and sSTFN were synthesized using the SSR route. STF was employed as a reference to compare the behavior to non Ni-doped material.

Table 5.1: Particle size distributions of the synthesized STF, STFN, and STFN powders.

Material¤	**$d_{10.}$ (µm)¤**	**$d_{50.}$ (µm)¤**	**$d_{90.}$ (µm)¤**
STF¤	0.60¤	1.10¤	3.12¤
STFN¤	0.69¤	1.41¤	5.02¤
sSTFN¤	0.55¤	1.15¤	3.33¤

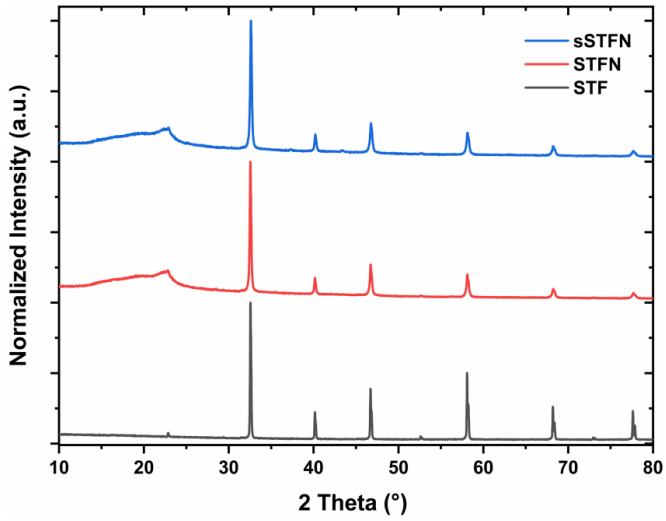

Figure 5.1: Diffractograms of the as prepared STF, STFN, and sSTFN powders.

The precursors were mixed, and ball milled in ethanol with 3 mm zirconia milling balls in a weight ratio of 1:1:1 for 24 h. The powders were dried at 80 °C for 24 h and subsequently calcined at 1200 °C for 8 h. After one calcination step, the powders contained some secondary phases identical to the precursor materials. Since the resulting powders were not phase pure, they were ball milled again for 24 h. A second calcination step at 1300 °C for 8 h was performed, resulting in a monomodal particle size distribution (see Table 5.1).

After the second ball milling and calcination step, STF and STFN powders were phase pure and showed no additional reflections according to XRD (see Figure 5.1). For sSTFN minor reflections are present indicating NiO. Broad reflections around ~12.5-20.0° are due to adhesive tape used for sample preparation.
The stoichiometry and purity of the synthesized powders were investigated by ICP-OES. The nominal stoichiometries according to ICP-OES are given in Table 5.2. The synthesized powders showed some minor impurities (Si, Co, Mn and main group II elements), most likely due to impurities in the precursor materials.
The synthesized and ball milled STF powder (as prepared) consists of square shaped, sharp-edged particles. Furthermore, some relatively small primary particles $<$ 50-100 nm are present (see Figure 5.2).
The as prepared STFN and sSTFN powders exhibit a more rounded shape compared to STF. Particle size distribution is comparable to STF (see Table 5.1). Similar to STF, some small primary particles are visible. Additionally, if Ni is present in the perovskite some lichen-like, melted-looking phases form on the facet of the particles

Table 5.2: Stoichiometries of the synthesized powders according to ICP-OES measurements.

Material	Sr (mol%)		Ti (mol%)		Fe (mol%)		Ni (mol%)		Impurities (mol%)
	Target value	Actual value	Target value	Actual value	Target value	Actual value	Target value	Actual value	
STF	50.0	50.5 ± 1.5	15.0	14.9 ± 0.3	35.0	34.0 ± 0.9	/	/	~ 0.6
STFN	50.0	50.4 ± 1.3	15.0	15.1 ± 0.4	31.5	30.7 ± 0.9	3.5	3.3 ± 0.2	~ 0.5
sSTFN	48.7	49.1 ± 1.4	15.4	15.4 ± 0.4	32.3	31.6 ± 1.1	3.6	3.4 ± 0.1	~ 0.5

and at the grain boundaries (see Figure 5.2(d); additional SEM micrographs are shown in Figure B.1, Appendix B). These lichen-like structures show similar material contrast to the bulk in BE micrographs (see Figure B.1(b), Appendix B).
Some minor grains are observed which do not seem to belong to the perovskite phase. These grains probably belong to leftovers of unreacted NiO precursors since these particles do not exsolve nanoparticles upon reduction and due to the indication of NiO reflections for as prepared sSTFN.

5.3 Microstructure and exsolution analysis

The microstructure and exsolution behavior of the three materials was analyzed by SEM and EDS. Powder samples were investigated in their as prepared (ap), reduced (red) and reoxidized (reox) states. The reduction process was carried out at 900 °C in 50 % Ar/ 50 % H_2 atmosphere for 8 h. Reoxidation was performed at 900 °C in ambient air. Additionally, polished cross-sections of pellets reduced at 900 °C were investigated. To investigate the carbon degradation behavior, the microstructure of polished cross-sections of pellets reduced at 710 °C for 3 h in 100 % H_2 and exposed to tar-containing biogas were analyzed (see Section 5.6). Furthermore, cross-sections of these pellets reduced at 710 °C were investigated in terms of their exsolution behavior.
The SEM micrographs of powder samples reduced and reoxidized at 900 °C are shown in Figure 5.2. Initially, it was intended to use pellets pre-reduced at 900 °C for carbon degradation experiments. The pre-reduced pellets fractured overnight and during transport after being exposed to ambient air (further discussed in Section 5.6). Cross-sections of pieces of these fractured pellets were investigated (see Figure 5.3). Therefore, pellets were reduced in situ at 710 °C (maximum temperature of the test rig), where they remained stable. After carbon degradation experiments, cross-sections of these pellets were examined (for an example of STFN, see Figure 5.4). Due to material instabilities, low accelerating voltages had to be chosen, which resulted in low signal-to-noise ratios. In addition, lower accelerating voltages improve

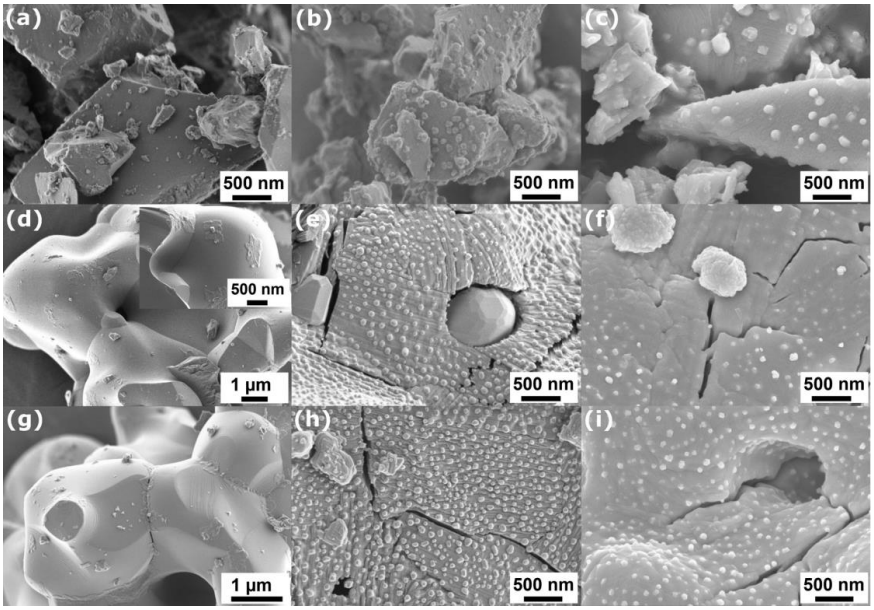

Figure 5.2: SEM micrographs of STF, STFN, and sSTFN in (a, d, g) as prepared, (b, e, h) reduced at 900 °C in 50 % Ar/ 50 % H_2, and (c, f, i) reoxidized state.

lateral resolution. Therefore, the accelerating voltage was adapted according to the samples' properties and desired resolution. In case the accelerating voltage was insufficient to resolve the respective spectral line, the signals were omitted from the analysis.

STF powder forms Fe nanoparticles with a diameter of ~50-130 nm upon reduction at 900 °C. They seem to be randomly distributed on the facets of the grains. The number of particles tends to decrease after reoxidation. A fraction of the particles remains stable but some agglomerate. In contrast to XRD analysis, nanoparticles are still present after reoxidation. (The fraction might just be too low to be resolved with XRD). During reduction and reoxidation, parts of the grains start to form small cracks in investigated powder.

SEM and EDS analyses of cross-sections (of a fractured pellet) reduced at 900 °C show severe crack formation in the structure (see Figure 5.3). It is visible that exsolution is not just limited to the surface, but also bulk exsolution takes place. Furthermore, some larger Fe particles are present. There seem to be spots where the number of nanoparticles increase (as in STFN) but this needs more detailed investigation.

A pellet reduced at 710 °C shows no cracks (see Figure B.2, Appendix B). It is not clear whether Fe nanoparticles exsolve at 710 °C since the as prepared material contains small primary particles. Exsolution takes place sporadically at best.

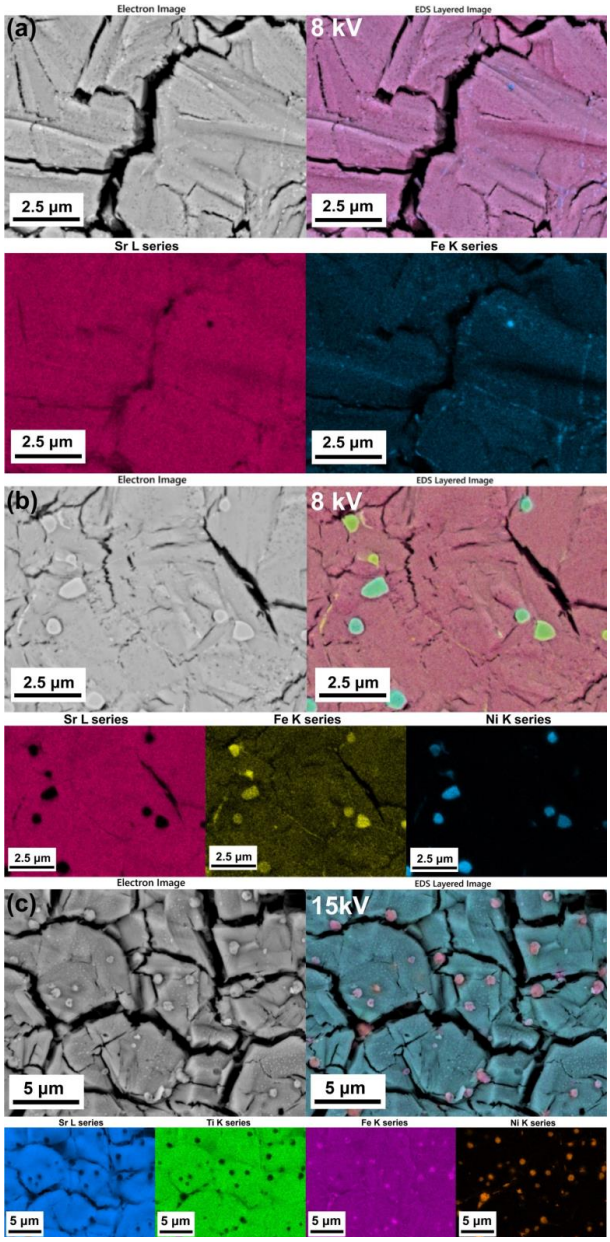

Figure 5.3: Cross-sections of (a) STF reduced at 900 °C in 50 % Ar/ 50 % H_2, (b) STFN reduced at 900 °C in 50 % Ar/ 50 % H_2, and (c) STFN reduced at 900 °C in 50 % Ar/ 50 % H_2 and reoxidized at 900 °C in air, analyzed with EDS.

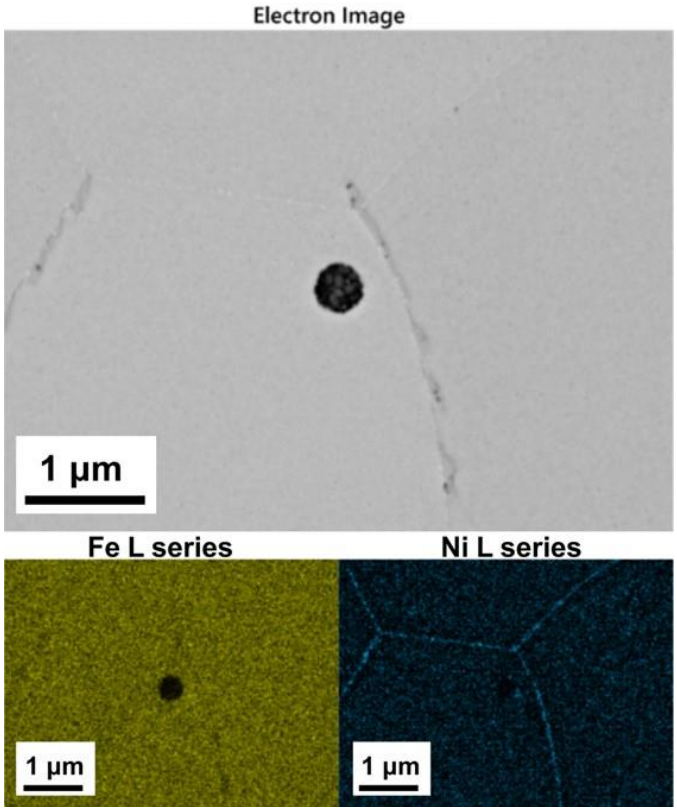

Figure 5.4: EDS analysis of a cross-section of STFN reduced at 710 °C in 100 % H_2. (Black spot belongs to a pore.)

STFN powder forms NiFe nanoparticles with a diameter of ~30-130 nm upon reduction at 900 °C. They uniformly cover the whole area of the grains. Exceptions are the unreacted NiO precursor particles which do not exsolve nanoparticles (see Figure 5.2(e)). Additionally, the average size of the nanoparticles in STFN appears to be smaller when compared to STF. After reduction, the material forms cracks similar to STF at 900 °C. The lichen-like phases on the surface vanish.
The material cracks further during reoxidation. The nanoparticles partially agglomerate, resulting in the formation of larger particles with a diameter of up to approximately 850 nm (see Figure 5.2(f)). In the vicinity of the agglomerated particles, the surface shows a depletion of nanoparticles.
Cross-sections of a fractured STFN pellet reduced at 900 °C show bulk exsolution (see Figure 5.3(b)). For better visibility of the nanoparticles, BE micrographs with a higher magnification are shown in the Appendix B, Figure B.3. The structure

shows prominent cracking after reduction and reoxidation. The reason why the cross-sections of the pellets reduced at 900 °C are not flat and look aged will be discussed in Section 5.6.
Powder and pellets reduced or reduced and reoxidized at 900 °C exhibit larger particles (~500-1500 nm). These particles primarily consist of an NiFe alloy, while some of the larger particles solely consist of Ni (see Figure 5.3(c)).
EDS mapping of the cross-section of a pellet reduced at 710 °C reveals that Ni nanoparticles nucleate at the grain boundaries (see Figure 5.4). It is not clear if Ni also segregates at grain boundaries of the as prepared material or if this accumulation is solely due to exsolution. Compared to pellets or powder reduced at 900 °C no or just some minor cracks between the grains form after reduction and reoxidation.
sSTFN powder and pellets behave similarly after reduction and reoxidation compared to STFN (see Figure 5.2(g-i)).
EDS analysis of a cross-section of the pellet reduced at 900 °C reveals bulk exsolution (see Figure B.4, Appendix B). Similarly, the pellet reduced at 710 °C shows preferable nucleation of Ni at the grain boundaries (see Figure B.5, Appendix B).
All materials exhibit a notable increase in crack formation and Fe exsolution when reduced at 900 °C which is not observable after reduction at 710 °C.

5.4 Thermogravimetric analysis

The thermal decomposition behavior of the materials was investigated by TGA in air and Ar/ 3 % H_2. Redox cycling experiments were performed at 900 °C. The samples were initially heated up in air with a heating rate of 5 °C/min. The samples were kept at 900 °C for 4 h to remove organics and reach an equilibrium state. The respective mass plateau was defined as a relative mass of 100 %. Afterwards, the samples were reduced in Ar/ 3 % H_2 for 12 h. This cycle was repeated three times to study the redox behavior of the materials.
Additionally, the materials were reduced in Ar/ 3 % H_2 at temperatures of 710 °C for 3 h and 900 °C for 30 h. The samples reduced at 710 °C have been reoxidized and cooled down slowly. Beforehand, the samples were reduced and reoxidized for 3 h each to remove organic impurities.

The results of the cycling experiments are shown in Figure 5.5(a). As can be seen in Figure 5.5(a), some loss of mass typically occurs during the first heating ramp, which is likely due to the evaporation of contaminations like humidity or carbonate species, and the loss of oxygen during heating. In order to unambiguously correlate mass loss to oxygen loss in the isothermal measurements, samples were exposed to cycling experiments, where the materials were reduced for 12 h in Ar/ 3 % H_2 followed by reoxidation for 4 h in air, repeated three times consecutively. The reversible mass loss in Ar/ 3 % H_2 and mass gain in air is clearly due to reduction and oxidation, therefore the reversible mass loss in the TGA experiments can be clearly assigned to oxygen loss.

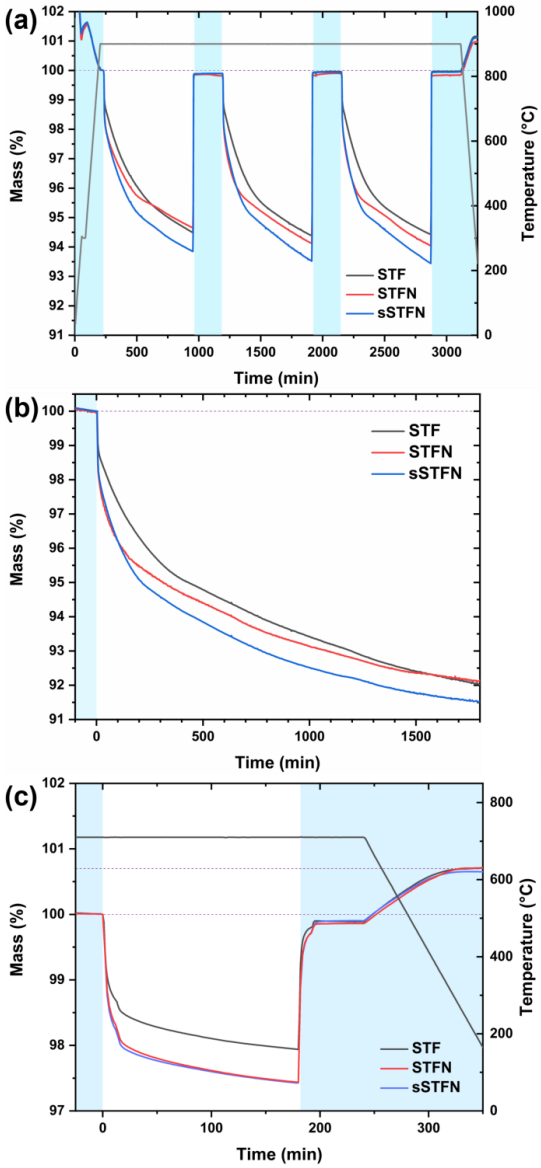

Figure 5.5: TGA analysis of STF, STFN, and sSTFN. Blue regions represent air atmosphere, while white regions represent Ar/ 3 % H_2 atmosphere. (a) Cycling experiments conducted at 900 °C, during which the materials underwent a reduction phase for 12 h followed by a subsequent reoxidation period for 4 h. This cyclic process was repeated three times. (b) Reduction of the materials at 900 °C for 30 h. (c) Reduction of the materials at 710 °C for 3 h, followed by 1 h of reoxidation and subsequent cooling down to room temperature (25°C).

At a reduction temperature of 900 °C, none of the materials reach an equilibrium oxygen non-stoichiometry δ after 12 h. At the beginning of the reduction, an abrupt initial mass loss in the first ~5-10 min is observable, followed by a constant but more moderate mass loss. The initial mass loss is ~1.2 % for STF, ~1.6 % for STFN and ~1.7 % for sSTFN. After 12 h reduction, STFN exhibits a higher mass loss compared to STF (~0.3 %) while sSTFN loses about 0.6 % more mass than STF. After reoxidation, the materials tend to reach their initial mass again.
Since an equilibrium was not reached after 12 h at 900 °C in the cycling experiments, the materials were further reduced for 30 h at 900 °C in Ar/ 3 % H_2 (see Figure 5.5(b)). Again, an abrupt initial mass loss occurred, but even after 30 h, no equilibrium was reached at 900 °C. Initially, STFN exhibited a faster mass loss compared to STF, but both materials ended up with a mass loss of approximately 8 % after 30 h of reduction. sSTFN experienced a mass loss of around 8.5 % after 30 h of reduction. The initial mass loss (pre-reduction) is assumed to be due to the reduction and oxygen release of the materials without metal exsolution. The subsequent constant mass loss, which is likely kinetically limited compared to the materials' pre-reduction, is attributed to further oxygen release accompanied by metal exsolution. The exsolution process is initiated after a critical amount of oxygen is released from the lattice, resulting in the reduction of the cations [48]. The results indicate that the materials constantly release oxygen and potentially exsolve nanoparticles while not reaching an equilibrium at 900 °C after 30 h of reduction.
When the materials are reduced at 710 °C for 3 h (see Figure 5.5(c)), the initial abrupt mass loss was still observed and is comparable to the reduction at 900 °C. The subsequent mass loss is significantly lower compared to reduction of the materials at 900 °C (approximately 2.5% for STFN and sSTFN and 2.1% for STF). The samples tend to almost reach an equilibrium at 710 °C but due to the short reduction time the mass loss did not fully equilibrate.The initial oxygen release provides the driving force (critical oxygen deficiency) for the exsolution of metallic cations [195]. However, the equilibrium of the oxygen release accompanied by exsolution is likely temperature-dependent.
In the upcoming Section 5.5, data that reveal a phase transition if the materials are reduced above a critical temperature will be provided. We occasionally observe drifts in the mass signal during the experiments, such as mass gain after reduction and during exsolution. Currently, we attribute these drifts to measurement artifacts like buoyancy or an unsteady gas atmosphere.
The equilibrium oxygen non-stoichiometry δ of the materials was determined based on the observed mass plateaus. To calculate δ, the thermodynamic model of Wagner [196] was employed, which was adapted by Nenning et al. [197]. Therefore, some assumptions were made to calculate δ. The differential $\frac{\partial \delta}{\partial \log (pO_2)}$ is minimized when the respective cations are present in their oxidation states of Sr^{2+}, Ti^{4+} and Fe^{3+}. The minimized value corresponds to the measured mass plateaus or an equilibrium oxygen stoichiometry under the given measurement conditions. In our case, this leads to a δ of 0.350, 0.455 and 0.505 for STF, STFN and sSTFN, respectively. That

Table 5.3: Calculated oxygen non-stoichiometries 3-δ of reduced and reoxidized (710 °C and 25 °C in air) STF, STFN, and sSTFN.

Material	Reduced 3-δ (710 °C)	Oxidized 3-δ (710 °C)	Oxidized 3-δ (25 °C)
STF	2.650	2.872	2.965
STFN	2.545	2.821	2.918
sSTFN	2.495	2.768	2.852

the cations Sr and Fe in fact prefer the above-mentioned oxidation states was confirmed by Mössbauer spectroscopy [198,199]. Although we were not able to obtain $p(O_2)$-values during our measurements, it can be assumed that $\frac{\partial \delta}{\partial \log (pO_2)}$ is sufficiently $p(O_2)$-independent at 710 °C [200,201]. According to these assumptions, we calculated the oxygen stoichiometries for the samples in equilibrium in air at 710 °C and after cooling down in air (see Table 5.3). To calculate the δ-values for the Ni-doped compositions STFN and sSTFN, we assume that Ni is fully exsolved at the equilibrium state under low $p(O_2)$ (which is not the case according to XRD analysis presented in Section 5.5 and indicated by EDS analysis in Figure 5.4).
In its fully oxidized state, Fe is conventionally presumed to be present as Fe^{4+}. However, due to suboptimal cooling conditions, the average oxidation state of Fe might diverge from Fe^{4+}.

5.5 Redox and exsolution stability

The phase stability during reduction was investigated using XRD analysis. Powders were reduced at temperatures of 710-900 °C in 50 % Ar/ 50 % H_2 atmosphere for 8 h. A subset of the samples reduced at 900 °C was subsequently reoxidized at 900 °C for 8 h in ambient air to assess their redox stability. The phase composition was analyzed using a polynomial fit to determine the position of the diffraction lines and a subsequent Rietveld refinement method. During certain reduction experiments, Ruddlesden-Popper (RP) phases were formed. Since the exact stoichiometries of the RP-phases are unknown due to broad reflections and material instabilities in ambient air, the stoichiometries were assumed to be $Sr_4Ti_3O_{10}$, Sr_2TiO_4 (ST-RP) and $Sr_3Fe_2O_6$ (SF-RP) for the purpose of Rietveld refinement to estimate the quantities of the original perovskite, the formed RP-, and nanoparticle phases.
For analysis of the secondary phase formation, upon exposing the materials to ambient air or H_2O, pieces of pellets that fragmented were used for the XRD analysis. These pellets were prepared analogously to the pellets prepared for carbon degradation experiments (see Section 5.6) but reduced at 900 °C in 50 % Ar/ 50 % H_2 atmosphere.

The diffractograms are shown in Figure 5.6(a, c, e). The calculated relative phase distributions, according to Rietveld refinement, are shown in Figure 5.6(b, d, f). The exact values are shown in Table B.2, Appendix B. Upon reduction, all materials

exhibited broadening and a shift towards lower 2Θ angles of the perovskite reflections, indicating increased lattice disorder and chemical expansion, respectively, due to the release of oxygen from the lattice. At a temperature of 780 °C, the emergence of metallic NiFe reflections was observed for STF and STFN, indicating the process of exsolution. In the case of sSTFN, metallic NiFe reflections were observable starting at 710 °C. Since Ni and Fe reflections share similar 2Θ angles and the corresponding peaks in this analysis are broadened, presumably due to the exsolution of either Ni, Fe, or their alloys in different compositions, the fraction of metallic reflections was summed up for the purpose of the analysis [202,203]. The amount of exsolved nanoparticles is higher for sSTFN. In SEM micrographs of pellets used for carbon degradation experiments, the exsolution of nanoparticles is visible starting at 710 °C for STFN and sSTFN (see Figure 5.4). For STF exsolution appears at best sporadically at 710 °C. Due to the detection limit of XRD being approximately 1-2 vol%, the method is not suited to resolve the nanoparticle fraction at reduction temperatures below 780 °C. For sSTFN the exsolution process is even detectable at 710 °C with XRD, indicating that exsolution is thermodynamically favored compared to the stoichiometric material. The nanoparticle reflections shift with rising temperature, presumably due to the higher iron content in the NiFe nanoparticle alloys. These reflections become more prominent with rising temperature. Furthermore, with rising temperature the perovskite reflections broaden, and at 780 °C, reflections related to a RP phase appear for STFN and sSTFN. In the case of STF, a sudden transition to the RP phase at a higher temperature of 860 °C occurs, coupled with a rapid increase in Fe nanoparticle exsolution. The slower exsolution response observed in STF, compared to STFN and sSTFN, suggests that the RP-phase transition occurs after a certain amount of oxygen release and cation exsolution has taken place. For all materials the RP-reflection is split up again at 860 °C, indicating the formation of two RP-phases. Interestingly, at 900 °C the amounts of RP-phases and nanoparticles decrease. As the measurements were not conducted in situ but rather with similar but separate samples of the same material sintered at different temperatures sequentially, it is possible that the observed effect could be related to the samples themselves. Since samples of the three different stoichiometries were sintered together at the respective temperatures in the same furnace, it is conceivable that issues related to furnace temperature gradients or the Ar/H_2 gas atmosphere heterogeneities may have arisen. This issue will require further investigation. In general, a temperature dependency of the exsolution behavior and the phase transition is evident.
The samples reduced at 900 °C were subsequently reoxidized. After reoxidation STFN and sSTFN transition back to the perovskite phase, although parts of the exsolved nanoparticles remain on the surface and form oxides. According to XRD the exsolved fractions decrease after reoxidation. For STF, small amounts of a strontium ferrite perovskite phase $SrFe_{12}O_{19}$ (SF-P) form, but most of the material transitions back to the original perovskite phase, while no metal oxide fraction is

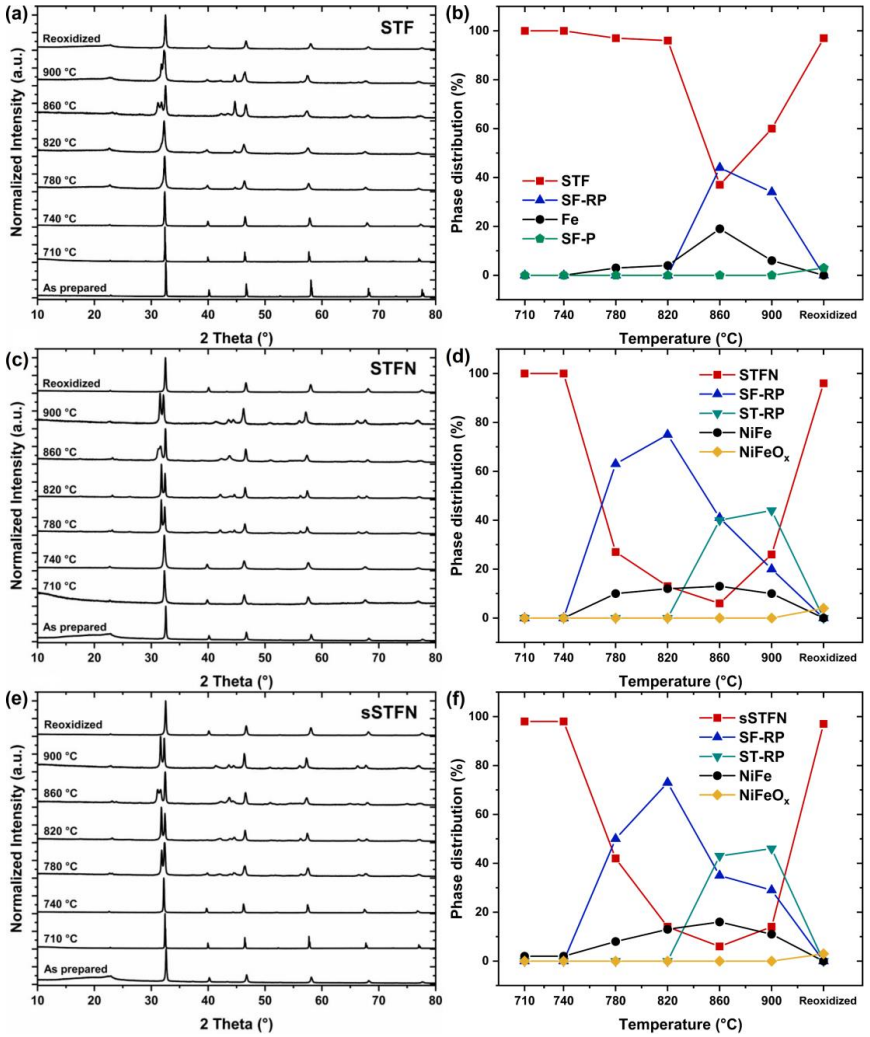

Figure 5.6: Diffractograms and relative phase distribution of (a, b) STF, (c, d) STFN, and (e, f) sSTFN in their as prepared, reduced (at 710-900 °C in 50 % Ar/ 50 % H_2), and reoxidized (at 900 °C for 8 h in air) states.

detectable. This indicates a partial reintroduction of the exsoluted metals back into the perovskite lattice.
It should be noted that, due to the broad nature of the reflections, the assignment of the phases for the purpose of Rietveld refinement is not distinct. Therefore, the calculated relative phase distributions indicate a broader trend.

5.6 Mechanical and moisture stability

Upon reduction at 900 °C, all materials form cracks in the grains. Furthermore, pellets that were reduced at 900 °C fractured and completely disintegrated during prolonged exposure to ambient air (4 weeks) or immersion in H_2O (24 h). Pellets reduced at 710 °C maintained mechanical stability. Diffractograms for sSTFN samples recently reduced, after four weeks of storage in ambient air, and after 24 h exposure to H_2O are shown in Figure 5.7. Samples stored in ambient air or immersed in H_2O show broadened reflections. Additionally, some new minor reflections appear. The diffractograms indicate the formation of strontium hydroxides and iron(oxide)hydroxides. However, due to the broadened reflections, the precise determination of the emerging side phases by XRD alone is not feasible. After embedding, grinding (using water as a coolant), and polishing, the prepared cross-sections exhibit signs of aging, displaying an irregular and non-flat surface, revealed in the subsequent SEM analyses (see Figure 5.3, additionally SE micrographs with topographic information are shown in Figure B.6, Appendix B). This further

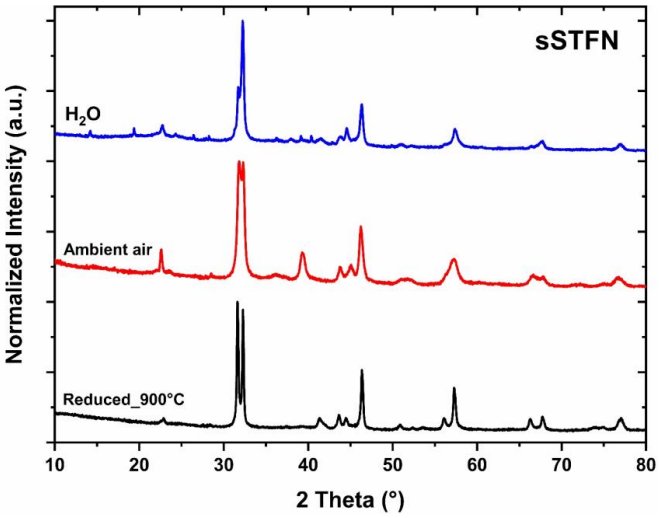

Figure 5.7: Diffractograms of sSTFN recently reduced (at 900 °C in 50 % Ar/ 50 % H_2), reduced and stored in ambient air for 4 weeks, or immersed into H_2O.

indicates that the materials are not stable in atmospheric conditions or moisture/ contact with H_2O. These phenomena are not observed for pellets reduced at 710 °C, suggesting that the mechanical instabilities are triggered by pronounced metal exsolution, the accompanied phase transitions, and potential secondary phase formation within the materials.

5.7 Carbon degradation experiments and Raman analysis

For carbon degradation experiments, the materials were pressed into pellets with 10 wt% starch and a drop of glycerine as a binder. An uniaxial press was used to apply a pressure of 60 MPa for 120 s, resulting in pellets with a diameter of 25 mm. The pellets were sintered at 1300 °C for 4 h, yielding samples with a diameter of ~20 mm. The heating rate was initially set to 2 °C/min up to 500 °C to remove the binder. Subsequently, the heating rate was increased to 5 °C/min.
The porosity of the pellets was investigated using the Archimedes' principle and by image analysis of cross-sections.
The carbon degradation behavior was investigated in a self-built tube reactor invented by the Chair of Energy Systems, TUM. The samples were placed on a Ni-mesh on top of a heated double tube. The gas flow originates from the bottom of the outer tube, flows through the sample, and leaves the reactor through the inner tube. The gas composition is controlled by mass flow controllers (EL-Flow Prestige, Bronkhorst Deutschland GmbH). For the H_2O fraction a liquid flow controller (Liqui-Flow, Bronkhorst Deutschland GmbH) was used, since it is vaporized shortly before mixing with the other components.
The pellets were reduced in situ at 710 °C (the maximum temperature reached by the test rig at that time) for 3 h in 100 % H_2 atmosphere, since pellets pre-reduced at 900 °C fragmented during transport. 18 g/Nm^3 of toluene as a model tar was used to assess the degradation behavior of the materials. The tar was dosed to an artificial bio-syngas for 3 h. The artificial biogas contained 25 vol% H_2/ 10 vol% CO_2/ 10 vol% CO/ 5 vol% CH_4/ 50 vol% H_2O. This gas composition was chosen since carbon degradation of the Ni-3YSZ material is expected, as shown in the subsequent paragraph. Between changing the gas atmospheres, the sample chamber was purged with N_2.
After carbon degradation experiments, Raman analysis was conducted on all materials. Several point measurements were performed. Data was collected in a wavenumber range of ~70-800 cm^{-1} and ~1260-2300 cm^{-1}.

The fabricated pellets possess a porosity of approximately 25-28 vol%, which is comparable to the reference Ni-3YSZ substrate material.
For the reference Ni-3YSZ substrate material, severe degradation in terms of carbon deposition and Ni-dusting was observed. The whole sample decomposed and turned black. Figure 5.8(d) shows a SEM micrograph of the carbon-degraded sample. The

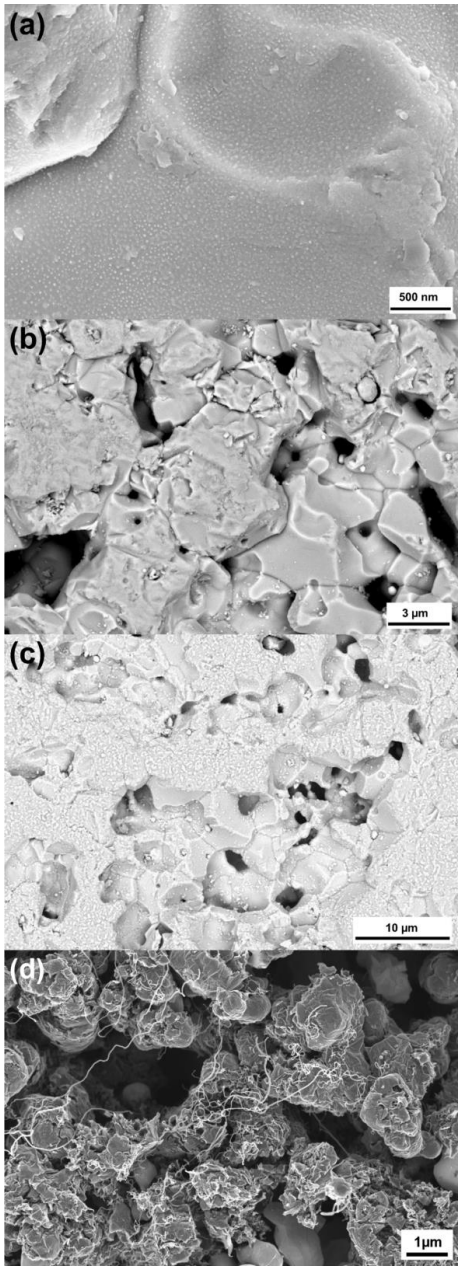

Figure 5.8: SEM micrographs of (a, b) reduced (710 °C), (c) reoxidized STFN, and (d) 8YSZ after carbon degradation experiments. (a, d) show secondary and (b, c) show backscattered electron micrographs.

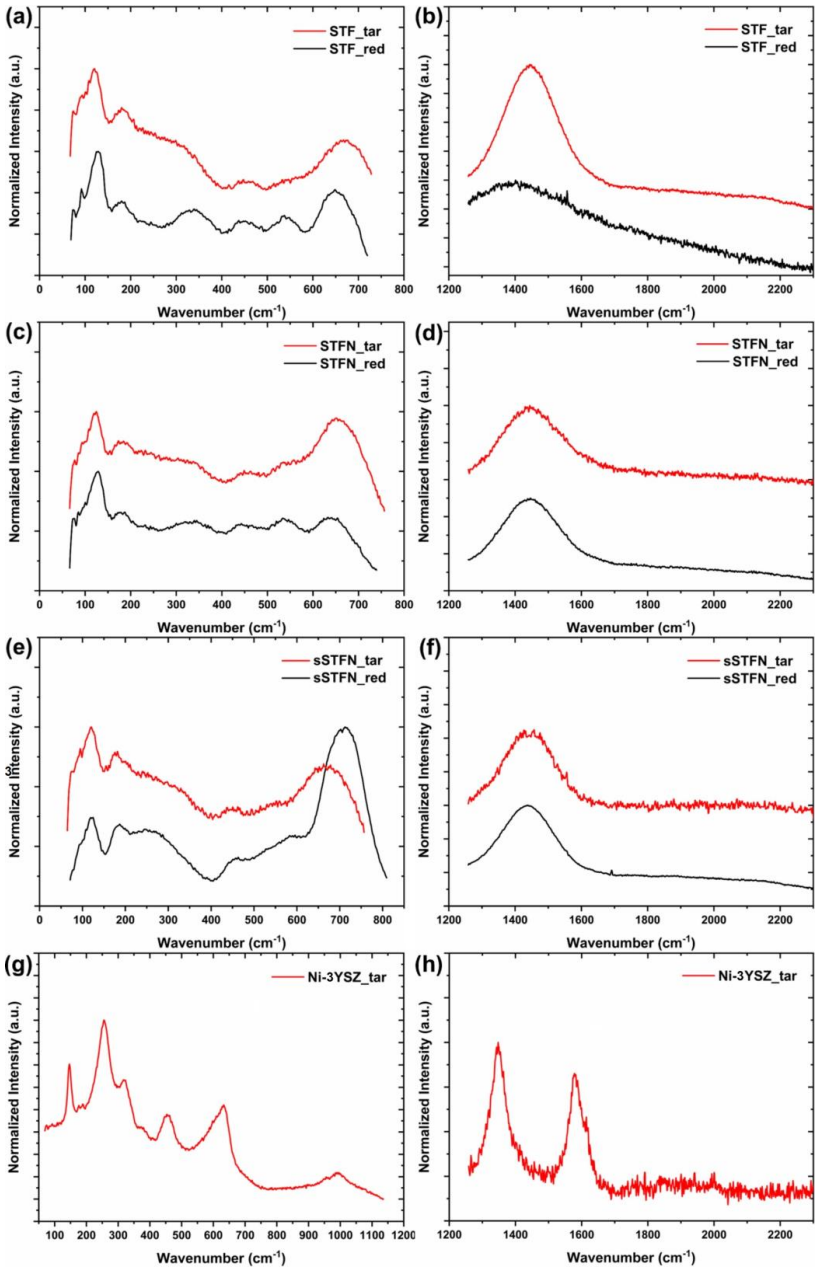

Figure 5.9: Raman spectra of (a, b) STF, (c, d) STFN, (e, f) sSTFN, and (g, h) Ni-3YSZ in reduced state (red) and after carbon degradation experiments (tar).

Ni-grains show carbon deposition in the form of fibers which disintegrate the microstructure. Raman measurements confirmed carbon in the structure due to the presence of the amorphous and graphitic carbon D' and G' band signals at ~1350 cm^{-1} and ~1580 cm^{-1} (see Figure 5.9(h)) [119,204].
In contrast to Ni-3YSZ, STF as well as STFN and sSTFN show no signs of carbon-related degradation or Ni-dusting either in the bulk or the nanoparticles. SEM micrographs show the clean material surfaces without any presence of carbon deposition (see Figure 5.8(a-b)). Raman spectra taken at different spots of the samples confirm the absence of carbon D' and G' band signals. It should be noted that potentially formed carbon species on the materials might have decomposed during cooling.
Moreover, Raman data is provided for the reduced materials stoichiometries, up to a wavenumber of 2300 cm^{-1} (see Figure 5.9(a-f)). The detection of vibrational modes for the materials provides evidence that they deviate from the ideal cubic perovskite structure [205]. Metallic Ni exhibits no allowed Raman mode. Peak broadening may be attributed to the presence of cationic defects and oxygen vacancies. Defects might not be distributed homogeneously throughout the sampling area. The signals in the range of 200-400 cm^{-1} and 550-800 cm^{-1} are related to Ti-O bonds. Signals around 200, 300, 600 and 700 cm^{-1} are related to Fe-O bonds, but they partly overlap with the Ti-O signals [199,206–208].
All materials exhibit a broad signal around 1440 cm^{-1} which could be related to two magnon scattering (observed in $SrFeO_{3-\delta}$ at ~1350-1400 cm^{-1}) [199]. The obtained spectra exhibit a low signal-to-noise ratio, likely attributed to a certain roughness of the surfaces of the investigated pellets. Furthermore, some signals shift slightly, likely induced by locally varying chemical configurations due to different sampling spots.
Following carbon degradation experiments, transformations of the materials' surfaces were observed that were in contact with Ni. In the tube reactor, Ni meshes are commonly used for sample placement, given the presence of Ni in common electrode materials or substrates for SOCs. The surfaces of all materials that are in direct contact with the Ni-mesh forms a melted-looking layer after degradation experiments. This layer still consists mainly of the bulk perovskite (see Figure B.7, Appendix B). After reoxidation, this layer shrinks and forms islands (see Figure 5.8(c)).

5.8 Conductivity

The ohmic resistances of the materials have been estimated using EIS. The high-frequency intercept was evaluated to estimate the total ohmic resistance of the sample. Compacted samples were used, similar to the ones used for degradation experiments (see Section 5.7). Impedance measurements were conducted in Ar/ 3 % H_2 at temperatures between 600–900 °C. A Pt-layer was applied on top and

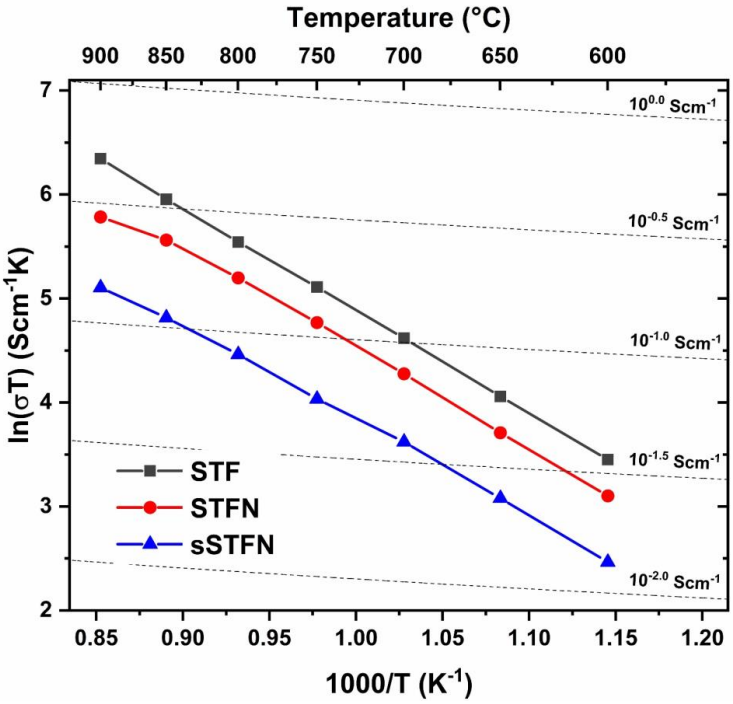

Figure 5.10: Arrhenius plot of the specific conductivities for STF, STFN, and sSTFN, measured at temperatures of 600-900 °C in Ar/ 3 % H_2.

bottom of the pellets to improve contacting between the samples and the Pt-mesh electrodes of the potentiostat.
STF shows the highest overall conductivity, followed by STFN and sSTFN (see Figure 5.10). The higher iron content of STF seems to have a higher impact on the total conductivity compared to further doping with Ni and exsolved NiFe nanoparticles. The obtained values are in the same order of magnitude compared to literature [40–42], although the samples exhibit a certain porosity (~25 %).

5.9 Discussion

As the materials were examined as potential candidates for SOC electrodes (or other suitable electrochemical devices) to be used in practical applications, the discussion will primarily focus on the results in this context. When considering a material for a SOC electrode, certain requirements need to be met, with cost aspects being neglected for the time being. These requirements include: i) Sufficient electrical and ionic conductivity, ii) sufficient catalytic activity, iii) low degradation and carbon

deposition tolerance and iv) electrochemical, chemical and mechanical stability during fabrication and operation conditions.
The suitability of STFN and sSTFN as SOC electrode materials will be discussed in the following. In this study, it is mainly focused on carbon deposition tolerance and stability-related aspects.
Data for electrochemical evaluation have been reported elsewhere [193,194].
Synthesis of a relative phase pure STF, STFN and sSTFN is rather uncomplicated if the precursors are milled down to similar particle sizes and if a calcination temperature of at least 1200 °C is employed. Impurities and secondary phases are below the detection limit of XRD. Some secondary phases and left-over precursors (primarily NiO) are present, potentially due to the solubility limit of Ni. For $SrTiO_{3-\delta}$, the suggested solubility limit is about 5 atom% [209]. Minor impurities of NiO are unlikely to significantly impact the electrochemical performance. It has been demonstrated that lower calcination temperatures (<1100 °C) can lead to the formation of Ni-perovskite secondary phases and RP-phases in Ni-doped $SrTiO_{3-\delta}$ [210].
Interestingly, the SEM analysis indicates that Ni(O) has an influence on the sintering/calcination behavior and potentially induces the formation of a transient liquid phase with the perovskite. This assumption is based on the presence of the lichen-like structures on the grains of Ni-doped STF after calcination, resembling melted material that solidified upon cooling. Additionally, similar melted-like structures were observed on pellets that were in contact with a Ni-mesh during carbon degradation experiments. The presence of Ni(O) is known to serve as a sintering aid and enhance cation diffusion in perovskite materials, as observed in compounds like $Ba(Zr,Ce,Y)O_{3-\delta}$ [180–182]. This behavior has also been documented in fluorite-type materials such as yttria-stabilized zirconia [176] or gadolinia-doped ceria [118,142,178,179].
After an initial pre-reduction of the materials, exsolution takes place in reducing conditions starting at 710 °C (for Fe-exsolution in STF probably later around 740-780 °C). At 710 °C the oxygen release and exsolution of metals tend to reach an equilibrium. Reduction at 900 °C leads to an increase in exsolved nanoparticles while no equilibrium is reached within 30 h of reduction, indicating continuous oxygen release and possibly exsolution beyond this point. The exsolution process is triggered by the oxygen loss of the host material. Therefore, after a certain pre-reduction, exsolution begins. It is expected that a higher degree of oxygen non-stoichiometry and faster oxygen release kinetics will enhance the amount of exsolved nanoparticles [195].
The exsolution of Ni (and probably Fe) in STFN is thermodynamically favored in comparison to Fe exsolution in STF. Furthermore, the exsolved Fe nanoparticles in STF are fewer by number and larger on average compared to NiFe nanoparticles exsolved in STFN and sSTFN. The doping with Ni reduces the onset temperature for Fe-reduction [211]. The Sr-substoichiometry further enhances the amount of released oxygen and favors metal exsolution. Due to the high nanoparticle coverage

observed on both STFN and sSTFN (particularly after reduction at 900 °C), it is reasonable to assume a certain level of catalytic activity.
All materials undergo a phase transition from the perovskite to a RP-phase when the reduction temperature exceeds about 820-860 °C for STF and 740-780 °C for STFN and sSTFN. This phase transition is accompanied or induced by an increase in exsolved nanoparticles. The calculated relative phase distributions indicate that sSTFN is slightly more stable compared to STFN since the formed amounts of RP-phases is lower, while the nanoparticle fraction is even larger. Notably, the investigated pellets reduced at 710 °C, which exhibit preferential Ni exsolution for STFN and sSTFN, do not undergo a phase transition. This suggests that the RP-phase transition may be triggered by the exsolution of a critical amount of Fe. Furthermore, the transition of STF to the RP-phase is accompanied by a sharp increase in the content of Fe-nanoparticles.
The conductivities of the synthesized materials are in the same order of magnitude compared to literature (see Section 5.8). Although the conductivity is improved by a high Fe-content in the perovskite, it still might be insufficient since the common $La_{0.6}Sr_{0.4}Co_{0.2}Fe_{0.8}O_{3-\delta}$ SOC air electrode material exhibits approximately two orders of magnitude higher conductivity [192]. Therefore, further doping may be required where Co might be a suitable candidate [212].
Regarding the carbon degradation tolerance in tar-containing biogas, the materials show promising properties. In fact, none of the materials exhibit any degradation under the same experimental conditions, in contrast to a common Ni-3YSZ cermet. The improved degradation tolerance is probably related to socketing of the nanoparticle and a strong host-particle interaction [26]. These factors hinder the tip-growth mechanism of carbon, wherein carbon dissolves into the Ni-lattice and grows at the Ni-oxide interface, thereby suppressing carbon deposition [25].
Regarding all the above discussed properties STFN and sSTFN might be suitable SOC electrode materials.
One of the major challenges associated with STFN and sSTFN as metal exsolution electrodes, both in practical SOC applications and potentially in other fields of use, is their chemical and mechanical stability. At a certain degree of oxygen non-stoichiometry and accompanied metal exsolution the perovskite transitions to RP-phases. These phase transitions are temperature-dependent and initiated at temperatures around 740-780 °C for STFN and sSTFN (and 860 °C for STF). Importantly, these temperatures fall within the range of typical application temperatures for SOC materials. The Sr-substoichiometric sSTFN seems to be slightly more stable compared to STFN, indicating that the initial A-site deficiency stabilizes the host during exsolution of B-site cations. The phase transition might not be a hinderance in terms of conductivity [36].
The essential problem is the mechanical stability of compacted or sintered structures. The processed pellets were not mechanically stable in a sense that they fragmented after reduction at 900 °C, despite having a porosity of approximately 25 %. Samples reduced and reoxidized at 900 °C show severe cracking. Furthermore, Fe-exsolution

tends to increase (compared to pellets reduced at 710 °C). The transition back to the perovskite phase during reoxidation, along with the accompanying volume change, is likely to further worsen the materials' stability over multiple redox cycles. Furthermore, agglomeration of nanoparticles was observed after reoxidation, which is likely to intensify during subsequent redox cycling.

The long-term exposure to ambient air or short-term contact with H_2O exacerbates fragmentation of the materials. Considering the operational temperature of a SOC reaching up to 900 °C and the presence of water vapor during SOC applications, either in fuel cell or in electrolysis mode, it becomes apparent that STFN and sSTFN might lack phase and mechanical stability under operating conditions. At first, the present $p(O_2)$ and temperature lead to the desired exsolution but also to further oxygen release and RP-phase transition. Subsequently, when exposed to a certain water vapor partial pressure ($p(H_2O)$), secondary phase formations can take place. In a real electrode structure, this would lead to deterioration of the microstructure, potentially worsening the contact at interfaces between the electrode and electrolyte. Furthermore, the loss of contact between individual grains can significantly impact the ionic and electronic percolation paths. In the worst-case scenario, the entire electrode may be destroyed.

Nevertheless, porous and thin layers on a mechanically stable substrate might be more tolerant against internal stresses as Zhu et al. [193] were able to measure electrochemical properties in model cells up to 850 °C. Notably, their Ni-exsolution electrode layers were pre-reduced in situ at 850°C. Furthermore, under real operating conditions the fuel gas is balanced by steam which might stabilize the materials by equilibrating the oxygen release and thus the nanoparticle exsolution and RP-phase transformation. Therefore, further experiments need to be conducted under more realistic operating conditions.

There might be some reasons for the mechanical instability and cracking of the materials reduced at 900 °C: i) the RP-phase transition during reduction (and reoxidation) resulting in a volume change of the unit cell which induces strain in the material, ii) the loss of oxygen during reduction and the possible oxygen uptake in ambient air or water leads to chemical strain, iii) during exposure to ambient air and moisture (or H_2O) segregated Sr(O) (a common phenomenon in perovskites and shown for STFN [194] and SOC air electrode like (La,Sr)(Co,Fe)$O_{3-\delta}$ [213]) and exsolved FeNi nanoparticles form secondary phases, e.g. strontiumhydroxides [214] and iron(oxide)-hydroxides [215] (corrosion). Since nanoparticles have a high surface area and the forming secondary phases might have large volumes, the pellets fragment. For example, $Fe(OH)_2$ possesses a volume 3.5 times higher than Fe, and Fe_3O_4 has a volume 5.9 times higher than Fe [216]. The reactions are favored in H_2O compared to ambient air.

It remains unclear which of these factors is the predominant cause of the mechanical instability observed. The observed bulk exsolution, especially of Fe, could be a severe problem regarding mechanical stability, especially if the mentioned secondary phases form.

Pellets of all materials, reduced in situ at 710 °C, seem to be mechanically stable, meaning they did not fragment. They do not reveal pronounced Fe-bulk exsolution compared to pellets reduced at 900 °C. This indicates that (bulk) exsolution, phase transitions, and the accompanied effects like secondary phase formation and volume changes are the triggers for crack formation.
This investigation highlights the existence of a temperature- and $p(O_2)$-range within which STFN and sSTFN can be potentially utilized for SOC operations. It is reasonable to expect that other exsolution materials may also possess such operating windows where the perovskite remains stable while exsolution takes place. Consequently, greater emphasis should be placed on evaluating the (mechanical) stability of potential SOC materials in the context of exsolution. Although the initial properties of STFN and sSTFN appear promising for SOC applications, their practical applicability is potentially compromised by the necessity to operate within a specific temperature range and by the presence of low and high H_2O partial pressures. To use STFN and sSTFN in an SOC, either the operation temperature must be lowered or precise control of the exsolution process and phase stability may be required, (potentially by restricting exsolution to the material's surface or a refinement of the microstructure) while maintaining its desirable properties.

5.10 Conclusion

$SrTi_{0.3}Fe_{0.7}O_{3-\delta}$ and its Ni-doped analogues $SrTi_{0.3}Fe_{0.63}Ni_{0.07}O_{3-\delta}$ and $Sr_{0.95}Ti_{0.3}Fe_{0.63}Ni_{0.07}O_{3-\delta}$ were successfully synthesized as potential SOC exsolution fuel electrode materials. Most of the materials were phase pure, according to XRD, but some minor particles of the precursors were still present, presumably NiO. The total conductivity is comparable to literature values. The exsolution of NiFe-nanoparticles was observed at temperatures of 710-900 °C. Samples reduced at 710 °C show preferential Ni-nucleation at grain boundaries. Bulk exsolution occurred, particularly at a reduction temperature of 900 °C and pronounced in the case of Fe.
Thermogravimetric analyses under reducing atmosphere reveal an abrupt mass loss in the beginning, attributed to the pre-reduction of the materials, which triggers the exsolution process. The materials tend to reach an equilibrium oxygen non-stoichiometry at 710 °C, while for reduction at 900 °C, no equilibrium was reached, even after 30 h, indicating continuous oxygen release, possibly associated with exsolution.
Above a certain threshold temperature (740-780 °C for STFN and sSTFN and 840-860 °C for STF) the perovskites underwent phase transitions to Ruddlesden-Popper phases. These phase transitions were accompanied by mechanical instabilities. Cracking of the materials was observed after reduction at 900 °C. Compacted and sintered pellets fragmented after contact with ambient air and H_2O. The formation of strontium hydroxides and iron(oxide)hydroxides is presumed. During reoxidation, the materials transition back to the perovskite phase through

oxygen uptake, which could lead to further mechanical degradation during redox cycling. Moreover, the nanoparticles show signs of agglomeration during reoxidation. Compared to a commonly used Ni-3YSZ cermet, the materials show no signs of carbon degradation in tar-containing fuels, as confirmed by microstructural and Raman analysis.
Despite promising initial properties and favorable carbon degradation behavior, the observed mechanical instabilities pose significant challenges for practical application. The general operating conditions of SOCs, including temperature, oxygen partial pressure, and water vapor, are likely to induce mechanical degradation in these materials. Future work should focus on the design of such materials for specific operation conditions and the stability of porous electrode layers during operation.

6 Summary and conclusions

The primary objective of this thesis was to enhance the tolerance of solid oxide fuel cells against carbon-based impurities in the fuel gas, especially in the fuel electrode-supported setup. Solid oxide cells have the potential to play a pivotal role in the energy transition and the hydrogen economy. These cells excel in utilizing clean fuels but face challenges when confronted with impurities, such as tars in biogas.

To address such issues, extensive research was conducted on potential fuel electrode materials within the framework of electrolyte-supported cells, where the advantage lies in reduced structural and functional changes of the employed materials during manufacturing owing to lower processing temperatures facilitated by pre-sintered electrolytes.

However, fuel electrode-supported cells face a significant challenge in the form of structural and functional changes during the high-temperature manufacturing process of the electrolyte, especially at interfaces between two distinct materials.

Gadolinia-doped ceria emerged as a promising alternative to yttria-stabilized zirconia as fuel electrode material, particularly in the intermediate temperature range, due to its enhanced ionic conductivity and potential carbon tolerance. Nevertheless, sintering-induced structural changes induced by interdiffusion led to the formation of pores at the interface with the yttria-stabilized zirconia electrolyte, severely impacting overall performance.

Thus, it was investigated whether modifying the dopants in ceria could suppress interdiffusion. The findings indicated that altering the dopant in ceria indeed influenced interdiffusion, with Sm and Y demonstrating reduced mixed phase formation and shorter interdiffusion lengths into yttria-stabilized zirconia compared to Gd. Nevertheless, this difference did not have a substantial impact on the performance of electrolyte-supported model cells, suggesting that it might not prevent performance degradation in actual fuel electrode-supported cells.

The introduction of a gadolinia-doped ceria barrier layer between yttria-stabilized zirconia and a Ni-gadolinia-doped ceria fuel electrode proved effective in preventing porosity in electrolyte-supported cells and restoring their performance. Efforts were then made to extend this concept to fuel electrode-supported cells, with the formulation and investigation of screen printing pastes for fuel electrode and barrier layers, focusing on rheology.

Rheological analysis revealed that the formulated screen printing pastes exhibited insufficient properties leaning more towards liquid-like characteristics, with inadequate structural recovery. However, after sintering, the resulting layers, particularly the fuel electrodes, showed appropriate microstructures. It was observed that there is room for improvement in the density of the barrier layers.

Consequently, it can be concluded that while rheology serves as a valuable tool for quality control purposes, it may not be the most reliable method for predicting the microstructures of layers derived from these pastes.

Nevertheless, porosity persisted between the gadolinia-doped ceria barrier layer and the yttria-stabilized zirconia electrolyte in fuel electrode-supported cells subjected to high sintering temperatures, possibly due to both components being sintered from a green body or just pre-sintered layers. Hence, for the successful incorporation of gadolinia-doped ceria in the fuel electrode, it is imperative to pair it with a dense gadolinia-doped ceria electrolyte.

Like gadolinia-doped ceria, Ni-exsolution perovskites are promising potential fuel electrode materials for solid oxide cells.
Ni-doped strontium titanium ferrite was successfully synthesized with a high Fe-content, to enhance the electrical conductivity of the perovskite backbone after exsolution. The exsolved NiFe-nanoparticles exhibited a high surface coverage. However, during reoxidation, they tended to agglomerate. The resulting electrical conductivity was found to be on par with existing literature, but a higher conductivity would be beneficial for application.
Nevertheless, these materials exhibited a lack of stability under more severe reducing conditions, which are within the temperature and oxygen partial pressure range relevant to solid oxide cell operation. These conditions triggered phase transitions to Ruddlesden-Popper phases after a critical amount of Fe-exsolution, consequently leading to cracks in the grains. Furthermore, when compacted, sintered, and reduced pellets were subjected to ambient atmosphere, moisture, or H_2O, they fragmented due to secondary phase formation. If these materials are to be utilized as fuel electrodes, it is imperative to enhance their stability or limit their application to specific operational windows.
Another challenge arises from the reactivity of strontium-containing materials with yttria-stabilized zirconia, affecting both the substrate and the electrolyte in a fuel electrode-supported cell. To mitigate this issue, gadolinium-doped ceria barrier layers are introduced, which, in turn, raises concerns related to porosity during fuel electrode-supported cell manufacturing.
Nevertheless, Ni-doped strontium titanium ferrite exhibited no carbon-related degradation when compared to a Ni-3YSZ cermet under similar testing conditions.

The examination of both materials underscores the challenge associated with adapting the half cell configuration of state-of-the-art fuel electrode-supported cells at IEK-1. This challenge primarily arises due to the elevated sintering temperatures and the manufacturing process being tailored to the substrate and electrolyte layers. The elevated sintering temperatures have resulted in interdiffusion and undesired microstructures as well as functional degradation of the layers when introducing new materials. Consequently, either the potential fuel electrode material is itself stable with the adjacent layers or a shift in the manufacturing strategy is necessary to align with the selected fuel electrode material to ensure sufficient compatibility with adjacent layers. An inert and flexible substrate might be key to improve versatility of fuel electrode supported cells.

Appendix A – Chapter 4

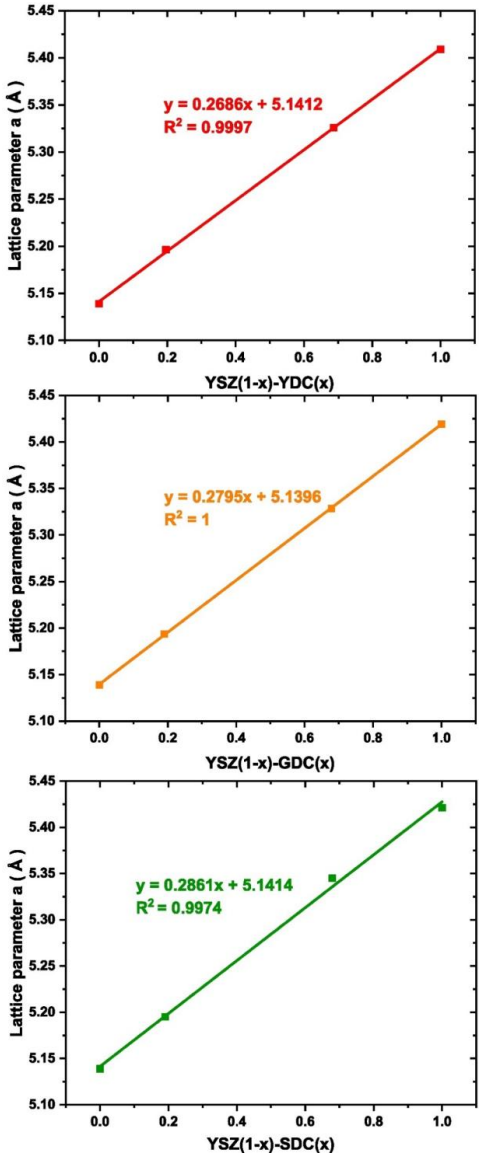

Figure A.1: Linear relationship between lattice parameter and composition (mol %) in (a) 8YSZ/10YDC, (b) 8YSZ/10GDC, and (c) 8YSZ/10SDC in sintered powder mixtures (1400 °C for 5 h).

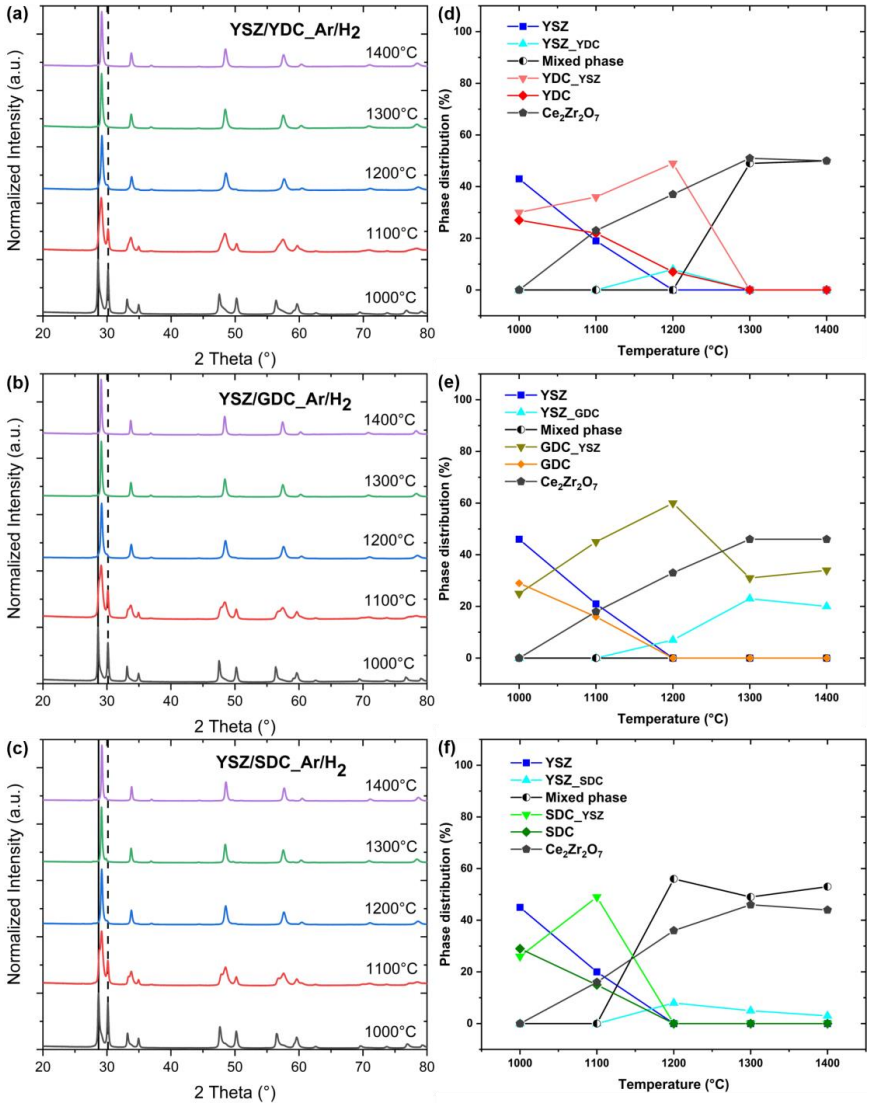

Figure A.2: Diffractograms and relative phase distribution (lines are a guide to the eye) of (a, d) 8YSZ/10YDC, (b, e) 8YSZ/10GDC, and (c, f) 8YSZ/10SDC powder mixtures sintered in saturated Ar/ 3 % H_2 atmosphere at temperatures between 1000 and 1400 °C for 5 h. Lines are a guide to the eye. Black and dashed black vertical lines represent the position of the (111) 8YSZ and 10GDC reflections, respectively.

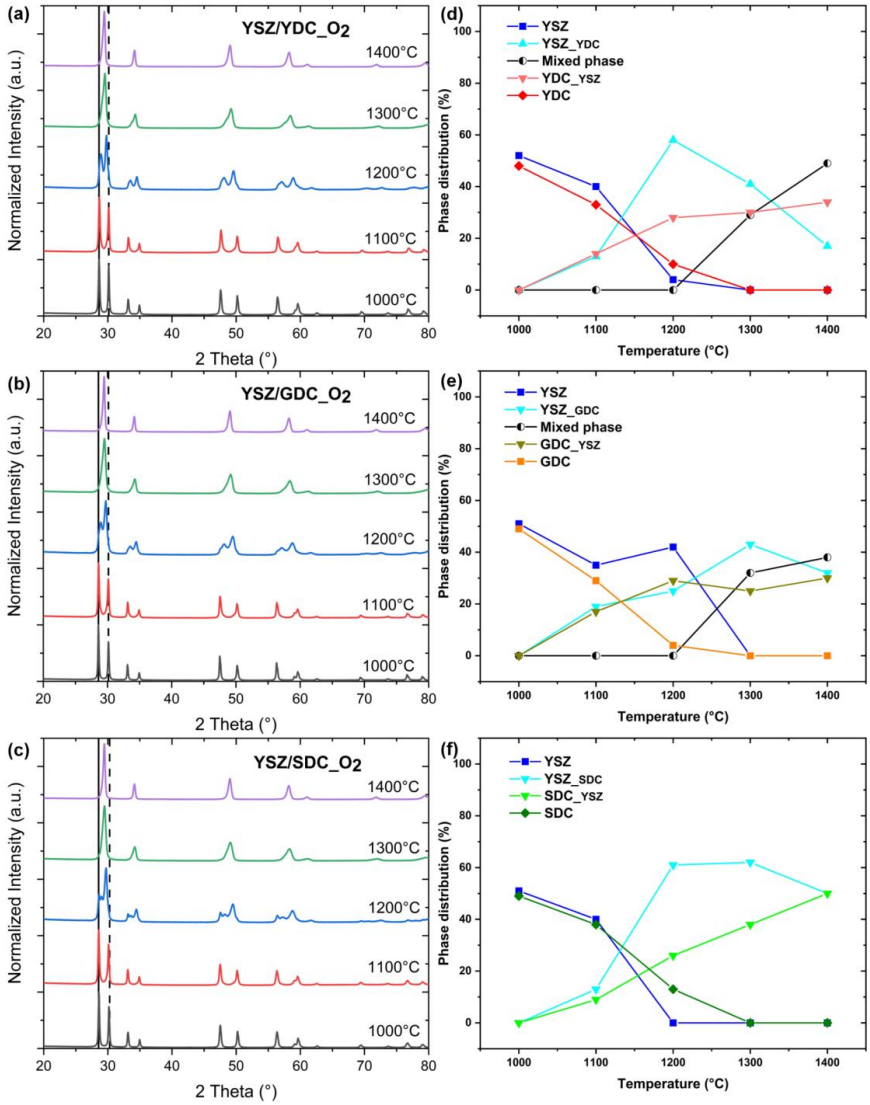

Figure A.3: Diffractograms and relative phase distribution (lines are a guide to the eye) of (a, d) 8YSZ/10YDC, (b, e) 8YSZ/10GDC, and (c, f) 8YSZ/10SDC powder mixtures sintered in saturated O_2 atmosphere at temperatures between 1000 and 1400 °C for 5 h. Black and dashed black vertical lines represent the position of the (111) 8YSZ and 10GDC reflections, respectively.

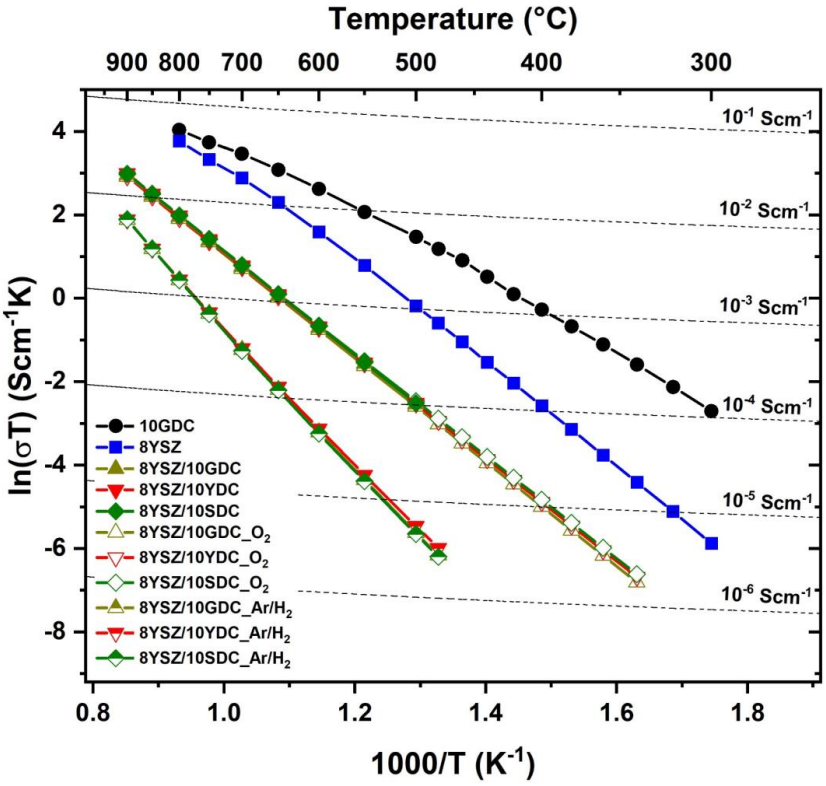

Figure A.4: Arrhenius plot of the ionic conductivity of 8YSZ/10XDC pellets sintered at 1400 °C for 5 h in ambient air, Ar/H_2, and O_2 compared to the conductivity of dense 8YSZ and 10GDC samples.

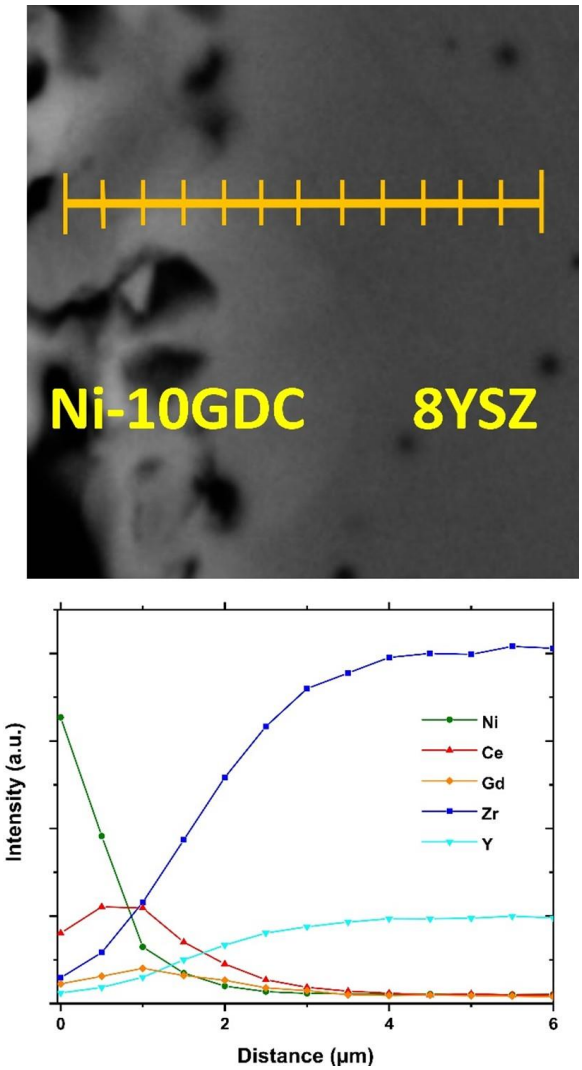

Figure A.5: EDS-line-scan of the interface Ni-10GDC|8YSZ in a symmetrical cell sintered at 1400 °C for 3 h without 10GDC barrier layer and porosity at the interface. Lines are a guide to the eye.

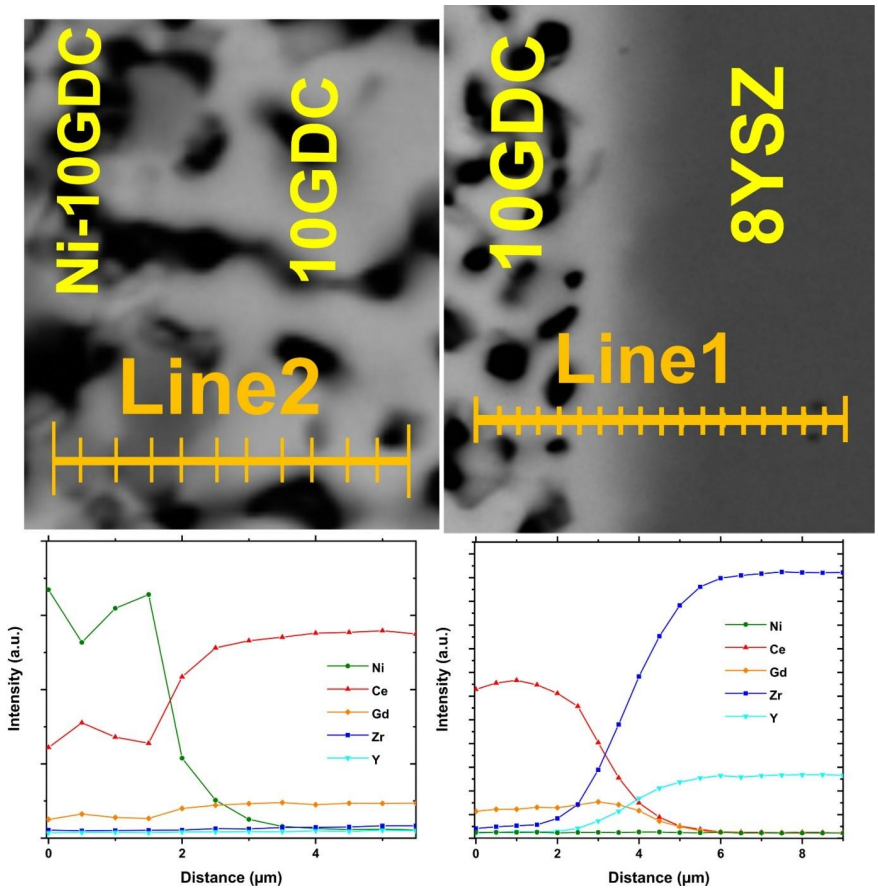

Figure A.6: EDS-line-scans of the interfaces Ni-10GDC|10GDC (Line2) and 10GDC|8YSZ (Line1) in a symmetrical Ni-10GDC|10GDC|8YSZ cell with sequentially sintered barrier (1300 °C for 3 h) and electrode (1400 °C for 3 h) layer. Lines are a guide to the eye.

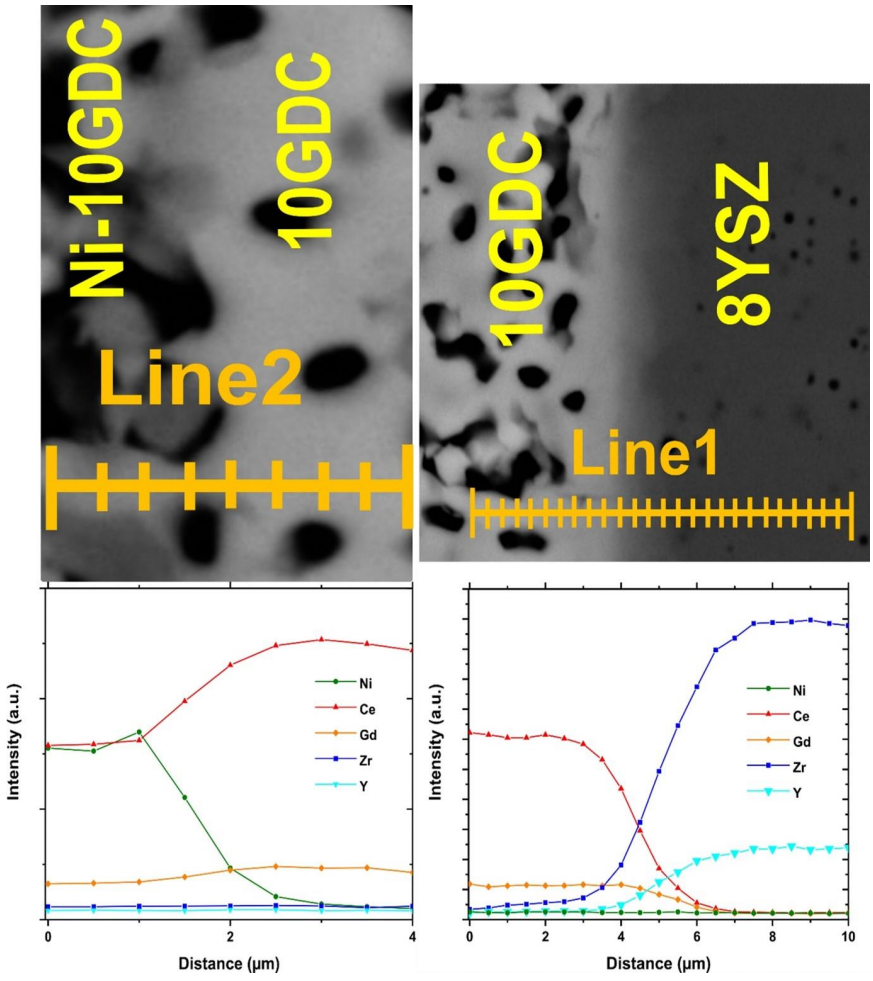

Figure A.7: EDS-line-scans of the interfaces Ni-10GDC|10GDC (Line2) and 10GDC|8YSZ (Line1) in a symmetrical Ni-10GDC|10GDC|8YSZ cell with co-sintered (1400 °C for 3 h) electrode and barrier layer. Lines are a guide to the eye.

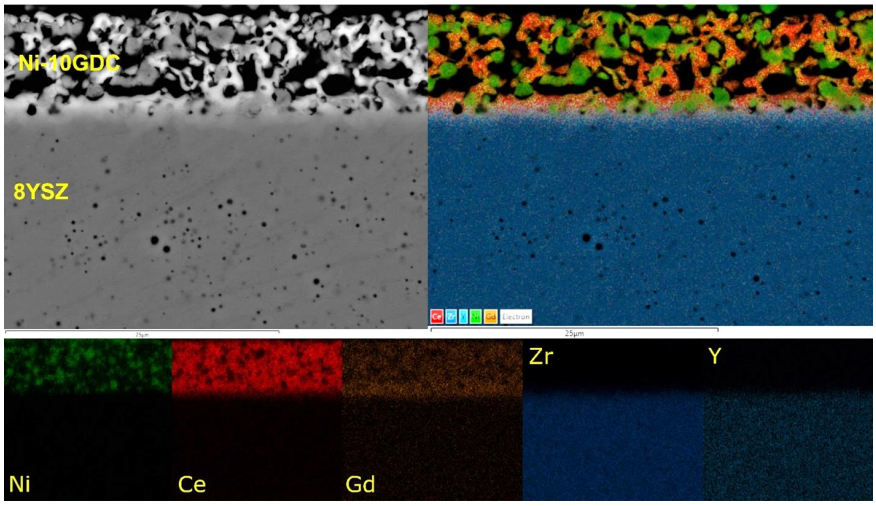

Figure A.8: EDS-map of the interface Ni-10GDC|8YSZ in a symmetrical cell sintered at 1400 °C for 3 h without 10GDC barrier layer and porosity at the interface.

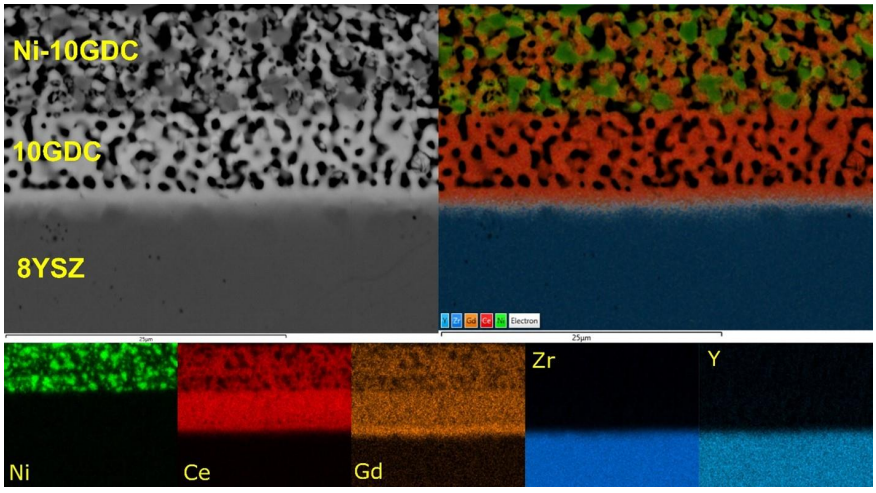

Figure A.9: EDS-map of the interfaces Ni-10GDC|10GDC and 10GDC|8YSZ in a symmetrical Ni-10GDC|10GDC|8YSZ cell with sequentially sintered barrier (1300 °C for 3 h) and electrode (1400 °C for 3 h) layer.

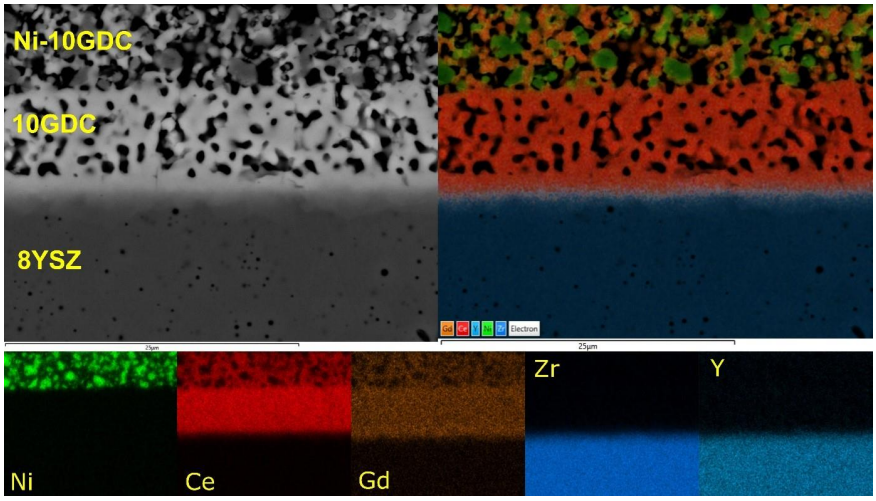

Figure A.10: EDS-map of the interfaces Ni-10GDC|10GDC and 10GDC|8YSZ in a symmetrical Ni-10GDC|10GDC|8YSZ cell with co-sintered (1400 °C for 3 h) electrode and barrier layer.

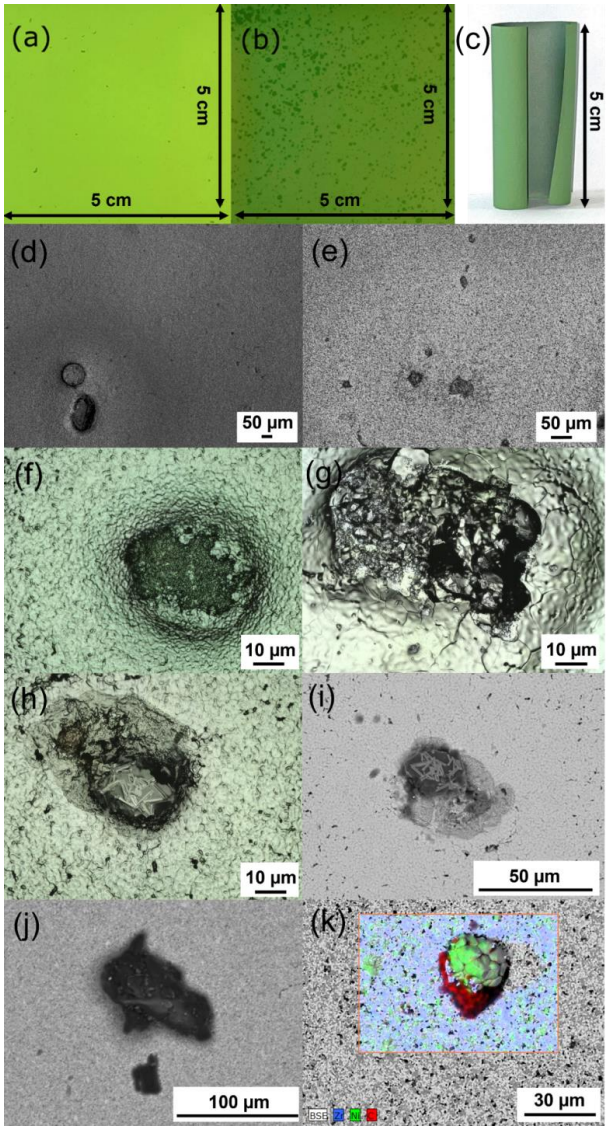

Figure A.11: Photographs of the (a) surface of 8YSZ electrolyte on a NiO-10GDC fuel electrode, (b) surface of 10GDC electrolyte on a NiO-10GDC fuel electrode, (c) coiled up NiO-3YSZ substrate with a NiO-10GDC fuel electrode; (a-c) are sintered at 1400 °C for 5 h. (d-h) Laser microscopy micrographs of defects occurring in half cells with an 8YSZ electrolyte on a NiO-10GDC fuel electrode after sintering at 1400 °C for 5 h. (i) SEM micrographs of a defect occurring in half cells with an 8YSZ electrolyte on a NiO-10GDC fuel electrode after sintering at 1400 °C for 5 h. j) SEM micrographs and (k) EDS analysis of defects occurring on NiO-3YSZ substrates sintered at 1400 °C for 5 h. The basis of all half cells in these pictures and micrographs is a NiO-3YSZ substrate.

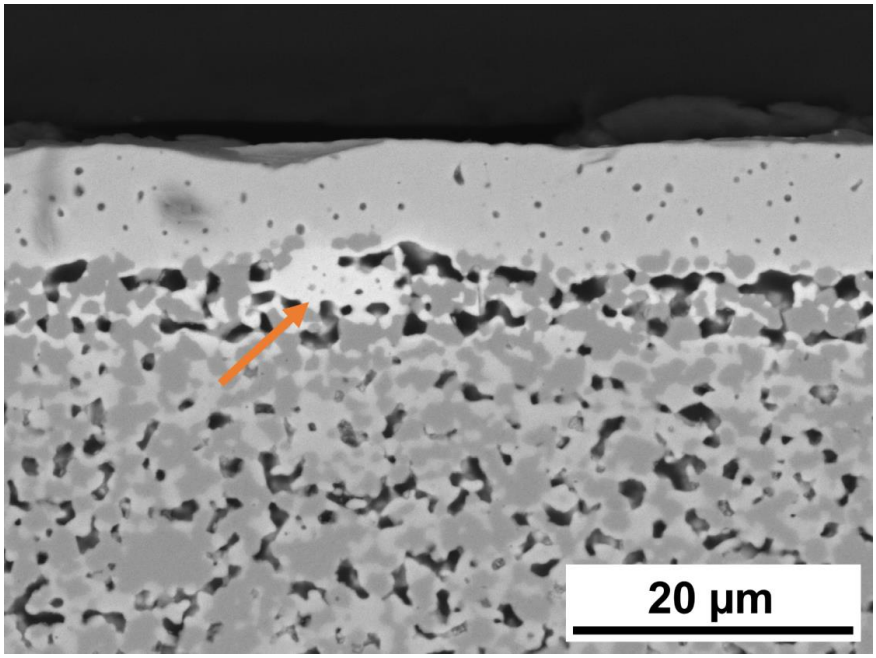

Figure A.12: SEM micrograph of a cross-section of a half cell with an 8YSZ electrolyte (top layer) on a NiO-10GDC fuel electrode (middle layer) sintered at 1400 °C for 5 h. Orange arrow marks a large 10GDC particle, probably due to agglomeration of 10GDC in the screen printing paste.

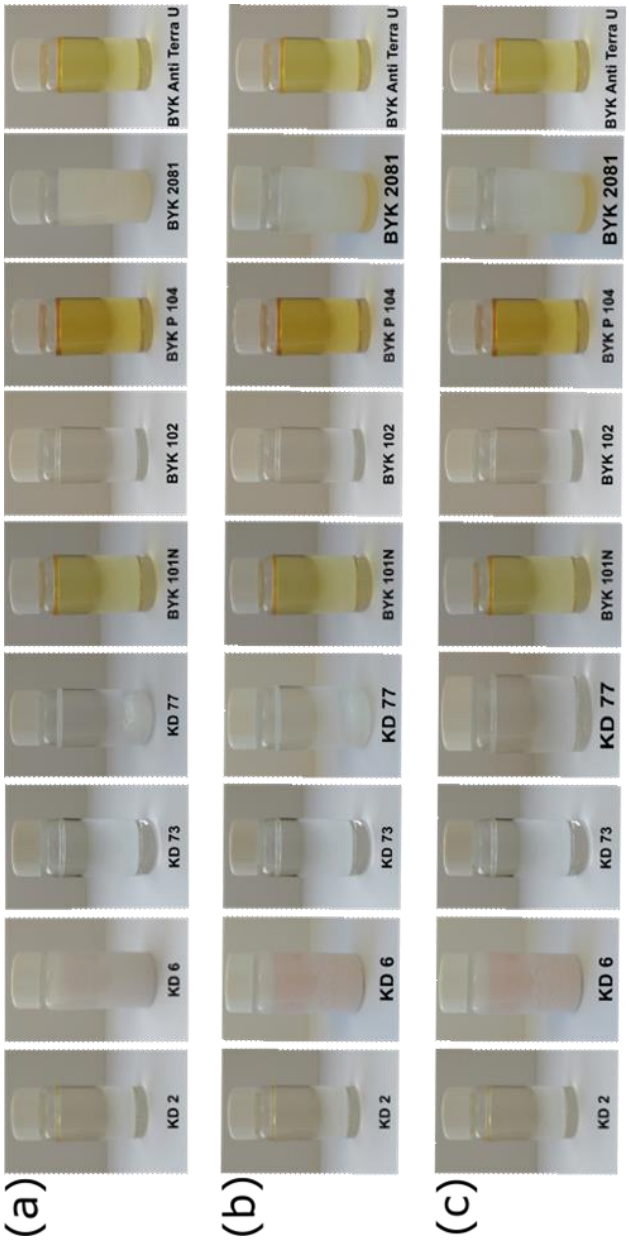

Figure A.13: Miscibility tests of various dispersants with terpineol in a weight ratio of 1:3. (a) Recently mixed, (b) after 24 h, and (c) heated up to 60 °C and after 24 h.

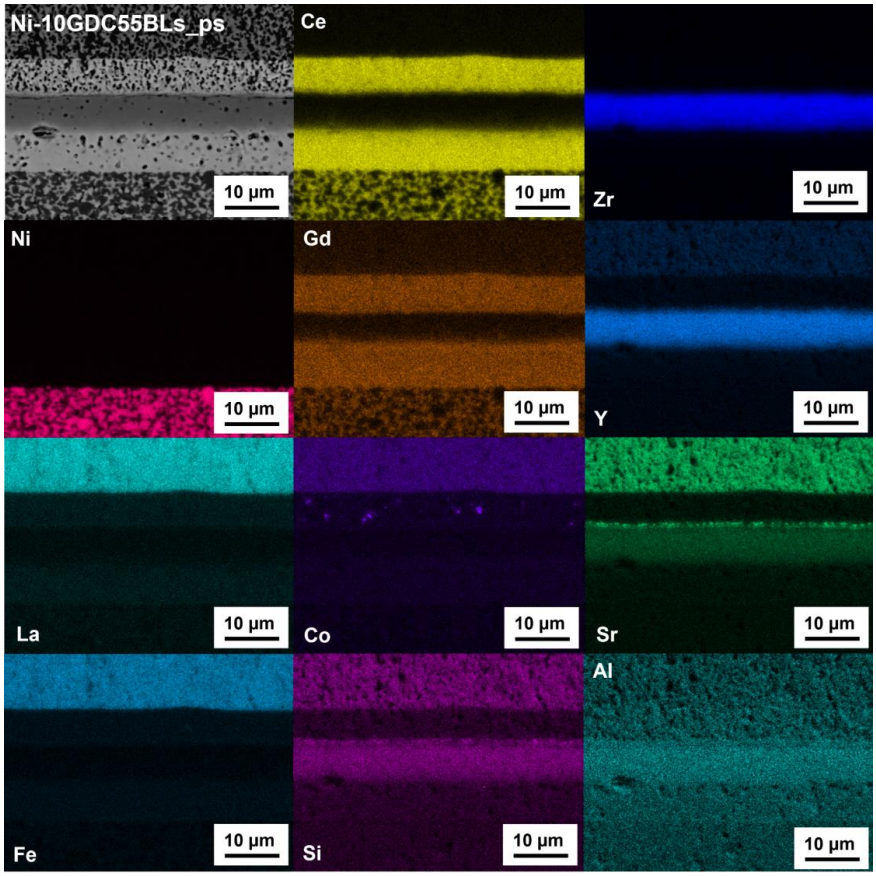

Figure A.14: EDS map of a cross-section of a Ni-10GDC55Bls_ps FESC.

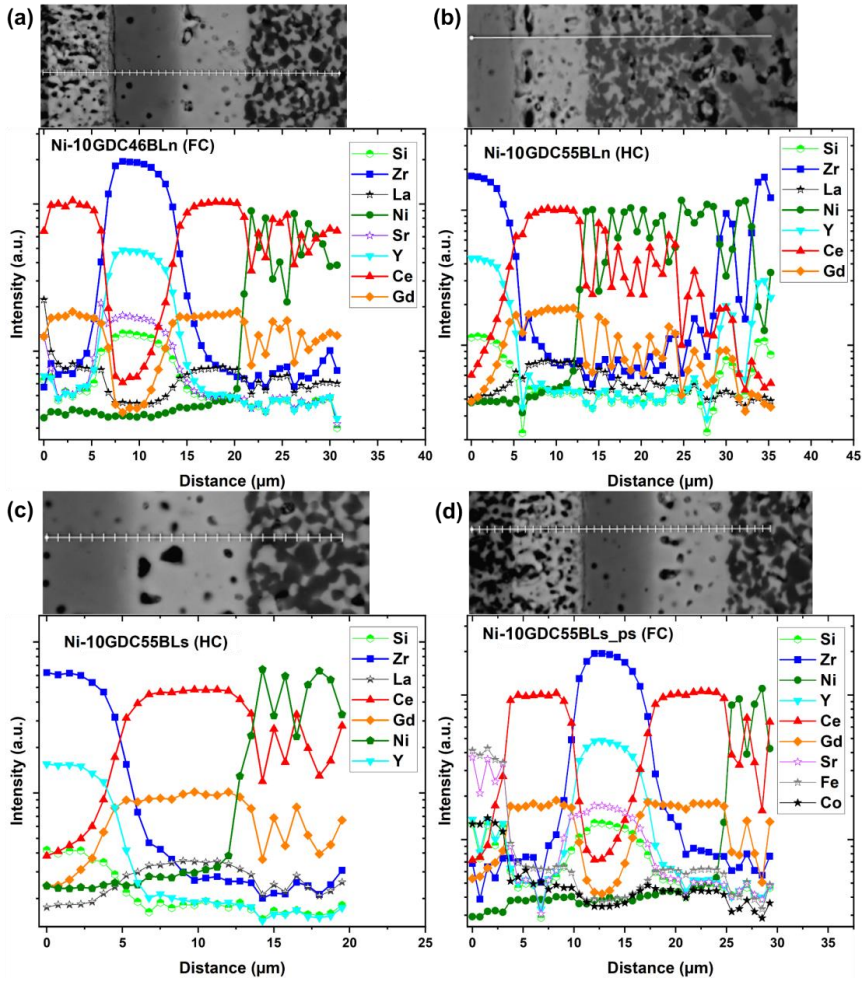

Figure A.15: EDS line scans of polished cross-sections of FESCs with Ni-10GDC fuel electrodes and GDC barrier layer.

Appendix B – Chapter 5

Table B.1: Cation distribution (wt%) of the starting powders NiO, $SrCO_3$, Fe_2O_3, and TiO_2.

Element (wt%)	**NiO**	**$SrCO_3$**	**Fe_2O_3**	**TiO_2**
Fe	0.00416 ± 0.00096	<0.0009	66.12 ± 0.97	<0.009
Ni	71 ± 4	0.0047 ± 0.0018	0.042 ± 0.011	0.0334 ± 0.0006
Mn	<0.0002	<0.0002	0.67 ± 0.03	/
Si	2.78 ± 0.15	<0.007	0.036 ± 0.003	0.006 ± 0.0008
Ti	0.0092 ± 0.0003	<0.0009	0.0098 ± 0.0005	58.1 ± 0.8
Ca	<0.0003	0.0395±0.0011	0.0084 ±0.0004	0.00649 ± 0.00014
Sr	<0.0009	55 ± 2	0.011 ± 0.003	<0.001
Ba	<0.0008	0.856 ± 0.019	<0.0009	/
Al	/	/	/	0.0201 ± 0.0008
K	/	/	/	0.162 ± 0.003
Na	/	/	/	0.0101 ± 0.0005

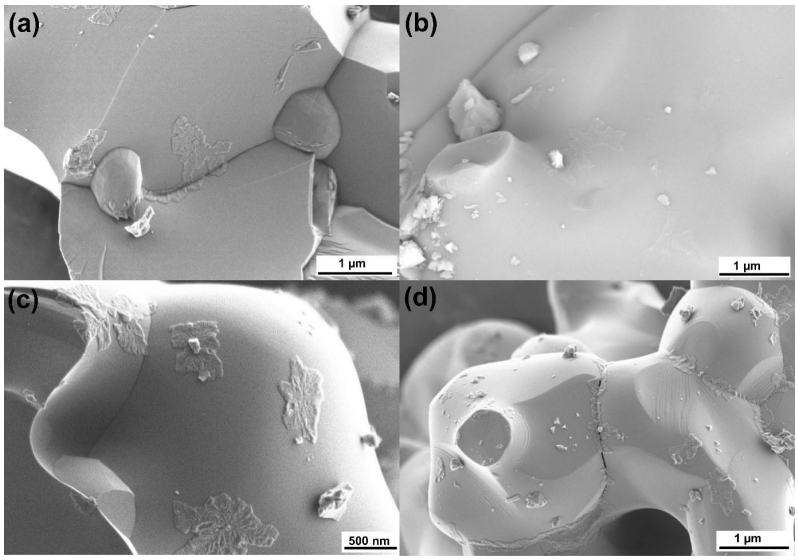

Figure B.1:SEM micrographs of lichen-like structures on the surface and at the grain boundaries of (a-c) STFN and (d) sSTFN. (a, c, d) show secondary electron micrographs. (b) shows a backscattered electron micrograph.

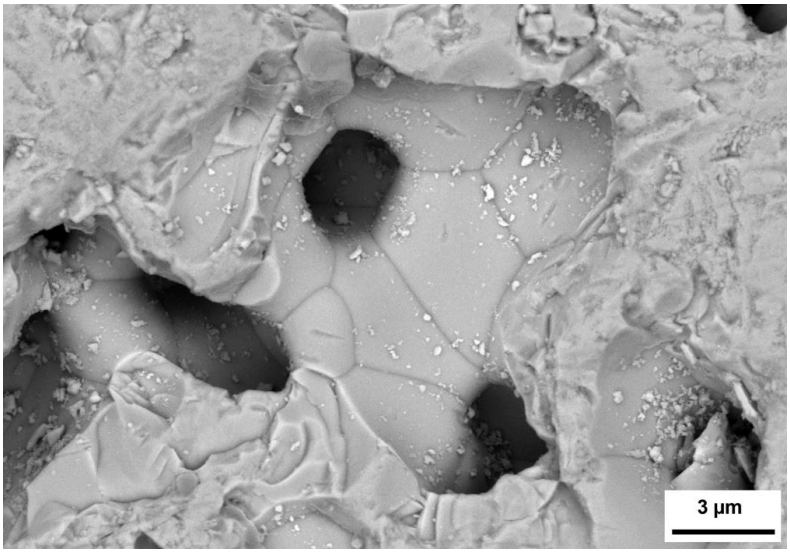

Figure B.2: Cross-section of STF reduced at 710 °C in 100 % H_2 after carbon degradation experiments.

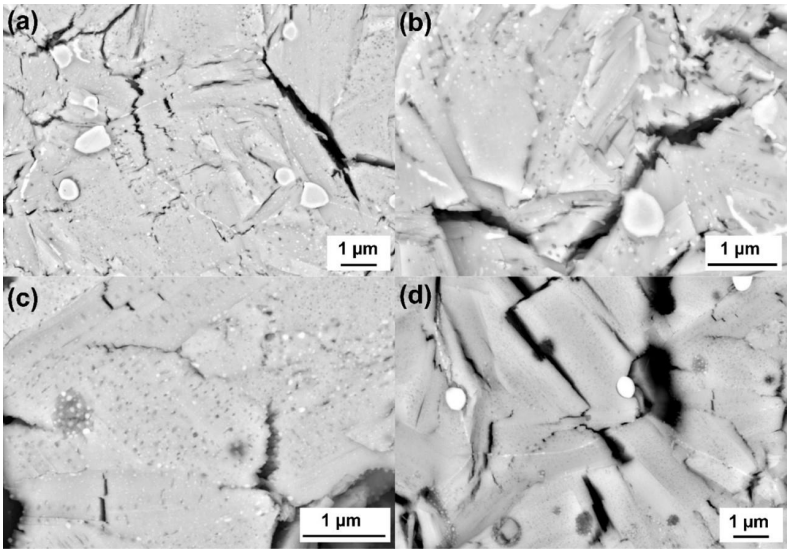

Figure B.3: Backscattered electron micrographs of cross-sections of (a, b) STFN and (c, d) sSTFN reduced at 900 °C in 50 % Ar/ 50 % H_2.

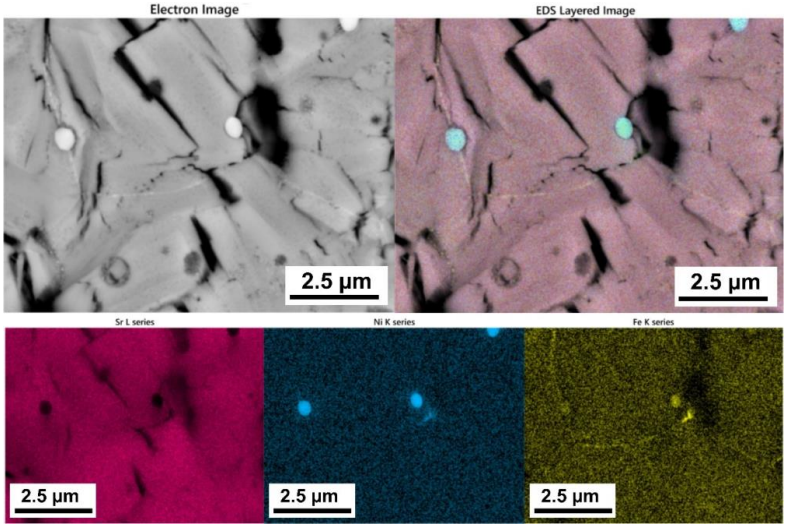

Figure B.4: EDS analysis of a cross-section of sSTFN reduced at 900 °C in 50 % Ar/ 50 % H_2.

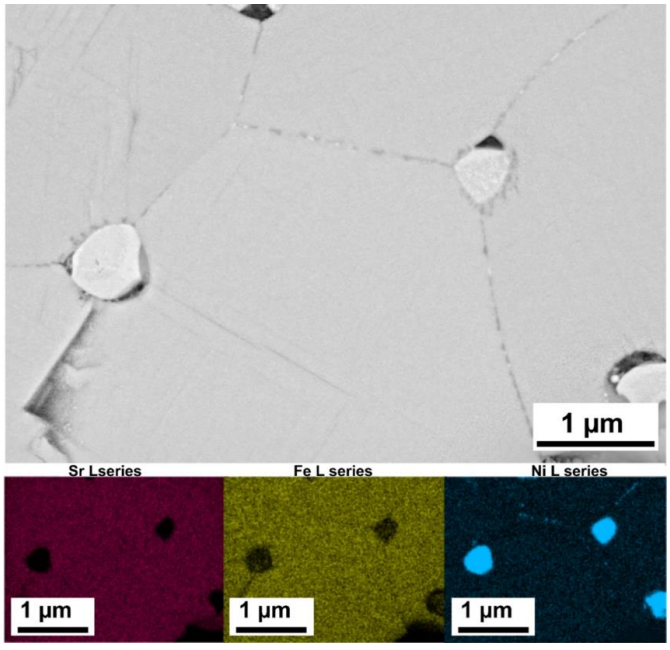

Figure B.5: EDS analysis of a cross-section of sSTFN reduced at 710 °C in 100 % H_2.

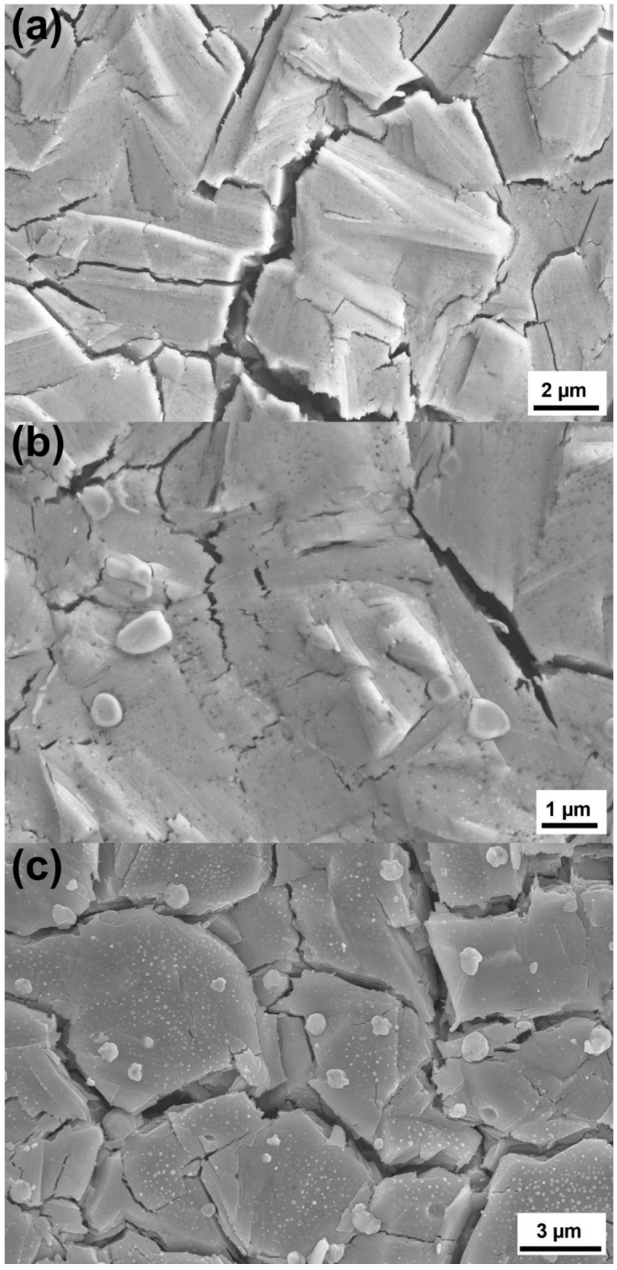

Figure B.6: Secondary electron micrographs of polished and aged cross-sections for (a) STF and (b, c) STFN reduced at 900 °C in 50 % Ar/ 50 % H_2.

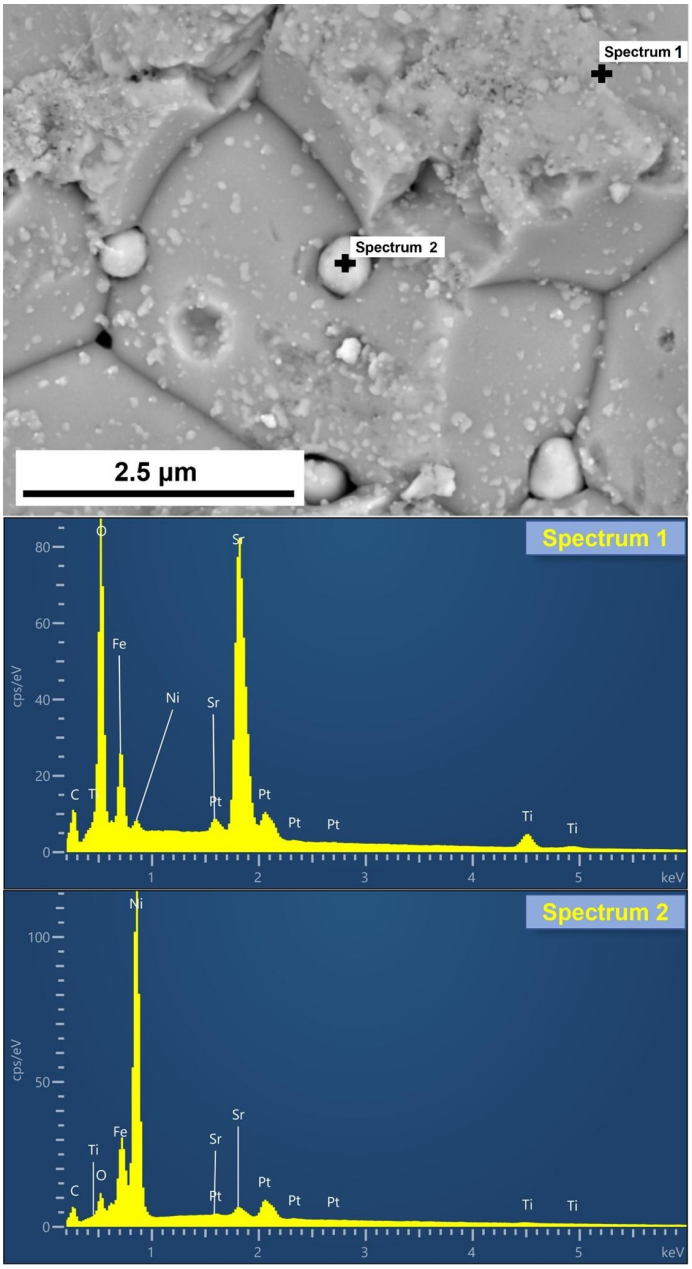

Figure B.7: Surface EDS point analysis (U = 8 kV) of a STFN pellet reduced in situ at 710 °C in 100 % H_2 after carbon degradation experiments.

Table B.2: Relative phase distribution of STF, STFN, and sSTFN reduced at temperatures of 710-900 °C in 50 % Ar/ 50 % H_2 for 8 h and reoxidized at 900 °C in air for 8 h.

	Material		**Reduction temperatures (°C)**						
			710	740	780	820	860	900	Re-oxidized (900 °C)
Relative phase distribution (%)	STF	STF	100	100	97	96	37	60	97
		SF-RP	0	0	0	0	44	34	0
		ST-RP	/	/	/	/	/	/	/
		Fe	0	0	3	4	19	6	0
		SF-P	/	/	/	/	/	/	3
	STFN	STFN	100	100	27	13	6	26	96
		SF-RP	0	0	63	75	41	20	0
		ST-RP	0	0	0	0	40	44	0
		NiFe	0	0	10	12	13	10	0
		$NiFeO_x$	/	/	/	/	/	/	4
	sSTFN	sSTFN	98	98	42	14	6	14	97
		SF-RP	0	0	50	73	35	29	0
		ST-RP	0	0	0	0	43	46	0
		NiFe	2	2	8	13	16	11	0
		$NiFeO_x$	/	/	/	/	/	/	3

References

[1] United Nations, The Sustainable Development Goals Report 2022, 2022. https://unstats.un.org/sdgs/report/2022/The-Sustainable-Development-Goals-Report-2022.pdf.

[2] UNEP, ed., The hydrogen economy: a non-technical review, United Nations Environment Programme, Nairobi, Kenya, 2006.

[3] Federal Ministry for Economic Affairs and Energy - Public Relations Division, The National Hydrogen Strategy Update, 11019 Berlin, Germany, 2023. www.bmwi.de.

[4] A. Hauch, R. Küngas, P. Blennow, A.B. Hansen, J.B. Hansen, B.V. Mathiesen, M.B. Mogensen, Recent advances in solid oxide cell technology for electrolysis, Science 370 (2020) eaba6118. https://doi.org/10.1126/science.aba6118.

[5] M.B. Mogensen, Materials for reversible solid oxide cells, Current Opinion in Electrochemistry 21 (2020) 265–273. https://doi.org/10.1016/j.coelec.2020.03.014.

[6] G. Squadrito, G. Maggio, A. Nicita, The green hydrogen revolution, Renewable Energy 216 (2023) 119041. https://doi.org/10.1016/j.renene.2023.119041.

[7] H.C. Butterman, M.J. Castaldi, CO_2 as a Carbon Neutral Fuel Source via Enhanced Biomass Gasification, Environ. Sci. Technol. 43 (2009) 9030–9037. https://doi.org/10.1021/es901509n.

[8] R. Baciocchi, E. Carnevale, G. Costa, R. Gavasci, L. Lombardi, T. Olivieri, L. Zanchi, D. Zingaretti, Performance of a biogas upgrading process based on alkali absorption with regeneration using air pollution control residues, Waste Management 33 (2013) 2694–2705. https://doi.org/10.1016/j.wasman.2013.08.022.

[9] H.J. Alves, C. Bley Junior, R.R. Niklevicz, E.P. Frigo, M.S. Frigo, C.H. Coimbra-Araújo, Overview of hydrogen production technologies from biogas and the applications in fuel cells, International Journal of Hydrogen Energy 38 (2013) 5215–5225. https://doi.org/10.1016/j.ijhydene.2013.02.057.

[10] K. Sasaki, Y. Teraoka, Equilibria in Fuel Cell Gases, Proc. Vol. 2003–07 (2003) 1225. https://doi.org/10.1149/200307.1225PV.

[11] H. Jeong, M. Hauser, F. Fischer, M. Hauck, S. Lobe, R. Peters, C. Lenser, N.H. Menzler, O. Guillon, Utilization of Bio-Syngas in Solid Oxide Fuel Cell Stacks: Effect of Hydrocarbon Reforming, J. Electrochem. Soc. 166 (2019) F137. https://doi.org/10.1149/2.1191902jes.

[12] J. Mermelstein, M. Millan, N. Brandon, The impact of steam and current density on carbon formation from biomass gasification tar on Ni/YSZ, and Ni/CGO solid oxide fuel cell anodes, Journal of Power Sources 195 (2010) 1657–1666. https://doi.org/10.1016/j.jpowsour.2009.09.046.

[13] V. Pawar, D. Ray, Ch. Subrahmanyam, V.M. Janardhanan, Study of Short-Term Catalyst Deactivation Due to Carbon Deposition during Biogas Dry Reforming on Supported Ni Catalyst, Energy Fuels 29 (2015) 8047–8052. https://doi.org/10.1021/acs.energyfuels.5b01862.

[14] C.M. Chun, J.D. Mumford, T.A. Ramanarayanan, Carbon-Induced Corrosion of Nickel Anode, J. Electrochem. Soc. 147 (2000) 3680. https://doi.org/10.1149/1.1393958.

[15] A.I. La Cava, C.A. Bernardo, D.L. Trimm, Studies of deactivation of metals by carbon deposition, Carbon 20 (1982) 219–223. https://doi.org/10.1016/0008-6223(82)90024-0.

[16] A.E. Lutz, R.S. Larson, J.O. Keller, Thermodynamic comparison of fuel cells to the Carnot cycle, International Journal of Hydrogen Energy 27 (2002) 1103–1111. https://doi.org/10.1016/S0360-3199(02)00016-2.

[17] E.D. Wachsman, K.T. Lee, Lowering the Temperature of Solid Oxide Fuel Cells, Science 334 (2011) 935–939. https://doi.org/10.1126/science.1204090.

[18] W.J. Khudhayer, Hydrogen Energy and Fuel Cell Technology, Chapter Four: Performance Characterization of Fuel Cell Systems, (2016).

[19] F. Barbir, PEM Fuel Cells: Theory and Practice, Academic Press, 2012.

[20] A. Kabza, Fuel cell formulary, Kabza, Ed (2015).

[21] H. Mahcene, H. Ben Moussa, H. Bouguetaia, B. Bouchekima, D. Bechki, Losses effect on solid oxide fuel cell stack performance, Fuel Cells Journal (2006).

[22] C. Mendonça, A. Ferreira, D.M.F. Santos, Towards the Commercialization of Solid Oxide Fuel Cells: Recent Advances in Materials and Integration Strategies, Fuels 2 (2021) 393–419. https://doi.org/10.3390/fuels2040023.

[23] K. Sasaki, Y. Teraoka, Equilibria in Fuel Cell Gases: II. The C-H-O Ternary Diagrams, J. Electrochem. Soc. 150 (2003) A885. https://doi.org/10.1149/1.1577338.

[24] C.H. Bartholomew, Carbon Deposition in Steam Reforming and Methanation, Catalysis Reviews 24 (1982) 67–112. https://doi.org/10.1080/03602458208079650.

[25] F. Abild-Pedersen, J.K. Nørskov, J.R. Rostrup-Nielsen, J. Sehested, S. Helveg, Mechanisms for catalytic carbon nanofiber growth studied by ab initio density functional theory calculations, Phys. Rev. B 73 (2006) 115419. https://doi.org/10.1103/PhysRevB.73.115419.

[26] D. Neagu, T.-S. Oh, D.N. Miller, H. Ménard, S.M. Bukhari, S.R. Gamble, R.J. Gorte, J.M. Vohs, J.T.S. Irvine, Nano-socketed nickel particles with enhanced coking resistance grown in situ by redox exsolution, Nat Commun 6 (2015) 8120. https://doi.org/10.1038/ncomms9120.

[27] J. Irvine, J.L.M. Rupp, G. Liu, X. Xu, S. Haile, X. Qian, A. Snyder, R. Freer, D. Ekren, S. Skinner, O. Celikbilek, S. Chen, S. Tao, T.H. Shin, R. O'Hayre, J. Huang, C. Duan, M. Papac, S. Li, V. Celorrio, A. Russell, B. Hayden, H. Nolan, X. Huang, G. Wang, I. Metcalfe, D. Neagu, S.G. Martín, Roadmap on inorganic perovskites for energy applications, J. Phys. Energy 3 (2021) 031502. https://doi.org/10.1088/2515-7655/abff18.

[28] N.P. Brandon, S. Skinner, B.C.H. Steele, Recent Advances in Materials for Fuel Cells, Annual Review of Materials Research 33 (2003) 183–213. https://doi.org/10.1146/annurev.matsci.33.022802.094122.

[29] M.L. Weber, C. Baeumer, D.N. Mueller, L. Jin, C.-L. Jia, D.S. Bick, R. Waser, R. Dittmann, I. Valov, F. Gunkel, Electrolysis of Water at Atomically Tailored Epitaxial Cobaltite Surfaces, Chem. Mater. 31 (2019) 2337–2346. https://doi.org/10.1021/acs.chemmater.8b04577.

[30] W.G. Hardin, D.A. Slanac, X. Wang, S. Dai, K.P. Johnston, K.J. Stevenson, Highly Active, Nonprecious Metal Perovskite Electrocatalysts for Bifunctional Metal–Air Battery Electrodes, J. Phys. Chem. Lett. 4 (2013) 1254–1259. https://doi.org/10.1021/jz400595z.

[31] S.K. Burnwal, S. Bharadwaj, P. Kistaiah, Review on MIEC Cathode Materials for Solid Oxide Fuel Cells, J. Mol. Eng. Mater. 04 (2016) 1630001. https://doi.org/10.1142/S2251237316300011.

[32] D.M. Smyth, The effects of dopants on the properties of metal oxides, Solid State Ionics 129 (2000) 5–12. https://doi.org/10.1016/S0167-2738(99)00312-4.

[33] M.J. Akhtar, Z.-U.-N. Akhtar, R.A. Jackson, C.R.A. Catlow, Computer Simulation Studies of Strontium Titanate, Journal of the American Ceramic Society 78 (1995) 421–428. https://doi.org/10.1111/j.1151-2916.1995.tb08818.x.

[34] C. Noguera, Physics and Chemistry at Oxide Surfaces, Cambridge University Press, Cambridge, 1996. https://doi.org/10.1017/CBO9780511524301.

[35] D.M. Smyth, The defect chemistry of metal oxides, Oxford University Press, New York, 2000.

[36] M.V. Patrakeev, I.A. Leonidov, V.L. Kozhevnikov, V.V. Kharton, Ion–electron transport in strontium ferrites: relationships with structural features and stability, Solid State Sciences 6 (2004) 907–913. https://doi.org/10.1016/j.solidstatesciences.2004.05.002.

[37] D. Emin, Optical properties of large and small polarons and bipolarons, Phys. Rev. B 48 (1993) 13691–13702. https://doi.org/10.1103/PhysRevB.48.13691.

[38] A.L. Shluger, A.M. Stoneham, Small polarons in real crystals: concepts and problems, J. Phys.: Condens. Matter 5 (1993) 3049. https://doi.org/10.1088/0953-8984/5/19/007.

[39] A.V. Nikonov, K.A. Kuterbekov, K.Zh. Bekmyrza, N.B. Pavzderin, A brief review of conductivity and thermal expansion of perovskite-related oxides for SOFC cathode, Eurasian Journal of Physics and Functional Materials 2 (2018) 274–292.

[40] N. Delïbaş, S.B. Gharamalekï, M. Mansourï, A. Nïaïe, Reduction of operation temperature in SOFCs utilizing perovskites: Review, Int. Adv. Res. Eng. J. 6 (2022) 56–67. https://doi.org/10.35860/iarej.972864.

[41] D.P. Fagg, V.V. Kharton, A.V. Kovalevsky, A.P. Viskup, E.N. Naumovich, J.R. Frade, The stability and mixed conductivity in La and Fe doped $SrTiO_3$ in the search for potential SOFC anode materials, Journal of the European Ceramic Society 21 (2001) 1831–1835. https://doi.org/10.1016/S0955-2219(01)00125-X.

[42] A. Mroziński, S. Molin, J. Karczewski, T. Miruszewski, P. Jasiński, Electrochemical properties of porous $Sr_{0.86}Ti_{0.65}Fe_{0.35}O_3$ oxygen electrodes in solid oxide cells: Impedance study of symmetrical electrodes, International Journal of Hydrogen Energy 44 (2019) 1827–1838. https://doi.org/10.1016/j.ijhydene.2018.11.203.

[43] Y. Takeda, K. Kanno, T. Takada, O. Yamamoto, M. Takano, N. Nakayama, Y. Bando, Phase relation in the oxygen nonstoichiometric system, $SrFeO_x$ ($2.5 \leq x \leq 3.0$), Journal of Solid State Chemistry 63 (1986) 237–249. https://doi.org/10.1016/0022-4596(86)90174-X.

[44] Y. Zhou, Z. Zhou, J. Sun, L. Liu, F. Luo, G. Xu, X.E. Cao, M. Xu, Ruddlesden-Popper-type perovskite $Sr_3Fe_2O_{7-\delta}$ for enhanced thermochemical energy storage, EcoMat 5 (2023) e12347. https://doi.org/10.1002/eom2.12347.

[45] P.A. Cox, Transition Metal Oxides: An Introduction to Their Electronic Structure and Properties, Oxford University Press, Oxford, New York, 2010.

[46] C. Noguera, B. Fritz, Solid Solution/Exsolution, in: P. Bobrowsky, B. Marker (Eds.), Encyclopedia of Engineering Geology, Springer International Publishing, Cham, 2018: pp. 1–8. https://doi.org/10.1007/978-3-319-39193-9_350-1.

[47] J. Mei, T. Liao, Z. Sun, Metal exsolution engineering on perovskites for electrocatalysis: a perspective, Materials Today Energy 31 (2023) 101216. https://doi.org/10.1016/j.mtener.2022.101216.

[48] O. Kwon, S. Joo, S. Choi, S. Sengodan, G. Kim, Review on exsolution and its driving forces in perovskites, J. Phys. Energy 2 (2020) 032001. https://doi.org/10.1088/2515-7655/ab8c1f.

[49] T. Cao, O. Kwon, R.J. Gorte, J.M. Vohs, Metal Exsolution to Enhance the Catalytic Activity of Electrodes in Solid Oxide Fuel Cells, Nanomaterials (Basel) 10 (2020) 2445. https://doi.org/10.3390/nano10122445.

[50] L. Lindenthal, R. Buchinger, H. Drexler, F. Schrenk, T. Ruh, C. Rameshan, Exsolution Catalysts—Increasing Metal Efficiency, Encyclopedia 1 (2021) 249–260. https://doi.org/10.3390/encyclopedia1010023.

[51] C.J. Fu, Q. Ma, L. Gao, S. Li, Recent Advances in Perovskite Oxides Electrocatalysts: Ordered Perovskites, Cations Segregation and Exsolution, ChemCatChem 15 (2023) e202300389. https://doi.org/10.1002/cctc.202300389.

[52] D. Neagu, V. Kyriakou, I.-L. Roiban, M. Aouine, C. Tang, A. Caravaca, K. Kousi, I. Schreur-Piet, I.S. Metcalfe, P. Vernoux, M.C.M. van de Sanden, M.N. Tsampas, In Situ Observation of Nanoparticle Exsolution from Perovskite Oxides: From Atomic Scale Mechanistic Insight to Nanostructure Tailoring, ACS Nano 13 (2019) 12996–13005. https://doi.org/10.1021/acsnano.9b05652.

[53] T. Zhang, Y. Zhao, X. Zhang, H. Zhang, N. Yu, T. Liu, Y. Wang, Thermal Stability of an in Situ Exsolved Metallic Nanoparticle Structured Perovskite Type Hydrogen Electrode for Solid Oxide Cells, ACS Sustainable Chem. Eng. 7 (2019) 17834–17844. https://doi.org/10.1021/acssuschemeng.9b04350.

[54] M.B. Mogensen, M. Chen, H.L. Frandsen, C. Graves, A. Hauch, P.V. Hendriksen, T. Jacobsen, S.H. Jensen, T.L. Skafte, X. Sun, Ni migration in solid oxide cell electrodes: Review and revised hypothesis, Fuel Cells 21 (2021) 415–429. https://doi.org/10.1002/fuce.202100072.

[55] P. Steiger, D. Burnat, H. Madi, A. Mai, L. Holzer, J. Van Herle, O. Kröcher, A. Heel, D. Ferri, Sulfur Poisoning Recovery on a Solid Oxide Fuel Cell Anode Material

through Reversible Segregation of Nickel, Chem. Mater. 31 (2019) 748–758. https://doi.org/10.1021/acs.chemmater.8b03669.

[56] K.-Y. Lai, A. Manthiram, Evolution of Exsolved Nanoparticles on a Perovskite Oxide Surface during a Redox Process, Chem. Mater. 30 (2018) 2838–2847. https://doi.org/10.1021/acs.chemmater.8b01029.

[57] B. Koo, K. Kim, J.K. Kim, H. Kwon, J.W. Han, W. Jung, Sr Segregation in Perovskite Oxides: Why It Happens and How It Exists, Joule 2 (2018) 1476–1499. https://doi.org/10.1016/j.joule.2018.07.016.

[58] S. Sultana, S. Mansingh, K. M. Parida, Crystal facet and surface defect engineered low dimensional CeO_2 (0D, 1D, 2D) based photocatalytic materials towards energy generation and pollution abatement, Materials Advances 2 (2021) 6942–6983. https://doi.org/10.1039/D1MA00539A.

[59] S.B. Khan, K. Akhtar, Cerium Oxide: Applications and Attributes, BoD – Books on Demand, 2019.

[60] S. Scirè, L. Palmisano, 1 - Cerium and cerium oxide: A brief introduction, in: S. Scirè, L. Palmisano (Eds.), Cerium Oxide (CeO_2): Synthesis, Properties and Applications, Elsevier, 2020: pp. 1–12. https://doi.org/10.1016/B978-0-12-815661-2.00001-3.

[61] C.R.A. Catlow, Defects in solid fluorides., London: Academic Press, 1985.

[62] J. Zhang, C. Lenser, N.H. Menzler, O. Guillon, Comparison of solid oxide fuel cell (SOFC) electrolyte materials for operation at 500 °C, Solid State Ionics 344 (2020) 115138. https://doi.org/10.1016/j.ssi.2019.115138.

[63] D. Udomsilp, C. Lenser, O. Guillon, N.H. Menzler, Performance Benchmark of Planar Solid Oxide Cells Based on Material Development and Designs, Energy Technology 9 (2021) 2001062. https://doi.org/10.1002/ente.202001062.

[64] M.S. Khan, S.-B. Lee, R.-H. Song, J.-W. Lee, T.-H. Lim, S.-J. Park, Fundamental mechanisms involved in the degradation of nickel–yttria stabilized zirconia (Ni–YSZ) anode during solid oxide fuel cells operation: A review, Ceramics International 42 (2016) 35–48. https://doi.org/10.1016/j.ceramint.2015.09.006.

[65] M.J. Escudero, I. Gómez de Parada, A. Fuerte, J.L. Serrano, Analysis of the electrochemical performance of MoNi–CeO_2 cermet as anode material for solid oxide fuel cell. Part I. H_2, CH_4 and H_2/CH_4 mixtures as fuels, Journal of Power Sources 253 (2014) 64–73. https://doi.org/10.1016/j.jpowsour.2013.12.027.

[66] M.J. Escudero, C.A. Maffiotte, J.L. Serrano, Long-term operation of a solid oxide fuel cell with MoNi–CeO_2 as anode directly fed by biogas containing simultaneously sulphur and siloxane, Journal of Power Sources 481 (2021) 229048. https://doi.org/10.1016/j.jpowsour.2020.229048.

[67] D. Papurello, S. Silvestri, S. Modena, Biogas trace compounds impact on high-temperature fuel cells short stack performance, International Journal of Hydrogen Energy 46 (2021) 8792–8801. https://doi.org/10.1016/j.ijhydene.2020.11.273.

[68] J.F.B. Rasmussen, A. Hagen, The effect of H_2S on the performance of Ni–YSZ anodes in solid oxide fuel cells, Journal of Power Sources 191 (2009) 534–541. https://doi.org/10.1016/j.jpowsour.2009.02.001.

[69] P.V. Aravind, J.P. Ouweltjes, N. Woudstra, G. Rietveld, Impact of Biomass-Derived Contaminants on SOFCs with Ni/Gadolinia-Doped Ceria Anodes, Electrochem. Solid-State Lett. 11 (2007) B24. https://doi.org/10.1149/1.2820452.

[70] P. Fan, X. Zhang, D. Hua, G. Li, Experimental Study of the Carbon Deposition from CH_4 onto the Ni/YSZ Anode of SOFCs, Fuel Cells 16 (2016) 235–243. https://doi.org/10.1002/fuce.201500038.

[71] C. Lenser, J. Zhang, N. Russner, A. Weber, O. Guillon, N.H. Menzler, Electro-chemo-mechanical analysis of a solid oxide cell based on doped ceria, Journal of Power Sources 541 (2022) 231505. https://doi.org/10.1016/j.jpowsour.2022.231505.

[72] J. Philibert, Atom Movements, EDP Sciences, Les Ulis, FRANCE, 2006. http://ebookcentral.proquest.com/lib/fz/detail.action?docID=3155118 (accessed August 28, 2023).

[73] A.D. Smigelskas, Zinc diffusion in alpha brass, Trans. AIME 171 (1947) 130–142.

[74] M.N. Rahaman, Ceramic Processing and Sintering, CRC Press, 2017.

[75] C.B. Carter, M.G. Norton, Ceramic Materials: Science and Engineering, Springer New York, New York, NY, 2013. https://doi.org/10.1007/978-1-4614-3523-5.

[76] R.-F. Guo, H.-R. Mao, Z.-T. Zhao, P. Shen, Ultrafast high-temperature sintering of bulk oxides, Scripta Materialia 193 (2021) 103–107. https://doi.org/10.1016/j.scriptamat.2020.10.045.

[77] J. Dong, V. Pouchly, M. Biesuz, V. Tyrpekl, M. Vilémová, M. Kermani, M. Reece, C. Hu, S. Grasso, Thermally-insulated ultra-fast high temperature sintering (UHS) of zirconia: A master sintering curve analysis, Scripta Materialia 203 (2021) 114076. https://doi.org/10.1016/j.scriptamat.2021.114076.

[78] C. Wang, W. Ping, Q. Bai, H. Cui, R. Hensleigh, R. Wang, A.H. Brozena, Z. Xu, J. Dai, Y. Pei, C. Zheng, G. Pastel, J. Gao, X. Wang, H. Wang, J.-C. Zhao, B. Yang, X. (Rayne) Zheng, J. Luo, Y. Mo, B. Dunn, L. Hu, A general method to synthesize and sinter bulk ceramics in seconds, Science 368 (2020) 521–526. https://doi.org/10.1126/science.aaz7681.

[79] T.P. Mishra, A.M. Laptev, M. Ziegner, S.K. Sistla, A. Kaletsch, C. Broeckmann, O. Guillon, M. Bram, Field-Assisted Sintering/Spark Plasma Sintering of Gadolinium-Doped Ceria with Controlled Re-Oxidation for Crack Prevention, Materials 13 (2020) 3184. https://doi.org/10.3390/ma13143184.

[80] O. Guillon, J. Gonzalez-Julian, B. Dargatz, T. Kessel, G. Schierning, J. Räthel, M. Herrmann, Field-Assisted Sintering Technology/Spark Plasma Sintering: Mechanisms, Materials, and Technology Developments, Advanced Engineering Materials 16 (2014) 830–849. https://doi.org/10.1002/adem.201300409.

[81] L. Porz, M. Scherer, D. Huhn, L.-M. Heine, S. Britten, L. Rebohle, M. Neubert, M. Brown, P. Lascelles, R. Kitson, D. Rettenwander, L. Fulanovic, E. Bruder, P. Breckner, D. Isaia, T. Frömling, J. Rödel, W. Rheinheimer, Blacklight sintering of ceramics, Mater. Horiz. 9 (2022) 1717–1726. https://doi.org/10.1039/D2MH00177B.

[82] B.M. Reddy, Redox Properties of Metal Oxides, ChemInform 37 (2006). https://doi.org/10.1002/chin.200610244.

[83] P. Stratton, Ellingham diagrams – their use and misuse, International Heat Treatment and Surface Engineering 7 (2013) 70–73. https://doi.org/10.1179/1749514813Z.00000000053.

[84] M. Hasegawa, Chapter 3.3 - Ellingham Diagram, in: S. Seetharaman (Ed.), Treatise on Process Metallurgy, Elsevier, Boston, 2014: pp. 507–516. https://doi.org/10.1016/B978-0-08-096986-2.00032-1.

[85] C. Baudín, Reaction Sintering, in: M. Pomeroy (Ed.), Encyclopedia of Materials: Technical Ceramics and Glasses, Elsevier, Oxford, 2021: pp. 278–285. https://doi.org/10.1016/B978-0-12-803581-8.11766-7.

[86] J. Hostaša, F. Picelli, S. Hříbalová, V. Nečina, Sintering aids, their role and behaviour in the production of transparent ceramics, Open Ceramics 7 (2021) 100137. https://doi.org/10.1016/j.oceram.2021.100137.

[87] R. Riedel, ed., Ceramics science and technology. 3: Synthesis and processing, Wiley-VCH, Weinheim, 2012.

[88] L.S. Mahmud, A. Muchtar, M.R. Somalu, Challenges in fabricating planar solid oxide fuel cells: A review, Renewable and Sustainable Energy Reviews 72 (2017) 105–116. https://doi.org/10.1016/j.rser.2017.01.019.

[89] J. Pan, G.L. Tonkay, A. Quintero, SCREEN PRINTING PROCESS DESIGN OF EXPERIMENTS FOR FINE LINE PRINTING OF THICK FILM CERAMIC SUBSTRATES, Journal of Electronics Manufacturing 09 (1999) 203–213. https://doi.org/10.1142/S096031319900012X.

[90] P.W. Hawkes, J.C.H. Spence, Springer Handbook of Microscopy, Springer Nature, 2019.

[91] O.C. Wells, Scanning Electron Microscopy, in: K.H.J. Buschow, R.W. Cahn, M.C. Flemings, B. Ilschner, E.J. Kramer, S. Mahajan, P. Veyssière (Eds.), Encyclopedia of Materials: Science and Technology, Elsevier, Oxford, 2001: pp. 8265–8269. https://doi.org/10.1016/B0-08-043152-6/01479-0.

[92] D.R. Pendse, A.K. Chin, Cathodoluminescence and Transmission Cathodoluminescence, in: Encyclopedia of Materials: Science and Technology, Elsevier, 2001: pp. 1–7. https://doi.org/10.1016/B0-08-043152-6/00190-X.

[93] S. Ortanderl, U. Ritgen, Chemie - das Lehrbuch für Dummies, 2. Auflage, Wiley-VCH Verlag GmbH & Co. KGaA, Weinheim, 2018.

[94] U. Ritgen, Analytical chemistry. 1, Springer, Berlin, 2023.

[95] M. Yoshikawa, Advanced Optical Spectroscopy Techniques for Semiconductors: Raman, Infrared, and Cathodoluminescence Spectroscopy, Springer International Publishing, Cham, 2023. https://doi.org/10.1007/978-3-031-19722-2.

[96] P.K. Mallick, Fundamentals of Molecular Spectroscopy, Springer Nature, 2023.

[97] M. Schönleber, D. Klotz, E. Ivers-Tiffée, A Method for Improving the Robustness of linear Kramers-Kronig Validity Tests, Electrochimica Acta 131 (2014) 20–27. https://doi.org/10.1016/j.electacta.2014.01.034.

[98] A.Ch. Lazanas, M.I. Prodromidis, Electrochemical Impedance Spectroscopy—A Tutorial, ACS Meas. Sci. Au 3 (2023) 162–193. https://doi.org/10.1021/acsmeasuresciau.2c00070.

[99] D. Pumiglia, D.P. Massimiliano, A. Monforti Ferrario, S. McPhail, S. Pylypko, Impedance-based Solid Oxide Fuel Cell testing as scalable and reliable Quality Control tool for cell and batch manufacturing: first findings, E3S Web Conf. 334 (2022) 04021. https://doi.org/10.1051/e3sconf/202233404021.

[100] A. Lasia, The Origin of the Constant Phase Element, J. Phys. Chem. Lett. 13 (2022) 580–589. https://doi.org/10.1021/acs.jpclett.1c03782.

[101] J.T.S. Irvine, D.C. Sinclair, A.R. West, Electroceramics: Characterization by Impedance Spectroscopy, Advanced Materials 2 (1990) 132–138. https://doi.org/10.1002/adma.19900020304.

[102] A.W. Coats, J.P. Redfern, Thermogravimetric analysis. A review, Analyst 88 (1963) 906–924. https://doi.org/10.1039/AN9638800906.

[103] E. Pavithra, Dilatometric Methods: Insights of other researchers, IOP Conf. Ser.: Mater. Sci. Eng. 923 (2020) 012041. https://doi.org/10.1088/1757-899X/923/1/012041.

[104] K. Hiraoka, ed., Fundamentals of Mass Spectrometry, Springer New York, New York, NY, 2013. https://doi.org/10.1007/978-1-4614-7233-9.

[105] S. Fearn, An Introduction to Time-of-Flight Secondary Ion Mass Spectrometry (ToF-SIMS) and its Application to Materials Science:, Morgan & Claypool Publishers, 2015. https://doi.org/10.1088/978-1-6817-4088-1.

[106] R.M. Twyman, ATOMIC EMISSION SPECTROMETRY | Principles and Instrumentation, in: P. Worsfold, A. Townshend, C. Poole (Eds.), Encyclopedia of Analytical Science (Second Edition), Elsevier, Oxford, 2005: pp. 190–198. https://doi.org/10.1016/B0-12-369397-7/00029-7.

[107] S. Ghosh, V.L. Prasanna, B. Sowjanya, P. Srivani, M. Alagaraja, Dr.D. Banji, Inductively Coupled Plasma –Optical Emission Spectroscopy: A Review, Asian Journal of Pharmaceutical Analysis 3 (2013) 24–33.

[108] J.E. Funk, D.R. Dinger, Predictive Process Control of Crowded Particulate Suspensions: Applied to Ceramic Manufacturing, Springer Science & Business Media, 2013.

[109] M.R. Somalu, A. Muchtar, W.R.W. Daud, N.P. Brandon, Screen-printing inks for the fabrication of solid oxide fuel cell films: A review, Renewable and Sustainable Energy Reviews 75 (2017) 426–439. https://doi.org/10.1016/j.rser.2016.11.008.

[110] M.R. Somalu, N.P. Brandon, Rheological Studies of Nickel/Scandia-Stabilized-Zirconia Screen Printing Inks for Solid Oxide Fuel Cell Anode Fabrication, Journal of the American Ceramic Society 95 (2012) 1220–1228. https://doi.org/10.1111/j.1551-2916.2011.05014.x.

[111] P.A. Janmey, P.C. Georges, S. Hvidt, Basic Rheology for Biologists, in: Methods in Cell Biology, Academic Press, 2007: pp. 1–27. https://doi.org/10.1016/S0091-679X(07)83001-9.

[112] P. Mohazzab, Archimedes' Principle Revisited, JAMP 05 (2017) 836–843. https://doi.org/10.4236/jamp.2017.54073.

[113] F. Ambroz, T.J. Macdonald, V. Martis, I.P. Parkin, Evaluation of the BET Theory for the Characterization of Meso and Microporous MOFs, Small Methods 2 (2018) 1800173. https://doi.org/10.1002/smtd.201800173.

[114] S. Brunauer, P.H. Emmett, E. Teller, Adsorption of Gases in Multimolecular Layers, J. Am. Chem. Soc. 60 (1938) 309–319. https://doi.org/10.1021/ja01269a023.

[115] G.B.J. de Boer, C. de Weerd, D. Thoenes, H.W.J. Goossens, Laser Diffraction Spectrometry: Fraunhofer Diffraction Versus Mie Scattering, Particle & Particle Systems Characterization 4 (1987) 14–19. https://doi.org/10.1002/ppsc.19870040104.

[116] I. Weiner, M. Rust, T.D. Donnelly, Particle size determination: An undergraduate lab in Mie scattering, American Journal of Physics 69 (2001) 129–136. https://doi.org/10.1119/1.1311785.

[117] W. Nai-Ning, Z. Hong-Jian, Y. Xian-Huang, A versatile Fraunhofer diffraction and Mie scattering based laser particle sizer, Advanced Powder Technology 3 (1992) 7–14. https://doi.org/10.1016/S0921-8831(08)60683-4.

[118] A. Schwiers, C. Lenser, O. Guillon, N.H. Menzler, Interdiffusion at electrochemical interfaces between yttria-stabilized zirconia and doped ceria, Journal of the European Ceramic Society 43 (2023) 6189–6199. https://doi.org/10.1016/j.jeurceramsoc.2023.06.015.

[119] H. Jeong, M. Geis, C. Lenser, S. Lobe, S. Herrmann, S. Fendt, N.H. Menzler, O. Guillon, Coupling SOFCs to biomass gasification – The influence of phenol on cell degradation in simulated bio-syngas. Part II – Post-test analysis, International Journal of Hydrogen Energy 43 (2018) 20911–20920. https://doi.org/10.1016/j.ijhydene.2018.09.006.

[120] H. He, J.M. Hill, Carbon deposition on Ni/YSZ composites exposed to humidified methane, Applied Catalysis A: General 317 (2007) 284–292. https://doi.org/10.1016/j.apcata.2006.10.040.

[121] C.M. Chun, G. Bhargava, T.A. Ramanarayanan, Metal Dusting Corrosion of Nickel-Based Alloys, J. Electrochem. Soc. 154 (2007) C231. https://doi.org/10.1149/1.2710215.

[122] A. Sciazko, T. Shimura, Y. Komatsu, N. Shikazono, Ni-GDC and Ni-YSZ electrodes operated in solid oxide electrolysis and fuel cell modes, Journal of Thermal Science and Technology 16 (2021) JTST0013–JTST0013. https://doi.org/10.1299/jtst.2021jtst0013.

[123] J. Pan, Y. Ye, M. Zhou, X. Sun, Y. Ling, K. Yashiro, Y. Chen, Improving the activity and stability of Ni-based electrodes for solid oxide cells through surface engineering: Recent progress and future perspectives, Materials Reports: Energy 1 (2021) 100025. https://doi.org/10.1016/j.matre.2021.100025.

[124] S.A. Barnett, B.-K. Park, R. Scipioni, Effect of Infiltration on Performance of Ni-YSZ Fuel Electrodes, ECS Trans. 91 (2019) 1791. https://doi.org/10.1149/09101.1791ecst.

[125] N.A.M. Fadzil, M.H.A. Rahim, G.P. Maniam, Brief review of ceria and modified ceria: synthesis and application, Mater. Res. Express 5 (2018) 085019. https://doi.org/10.1088/2053-1591/aad2b5.

[126] R. Schmitt, A. Nenning, O. Kraynis, R. Korobko, A. I. Frenkel, I. Lubomirsky, S. M. Haile, J.L. M. Rupp, A review of defect structure and chemistry in ceria and its solid solutions, Chemical Society Reviews 49 (2020) 554–592. https://doi.org/10.1039/C9CS00588A.

[127] M. Liu, A. van der Kleij, A.H.M. Verkooijen, P.V. Aravind, An experimental study of the interaction between tar and SOFCs with Ni/GDC anodes, Applied Energy 108 (2013) 149–157. https://doi.org/10.1016/j.apenergy.2013.03.020.

[128] J. Uecker, I.D. Unachukwu, V. Vibhu, I.C. Vinke, R.-A. Eichel, L.G.J. (Bert) de Haart, Performance, electrochemical process analysis and degradation of gadolinium doped ceria as fuel electrode material for solid oxide electrolysis cells, Electrochimica Acta 452 (2023) 142320. https://doi.org/10.1016/j.electacta.2023.142320.

[129] R. Mücke, N.H. Menzler, H.P. Buchkremer, D. Stöver, Cofiring of Thin Zirconia Films During SOFC Manufacturing, Journal of the American Ceramic Society 92 (2009). https://doi.org/10.1111/j.1551-2916.2008.02707.x.

[130] H. Xu, K. Cheng, M. Chen, L. Zhang, K. Brodersen, Y. Du, Interdiffusion between gadolinia doped ceria and yttria stabilized zirconia in solid oxide fuel cells: Experimental investigation and kinetic modeling, Journal of Power Sources 441 (2019) 227152. https://doi.org/10.1016/j.jpowsour.2019.227152.

[131] K. Yang, J.-H. Shen, K.-Y. Yang, I.-M. Hung, K.-Z. Fung, M.-C. Wang, Formation of $La_2Zr_2O_7$ or $SrZrO_3$ on cathode-supported solid oxide fuel cells, Journal of Power Sources 159 (2006) 63–67. https://doi.org/10.1016/j.jpowsour.2006.04.049.

[132] J. Szász, F. Wankmüller, V. Wilde, H. Störmer, D. Gerthsen, N.H. Menzler, E. Ivers-Tiffée, Nature and Functionality of $La_{0.58}Sr_{0.4}Co_{0.2}Fe_{0.8}O_{3-\delta}$ / $Gd_{0.2}Ce_{0.8}O_{2-\delta}$ / $Y_{0.16}Zr_{0.84}O_{2-\delta}$ Interfaces in SOFCs, J. Electrochem. Soc. 165 (2018) F898. https://doi.org/10.1149/2.0031811jes.

[133] Z. Lu, S. Darvish, J. Hardy, J. Templeton, J. Stevenson, Y. Zhong, $SrZrO_3$ Formation at the Interlayer/Electrolyte Interface during $(La_{1-x}Sr_x)_{1-\delta}Co_{1-y}Fe_yO_3$ Cathode Sintering, J. Electrochem. Soc. 164 (2017) F3097. https://doi.org/10.1149/2.0141710jes.

[134] V. Wilde, H. Störmer, J. Szász, F. Wankmüller, E. Ivers-Tiffée, D. Gerthsen, Effect of $Gd_{0.2}Ce_{0.8}O_2$ Sintering Temperature on Formation of a $SrZrO_3$ Blocking Layer between $Y_{0.16}Zr_{0.84}O_2$, $Gd_{0.2}Ce_{0.8}O_2$ and $La_{0.58}Sr_{0.4}Co_{0.2}Fe_{0.8}O_3$, ECS Trans. 66 (2015) 103. https://doi.org/10.1149/06602.0103ecst.

[135] J. Szász, F. Wankmüller, V. Wilde, H. Störmer, D. Gerthsen, N.H. Menzler, E. Ivers-Tiffée, High-Performance Cathode/Electrolyte Interfaces for SOFC, ECS Trans. 68 (2015) 763. https://doi.org/10.1149/06801.0763ecst.

[136] T. Kawada, H. Yokokawa, M. Dokiya, N. Sakai, T. Horita, J. Van Herle, K. Sasaki, Ceria-Zirconia Composite Electrolyte for Solid Oxide Fuel Cells, Journal of Electroceramics 1 (1997) 155–164. https://doi.org/10.1023/A:1009976700704.

[137] A. Tsoga, A. Gupta, A. Naoumidis, D. Skarmoutsos, P. Nikolopoulos, Performance of a double-layer CGO/YSZ electrolyte for solid oxide fuel cells, Ionics 4 (1998) 234–240. https://doi.org/10.1007/BF02375951.

[138] A. Tsoga, A. Gupta, A. Naoumidis, P. Nikolopoulos, Gadolinia-doped ceria and yttria stabilized zirconia interfaces: regarding their application for SOFC technology, Acta Materialia 48 (2000) 4709–4714. https://doi.org/10.1016/S1359-6454(00)00261-5.

[139] K. Eguchi, N. Akasaka, H. Mitsuyasu, Y. Nonaka, Process of solid state reaction between doped ceria and zirconia, Solid State Ionics 135 (2000) 589–594. https://doi.org/10.1016/S0167-2738(00)00416-1.

[140] J.A. Labrincha, F.M.B. Marques, J.R. Frade, Protonic and oxygen-ion conduction in $SrZrO_3$-based materials, JOURNAL OF MATERIALS SCIENCE 30 (1995) 2785–2792. https://doi.org/10.1007/BF00349644.

[141] J. Szász, F. Wankmüller, J. Joos, V. Wilde, H. Störmer, D. Gerthsen, E. Ivers-Tiffée, Correlating Cathode/Electrolyte Interface Characteristics to SOFC Performance, ECS Trans. 77 (2017) 27. https://doi.org/10.1149/07710.0027ecst.

[142] C. Lenser, H. Jeong, Y.J. Sohn, N. Russner, O. Guillon, N.H. Menzler, Interaction of a ceria-based anode functional layer with a stabilized zirconia electrolyte: Considerations from a materials perspective, Journal of the American Ceramic Society 101 (2018) 739–748. https://doi.org/10.1111/jace.15214.

[143] R.D. Shannon, Revised effective ionic radii and systematic studies of interatomic distances in halides and chalcogenides, Acta Cryst A 32 (1976) 751–767. https://doi.org/10.1107/S0567739476001551.

[144] M. Zienius, K. Bockute, D. Virbukas, G. Laukaitis, Oxygen ion conductivity in samarium and gadolinium stabilized cerium oxide heterostructures, Solid State Ionics 302 (2017) 138–142. https://doi.org/10.1016/j.ssi.2016.11.025.

[145] S. Kuharuangrong, Ionic conductivity of Sm, Gd, Dy and Er-doped ceria, Journal of Power Sources 171 (2007) 506–510. https://doi.org/10.1016/j.jpowsour.2007.05.104.

[146] A. Tsoga, A. Naoumidis, D. Stöver, Total electrical conductivity and defect structure of ZrO_2–CeO_2–Y_2O_3–Gd_2O_3 solid solutions, Solid State Ionics 135 (2000) 403–409. https://doi.org/10.1016/S0167-2738(00)00477-X.

[147] A. Varez, E. Garcia-Gonzalez, J. Sanz, Cation miscibility in CeO_2 –ZrO_2 oxides with fluorite structure. A combined TEM , SAED and XRD Rietveld analysis, Journal of Materials Chemistry 16 (2006) 4249–4256. https://doi.org/10.1039/B607778A.

[148] A. Tsoga, A. Naoumidis, A. Gupta, D. Stöver, Microstructure and Interdiffusion Phenomena in YSZ-CGO Composite Electrolyte, Materials Science Forum 308–311 (1999) 794–799. https://doi.org/10.4028/www.scientific.net/MSF.308-311.794.

[149] E. Tani, M. Yoshimura, S. Somiya, Revised Phase Diagram of the System ZrO_2-CeO_2 Below 1400°C, Journal of the American Ceramic Society 66 (1983) 506–510. https://doi.org/10.1111/j.1151-2916.1983.tb10591.x.

[150] M. Price, J. Dong, X. Gu, S.A. Speakman, E.A. Payzant, T.M. Nenoff, Formation of YSZ–SDC Solid Solution in a Nanocrystalline Heterophase System and Its Effect

on the Electrical Conductivity, Journal of the American Ceramic Society 88 (2005) 1812–1818. https://doi.org/10.1111/j.1551-2916.2005.00389.x.

[151] T. Sasaki, Y. Ukyo, K. Kuroda, S. Arai, S. Muto, H. Saka, Crystal Structure of $Ce_2Zr_2O_7$ and b$Ce_2Zr_2O_{7.5}$, Journal of the Ceramic Society of Japan 112 (2004) 440–444.

[152] I. Kosacki, V. Petrovsky, H.U. Anderson, P. Colomban, Raman Spectroscopy of Nanocrystalline Ceria and Zirconia Thin Films, Journal of the American Ceramic Society 85 (2002) 2646–2650. https://doi.org/10.1111/j.1151-2916.2002.tb00509.x.

[153] T. Otake, H. Yugami, H. Naito, K. Kawamura, T. Kawada, J. Mizusaki, Ce^{3+} concentration in ZrO_2–CeO_2–Y_2O_3 system studied by electronic Raman scattering, Solid State Ionics 135 (2000) 663–667. https://doi.org/10.1016/S0167-2738(00)00428-8.

[154] T. Cooper, J.R. Scheffe, M.E. Galvez, R. Jacot, G. Patzke, A. Steinfeld, Lanthanum Manganite Perovskites with Ca/Sr A-site and Al B-site Doping as Effective Oxygen Exchange Materials for Solar Thermochemical Fuel Production, Energy Technology 3 (2015) 1130–1142. https://doi.org/10.1002/ente.201500226.

[155] G. Kim, J.M. Vohs, R.J. Gorte, Enhanced reducibility of ceria–YSZ composites in solid oxide electrodes, J. Mater. Chem. 18 (2008) 2386–2390. https://doi.org/10.1039/B718931A.

[156] Z. Yang, T.K. Woo, K. Hermansson, Effects of Zr doping on stoichiometric and reduced ceria: A first-principles study, The Journal of Chemical Physics 124 (2006) 224704. https://doi.org/10.1063/1.2200354.

[157] N. Yang, P. Orgiani, E. Di Bartolomeo, V. Foglietti, P. Torelli, A.V. Ievlev, G. Rossi, S. Licoccia, G. Balestrino, S.V. Kalinin, C. Aruta, Effects of Dopant Ionic Radius on Cerium Reduction in Epitaxial Cerium Oxide Thin Films, J. Phys. Chem. C 121 (2017) 8841–8849. https://doi.org/10.1021/acs.jpcc.7b00386.

[158] J.E. Bauerle, Study of solid electrolyte polarization by a complex admittance method, Journal of Physics and Chemistry of Solids 30 (1969) 2657–2670. https://doi.org/10.1016/0022-3697(69)90039-0.

[159] T. van Dijk, A.J. Burggraaf, Grain boundary effects on ionic conductivity in ceramic GdxZr1–xO2–(x/2) solid solutions, Physica Status Solidi (a) 63 (1981) 229–240. https://doi.org/10.1002/pssa.2210630131.

[160] J. Fleig, J. Maier, The impedance of ceramics with highly resistive grain boundaries: validity and limits of the brick layer model, Journal of the European Ceramic Society 19 (1999) 693–696. https://doi.org/10.1016/S0955-2219(98)00298-2.

[161] J. Luo, R.J. Ball, R. Stevens, Gadolinia doped ceria/yttria stabilised zirconia electrolytes for solid oxide fuel cell applications, Journal of Materials Science 39 (2004) 235–240. https://doi.org/10.1023/B:JMSC.0000007749.72739.bb.

[162] V. Rührup, H.-D. Wiemhöfer, Ionic Conductivity of Gd- and Y-Doped Ceria-Zirconia Solid Solutions, Zeitschrift Für Naturforschung B 61 (2006) 916–922. https://doi.org/10.1515/znb-2006-0721.

[163] A. Arabaci, Effect of Sm and Gd dopants on structural characteristics and ionic conductivity of ceria, Ceramics International 41 (2015) 5836–5842. https://doi.org/10.1016/j.ceramint.2015.01.013.

[164] S.B. Herner, B.P. Gila, K.S. Jones, H. -J. Gossmann, J.M. Poate, H.S. Luftman, Surface roughness-induced artifacts in secondary ion mass spectrometry depth profiling and a simple technique to smooth the surface, Journal of Vacuum Science & Technology B: Microelectronics and Nanometer Structures Processing, Measurement, and Phenomena 14 (1996) 3593–3595. https://doi.org/10.1116/1.588731.

[165] G.E. Lloyd, Atomic number and crystallographic contrast images with the SEM: a review of backscattered electron techniques, Mineralogical Magazine 51 (1987) 3–19. https://doi.org/10.1180/minmag.1987.051.359.02.

[166] F. Wankmüller, J. Szász, J. Joos, V. Wilde, H. Störmer, D. Gerthsen, E. Ivers-Tiffée, Correlative tomography at the cathode/electrolyte interfaces of solid oxide fuel cells, Journal of Power Sources 360 (2017) 399–408. https://doi.org/10.1016/j.jpowsour.2017.06.008.

[167] M. Ozawa, K. Imura, Cation Diffusion at Interface between Y_2O_3 Stabilized ZrO_2 and CeO_2, **粉体および粉末冶金** 65 (2018) 187–190. https://doi.org/10.2497/jjspm.65.187.

[168] A.E. Hughes, B.A. Sexton, XPS study of an intergranular phase in yttria-zirconia, J Mater Sci 24 (1989) 1057–1061. https://doi.org/10.1007/BF01148798.

[169] A.E. Hughes, S.P.S. Badwal, Impurity and yttrium segregation in yttria-tetragonal zirconia, Solid State Ionics 46 (1991) 265–274. https://doi.org/10.1016/0167-2738(91)90225-Z.

[170] P.J. Scanlon, R.A.M. Bink, F.P.F. van Berkel, G.M. Christie, L.J. van IJzendoorn, H.H. Brongersma, R.G. van Welzenis, Surface composition of ceramic CeGd–oxide, Solid State Ionics 112 (1998) 123–130. https://doi.org/10.1016/S0167-2738(98)00198-2.

[171] G.S.A.M. Theunissen, A.J.A. Winnubst, A.J. Burggraaf, Segregation aspects in the ZrO_2-Y_2O_3 ceramic system, J Mater Sci Lett 8 (1989) 55–57. https://doi.org/10.1007/BF00720250.

[172] H.B. Lee, F.B. Prinz, W. Cai, Atomistic simulations of surface segregation of defects in solid oxide electrolytes, Acta Materialia 58 (2010) 2197–2206. https://doi.org/10.1016/j.actamat.2009.12.005.

[173] S.A. Acharya, V.M. Gaikwad, S.W. D'Souza, S.R. Barman, Gd/Sm dopant-modified oxidation state and defect generation in nano-ceria, Solid State Ionics 260 (2014) 21–29. https://doi.org/10.1016/j.ssi.2014.03.008.

[174] A. Nenning, C. Bischof, J. Fleig, M. Bram, A.K. Opitz, The Relation of Microstructure, Materials Properties and Impedance of SOFC Electrodes: A Case Study of Ni/GDC Anodes, Energies 13 (2020) 987. https://doi.org/10.3390/en13040987.

[175] J.D. Vero, K.D.- Bagarinao, D.-H. Cho, H. Kishimoto, K. Yamaji, H. Yokokawa, T. Horita, Effect of LSCF Microstructure on GDC Interlayer Stability and Cation

Diffusion in Porous and Dense LSCF/GDC/YSZ Triplets, ECS Trans. 68 (2015) 1943. https://doi.org/10.1149/06801.1943ecst.

[176] R.M. Batista, E.N.S. Muccillo, Densification and grain growth of 8YSZ containing NiO, Ceramics International 37 (2011) 1047–1053. https://doi.org/10.1016/j.ceramint.2010.11.031.

[177] C.-Y. Chen, Y.-R. Lyu, Effect of NiO addition on properties of bulk yttria-doped ceria sintered from their spray pyrolyzed powder, Ceramics International 38 (2012) 3291–3300. https://doi.org/10.1016/j.ceramint.2011.12.036.

[178] D. Xu, K. Li, Y. Zhou, Y. Gao, D. Yan, S. Xu, The effect of NiO addition on the grain boundary behavior and electrochemical performance of Gd-doped ceria solid electrolyte under different sintering conditions, Journal of the European Ceramic Society 37 (2017) 419–425. https://doi.org/10.1016/j.jeurceramsoc.2016.07.026.

[179] F. Ye, T. Mori, D.R. Ou, J. Zou, J. Drennan, S. Nakayama, M. Miyayama, Effect of nickel diffusion on the microstructure of Gd-doped ceria (GDC) electrolyte film supported by Ni–GDC cermet anode, Solid State Ionics 181 (2010) 646–652. https://doi.org/10.1016/j.ssi.2010.03.012.

[180] S. Nikodemski, J. Tong, R. O'Hayre, Solid-state reactive sintering mechanism for proton conducting ceramics, Solid State Ionics 253 (2013) 201–210. https://doi.org/10.1016/j.ssi.2013.09.025.

[181] K.-R. Lee, C.-J. Tseng, S.-C. Jang, J.-C. Lin, K.-W. Wang, J.-K. Chang, T.-C. Chen, S.-W. Lee, Fabrication of anode-supported thin BCZY electrolyte protonic fuel cells using NiO sintering aid, International Journal of Hydrogen Energy 44 (2019) 23784–23792. https://doi.org/10.1016/j.ijhydene.2019.07.097.

[182] Y. Huang, R. Merkle, J. Maier, Effects of NiO addition on sintering and proton uptake of $Ba(Zr,Ce,Y)O_{3-\delta}$, Journal of Materials Chemistry A 9 (2021) 14775–14785. https://doi.org/10.1039/D1TA02555D.

[183] J.C. Chen, G.H. Shen, L.J. Chen, Interfacial reactions of Gd thin films on (111) and (001)Si, Applied Surface Science 142 (1999) 291–294. https://doi.org/10.1016/S0169-4332(98)00639-4.

[184] Y. Wang, F. Wang, Q. Song, Q. Xin, S. Xu, J. Xu, Heterogeneous Ceria Catalyst with Water-Tolerant Lewis Acidic Sites for One-Pot Synthesis of 1,3-Diols via Prins Condensation and Hydrolysis Reactions, J. Am. Chem. Soc. 135 (2013) 1506–1515. https://doi.org/10.1021/ja310498c.

[185] T. Nakamura, K. Yashiro, A. Kaimai, T. Otake, K. Sato, T. Kawada, J. Mizusaki, Determination of the Reaction Zone in Gadolinia-Doped Ceria Anode for Solid Oxide Fuel Cell, J. Electrochem. Soc. 155 (2008) B1244. https://doi.org/10.1149/1.2975322.

[186] J. Nielsen, T. Klemensø, P. Blennow, Detailed impedance characterization of a well performing and durable Ni:CGO infiltrated cermet anode for metal-supported solid oxide fuel cells, Journal of Power Sources 219 (2012) 305–316. https://doi.org/10.1016/j.jpowsour.2012.07.031.

[187] A. Sciazko, Y. Komatsu, T. Shimura, Y. Sunada, N. Shikazono, Correlation Between Microstructure and Performance of GDC-Based Electrodes, ECS Trans. 111 (2023) 349. https://doi.org/10.1149/11106.0349ecst.

[188] S. Dierickx, T. Mundloch, A. Weber, E. Ivers-Tiffée, Advanced impedance model for double-layered solid oxide fuel cell cermet anodes, Journal of Power Sources 415 (2019) 69–82. https://doi.org/10.1016/j.jpowsour.2019.01.043.

[189] A. Schwiers, D. Röhrer, C. Lenser, B. Steinrücken, D. Sebold, H. Spliethoff, O. Guillon, N.H. Menzler, Phase stability, redox-behavior and carbon-tolerance of $Sr_{1-x}(Ti_{0.3}Fe_{0.7-y}Ni_y)O_{3-\delta}$ with exsolved nanoparticles, J. Mater. Chem. A (2024). https://doi.org/10.1039/D3TA05813A.

[190] P. Goel, S. Sundriyal, V. Shrivastav, S. Mishra, D.P. Dubal, K.-H. Kim, A. Deep, Perovskite materials as superior and powerful platforms for energy conversion and storage applications, Nano Energy 80 (2021) 105552. https://doi.org/10.1016/j.nanoen.2020.105552.

[191] S. Molin, W. Lewandowska-Iwaniak, B. Kusz, M. Gazda, P. Jasinski, Structural and electrical properties of $Sr(Ti, Fe)O_{3-\delta}$ materials for SOFC cathodes, J Electroceram 28 (2012) 80–87. https://doi.org/10.1007/s10832-012-9683-x.

[192] W. Jung, H.L. Tuller, Impedance study of $SrTi_{1-x}FexO_{3-\delta}$ (x=0.05 to 0.80) mixed ionic-electronic conducting model cathode, Solid State Ionics 180 (2009) 843–847. https://doi.org/10.1016/j.ssi.2009.02.008.

[193] T. Zhu, H.E. Troiani, L.V. Mogni, M. Han, S.A. Barnett, Ni-Substituted $Sr(Ti,Fe)O_3$ SOFC Anodes: Achieving High Performance via Metal Alloy Nanoparticle Exsolution, Joule 2 (2018) 478–496. https://doi.org/10.1016/j.joule.2018.02.006.

[194] M. Santaya, C.E. Jiménez, H.E. Troiani, E.A. Carbonio, M.D. Arce, L.M. Toscani, R. Garcia-Diez, R.G. Wilks, A. Knop-Gericke, M. Bär, L.V. Mogni, Tracking the nanoparticle exsolution/reoxidation processes of Ni-doped $SrTi_{0.3}Fe_{0.7}O_{3-\delta}$ electrodes for intermediate temperature symmetric solid oxide fuel cells, J. Mater. Chem. A 10 (2022) 15554–15568. https://doi.org/10.1039/D2TA02959F.

[195] J. Wang, D. Kalaev, J. Yang, I. Waluyo, A. Hunt, J.T. Sadowski, H.L. Tuller, B. Yildiz, Fast Surface Oxygen Release Kinetics Accelerate Nanoparticle Exsolution in Perovskite Oxides, J. Am. Chem. Soc. 145 (2023) 1714–1727. https://doi.org/10.1021/jacs.2c10256.

[196] C. Wagner, The determination of small deviations from the ideal stoichiometric composition of ionic crystals and other binary compounds, Progress in Solid State Chemistry 6 (1971) 1–15. https://doi.org/10.1016/0079-6786(71)90026-4.

[197] A. Nenning, L. Volgger, E. Miller, L.V. Mogni, S. Barnett, J. Fleig, The Electrochemical Properties of $Sr(Ti,Fe)O_{3-\delta}$ for Anodes in Solid Oxide Fuel Cells, J. Electrochem. Soc. 164 (2017) F364. https://doi.org/10.1149/2.1271704jes.

[198] L. Fournès, Y. Potin, J.C. Grenier, G. Demazeau, M. Pouchard, High temperature Mössbauer spectroscopy of some $SrFeO_{3-y}$ phases, Solid State Communications 62 (1987) 239–244. https://doi.org/10.1016/0038-1098(87)90803-9.

[199] O.I. Barkalov, S.V. Zaitsev, V.D. Sedykh, Strontium ferrite $SrFeO_{3-\delta}$ ($2.50 \leq 3-\delta \leq 2.87$) studied by Raman and Mössbauer spectroscopy, Solid State Communications 354 (2022) 114912. https://doi.org/10.1016/j.ssc.2022.114912.

[200] J. Mizusaki, M. Yoshihiro, S. Yamauchi, K. Fueki, Nonstoichiometry and defect structure of the perovskite-type oxides $La_{1-x}Sr_xFeO_{3-\delta}$, Journal of Solid State Chemistry 58 (1985) 257–266. https://doi.org/10.1016/0022-4596(85)90243-9.

[201] M. Kuhn, S. Hashimoto, K. Sato, K. Yashiro, J. Mizusaki, Oxygen nonstoichiometry, thermo-chemical stability and lattice expansion of $La_{0.6}Sr_{0.4}FeO_{3-\delta}$, Solid State Ionics 195 (2011) 7–15. https://doi.org/10.1016/j.ssi.2011.05.013.

[202] K. Sreedeviamma Dijith, R. Aiswarya, M. Praveen, S. Pillai, K. Peethambharan Surendran, Polyol derived Ni and NiFe alloys for effective shielding of electromagnetic interference, Materials Chemistry Frontiers 2 (2018) 1829–1841. https://doi.org/10.1039/C8QM00264A.

[203] S.H. Khezri, A. Yazdani, R. Khordad, Pure iron nanoparticles prepared by electric arc discharge method in ethylene glycol, The European Physical Journal - Applied Physics 59 (2012) 30401. https://doi.org/10.1051/epjap/2012110303.

[204] A. Cuesta, P. Dhamelincourt, J. Laureyns, A. Martínez-Alonso, J.M.D. Tascón, Raman microprobe studies on carbon materials, Carbon 32 (1994) 1523–1532. https://doi.org/10.1016/0008-6223(94)90148-1.

[205] B.E. Hayden, F.K. Rogers, Oxygen reduction and oxygen evolution on $SrTi_{1-x}Fe_xO_{3-y}$ (STFO) perovskite electrocatalysts, Journal of Electroanalytical Chemistry 819 (2018) 275–282. https://doi.org/10.1016/j.jelechem.2017.10.056.

[206] M. Vračar, A. Kuzmin, R. Merkle, J. Purans, E.A. Kotomin, J. Maier, O. Mathon, Jahn-Teller distortion around Fe^{4+} in $Sr(Fe_xTi_{1-x})O_{3-\delta}$ from x-ray absorption spectroscopy, x-ray diffraction, and vibrational spectroscopy, Phys. Rev. B 76 (2007) 174107. https://doi.org/10.1103/PhysRevB.76.174107.

[207] W.G. Nilsen, J.G. Skinner, Raman Spectrum of Strontium Titanate, The Journal of Chemical Physics 48 (2003) 2240–2248. https://doi.org/10.1063/1.1669418.

[208] V. Damljanovic, Raman scattering, magnetization and magnetotransport study of $SrFeO_{3-delta}$, Sr3Fe2$O_{7-delta}$ and $CaFeO_3$, Dissertation, Universität Stuttgart & Max-Planck-Institut für Festkörperforschung, 2008. https://doi.org/10.18419/OPUS-6680 (accessed July 29, 2023).

[209] A.M. Beale, M. Paul, G. Sankar, R.J. Oldman, C.R.A. Catlow, S. French, M. Fowles, Combined experimental and computational modelling studies of the solubility of nickel in strontium titanate, J. Mater. Chem. 19 (2009) 4391–4400. https://doi.org/10.1039/B902591J.

[210] I.A. Sluchinskaya, A.I. Lebedev, A. Erko, Structural position and oxidation state of nickel in $SrTiO_3$, J. Adv. Dielect. 03 (2013) 1350031. https://doi.org/10.1142/S2010135X13500318.

[211] M.C.D. Lacharme, A. Donazzi, Characterization and Testing of Exsolution-Based Solid Oxide Cells for Reversible Operations in CO_2 Electrolysis, ECS Trans. 111 (2023) 1867. https://doi.org/10.1149/11106.1867ecst.

[212] Y. Liu, S. Baumann, F. Schulze-Küppers, D.N. Mueller, O. Guillon, Co and Fe co-doping influence on functional properties of $SrTiO_3$ for use as oxygen transport membranes, Journal of the European Ceramic Society 38 (2018) 5058–5066. https://doi.org/10.1016/j.jeurceramsoc.2018.07.037.

[213] X. Yin, L. Bencze, V. Motalov, R. Spatschek, L. Singheiser, Thermodynamic perspective of Sr-related degradation issues in SOFCs, International Journal of Applied Ceramic Technology 15 (2018) 380–390. https://doi.org/10.1111/ijac.12809.

[214] V.A. Mikhailov, G. Akibo-Betts, A.J. Stace, On the Reactions of Ca_n^+, Sr_n^+, and Ba_n^+ with Water and Alcohols, J. Phys. Chem. A 106 (2002) 8583–8589. https://doi.org/10.1021/jp021091k.

[215] P. Sarin, V.L. Snoeyink, D.A. Lytle, W.M. Kriven, Iron Corrosion Scales: Model for Scale Growth, Iron Release, and Colored Water Formation, Journal of Environmental Engineering 130 (2004) 364–373. https://doi.org/10.1061/(ASCE)0733-9372(2004)130:4(364).

[216] S. Caré, R. Crane, P.S. Calabrò, A. Ghauch, E. Temgoua, C. Noubactep, Modeling the Permeability Loss of Metallic Iron Water Filtration Systems, CLEAN – Soil, Air, Water 41 (2013) 275–282. https://doi.org/10.1002/clen.201200167.

List of tables

List of figures

Acknowledgements

I would like to express my gratitude to my supervisors, Hon. Prof. Norbert H. Menzler and Dr. Christian Lenser, for giving me the opportunity to pursue my Ph.D. journey. Despite the initial challenges, and the disruptive impact of the corona pandemic that left the institute's corridors empty, you were always available for questions and discussions.

A special mention goes to Univ. Prof. Joachim Mayer, who graciously agreed to be the examiner for my thesis.

I owe a debt of gratitude to Dr. Moritz L. Weber, whose introduction led me to the research environment at FZJ, where I successfully completed my master's thesis at PGI-7. Likewise, Dr. Felix Gunkel played a pivotal role in introducing me to IEK-1, where I continued my academic journey.

From the beginning of my bachelor's degree to my current pursuit of a Ph.D., my friends from Lerngruppe 1* have been a constant source of support. Their willingness to engage in discussions, offer assistance, and, let's not forget, enjoy a few beers together, has made this journey all the more enjoyable.

Within the institute, my colleagues and friends, especially "RAUM 152," have been a tremendous source of support during the challenging and stressful times, significantly enhancing my overall experience. I am grateful to Daniel Röhrer who supported me with experimental work in the framework of his master's thesis.

Midway through my Ph.D. endeavor, I had the privilege of meeting my girlfriend, Pia, whose support and encouragement were instrumental in helping me overcome moments of overwhelming stress. Thank you, Pia, for being by my side.

Last but certainly not least, I need to deeply thank my parents, who have been my support system throughout my entire life, and continue to be to this day. It is your unwavering belief in me that laid the foundation for all of this to become possible in the first place.

Thank you to each and every one of you for being an integral part of my journey and for making it a memorable and enriching experience.

Band / Volume 621
Ceria-based composites for application in Oxygen transport membranes
L. Fischer (2024), xiii, 216 pp
ISBN: 978-3-95806-739-4

Band / Volume 622
Investigations of Air Quality Aspects with the Urban Climate Model PALM4U
R. Wegener, U. Javed, R. Dubus, and D. Klemp (2024), 93 pp
ISBN: 978-3-95806-741-7

Band / Volume 623
The Chemical Budget of Radicals and Reaction Mechanisms of the Atmospheric Oxidation of Monoterpenes Investigated in the Atmospheric Simulation Chamber SAPHIR
Y. S. Pang (2024), VI, 158 pp
ISBN: 978-3-95806-742-4

Band / Volume 624
Optimizing spectral electrical impedance tomography technology for improved subsurface characterization
H. Wang (2024), xxix, 113 pp
ISBN: 978-3-95806-744-8

Band / Volume 625
On a multi-spectral method for measuring aerosol properties, suitable for operation on iagos passenger aircraft
P. Weber (2024), ca 123 pp
ISBN: 978-3-95806-746-2

Band / Volume 626
Modellierung der flächendifferenzierten Grundwasserneubildung für Schleswig-Holstein
Endbericht
I. McNamara, B. Tetzlaff, T. Wolters, F. Wendland (2024), 96 pp
ISBN: 978-3-95806-748-6

Band / Volume 627
Modeling orographic gravity waves from source to termination to improve parameterization schemes in climate models
S. Rhode (2024), xii, ii, 138 pp
ISBN: 978-3-95806-750-9

Band / Volume 628
Abscheidung kolumnarer Wärmedämmschichten mittels Suspensionsplasmaspritzen (SPS) und Plasma Spray – Physical Vapor Deposition (PS-PVD) Prozess
J. Joeris (2024), vii, 133 pp
ISBN: 978-3-95806-752-3

Band / Volume 629
Structure and properties of electrochemical interfaces from first principles simulations
R. Tesch (2024), xvi, 161 pp
ISBN: 978-3-95806-753-0

Band / Volume 630
Elucidation of Barocaloric Effect in Spin Crossover Compounds
H. Shahed (2024), x, 261 pp
ISBN: 978-3-95806-758-5

Band / Volume 631
Computational Investigation of Solvation Phenomena at Metal-Electrolyte Interfaces
O. Cheong (2024), xvii, 142 pp
ISBN: 978-3-95806-759-2

Band / Volume 632
Senkung zukünftiger Stickoxid- und Partikelemissionen in Nordrhein-Westfalen durch den Einsatz alternativer Energieträger und Antriebe
J. L. Breuer (2024), vii, 339 pp
ISBN: 978-3-95806-760-8

Band / Volume 633
Development of Model-Based Correction Methods for Temperature-Dependent Electromagnetic Induction (EMI) Measurement Errors in Soil Conductivity Estimations
T. M. Tchantcho Amin (2024), xx, 100 pp
ISBN: 978-3-95806-761-5

Band / Volume 634
Investigation and implementation of improved and degradation-tolerant fuel electrodes for solid oxide cells
A. Schwiers (2024), VI, 163, XIII pp
ISBN: 978-3-95806-762-2

Energie & Umwelt / Energy & Environment
Band / Volume 634
ISBN 978-3-95806-762-2

Mitglied der Helmholtz-Gemeinschaft

JÜLICH
Forschungszentrum